Titre: Title:	Eumelanin for Organic Electronics : Film Formation and Transport Physics
Auteur: Author:	Manuel Reali
Date:	2021
Type:	Mémoire ou thèse / Dissertation or Thesis
Référence: Citation:	Reali, M. (2021). Eumelanin for Organic Electronics : Film Formation and Transport Physics [Ph.D. thesis, Polytechnique Montréal]. PolyPublie. https://publications.polymtl.ca/9953/

Document en libre accès dans PolyPublie
Open Access document in PolyPublie

URL de PolyPublie: PolyPublie URL:	https://publications.polymtl.ca/9953/
Directeurs de recherche: Advisors:	Clara Santato, & Fabio Cicoira
Programme: Program:	Génie physique

POLYTECHNIQUE MONTRÉAL

affiliée à l'Université de Montréal

Eumelanin for Organic Electronics : Film Formation and Transport Physics

MANUEL REALI

Département de génie physique

Thèse présentée en vue de l'obtention du diplôme de *Philosophiae Doctor*

Génie physique

Décembre 2021

POLYTECHNIQUE MONTRÉAL

affiliée à l'Université de Montréal

Cette thèse intitulée :

Eumelanin for Organic Electronics : Film Formation and Transport Physics

présentée par **Manuel REALI**

en vue de l'obtention du diplôme de *Philosophiae Doctor*

a été dûment acceptée par le jury d'examen constitué de :

Arthur YELON, président

Clara SANTATO, membre et directrice de recherche

Fabio CICOIRA, membre et codirecteur de recherche

Lucien WEISS, membre

Oana JURCHESCU, membre externe

DEDICATION

"Imagination is more important than knowledge.

Imagination takes you everywhere.

Imagination is everything: it is the preview of life's coming attractions."

Albert Einstein

ACKNOWLEDGEMENTS

Un ringraziamento unico spetta a tutta la famiglia e agli amici più cari. Vorrei anzitutto iniziare da mia moglie, Francesca. Ti ho ritenuta unica da sempre, sin dal primo momento che ti ho conosciuta. E non mi sbagliavo! In questa esperienza di vita che abbiamo intrapreso in Canada con l'inizio del mio dottorato, hai messo da parte per un po' i tuoi sogni e ambizioni. Hai sofferto in silenzio, senza mai darlo a vedere e tutto questo per seguire me e la mia passione per la scienza. Ripensando a tutto il cammino fatto insieme, senza il tuo supporto (e sopportazione!), il tuo amore incondizionato, il tuo continuo incoraggiamento, non avrei mai potuto raggungere gli obiettivi di questo dottorato. Sei stata la mia estenzione, la mia forza, spesso e volentieri la mia coscienza. Hai sempre stimolato e supportato la mia creatività, mi hai spinto a dare il meglio di me in ogni circostanza e a non mollare mai. Sei la mia anima gemella, la metà che mi completa, l'amore della vita. Grazie per tutto quello che mi dai quotidianamente, grazie del tuo amore infinito. Ti amo infinitamente.

Mamma, papà, grazie di tutto il supporto, del sostegno e dell' amore incondizionato. So che non è stato facile per voi accettare la partenza di un figlio per un paese lontano. Avete contribuito a rendermi l'uomo che sono oggi. Spero di avervi reso fieri, di poter fare altrettanto per il resto dei miei giorni e di potervi dare anche solo una piccola parte di ciò che voi avete dato a me. Grazie di tutto di cuore, vi voglio tanto bene.

Grazie ad Annarita, Dennis, Matteo, Sara, Giacomo e alla mia nipotina Giulia. Vi ringrazio per aver sempre creduto in me, per avermi incoraggiato quando le cose non andavano per il verso giusto. Vi ringrazio infinitamente di essere parte della mia vita! Siete tutti speciali e sono orgoglioso di far parte di questa famiglia. Grazie a Dora, Benedetto e Anna, Anna Nicolai, Piera.

Un grazie unico ai miei nonni Nerina e Franco per il loro amore sconfinato e il loro supporto. Siete due rocce e da voi ho imparato a non mollare mai! Vi voglio bene! Nonna Francesca e nonno Filippo, mi mancate come l'aria, vi penso ogni giorno. Nonno Filippo, questa tesi di dottorato la dedico a te per il tuo amore per la conoscenza e per la cultura. Sei stato un esempio di vita per me e non dimenticherò mai i tuoi insegnamenti. Ringrazio gli zii Daniela, Enzo, Marcello, Elena, Peppe e le mie due adorate cugine Luana e Simona per aver sempre creduto in me, per il supporto e il vivo interesse mostrato per questo lavoro di dottorato.

RÉSUMÉ

Les Nations unies ont défini le développement durable comme "la capacité de répondre aux besoins des générations actuelles sans compromettre ceux des générations futures [...]"[1]. L'accès à une énergie propre et peu coûteuse est primordial pour atteindre le développement durable à l'échelle mondiale. Les formidables progrès technologiques des dernières décennies, parallèlement à un pouvoir d'achat élevé, à une urbanisation et une industrialisation croissante, ont élargi l'accès à l'électronique grand public, entraînant une demande croissante d'équipements électriques et électroniques (EEE). La croissance rapide de la demande du marché donne lieu à des processus de fabrication qui ne sont pas durables en termes de flux de déchets électroniques (e-déchets ou DEEE), d'épuisement d'éléments chimiques clés, de consommation d'énergie et d'écotoxicité. Dans ce scénario, l'électronique organique verte (dite durable) pourrait constituer une voie prometteuse pour atténuer l'empreinte écologique de l'électronique.

L'électronique organique verte est basée sur l'utilisation de matériaux organiques à base de carbone biosourcés (c'est-à-dire extraits de sources naturelles ou synthétisés en suivant les principes de la chimie verte), à faible énergie intrinsèque, à faible coût, biocompatibles, biodégradables, pouvant être traités en solution. La structure moléculaire des matériaux utilisés en électronique organique présente des caractéristiques de conjugaison (alternance de simple et doubles liaisons carbone). Cette structure peut aussi permettre liaisons hydrogène. La souplesse mécanique des matériaux organiques permet un transport combiné électronique et ionique (parfois protonique). De façon remarquable, la conductivité mixte ionique-électronique permet la connexion entre la biologie, qui parle le langage des protons, et l'électronique conventionnelle basée sur le transport des électrons et des trous. Les dispositifs électroniques organiques ne peuvent actuellement pas rivaliser avec la technologie du silicium en termes de performances, mais ils représentent son complément le plus prometteur.

L'eumélanine, un sous-groupe brun-noir des mélanines (biopigments abondants dans la faune et la flore), s'est révélée être un candidat idéal dans le domaine de l'électronique organique verte et

---

[1] Tiré de l'anglais, traduit par M. Reali.

de la bioélectronique. L'eumélanine est une biomacromolécule conjuguée, non toxique, biocompatible, pouvant être mise en solution et présentant des propriétés d'absorption UV-Vis, de chélation des ions métalliques, de piégeage des radicaux, d'activité red-ox et de transport mixte ionique (protonique) et électronique. Plusieurs applications basées sur l'eumélanine ont été démontrées, y compris les dispositifs de mémoire, les hétérojonctions poreuses de type n-p Si/eumélanine, les électrodes pour les dispositifs de stockage d'énergie, les transistors électrochimiques et les phototransistors.

Cette thèse de doctorat se concentre sur l'étude de propriétés fondamentales des films et des pastilles d'eumélanine pour la conception et le développement de technologies électroniques et bioélectroniques optimisées et durables à base d'eumélanine.

Dans le **chapitre 1**, nous fournissons le contexte de recherche et présentons les objectifs clés de ce travail de doctorat, à savoir : (i) l'étude du processus de formation et de la morphologie des couches de (5,6)-dihydroxyindole (DHI)- et d'acide (5,6)-dihydroxyindole-2-carboxylique (DHICA))-eumélanine, déterminés par des interactions physiques et chimiques, (ii) l'exploration d'un transport électronique exclusif dans des pastilles sèches de mélanine de Sepia (c'est-à-dire, poudres d'eumélanine extraites et purifiées du sac d'encre de la seiche) et en mettant en lumière leur comportement de commutation résistif. En fin de chapitre, nous présentons la structure de cette thèse de doctorat. Dans le **chapitre 2**, nous donnons un aperçu général des mélanines, avec une attention particulière à la structure supramoléculaire, au désordre chimique et physique et aux propriétés physico-chimiques de l'eumélanine. Dans le **chapitre 3**, nous fournissons un résumé approfondi de la technologie des couches d'eumélanine, en mettant l'accent sur la morphologie et les techniques de traitement des couches. Ensuite, nous passons en revue les propriétés de transport électronique et protonique des matériaux bio-sourcés afin de fournir un contexte détaillé pour présenter les propriétés de transport des porteurs de charge de l'eumélanine. À la fin du chapitre 3, nous présentons l'état de l'art des applications de l'électronique organique et de la bioélectronique démontrées pour l'eumélanine. Dans le **chapitre 4**, nous donnons une description des techniques de caractérisation utilisées pour atteindre les objectifs de recherche de ce travail. Dans le **chapitre 5**, nous étudions l'évolution dynamique de l'état moléculaire à la couche, après l'application par centrifugation de solutions (*spin-coating*) de monomères d'eumélanine DHI et DHICA (eumélanine synthétique) sur SiO_2/Si. Nous suivons la croissance des couches (*films*)

dans différentes conditions environnementales (c'est-à-dire l'obscurité par rapport à la lumière du jour et du laboratoire, les conditions ambiantes par rapport à une atmosphère enrichie en ammoniac (catalyseur de polymérisation)) par microscopie à force atomique (AFM), spectroscopie infrarouge (FT-IR) et spectroscopie UV-Vis. Nous constatons que les couches de DHI et DHICA subissent des changements spectaculaires de propriétés morphologiques et chimiques au fil du temps. Les couches de DHI conservés dans l'obscurité présentent des structures de type '*fougère*' que nous attribuons à des processus d'agrégation limités par diffusion (DLA). Lors de l'exposition à la lumière du jour, des structures semblables à des *piliers* et à des *cristaux* se développent au-dessus des *fougères*. Les couches de DHICA conservés dans l'obscurité puis exposés à la lumière du jour en laboratoire forment des structures en forme de *tige*. D'autre part, les couches de DHI et de DHICA exposés à l'ammoniac sont caractérisées par un polymorphisme prononcé. La spectroscopie IR suggère l'apparition d'interactions physiques (c'est-à-dire l'empilement π-π et la liaison hydrogène) et chimiques (formation de nouvelles liaisons covalentes par l'oxydation des films) dans les couches en fonction du temps après la déposition. Dans le **chapitre 6,** nous étudions la réponse électrique de pastilles sèches et fortement hydratées (humides) de mélanine de Sépia afin de trouver les conditions dans lesquelles l'eumélanine présente un transport électronique prédominant. Nous compressons des granules sèches et humides de mélanine de Sépia en configuration sandwich entre du cuivre et de l'acier inoxydable. Avant la compression, les poudres sèches et humides sont maintenues dans une atmosphère inerte (argon) et à 90% d'humidité relative (%HR), ce dernier qui correspond à environ 20% de gain de poids. Nous mesurons la réponse électrique des pastilles de mélanine Sépia sèches et humides en effectuant des balayages I-V séquentiels à 100 mVs^{-1} et en le modifiant de la vitesse de balayage de tension de 1 mVs^{-1} à 4500 mVs^{-1}. A 100 mVs^{-1} (i) les pastilles sèches commutent électriquement pendant le premier balayage. A partir du deuxième balayage, la réponse I-V étant linéaire avec une diminution de la résistance électrique balayage par balayage ; (ii) les pastilles humides commutent de manière répétée pendant tous les balayages I-V testés. De plus, la réponse I-V des pastilles sèches (humides) étant indépendante (dépendante) de la vitesse de balayage de la tension après la commutation. En particulier, les pastilles humides présentent une linéarisation de la réponse I-V sans commutation au-delà de 2000 mVs^{-1}. Les mesures de courant transitoire des pastilles sèches après commutation montrent un comportement

de type plateau attribuable au transport électronique. Inversement, les caractéristiques courant-temps des pastilles humides étant une décroissance exponentielle attribuable à la formation de doubles couches ioniques. Le graphique de Nyquist (c'est-à-dire la partie imaginaire négative de l'impédance par rapport à la partie réelle) des pastilles sèches et humides montre un demi-cercle et plusieurs demi-cercles que nous interprétons comme la signature d'un transport électronique et ionique prédominant, respectivement. Dans l'ensemble, ces observations nous conduisent à expliquer la commutation électrique résistive des pastilles de mélanine de Sépia sèches (humides) par la formation de couches de charges spatiales électroniques (ioniques) aux interfaces mélanine de Sépia/métal, respectivement. La possibilité d'observer, pour la première fois, un transport électronique exclusif dans l'eumélanine sèche à travers la structure empilée π-π attendue dans les granules de mélanine de Sepia, ouvre de nouvelles opportunités pour exploiter le plein potentiel du biopigment pour des applications en électronique organique. Dans le **chapitre 7**, nous discutons des connaissances acquises en matière de formation de couches d'eumélanine et de la physique du transport, en référence à la littérature présentée dans les chapitres 2 et 3. Dans le **chapitre 8**, nous résumons les connaissances globales acquises dans cette thèse en référence aux objectifs de recherche de ce doctorat et nous introduisons un certain nombre de recherches futures possibles que ce travail ouvre en ce qui concerne l'étude de la formation du film d'eumélanine et ses propriétés de transport de porteurs de charge.

En conclusion, dans cette thèse, nous avons examiné les propriétés physico-chimiques du biopigment eumélanine tels que les paramètres de traitement du film synthétique, la morphologie, les propriétés électriques et chimiques, le transport électronique, la commutation électrique résistive et les phénomènes de percolation des porteurs de charge électroniques dans les pastilles et les couches de mélanine de Sepia pour applications en électronique organique verte. Dans l'ensemble, ce travail souligne l'importance de (i) démêler la relation structure-propriété de l'eumélanine et (ii) de décrire les propriétés de transport des porteurs de charge du biopigment avec le modèle approprié pour la conception et le développement de technologies électroniques organiques à faible énergie intrinsèque, basées sur l'eumélanine.

ABSTRACT

The United Nations defined sustainability as "the ability to meet the needs of the present generations without compromising future generations […]". The access to clean and low-cost energy is paramount to achieve sustainability on the global scale. The formidable technological advances of recent decades, paralleled by high purchasing power, growing urbanization and industrialization, have broadened access to consumer electronics, leading to a growing demand for electrical and electronic equipment (EEE). The rapid growth of market demand is giving rise to manufacturing processes that are unsustainable in terms of electronic waste (e-Waste or WEEE) streams, depletion of key chemical elements, energy consumption and ecotoxicity. In this scenario, green (sustainable) organic electronics can constitute a valuable route to alleviate the footprint of electronics.

Green organic electronics is based on the use of organic carbon-based bio-sourced (i.e., extracted from natural sources or synthesized following the green chemistry principles), low embodied energy, low-cost, biocompatible, biodegradable, solution processable materials. The molecular structure of organic electronic materials exhibits conjugation (alternance of single double carbon bonds). This structure can also allow the formation of hydrogen bonds. The mechanical flexibility of organic materials allows a combined electronic and ionic (sometimes protonic) transport. Remarkably, mixed ionic-electronic conductivity enables the connection between biology, which speaks the language of protons, and conventional electronics based on electron and hole transport. Organic electronics devices cannot currently compete in terms of performance with silicon technology, but they represent its most promising complement.

Eumelanin, a black-brown subgroup of melanins (abundant biopigment in flora and fauna), has proven an ideal candidate in the field of green organic electronics and bioelectronics. Eumelanin is non-toxic, biocompatible, solution-processable, conjugated biomacromolecule exhibiting UV-Vis absorption, metal-ion chelation, radical scavenging, redox activity and mixed ionic (protonic)-electronic transport. Several eumelanin-based applications have been demonstrated, including memory devices, n-p type porous Si/eumelanin heterojunctions, electrodes for energy storage devices, electrochemical transistors and phototransistors.

This PhD thesis focuses on the study of a few fundamental properties of eumelanin films and pellets for the optimal design and development of eumelanin-based sustainable organic electronic and bioelectronic technologies.

In **chapter 1**, we provide the research context and present the key objectives of this PhD work, namely: (i) investigating the process of formation and the morphology of (5,6)-dihydroxyindole (DHI)- and (5,6)-dihydroxyindole-2-carboxylic acid (DHICA))-eumelanin films as determined by physical and chemical interactions, (ii) exploring the possibility of exclusive electronic transport in dry Sepia melanin pellets (i.e., eumelanin powders extracted and purified from the ink sac of cuttlefish) and shedding light on their resistive switching behavior. At the end of the chapter, we provide the structure of this PhD thesis. In **chapter 2**, we provide a general overview on melanins, with special attention to supramolecular structure, chemical and physical disorder and to the physicochemical properties of eumelanin. In **chapter 3**, we provide an in-depth summary of eumelanin's film technology, with focus on morphology and film processing techniques. Afterwards, we review the electronic and protonic transport properties of bio-sourced materials to provide a detailed context for presenting the charge carrier transport properties of eumelanin. At the end of the chapter 3, we present the state-of-the-art of the organic electronics and bioelectronics applications demonstrated for eumelanin. In **chapter 4**, we give a description of the characterization techniques used to achieve the research objectives of this work. In **chapter 5**, we investigate the dynamic evolution from molecular state to film, after spin coating solutions of DHI and DHICA eumelanin building blocks (synthetic eumelanin) on SiO_2/Si. We follow film growth in different environmental conditions (i.e., dark versus laboratory daylight, ambient conditions versus an ammonia enriched atmosphere (polymerization catalyst)) by atomic force microscopy (AFM), Infrared Spectroscopy (FT-IR), and UV-Vis spectroscopy. We find that DHI and DHICA films undergo changes of morphological and chemical properties over time. DHI films kept in the dark exhibit the presence of fern-like structures that we attribute to diffusion limited aggregation processes (DLA). Upon exposure to laboratory daylight, pillar-like and crystal-like structures grow on top of ferns. DHICA films kept in the dark and then exposed to laboratory daylight, form rod-shaped like structures. On the other hand, DHI and DHICA films exposed to ammonia are characterized by pronounced polymorphism. IR spectroscopy suggests the occurrence of physical (i.e., π-π stacking and hydrogen bonding) and chemical interactions

(formation of new covalent bonds by films oxidation) in the films as a function of time after deposition. In **chapter 6**, we investigate the electrical response of dry and highly hydrated (wet) Sepia melanin pellets to find conditions under which dry eumelanin features predominant electronic transport. We press dry and wet pellets Sepia melanin powders in sandwich configuration between copper and stainless steel. Prior to pressing, dry and wet powders are kept in inert atmosphere (argon) and at 90% relative humidity (%RH), corresponding to about 20% of weight gained. We measure the electrical response of dry and wet Sepia melanin pellets by performing sequential I-V scans at 100 mVs^{-1} and by changing it from the voltage scan rate from 1 mVs^{-1} to 4500 mVs^{-1}. At 100 mVs^{-1} (i) dry pellets electrically switch during the first scan. From the second scan I-V response is linear with decrease of the electrical resistance scan by scan; (ii) wet pellets repeatedly switch during all tested I-V scans. Furthermore, the I-V response of dry (wet) pellets is independent (dependent) on the voltage scan rate after switching. Particularly, wet pellets feature linearization of the I-V response without switching beyond 2000 mVs^{-1}. Transient current measurements of dry pellets after switching show a plateau-like behavior attributable to electronic transport. Conversely, the current-time characteristics of wet pellets is an exponential decay attributable to the formation of ionic double layers. Nyquist plots (i.e., the negative imaginary part of the impedance vs the real part) of dry and wet pellets show one semicircle and multiple semicircles that we interpret as signature of predominant electronic and ionic transport, respectively. All in all, these observations lead us to explain the electrical resistive switching of dry (wet) Sepia melanin pellets by the formation of electronic (ionic) space charge layers at the Sepia melanin/metal interfaces, respectively. The possibility to observe, for the first time, exclusive electronic transport in dry eumelanin through the π-π stacked structure expected in Sepia melanin granules, opens new opportunities to exploit the full potential of the biopigment for applications in organic electronics. In **chapter 7**, we discuss the insights gained with respect to eumelanin film formation and transport physics, and with reference to the literature presented in chapter 2 and chapter 3. In **chapter 8**, we summarize the global insights gained in this thesis with reference to the research objectives of this PhD and introduce a number of possible future investigations that this work opens in regard to the study of eumelanin film formation and its charge carrier transport properties.

In conclusions, in this thesis we examine the physicochemical properties biopigment eumelanin such as synthetic film processing parameters, morphology electrical and chemical properties as well as electronic transport and electrical resistive switching in Sepia melanin pellets for applications in green organic electronics. All in all, this work highlights the importance of (i) unraveling eumelanin structure-property relationship and (ii) describing the charge carrier transport properties of the biopigment with the appropriate model for the design and the development of low embodied energy, eumelanin-based organic electronics technologies.

TABLE OF CONTENTS

LIST OF TABLES

LIST OF FIGURES

LIST OF SYMBOLS AND ABBREVIATIONS

ABTS   2,2'-azinobis(3-ethyl-benzothiazoline-6-sulfonic acid)

AC   Ambient conditions

AFM   Atomic force microscopy

Ag   Silver

AISSP   Ammonia-induced solid-state polymerization

ASc   Amorphous semiconductor

ASM   Amorphous semiconductor model

Au   Gold

BaF_2 Barium fluoride

BE   Binding energy

CB   Conduction band

CCR   Carbon-centered radicals

Co   Cobalt

CPE   Constant phase element

C_T Total sepia melanin film capacitance

Cu   Copper

CV   Cyclic voltammetry

D   Dark

DC   Direct current

Dct   Dopachrome tautomerase

DFM   Dimethylformamide

DHI   (5,6)-dihydroxyindole

DHICA   (5,6)-dihydroxyindole-2-carboxylic acid

DI	De-ionized
DLA	Diffusion-limited aggregation
DMSO	Dimethyl sulfoxide
DPPH	(1,1)-diphenyl-2-picrylhydrazyl
DQ	Dopaquinone
DSSCs	Dye-sensitized solar cells
EDX	Energy-dispersive X-ray spectra
EGFETs	Extended gate field effect transistors
EIS	Electrochemical impedance spectroscopy
EPR	Electron paramagnetic resonance
FT-IR	Fourier transform-infrared spectroscopy
Ge	Germanium
H_2O	Water
H2Q	Hydroquinone
HCl	Hydrochloric acid
HOMO	Highest occupied molecular orbital
I	Current intensity
In	Indium
INS	Inelastic neutron scattering
IPES	Inverse photoemission spectroscopy
IR	Infrared
ITO	Indium titanium oxide
I-V	Current-voltage
J	Current density

J_- (V=0)   Negative current density at zero voltage

J_+ (V=0)   Positive current density at zero voltage

J-V   Current density-voltage

KE   Kinetic energy

L   Laboratory daylight

L-dopa   L-3-(3,4-dihydroxyphenyl)-alanine

LEDs   Light emitting diodes

LUMO   Lowest unoccupied molecular orbital

MAPLE   Matrix-assisted pulsed laser evaporation

MOSFETs   Metal oxide semiconductor field effect transistors

NNH   Nearest neighbor hopping

NO   Nitric Oxide

OM   Optical Microscopy

OPTs   Organic phototransistors

P6Ome   3-(6-methoxylhexyl) thiophene

PCE   Power conversion efficiency

Pd   Palladium

PEDOT:PSS   Poly (3,4-ethylenedioxythiophene):poly(4-styrenesulfonate)

p-EPR   Photoinduced electron paramagnetic resonance spectroscopy

PET   Polyethylene terephthalate

PVB   Polyvinyl butyral

PVP   Polyvinyl pyrrolidone

Pt   Platinum

q Charge stored

Q	Quinone
QI	Quinone Imine
R_b	Bulk resistance
RC	Resistor-capacitor behavior
R_e	Electronic resistance
RH	Relative humidity
R_i	Ionic resistance
R_{if}	Interface resistance of Sepia melanin pellets
RMS	Root mean square roughness
R_{OFF}	OFF resistance
R_{ON}	ON resistance
R_{opt}	Optical resolution
ROS	Reactive oxygen species
RT	Room temperature
SCE	Standard calomel electrode
SCLC	Space charge limited current
SCs	Solar cells
SEM	Scanning electron microscopy
SiO_2	Silicon dioxide
SQ	Semiquinone
SQR	Semiquinone radicals
STM	Scanning tunneling microscopy
Ti	Titanium
UPS	Ultraviolet photoemission spectroscopy

UV-Vis-NIR Ultraviolet-visible near-infrared

V_- (J=0)   Negative voltage at zero current density

V_+ (J=0)   Positive voltage at zero current density

VB   Valence band

vdP   van der Pauw

VRH   Variable range hopping

V_T Threshold voltage

WEEE   Waste electric and electronic equipment

XPS   X-ray photoelectron spectroscopy

XRD   X-ray diffraction

Z_{CPE} Constant phase element impedance

Z_W Diffusion hindered impedance

μSR   Muon-spin relaxation spectroscopy

LIST OF APPENDICES

CHAPTER 1   INTRODUCTION

1.1   Context of Investigation: Green Organic Electronics and Bioelectronics

The United Nations defined sustainability as "the ability to meet the needs of the present generations without compromising future generations". In this regard, the access to clean and low-cost energy is the underpinning to achieve sustainability at the global level. We are living an era of tremendous technological achievements. Electronics progress at a terrific pace to the point that our lives are becoming more and more dependent on it. Although we undoubtedly benefit from electronic technologies and devices, such a terrific boom poses environmental and health concerns. Quoting SONY's founding chairman A. Morita, "*we are moving from consumer to consumable electronics*": replacement cycles and lifetime of electronics are becoming shorter and shorter [1], [2]. According to the Global E-Waste Monitor 2020, 53.6 Mt of E-Waste have been produced worldwide in 2019 and this amount is expected to reach 74.7 Mt by 2030 [3]. Such an increase of E-waste stream is accompanied by the depletion of natural resources [4], [5] including precious (e.g., gold (Au), silver (Ag), copper (Cu), platinum (Pt)) and critical raw materials (e.g., cobalt (Co), germanium (Ge), palladium (Pd), indium (In)) [3]. Furthermore, another issue of concern is the high energy embodied[2] into conventional (inorganic) optoelectronic devices. Indeed, the electronic sector has primarily focused on performance, reliability and cost; concepts like energy efficiency, endangered chemical elements [6], green chemistry and sustainability[3] [7], have been so far only marginally addressed. A global effort is now in place towards achieving a paradigm shift from linear to circular electronics, focusing on durability, reuse, refurbishment and advanced recycling [8].

---

[2]Energy used to manufacture an usable object, including the energy for extracting, refining, processing and transporting of primary materials. This definition often comes along with the concept of embodied carbon or CO_2 footprint.

[3] In 1987 the United Nations defined sustainability as "the ability of satisfying one generation's needs without compromising the ability of future generations to meet their own needs".

In this context, great attention has been given to Green (Sustainable) Organic Electronics, having as essential principles the use of (i) abundant bio-sourced (extracted from biomass and/or agriculture-waste feedstocks), low-cost, solution-processed materials, (ii) potentially compostable materials featuring (at least) acceptable charge carrier transport properties and (iii) the development of devices featuring low embodied energy and conceived for sustainable end-of-life scenarios.

Organic electronics relies on carbon-based conjugated materials (i.e., featuring alternance of single-double carbon bonds) as the main active components of devices [9]. In 2000, Heeger, MacDiarmid, and Shirakawa were awarded the Nobel Prize in Chemistry for their discovery that the electrical conductivity of conjugated materials can increase of several orders of magnitude via chemical doping. Since then, bio-sourced and/or bio-inspired materials have been applied to devices such as organic field-effect transistors (e.g. indigo, epindolidione, quinacridone, tyrian-purple) [10], [11], organic solar cells [12], light-emitting diodes [13], [14], organic sensors [4], p-n *ionic junctions* (i.e. chitosan) [15] and many others [16]–[18]. Organic electronics constitute thus a promising complement of silicon (Si)-based technologies for printable, stretchable and flexible applications [19].

In this context, Nature developed plenty of materials with a wide variety of chemical structures and functional properties that are of tremendous inspiration for humankind. We could say that nanotechnology was born with Nature: evolution relies on self-assembly of ubiquitous organic molecules. Nature selected organic over inorganic materials to create complex living beings equipped with all kinds of biodevices, from ion-to-electron transducers to sensors, solar cells, memory switching, energy storage, and many others [4], [5], [10], [16], [20].

Melanins are among the most interesting bio-sourced conjugated and hydrogen-bonded materials available in nature. Melanins are a large class of natural pigments, ubiquitous in flora and fauna, originating from the oxidative polymerization of phenolic precursors in plants and animals. Melanins are divided into four main subgroups of pigments: (i) the black-brown insoluble eumelanin found in human skin and in several animals (ii) the yellow-reddish brown pheomelanin, found in the human red-hair and in birds' feathers, the dark (iii) neuromelanin, present in the *substantia nigra* and *locus coeruleus* of the human brain and large primates and (iv) pyomelanin, present in various microorganisms.

Eumelanin originates from the oxidative polymerization of (5,6)-dihydroxyindole (DHI) and (5,6)-dihydroxyindole-2-carboxylic acid (DHICA) building blocks (Figure 1.1 (a) and (b)). Eumelanin is by far the most studied melanin pigment. Eumelanin exhibits several physicochemical properties, including electronic conjugation, UV-Vis broadband optical absorption, metal-ion chelation, radical scavenging, redox activity and mixed ionic (protonic)-electronic transport [21], [22], [23]. As such, eumelanin is a very promising multifunctional material for organic electronics. Furthermore, eumelanin is abundant and can be extracted from various natural sources such as cephalopods (e.g., *Sepia Officinalis*), cuticles of insects and arachnids. Sepia melanin is the standard natural source of eumelanin and can be extracted from the ink sac of *Sepia Officinalis* [24] .

Several eumelanin-based organic electronic applications have been demonstrated, including n-p type porous Si/eumelanin heterojunctions, organic electrochemical transistors (OECTs), phototransistors (OPTs) and electrodes for energy storage devices [25]–[32].

In this PhD thesis, focus is given on the study of physicochemical properties of (i) synthetic DHI-and DHICA eumelanin films and (ii) Sepia melanin pellets, for the design and development of eumelanin-based sustainable organic electronic technologies.

a)

(5,6)-dihydroxyindole (DHI)

b)

(5,6)-dihydroxyindole-2-carboxylic acid (DHICA)
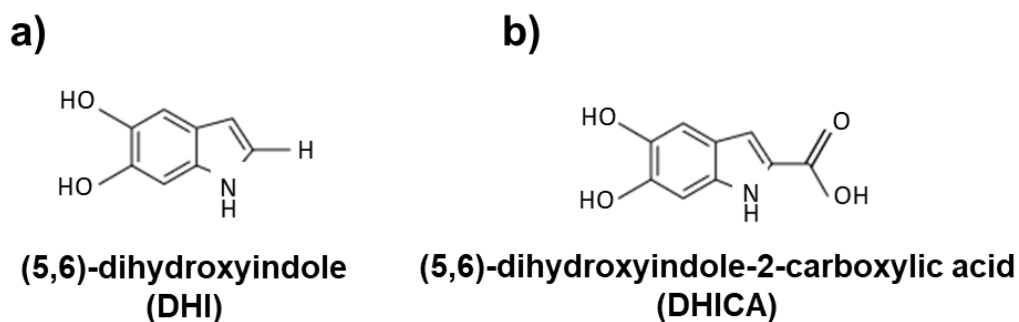
Figure 1.1 Eumelanin building blocks: (a) (5,6)-dihydroxyindole (DHI) and (b) (5,6)-dihydroxyindole-2-carboxylic acid (DHICA).

1.2 **Research Objectives**

As we shall see in detail in chapter 2 and chapter 3, a few fundamental aspects of the physicochemical properties of eumelanin remain poorly understood [22], [28], [33]–[35]. Because of that, the full technological exploitation of eumelanin still entails issues.

Firstly, eumelanin is insoluble in most common solvents: electronic devices rely on smooth, continuous, and uniform thin films. Therefore, the limited solubility of the biopigment is a crucial challenge to address. Secondly, eumelanin exhibits chemical heterogeneity and structural disorder which prevent the fabrication of device-quality films. In addition, the degree of structural disorder is such that the mechanisms of solid-state aggregation (supramolecular self-assembly) and polymerization (covalent bonding) have proven challenging to unravel in eumelanin.

The access to chemically controlled eumelanin powders (i.e., only based on one of the two building blocks DHI and DHICA, see chapter 3) offers a great tool to circumvent the insolubility issue and fabricate synthetic eumelanin films mimicking the natural biopigment [36]. However, there are no current studies on the early stages of formation of DHI- and DHICA-eumelanin-based films as determined by physical (hydrogen (H)-bonding and π-π stacking) and chemical interactions.

A third important challenge is the study of the transport physics of eumelanin. The biopigment has been considered an amorphous semiconductor since McGinness *et al.* reported on an electrical resistive switching behavior in synthetic and natural hydrated melanin pressed pellets [37]. Indeed, the electrical resistive switching has been commonly observed in the current-voltage response of inorganic amorphous semiconductors (e.g. a-Si, a-Ge, a-Se and a-Te) [38]–[40]. Recently, studies on the electrical conductivity of eumelanin pellets as a function of hydration seemed to undermine the amorphous semiconductor model in favor of the mixed ionic-electronic conductor model for eumelanin [27], [41]–[45].

Thus, the charge carrier transport properties of eumelanin have been only partially understood since different works point to different interpretations. In this context, describing the charge transport properties of the biopigment with appropriate models is the underpinning to

demonstrate ion-to-electron transducers (in the case of mixed- ionic electronic conductors, proton membranes) and organic electronic devices based on exclusive electronic transport.

Based on the state-of-the-art of eumelanin film formation and transport physics (thoroughly provided in the next two chapters), **the objectives of this PhD thesis are the following**:

1. Exploring the early stages of film formation and morphology of synthetic DHI-and DHICA-eumelanin as determined by physical and chemical interactions in different environmental conditions (see experimental section, Article 1, chapter 5). The motivation is to pave the way toward the construction of structure-functional property-device performance relationships for eumelanin films notoriously exhibiting chemical and structural disorder (Article 1, chapter 5).

To achieve objective 1, we:

- Use atomic force microscopy (AFM), to study the morphological changes occurring in DHI- and DHICA eumelanin-based films during their formation.

- Collect the Fourier-Transform Infrared Spectroscopy (FT-IR) and UV-Vis-NIR spectroscopy spectra of DHI-and DHICA-eumelanin-based films to investigate the changes of physical and chemical interactions taking place during film formation.

2. Gaining insights on the possibility to observe exclusive electronic transport in Sepia melanin pellets, beside proton and mixed protonic-electronic transport already reported in the literature (Article 2, chapter 6).

To achieve objective 2, we:

- Perform direct current measurement experiments (DC), to acquire and compare current-voltage resistive switching response of dry and highly hydrated (wet) Sepia melanin pellets.

- Collect the impedance spectroscopy (IS) spectra of dry and wet Sepia melanin pellets, before and after the occurrence of the electrical resistive switching, to shed light on electronic and ionic processes taking place in the bulk of the active layer and at the Sepia melanin pellets/metal contact interfaces (i.e., charge transport, charge transfer and diffusion).

- Collect the scanning electron microscopy (SEM) images and Energy Dispersive X-Ray Spectrometry (EDX) spectra of Sepia melanin pellets metal electrodes, to exclude the occurrence of electrodes' dissolution processes during the electrical tests that could lead to the formation of metallic filaments bridging the electrodes.

- Collect the Raman Spectroscopy spectra and the X-Ray Photoelectron Spectroscopy (XPS) spectra of dry and wet Sepia melanin pellets, before and after switching, to exclude that a Joule-heating-induced phase transition from amorphous to graphitic carbon is at the origin of the electrical resistive switching behavior of eumelanin.

1.3   **Structure of the Thesis**

This PhD thesis is organized into 8 chapters. Below the detailed structure of the document:

1. Chapter 1 provides the research context, the gaps of knowledge and illustrates the key objectives and the structure of this PhD thesis.

2. Chapter 2 presents an overview of the melanins pigments, with special focus on to the supramolecular self-assembly, physical and chemical properties of eumelanin, the organic electronic material study case of this PhD thesis.

3. Chapter 3 firstly gives the state-of-the-art of eumelanin film processing and morphology. Afterwards, the chapter reviews the electronic and protonic transport properties of bio-sourced materials to provide a detailed context of the charge carrier transport properties of eumelanin. The final part of the chapter provides a the state-of-the-art of the organic electronic applications reported for eumelanin. For a portion of chapter 3, we considered the following publications: (i) M. Reali and C. Santato, "Eumelanin: semiconductor, protonic conductor or mixed electronic-ionic conductor?", published on December 19th 2019 as a book chapter in the *Handbook of Nanoengineering, Quantum Science and Technology*, pp. 101-113 [34]; (ii) M. Reali, P. Saini and C. Santato, "Electronic and Protonic Transport in Bio-sourced Materials: A new Perspective on Semiconductivity", published as a review article on October 13th 2020 in *Materials Advances*, 2(1), 15-31 [46].

4. Chapter 4 provides a description of the characterization techniques used to achieve the research objectives of this PhD thesis, namely: AFM, UV-Vis-NIR spectroscopy and FT-IR spectroscopy (<u>Article 1</u>, chapter 5) and SEM, EDX spectrometry, DC measurements, impedance spectroscopy, Raman spectroscopy and XPS spectroscopy (<u>Article 2</u>, chapter 6).

5. Chapter 5 presents the first publication of this PhD work (i.e., <u>Article 1</u>) pertaining to the study of the early stages of formation of DHI-and DHICA-eumelanin-based films (<u>Objective 1</u>, section 1.2). The article, entitled "Eumelanin: from Molecular State to Film" has been published in *The Journal of Physical Chemistry* C (JPCC) on February 3rd, 2021. The Supplementary Information is provided in Appendix A.

6. Chapter 6 presents the second publication of this PhD work (i.e., <u>Article 2</u>) pertaining to the study of electronic and protonic transport properties of dry and wet Sepia melanin pellets (<u>Objective 2</u>, section 1.2). The article, entitled "Electronic Transport in the Biopigment Sepia melanin" has been published on the *American Chemical Society* (ACS) *Applied Bio Materials* on July 6th, 2020. The Supplementary Information is provided in Appendix B.

7. Chapter 7 discusses the insights gained in chapter 5 and 6 with respect to eumelanin film formation and transport physics, and with reference to the literature presented in chapter 2 and chapter 3.

8. Chapter 8 concludes this PhD thesis document by (i) summarizing the global insights gained in this thesis as related to the research objectives of this PhD work and (ii) introducing a number of possible future investigations that this work opens in regard to the study of eumelanin film formation and its charge carrier transport properties.

CHAPTER 2   EUMELANIN

2.1 Classification of Melanins

The word *melanin* (from Greek μέλας=black) indicates a vast category of black biopigments presents in humans and other mammals, birds, reptiles, amphibians, insects, cephalopods as well as plants and microorganisms [47], [48]. The chemist Berzelius was the first researcher to coin the word melanin to refer to black animal pigments [49]. A few years later, Nicolaus provided a classification of melanins based on their formation process in the living beings where they could be found. Accordingly, the term melanins was referred to pigments formed via intracellular processes in humans and animals whereas the word allomelanins to pigments formed via extracellular processes in plants and microorganisms [48], [50].

d'Ischia *et al*. proposed a more rigorous classification based on the chemistry of the pigments [47], [48]. Melanins were defined as "pigments of diverse structures and origin derived by the oxidation and polymerization of tyrosine in animals and phenolic compounds in lower organisms [47], [48] (Figure 2.1 (a)). Based on this definition, they identified four main subgroups of melanin pigments:

1. Eumelanin (from Greek εὖ=well and μέλας=black) is a black-brown insoluble pigment originated from the oxidative polymerization of L-3-(3,4-dihydroxyphenyl)-alanine (L-dopa) (Figure 2.1 (b)) via (5,6)-dihydroxyindoles intermediates, namely (5,6)-dihydroxyindole (DHI) and (5,6)-dihydroxyindole-2-carboxylic acid (DHICA) (Figure 2.1 (c) and (d)). Sepia melanin and black hair melanin are two examples of natural eumelanin [51].

2. Pheomelanin (from Greek φαιός=dusky, grey), is a yellow-reddish brown subgroup of sulfonated melanins. Pheomelanin originates from the oxidative polymerization of cysteinyl-dopa (Figure 2.1. (e)) via benzothiazine and benzothiazole intermediates (Figure 2.1. (f) and (g)). Melanin in human red hair and in hens' feathers are two examples of natural pheomelanin.

3. Neuromelanin is a dark subgroup of melanin pigments present in the *substantia nigra* and *locus coeruleus* of the human brain and large primates. Neuromelanin is derived from the

oxidation of dopamine and other precursors within the human neurons (Figure 2.1 (h)). Human neuromelanin consists of a pheomelanin core surrounded by a eumelanin shell [52], [53].

4. Pyomelanin is a dark pigment mainly present in microorganisms and derived from (2,5)-dihydroxyphenil-acetate via oxidative coupling of (1,8)-dihydroxynaphtalene (DHN) (Figure 2.1 (i) and (l)).
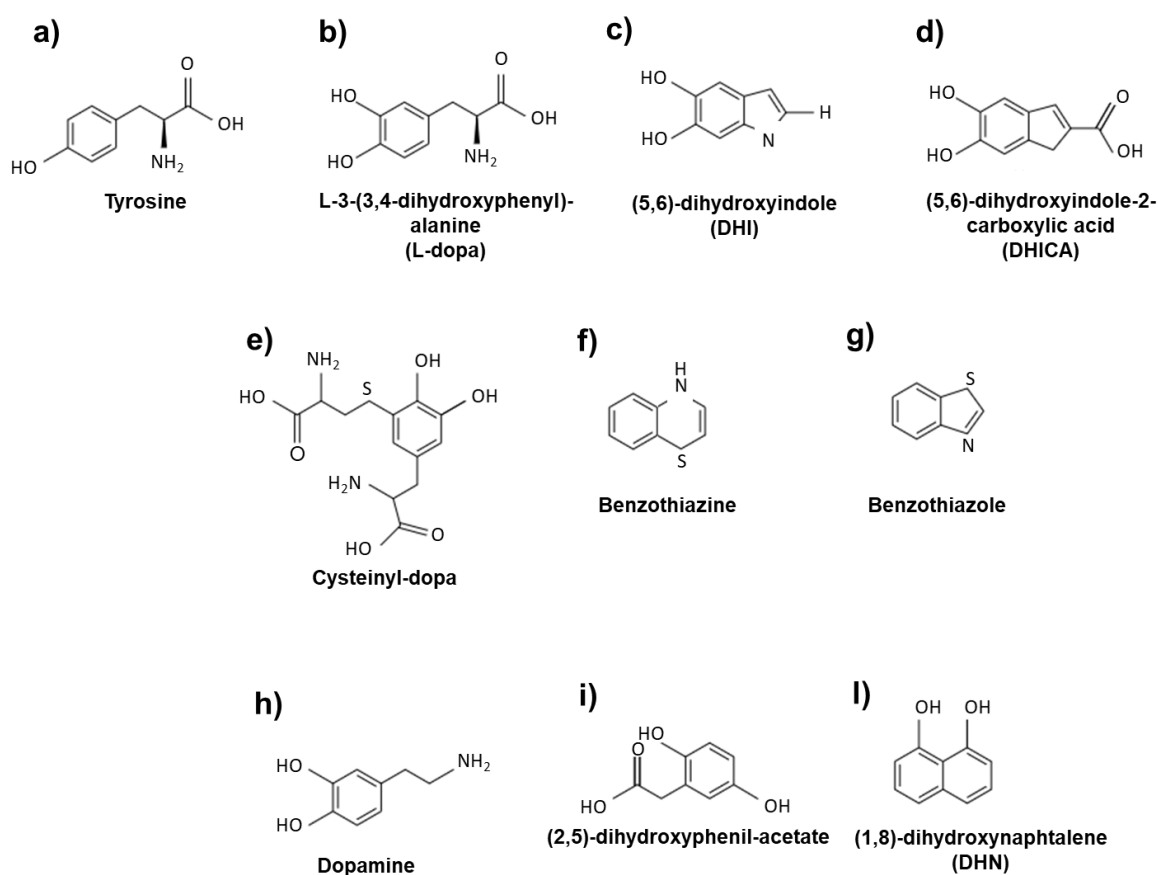
Figure 2.1 Key precursors of melanins: (a) tyrosine; (b) L-3-(3,4-dihydroxyphenyl)-alanine (L-dopa); (c) (5,6)-dihydroxyindole (DHI); (d) (5,6)-dihydroxyindole-2-carboxylic acid (DHICA); (e) cysteinyl-dopa; (f) benzothiazine; (g) benzothiazole; (h) dopamine; (i) (2,5)-dihydroxyphenil-acetate; (l) (1,8)-dihydroxynaphtalene (DHN).

The words melanin and eumelanin are often used as synonyms in the literature, mainly due to the relevance of eumelanin in the scientific community. From now on, the two words will be interchangeably used.

2.2 **Eumelanin**

2.2.1 **Eumelanin in the Biosphere**

Eumelanin can be found in several outer and inner parts of the body of mammalian vertebrates, including the epidermis, hair, eyes, ears, as well as heart, lungs, kidneys, liver, spleen and tissues [21]. In the human body, eumelanin partially screens the epidermis from ultraviolet (UV) radiation and regulates skin complexion. Prolonged exposure to harmful UV light brings about the formation of radicals in the epidermis that can cause skin cancer (melanoma). The physiological roles of inner eumelanin are manifold, from antioxidant and photoprotection in the iris of the eyes [54], [55], the protection of the inner ear from noise-induced stress [56], to stiffening the tissues surrounding heart and lungs [21].

Birds, cephalopods and insects are the groups of non-mammalian vertebrates where the biological functions of eumelanin have been studied the most [47], [51]. In birds, eumelanin is responsible for the thermoregulation of the body [57], the pigmentation of the feathers and their protection against abrasions [58], [59]. Eumelanin can be found in cephalopods ink produced by the glands in the ink sac. Due to its high content of tyrosinase, the ink is toxic and serves as a defence against potential attacks of predators [60]. In insects, eumelanin originates from dopamine (Figure 2.1 (h)) and is mainly involved in cuticle sclerotization, camouflage, wound healing and immune response against pathogens [51], [61].

Melanin is present in plants and fungi, too, where (1,8)-dihydroxynaphtalene (DHN) is the main precursor (Figure 2.1 (l)). Strengthening and hardening the cells walls at a site of injury are central biofunctions of melanin in plants [5]. Fungal melanin has crucial roles including cell walls strengthening and UV photoprotection [62]. Microorganisms such as bacteria have also been reported as sources of melanin. Bacterial melanin originates from the oxidation of (3,4)-dihydroxyphenyl-acetate (Figure 2.1 (i)) and is responsible for the protection of the microorganisms against environmental stress.

2.2.2 Isolation from Natural Sources

The isolation of eumelanin from natural sources has proven difficult. The limited solubility of eumelanin in most common solvents is the major obstacle to its isolation [23], [47], [63]. The presence of tightly bound cellular components, metal cations, and residual amounts of proteins in cells where the melanogenesis happens and plays its functions, affects the structural aggregation and physical properties of the natural biopigment [64]. Current strategies of isolation comprise the homogenization of the source tissue in blenders followed by several acidic treatments. These approaches has proven effective to remove cellular components and proteins without altering the physicochemical properties of natural pigment [48], [50], [51]. The extraction of eumelanin from human hair (black hair eumelanin), from the ink sac of cuttlefish *Sepia Officinalis* (Sepia melanin) and from birds' feathers are examples of successful isolation protocols. Black hair eumelanin is a granular pigment found in the core of the human hair fiber (i.e., the medulla) and in the hair cortex [47], [48]. Sepia melanin is considered the standard natural source of eumelanin [24]. The extraction of Sepia melanin includes sequential washings and centrifugations of the raw ink with HCl, ethyl acetate, ethanol and water, followed by lyophilization at -80°C [64]–[67]. Among all methods of isolation, the protocol of extraction of Sepia melanin provides the highest extraction yield (about 80%).

2.2.3 Synthetic Eumelanogenesis and Redox Forms

A terrific effort has been devoted to develop synthetic eumelanin in biomimetic conditions (i.e., resembling the melanogenesis in the biological environment) [68]. The structural and physical properties of synthetic eumelanin depend on precursors, environment of reaction and post-synthesis conditions. The Raper-Mason-Prota scheme provides biosynthetic pathways leading to the formation of eumelanin (Figure 2.2) [69]. During the biosynthesis of eumelanin, the enzyme tyrosinase oxidizes tyrosine into dopaquinone (DQ), which forms cyclodopa via intermolecular cyclization. Redox exchanges between DQ and cyclodopa generate dopachrome and L-Dopa (Figure 2.1. (b)). In the absence of the enzyme dopachrome tautomerase (Dct) dopachrome spontaneously decarboxylates into DHI (Figure 2.1. (c)). The enzymatic assistance of Dct leads to the tautomerization of dopachrome with formation of DHICA (Figure 2.1 (d)).
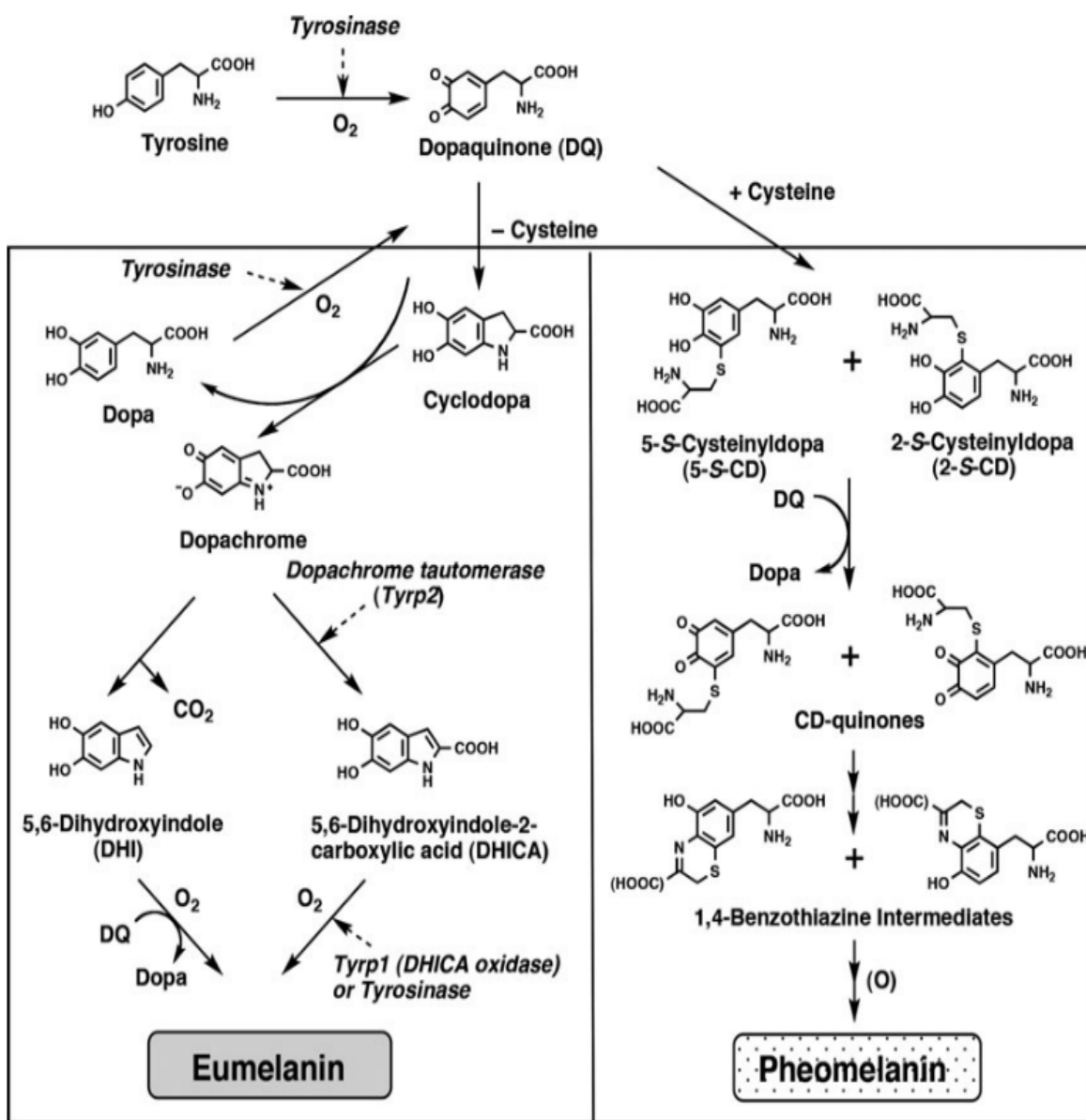
Figure 2.2 Biosynthetic pathways leading to the formation of eumelanin and pheomelanin. Reproduced with permission from Ref. [69].

DHI and DHICA are the building blocks of eumelanin. The building blocks can be reversibly oxidized into their orto-quinone forms by means of two processes of one-electron one-proton removal [70]. Thus, eumelanin is a good electron transfer agent in several reduction-oxidation systems [71].

The redox forms of DHI and DHICA, i.e. the reduced hydroquinone (H2Q), the intermediate semiquinone (SQ) and the oxidized quinone (Q), coexist in eumelanin [35] (Figure 2.3). The comproportionation equilibrium regulates the relative concentrations of the three redox states in presence of water (Figure 2.4). This reaction plays a fundamental role in defining the paramagnetic and the electrical properties of eumelanin (see section 2.3.4 and chapter 3).
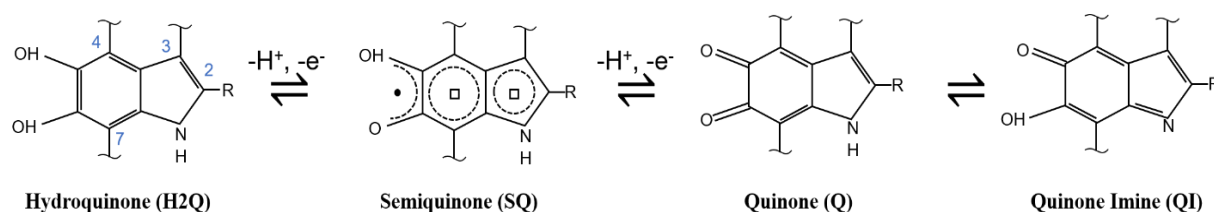
Figure 2.3 Redox forms of DHI and DHICA eumelanin building blocks: hydroquinone (H2Q), semiquinone (SQ), Quinone (Q) and the tautomer quinone imine (QI). R is -H in DHI and -COOH in DHICA. The binding sites at each carbon position are shown anticlockwise in the H2Q form. Granted by authorship from Ref. [72].
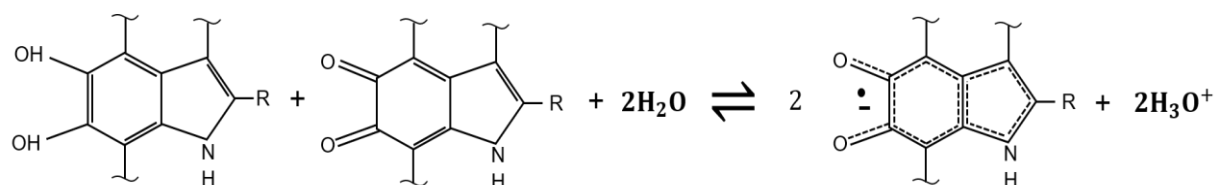
Figure 2.4 The comproportionation equilibrium reaction controlling the relative concentration of hydroquinone (H2Q), semiquinone (SQ) and quinone (Q) species in presence of water. R denotes an H atom and a COOH group in DHI and DHCA, respectively. Granted by authorship from Ref. [72].

2.2.4 Supramolecular Structure and Physical Disorder in Eumelanin

The supramolecular structure of eumelanin has been investigated by X-ray diffraction (XRD) [73]–[75], mass spectrometry [76]–[80], atomic force microscopy (AFM) [64], [81], [82], scanning tunneling microscopy (STM) [83], ultrafast vibrational spectroscopy [84] and quantum mechanical simulations [85]–[90]. Despite this extensive body of work, a definitive structural model for eumelanin does not currently exist. There is, however, general agreement to a structural model based on stacked aggregates. Accordingly, the supramolecular buildup of eumelanin is a three-steps process involving four levels of aggregation [91], [92]: (i) oligomerization (level 1), (ii) formation of nanoaggregates (level 2) by π-π stacking and (iii) agglomeration of small aggregates (10-20 nm, level 3) and large spherical particles via edge-to-edge stacking (100-200 nm, level 4) (Figure 2.5). The first step involves the formation of oligomers of up to a few tens of monomers through their oxidative polymerization. Oxidation of DHI leads to the oxidative coupling of dimers in which indoles are mainly linked through 2-2 and 2-7-bonds. Further oxidation of the dimers brings about the formation of tetramers featuring 2-3, 2-4, 4-4, and 7-7-bonds. The presence of carboxyl groups (COOH) at 2-position limits the range of sites available for oxidative coupling in DHICA. Thus, the oxidative polymerization of DHICA leads to dimers and tetramers mainly linked via 4-4 and 4-7 bonds [92], [93].

During the second step, three-four sheets of oligomers form nanoaggregates via π-π stacking (non-covalent bonds) with typical interplanar distance of about 3.4 Å, and vertical and lateral extension of about 13.6 Å and 20 Å, respectively [74], [75], [94]. Throughout this phase, the degree of physical organization of growing oligomers affects the supramolecular arrangement by generating a certain level of structural disorder. The efficiency of π-π stacking, the presence of coexisting π-π stacked regions of oligomers with different extension and orientation (i.e., planar vs twisted segments), and the extent of H-bonding are all factors contributing to supramolecular structure [87], [93], [95]. In the third step, protomolecules agglomerate via edge-to-edge stacking bringing about the formation of 10 nm-to 20 nm-sized aggregates. In the case of Sepia melanin, these aggregates finally assemble into 100 nm- to 200 nm-sized granules (Figure 2.5) [64], [85].
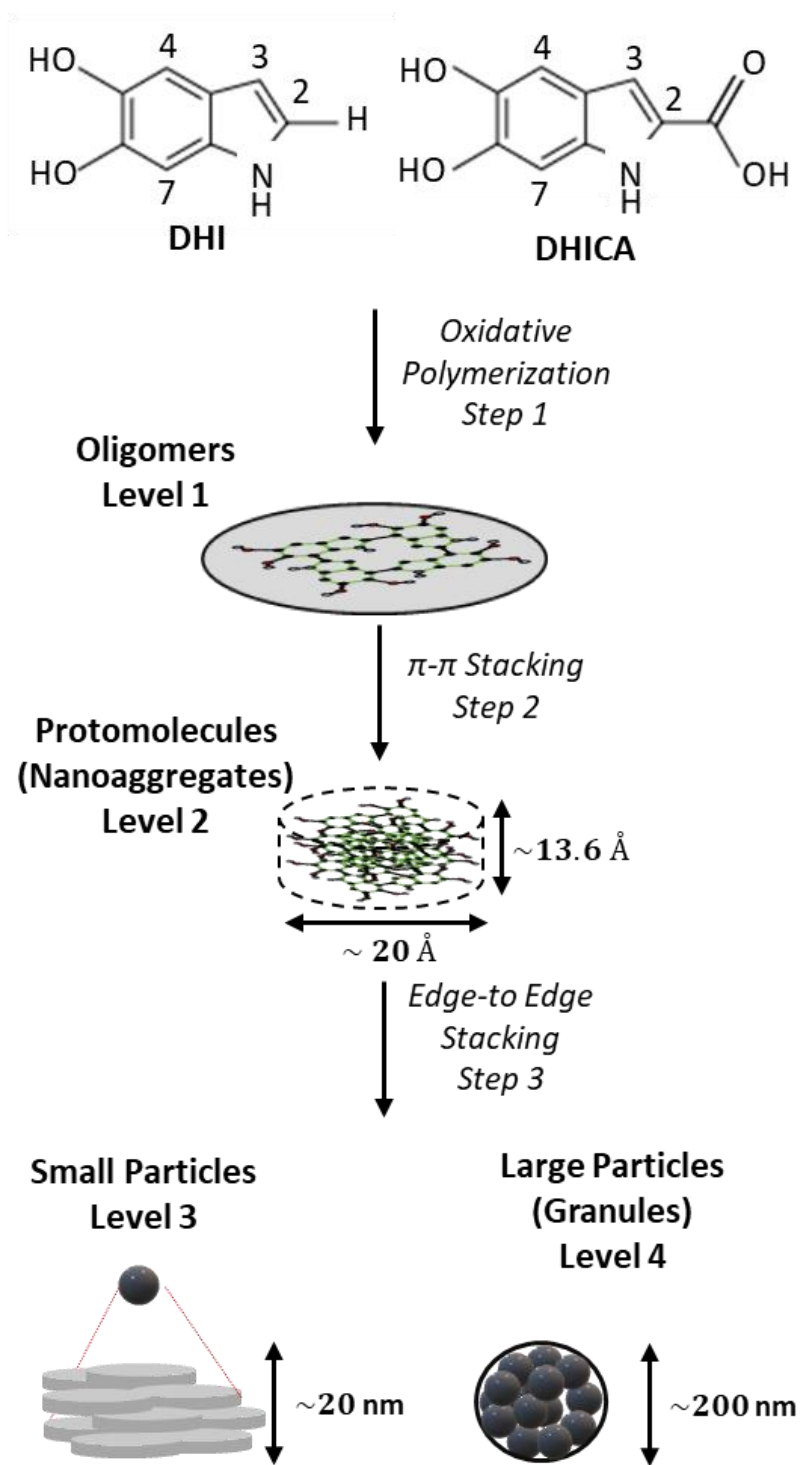
Figure 2.5 Schematic representation of the supramolecular buildup of eumelanin.

2.2.5 Chemical Disorder in Eumelanin

The presence of several available binding sites in the molecular structures of DHI and DHICA building blocks, paralleled by their coexistence in various redox forms (i.e, H2Q, SQ and Q, Figures 2.3 and 2.4), make eumelanin a chemically heterogeneous biopigment. Recently, the chemical heterogeneity of eumelanin has been summarized in terms of hierarchical chemical disorder entailing various levels of complexity [96]:

1. Building block disorder, stemming from the chemical diversity of the structural units involved in the polymerization pathway. Different starting ratios of DHI/DHICA, the presence of unreacted monomers and their degradation during the polymerization are the main causes of building block disorder [93], [97]. Different starting ratios of DHI/DHICA brings about differences in the structures of natural and synthetic eumelanin. Sepia melanin contains up to 50% of DHICA in molecular ratio [23], [98] whereas synthetic eumelanin contains about 10% [99]. As we shall see later, the ratio DHI/DHICA also affects the optical absorption and radical scavenging properties of eumelanin (see sections 2.3.1 and 2.3.3, respectively).

2. Molecular-size disorder, arising from the presence of oligomers with different molar masses that causes molecular weight dispersion during polymerization [80].

3. Molecular disorder *sensu stricto*, mainly caused by the extent of chemical reactivity of the monomers during the polymerization (availability of binding sites) and by the presence of several isomers populating each oligomer [100].

4. Redox disorder, due to the various redox forms of the monomers populating the oligomers. This type of disorder is mainly driven by intrinsic oxidation capability of DHI and DHICA and degree of π-electron delocalization.

Based on the above information, eumelanin has been defined as a physicochemically disordered biopigment. Because of physicochemical disorder, the underlying mechanisms of solid-state aggregation (supramolecular self-assembly) and polymerization (covalent bonding) have proven challenging to unravel and are still object of debate.

2.3 Physicochemical Properties of Eumelanin

Apart from its biological importance, eumelanin exhibits a set of distinctive physicochemical properties, including electronic conjugation (i.e. alternance of single and double carbon-carbon bonds), broadband UV-Vis absorption, radical scavenging (a radical is a molecular entity with an unpaired electron), metal-ion chelation, hydration-dependent electrical response, photoconductivity and redox activity [23], [98]. In a biological environment, an antioxidant is a substance that considerably delays and/or prevents the oxidation of an oxidizable substance. Radical scavengers and metal-ion chelators materials match this definition [101]. Thus, eumelanin is *de facto* an antioxidant. Eumelanin is filmable, biocompatible [102] and potentially biodegradable [65].

We note that the terms "radical" and "free radical" have been interchangeably used in the literature. However, in this thesis the term "free radical" will be avoided whenever possible, according to IUPAC recommendations: " […] in the context of physical organic chemistry, it seems desirable cease using the adjective 'free' in the general name of this type of molecular entities […]" [103].

Being the key objects of investigation of this PhD work, the fundamentals of eumelanin filmability and charge carrier transport properties, are provided in the literature review (see chapter 2).

2.3.1 Optical Properties

2.3.1.1 Broadband Optical Absorption

Eumelanin displays broadband optical absorption, both in solution and in solid form [23], [104] (Figure 2.6 (a)). The lack of any absorption peak in the excitation and absorption spectra, usually associated with individual and/or combined vibro-electronic transitions of molecules, makes eumelanin an atypical organic pigment. In virtue of its absorption, eumelanin is an effective photoprotector [22].

Several hypotheses and models have been proposed to explain the origin of the broadband optical absorption of eumelanin: (i) Rayleigh scattering dominates the absorbance, (ii) the chemical and

the geometrical disorder model, and (iii) eumelanin is an organic amorphous semiconductor (ASc), due to the similarity between the optical absorption spectra of eumelanin and those of amorphous semiconductors.

Regarding hypothesis (i), the optical absorption properties of eumelanin were initially ascribed to Rayleigh scattering [105], due to the presence of 20 nm-200 nm-sized aggregates during the third and fourth level of supramolecular buildup (Figure 2.5). Indeed, Rayleigh scattering is a wavelength-dependent interaction ($\sim\lambda^{-4}$) between the electromagnetic radiation and matter occurring in presence of structures with dimensions lower than the wavelength of the incident light. Rayleigh scattering has the effect of superimposing a broad background on any individual electronic transition. For this reason, it was invoked to explain the steep rise in absorption in the high-energy end of the spectrum. However, it was found that, under spectroscopic conditions, scattering contributes less than 6% and 12% to the total light attenuation in solid state and in solution, respectively [105], [106].

In regard to hypothesis (ii), the chemical disorder model posits that the oxidative polymerization brings about the formation of several chemically distinct species (i.e., groups of oligomers differing by bonding configurations, number and type of monomers). The wide variety of these chemical species generates ensembles of oligomers with different secondary structures (see section 2.2.5, point 1). In this picture, the broadband absorption is a consequence of superimposed, non-homogeneously broadened Gaussian transitions associated to each secondary structure composing the ensemble (superposition principle, Figure 2.6 (a)) [22], [23]. The geometrical disorder model is based upon the supramolecular structural disorder featured by the biopigment (see section 2.2.4). The model suggests that eumelanin's optical absorption properties stem from peculiar excitonic couplings between stacked oligomers differing by size and orientation [107]. The geometrical disorder model undermined the chemical disorder one, this latter being uncapable to predict the monotonic increase of the optical absorption in the UV region of the spectrum.

As mentioned in section 2.2.5, the ratio DHI/DHICA plays a central role in defining the optical absorption properties of eumelanin. It has been observed that the optical absorption of DHI-eumelanin (i.e., eumelanin made up of only of DHI monomers) in the visible region of the

spectrum is higher than that of DHICA-eumelanin (i.e., eumelanin made up of only DHICA monomers). In DHI-eumelanin the planar configuration of oligomers promotes a high degree of π-π stacking and favors electronic delocalization (stacking increases visible absorption, Figure 2.6 (b)) [104]. Conversely, the presence of carboxyl groups in DHICA-eumelanin limits the extension of inter-units π-conjugation and the structure is highly non-planar (twisted, Figure 1.6 (c)).

The formulation and the implications of hypothesis (iii) are central to the investigations of this PhD work and will be discussed in detail in the literature review (see chapter 3).
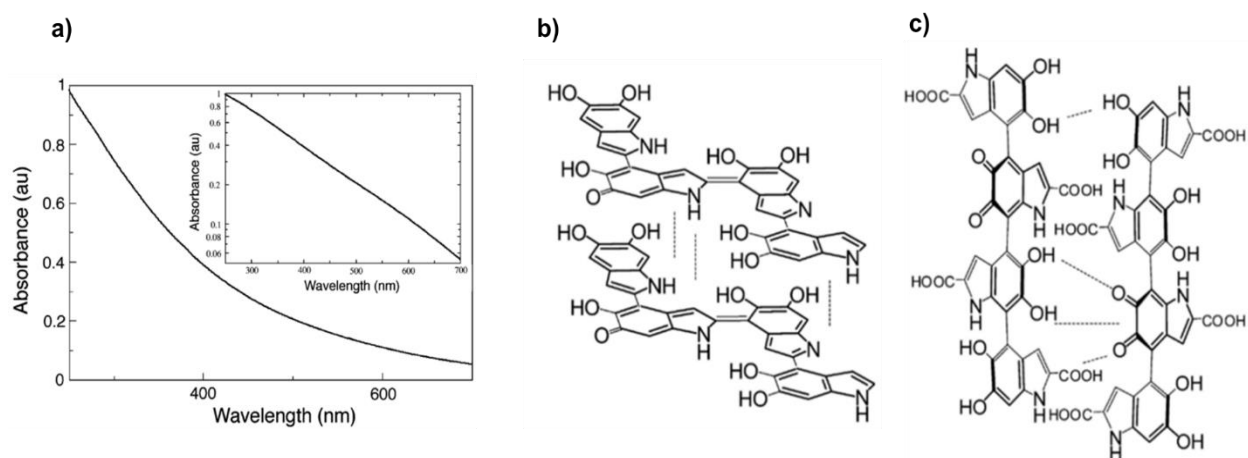
Figure 2.6 (a) UV-Vis absorption spectrum of eumelanin with its corresponding log-linear plot in the inset; representative sketch of (b) DHI- and (c) DHICA-eumelanin structures. Reproduced and adapted with permission from Refs. [98] and [108].

2.3.1.2 Optical Excitation and Emission

Numerous steady state and time-resolved studies have been carried out to clarify the mechanisms of relaxation after the optical excitation in natural and synthetic eumelanin [109]–[112]. These investigations showed that eumelanin features radiative emission (fluorescence) with typical quantum yield of 10^{-4} [105], [113]–[115]. Picosecond and femtosecond time-resolved spectroscopy measurements enabled researchers to explain the dynamics of excitation and

relaxation in the biopigment [84], [116]–[119]. The results of this body of work can be summarized by the three following points:

1. The radiative emission is composed of four main components, each one decaying on the order of nanoseconds.

2. The radiative emission energy constitutes a small portion of the total energy of the absorbed photons.

3. All remaining excited states decay via non-radiative paths. The repopulation of the ground state takes place via vibrational relaxation and/or internal conversion processes.

2.3.2 Metal-Ion Binding

Natural and synthetic eumelanin, as well as DHI-and DHICA-eumelanin can bind metal-ions including lithium (Li^+) [120], sodium (Na^+) [102], [120]–[122], potassium (K^+) [120], [123], calcium (Ca^{2+}) [120], [124]–[128], zinc (Zn^{2+}) [124], [129], [130], magnesium (Mg^{2+}) [120], [124], [131], manganese (Mn^{2+}) [132], iron (Fe^{3+}) [133]–[136], copper (Cu^{2+}) [130], [136], [137] and many others [35]. Ion binding takes places via coulombic interactions and/or coordination, this last through chelation (from Greek χηλή=claw). Typical primary and secondary binding sites are the catechol hydroxyl groups, the amine groups in DHI and DHICA, and the carboxyl groups in DHICA [35].

The incorporation of metal cations influences eumelanin's formation rate as well as the ratio DHI/DHICA during melanogenesis. However, it is currently unclear what is the role of metal-ion binding in regard to the supramolecular aggregation of the biopigment [115]. Recently, Mostert *et al.* showed that it is possible to modulate the protonic conductivity of hydrated synthetic eumelanin pellets by chelating Cu^{2+} cations [138].

Finally, the metal-ion binding properties of Sepia melanin, DHI- and DHICA-eumelanin have been recently probed by electrochemical studies in buffer solutions. Results showed that binding capability, binding site (i.e., primary vs secondary) and binding affinity depend on pH, type of eumelanin (i.e., natural vs synthetic) and type of cation [139], [140].

2.3.3 Radical Scavenging

The redox state of eumelanin determines its ability to scavenge radicals. It must be in an oxidized (reduced) state to receive (donate) electrons and scavenge reductive (oxidative) radicals [70], [71], [141].

The radical scavenging and photoprotection properties of biological systems are profoundly connected [23], [54], [92], [142]. Forest *et al.* showed that photoprotection mechanisms take place in the UVA (320 nm-400 nm) and UVB (280 nm-320 nm) irradiations [143]. On the other hand, when exposed to UVC photons (220 nm-280 nm), eumelanin can generate reactive oxygen species (ROS) and become cytotoxic (photodamaging behavior) [144]–[147]. Eventually, eumelanin can scavenge ROS species that lead to severe skin damage [148]. Nofsinger *et al.* proposed that the dualism between photoprotective and photodamaging behavior depends on the degree of structural aggregation of the biopigment [149]. In this context, the authors found that a structure made of few nm-sized aggregates is likely involved in photodegradation processes leading to the formation of ROS. On the other hand, a few hundreds of nm-sized aggregates are expected to promote photothermal conversion.

Several studies showed that the ratio DHI/DHICA affects the radical scavenging properties of eumelanin [149]–[151]. The radical scavenging capability of DHI and DHICA monomers and DHI- and DHICA-eumelanin were determined by scavenging tests using nitric oxide (NO) [152], (1,1)-diphenyl-2-picrylhydrazyl (DPPH) [153] and (2,2')-azinobis(3-ethyl-benzothiazoline-6-sulfonic acid) (ABTS) [154].

Results can be wrapped up as it follows: (i) DHICA is a superior radical scavenger with respect to DHI. Particularly, the planar π-π stacked structure and high degree of π-electron delocalization make DHI less accessible than DHICA to radical species (Figure 2.6 (b) and (c)); (ii) DHI and DHICA feature superior radical scavenging properties with respect to their polymerized counterparts. Indeed, the oxidative polymerization of DHI- and DHICA-eumelanin decreases the number of O-H and N-H groups participating to radical scavenging due to the oxidation of H2Q forms into Q ones [93], [150], [151]; (iii) as in the case of the monomers, DHICA-eumelanin has proven a better radical scavenger than DHI-eumelanin [93].

2.3.4 Paramagnetic Properties

Eumelanin exhibits a permanent electron paramagnetic resonance (EPR) signal both in solution and in solid state [23], [33], a marked signature of the presence of radical centers [155]. These lasts are associated with the comproportionation reaction, namely the chemical equilibrium between the relative content of H2Q, SQ and Q redox forms of the building blocks (Figure 2.4) [155], [156].

EPR surveys showed that the relative concentrations of radicals depends on pH [157], [158], temperature [159], exposure to redox agents [160], photo generation [45], [161] and metal-ion binding [162]. More importantly, EPR studies revealed that the comproportionation reaction determines both type and content of radicals [163], [164]. In this regard, in eumelanin there are two types of radicals: (i) intrinsic, carbon-centered radicals (CCR), derived from the polymerization process and (ii) extrinsic radicals associated to the SQ population (i.e. referred as semiquinone radicals (SQR)) [165]. SQR have been observed in strongly hydrated eumelanin and are considered mobile charge carriers. On the other hand, it seems that CCR play no role in defining the electrical properties of eumelanin [166].

The contribution of intrinsic and extrinsic radicals to the transport physics of eumelanin will be thoroughly discussed in the literature review (see section 3.4, chapter 3).

2.3.5 Redox Properties

The redox properties of eumelanin are determined by the electron transfer ability of DHI and DHICA building blocks and their redox state (e.g., H2Q, SQ, Q, and QI, Figure 2.3 and Figure 2.4).

Several works investigated the redox properties of synthetic and natural eumelanin mainly by cyclic voltammetry (CV). Rozanowska *et al.* found a one-electron reduction process for synthetic eumelanin at a potential of about 500 mV versus the normal hydrogen electrode (NHE) [167]. Serpentini and co-workers reported on oxidation processes for Dopa melanin at 460 mV and 530 mV versus the saturated calomel electrode (SCE), respectively [168]. Gidanian and Farmer studied the redox properties of eumelanin films derived from the oxidative polymerization of DHI [169]. The authors reported on an oxidation process at a potential of 125 mV versus the Ag-

AgCl electrode that was attributed to the formation of quinone-imine (QI, Figure 1.3). Electrochemical studies on electropolymerized eumelanin films immersed in different electrolytes, revealed that the redox activity of eumelanin depends on pH and presence of metal ions. Robinson *et al.* and Horak *et al.* showed that changing the pH of the electrolyte can shift and/or suppress anodic and cathodic peaks [170], [171]. Kim and co-workers reported on the appearance (disappearance) of an oxidation peak at 160 mV versus saturated hydrogen electrode (SHE) in presence (absence) of Mg ions in the electrolyte [131]. Recently, Xu *et al.* performed an in-depth electrochemical study on DHI-, DHICA-eumelanin and Sepia melanin in different buffer solutions and in presence of several metal ions including monovalent (Na^+, K^+ and NH_4^+) and divalent (Cu^{2+}) cations. As opposed to previous studies, where no clear voltammetric peaks were found for natural eumelanin [25], the authors observed an oxidation and a reduction peak at 150 mV and -60 mV versus Ag/AgCl in presence of monovalent cations, respectively [139]. Furthermore, all eumelanin samples immersed in buffer solutions with Cu^{2+} cations featured a strong oxidation peak at 100 mV. As we shall see in section 1.5, these studies on the synergy between redox activity and metal ion binding have set the basis for the use of eumelanin in energy storage applications.

2.3.6 Other Properties

2.3.6.1 Hydrophilicity

When exposed to an enriched water vapor environment, eumelanin can incorporate an amount of water up to 20% of its own mass in 24 hours (hydrophilicity) [41], [123], [172], [173]. Two "forms" of water are found in solid eumelanin: weakly bound water (i.e., adsorbed in a few surface layers) and strongly bound water (i.e., absorbed in the bulk and retained in the inner macromolecular structure of the biopigment) [23], [173]. In this regard, Albano *et al.* performed thermogravimetric analysis (TGA) on Sepia melanin powders hydrated at 70% relative humidity (RH) for 24 hours. Results revealed the loss of weakly and strongly bound water at about 53 °C and from 124 °C to 171 °C, respectively. Mostert *et al.* performed a systematic study on water- and ethanol-adsorption isotherms in synthetic eumelanin pressed pellets. Both adsorbates were adsorbed in equal amounts (about 20% of weight gain) but at very different time scales, namely from 24 min to 30 min and from 1 hour to 30 hours for water and ethanol, respectively [41].

Recently, Martinez-Gonzales *et al*. used inelastic neutron scattering (INS) to unravel the structural order/disorder of water molecules in synthetic eumelanin pellets upon water adsorption. Inelastic neutron scattering spectra suggest that the adsorption of weakly bound water leads to the formation of 3-5 layers featuring structure akin to that of amorphous ice [174]. Despite these efforts, there are no studies on the structural properties of strongly bound water for eumelanin.

2.3.6.2 Biodegradability

Eumelanin is biocompatible as well as bioresorbable [102]. We note that in the eumelanin community the words bioresorbable and biodegradable were often interchanged, leading to a certain confusion. Bioresorbable refers to the degradation of a material in contact with body fluids, whereas biodegradation relies on the spontaneous decomposition of a material under the attack of microorganisms (i.e., bacteria and fungi). Human hair eumelanin, synthetic eumelanin and fungal melanin were considered biodegradable in some works [175], [176] and non-biodegradable in others [177], [178]. At the origin of this controversy there are the complex experimental conditions required to assess the extent of biodegradation. Indeed, the outcomes of a biodegradation experiment depend on type of microorganisms, nutrients and, in the case of eumelanin, on the degree of supramolecular buildup. An additional issue is the lack of standards to evaluate the biodegradability of organic electronics materials. This concern has recently been addressed by Di Mauro *et al.* who studied the mesophilic (25 °C) and thermophilic (58 °C) biodegradation of natural Sepia melanin in industrial compost conditions [65]. Sepia melanin biodegradation reached 4.1% in 97 days and 37% in 98 days in mesophilic and thermophilic conditions, respectively. According to ASTM 5338 (http://www.astm.org/cgi-bin/resolver.cgi?D5338), Sepia melanin was not considered biodegradable.

2.4 Other types of Melanins

2.4.1 Pheomelanin

The oxidation of tyrosine into DQ by tyrosinase starts the biosynthesis of pheomelanin (Figure 2.2). In presence of the enzyme cysteine, the oxidation of 5-S-cysteinyldopa (5-S-CD) and 2-S-cysteinyldopa (2-S-CD) leads to the formation of pheomelanin through the precursors

benzothiazine and (g) benzothiazole (Figure 2.1 (f) and (g)). Pheomelanin is mainly found in human red hair and hen feathers, and it has poorer photoprotective properties than eumelanin. The photoreactive properties of benzothiazine and benzothiazole building blocks are still under investigation [179].

2.4.2 Neuromelanin

The biosynthetic pathways leading to the formation of neuromelanin differ from that of eumelanin and pheomelanin and it is poorly understood. Neuromelanin is a dark, insoluble biomacromolecule mainly composed of melanin, lipids and proteins and metal ions. Neuromelanin is only found in the large primates. In humans, neuromelanin accumulates in the neurons of the substantia nigra and locus coeruleus of the brain [52], [53], where its concentration increases with aging. The loss of neuromelanin in the neurons of patients with Parkinson's disease, is likely responsible for the occurrence of such a neurodegenerative syndrome as well as brain aging [180]. However, neuromelanin also play a role of neuroprotection through chelation of toxic metals and release of non-redox active moieties [181].

CHAPTER 3   LITERATURE REVIEW

3.1   **Eumelanin Films: Processing Techniques and Morphology**

In the quest to design and develop high-performance optoelectronic devices, organic electronics and bioelectronics rely on solution processing and evaporation of continuous and smooth organic thin films. In this regard, the preparation of eumelanin films of device quality has proven difficult, owing to its (i) limited solubility in most organic solvents and (ii) oligomeric disordered nature that also makes the thermal evaporation a challenging task [22], [23], [47], [51] (see section 2.2, chapter 2). Over the last twenty years, several research groups focused on the solution processing of eumelanin thin films [36], [182]–[188]. Alternative fabrication techniques such as spray-coating [189], electrospray deposition [190], matrix-assisted pulsed laser deposition [191], [192], thermal evaporation [83] and electropolymerization [193], [194] were also explored.

Déziderio *et al.* da Silva *et al*. fabricated synthetic eumelanin films by spin coating and drop casting from dimethylformamide (DMF) and dimethyl sulfoxide (DMSO) solutions on Si and quartz substrates. Atomic force microscopy (AFM) images showed the superior homogeneity and smoothness of DMSO films with respect to DMF. The morphology of films processed from DMSO were characterized by spherical aggregates and terraces featuring height of 50 nm and lateral extension of about 10 µm [182], [183]. A few years later, the better filmability (i.e. high thin film stability) of DMSO eumelanin films compared with DMF films was explained by the high chemical stability provided by sulfonated groups bonded to the catechol groups of eumelanin [184]. Bothma *et al.* spin coated eumelanin films on Si and glass substrates from an ammonia solution [188] and reported on the formation of smooth films characterized by 20 nm-sized spherical aggregates. Langer's group exploited the solubility of eumelanin in strongly alkaline aqueous solutions to compare the morphology of eumelanin films spin coated from sodium hydroxide (NaOH) and DMSO solutions [185]. The authors observed that films prepared from NaOH were rough and characterized by micrometer-sized dendrites. On the other hand, films spin coated from DMSO formed spherical aggregates and were molecularly smooth (root mean square roughness (RMS) of about 0.3 nm). Recently, Wünsche *et al*. performed an in-depth investigation of the morphological properties of eumelanin films obtained by dissolving Dopa

melanin, DMSO melanin and commercial melanin (Sigma melanin) in DMSO and ammonia (NH_3) [186]. The spin coating of either Dopa melanin or Sigma melanin from DMSO solutions generated eumelanin films of superior quality in terms of homogeneity and smoothness with respect to films obtained from NH_3 solutions. Remarkably, Sigma melanin films spin coated from DMSO were the smoothest (RMS roughness of 0.35 nm) and featured stable nanoaggregates about 2 nm-high and 30 nm-wide.

Pezzella's group synthesized chemically controlled DHI- and DHICA- powders (melanin obtained exclusively from one of the two building blocks) soluble in methanol and other organic solvents. The same group obtained DHI-and DHICA-eumelanin films via an ammonia-induced solid state polymerization (AISSP) protocol [36], [187]. This procedure involves the deposition of DHI and DHICA films (e.g., via drop casting or spin coating) from methanol solutions and the subsequent exposure to an ammonia (polymerization catalyst)-enriched atmosphere. The authors reported on very stable, homogeneous, and smooth eumelanin films. In the atomic force microscope, films showed the presence of columnar structures a few nm high. Recently, Pezzella *et al*. observed the spontaneous formation at ambient conditions of wrinkles in AISSP-DHI films deposited on glass from DHI solutions with concentrations from 25 mg ml^{-1} to 200 mg ml^{-1} [187]. The formation of wrinkles took place only in films thicker than 250 nm (thinner films were smooth and exhibited columnar-like structures). Based on these observations, self-wrinkling of AISSP-DHI was attributed to inhomogeneous oxidation processes occurring in thick films, where inner and outer layers would experience slower and faster oxidation rates, respectively. In terms of film growth, faster (slower) oxidation rates were associated with faster (slower) molecular mobility as well as higher (lower) degree of crosslinking and stiffening in the films.

Abbas *et al*. deposited spray-coated eumelanin films on glass substrates from dispersions in a solvent mixture of methanol:DMSO [189]. Scanning electron microscopy (SEM) and AFM images revealed the formation of smooth surfaces (RMS roughness of 0.4 nm) with the presence of micrometric filamentary structures. In a subsequent study, the same group succeeded in depositing eumelanin films on glass substrates by electrospray deposition from the same solvent mixture of methanol:DMSO [190]. Despite good continuity and homogeneity, these films were considerably rougher than their counterparts fabricated by spray deposition.

Bloisi *et al*. prepared eumelanin films via matrix-assisted pulsed laser evaporation (MAPLE) deposition from suspensions of DHI in phosphate buffer solutions. The authors obtained relatively rough and thick eumelanin films (RMS roughness and thickness of about 100 nm and 250 nm, respectively). In an independent study, they also showed that film RMS roughness and thickness uniformity were strongly dependent on the frequency of the laser pulse and on the substrate temperature. Notably, the lower the frequency and the substrate temperature, the smoother and thinner the films [192].

Eumelanin films have been also deposited on Au and ITO electrodes by electropolymerization in aqueous suspensions [193]–[195].

Irrespective of the body of work herein summarized, the question whether and how the synergy between supramolecular self-assembly (i.e., π-π stacking) and polymerization (i.e., formation of covalent bonding) govern eumelanin film formation and morphology has not been answered yet.

3.2 Concepts in Electron-Band Theory to Understand Charge Transport in Bio-sourced Materials

Here, we present introductory aspects of the band theory for ordered (crystalline) and disordered (amorphous) materials that are fundamental to understand the transport physics of bio-sourced materials akin to eumelanin. To this aim, we briefly give an overview on the band theory of electrical conduction for conventional crystalline solids (section 3.2.1) and then its modification for amorphous materials (section 3.2.2).

The charge carrier transport properties of any material can be described by basic conductivity (σ) equation:

$$\sigma = nq\mu \hspace{4cm} \text{Eq. 3.1}$$

where σ is the conductivity, n is charge density, q is fundamental charge, and μ is the mobility of the charge carrier (i.e., electrons and holes). Indeed, any discussion on charge carrier transport properties in solids can be carried out only by understanding σ in terms of μ and n. In Section 3.2.3, we shortly discuss the relevance of these transport models to bio-sourced materials.

Then, we discuss fundamental aspects of proton transport mechanisms (e.g., vehicle and Grotthus) in hydrated protonic bio-conductors to introduce the concept of *protonic semiconductor* by means of a quantum mechanical description of protonic transport in H-bonded chains of proton conductors (sections 3.2.4, 3.2.5 and 3.2.6).

At the end of the chapter, we will provide a state-of-the-art picture of the charge carrier transport properties of eumelanin (section 3.3). The focus on a central topic of this PhD work, i.e. the dichotomy between two models of transport proposed for eumelanin: (i) the MD amorphous semiconductor model suggested in the 1970s by J. McGinness (section 3.3.1); (ii) the mixed ionic (protonic)-electronic conductor model proposed between 2010 and 2018 by P. Meredith's group (section 3.3.2).

A summary on the charge carrier transport properties of hydrated and dry eumelanin pellets and films is also provided in Article 2 (chapter 6, Table 6.1).

All in all, what follows aims to provide the reader with the necessary elements to understand the current challenges faced when describing charge transport in eumelanin.

3.2.1 Band Theory of Electrons

The properties of electrons in crystalline solids are explained by the band theory. In crystalline solids (inorganic and organic) the structure is constituted of unit cells (e.g., atoms, ions, molecules) arranged in periodic planes of arrays (*Bravais lattice*). This periodicity is responsible for highly ordered structures and profoundly impacts the foundations of band transport theories [196]. The energy levels of an electron are determined considering a steady state single-electron Hamiltonian with periodicity of underlying lattice. Indeed, the electron interacts with the lattice units through periodic potential wells. In this framework, the long-range order enables the extended delocalization of the electronic wavefunction, and the motion of electrons is described by *Bloch waves*.

The delocalization of the electronic charge carriers generates energy bands, namely valence band (VB) and conduction band (CB), for the occupancy state of holes and electrons respectively. The states are extended within the band i.e. the wavefunction occupies the entire volume. The energy difference between the top of the VB (E_V) and the bottom of the CB (E_C) defines the crystalline

band gap region (E_G). In a crystal with N primitive unit cells, the number of allowed values of the electron wavevector (**k**) is exactly N (i.e., each unit cell contributes with an independent value of wavevector **k** to each energy band). Considering that electrons exhibit two spin orientations, there are 2N independent electronic states in each energy band. Thus, a crystal with one valence atom per unit cell exhibits a half-filled energy band (Figure 3.1 (a)). This is the case of electrical conductors such as alkaline metals and noble metals. In these systems, the application of an electric field, small enough not to perturb the electronic structure of the crystal, gives rise to an electric current. On the other hand, given an even number of valence atoms per unit cell, two cases are possible:

1. The valence band partially overlaps in energy with the nearest top energy band: instead of a fully occupied band giving rise to an insulator, there are one or more partially filled bands such that the crystal is broadly defined a semimetal. Examples of semimetals are the alkaline hearth metals. While the application of an electric field to semimetals gives rise to an electric current, the electrical conductivity of these systems is lower than that of metals (Figure 3.1 (b)).

2. One or more energy bands are fully filled and separated with an energy gap from the nearest top energy band. In this case, the crystal is insulator: the application of an external electric will not give rise to an electric current. In insulators, E_G is typically greater than 3 eV (Figure 3.1 (c)).

Crystalline semiconductors at the absolute zero (T=0 K) are insulators because they exhibit a fully occupied VB separated by an energy gap (about 1 eV to 3 eV) from a fully empty topmost CB (Figure 3.1 (d)). In intrinsic semiconductors (i.e., a defect and impurity free semiconductor) the Fermi energy level ε_F lies between E_V and E_C (the band gap) where no electronic states are found. In semiconductors, electronic conduction arises from the addition of dopants (impurities) by doping. The doping introduces energy levels in the energy gap with significant modification of charge carrier concentration and electrical conductivity. For example, the addition of pentavalent (Arsenic (As)) or trivalent (Gallium (Ga)) impurities to Germanium, introduces electron donors (electron acceptors) energy levels close to the CB (VB) of the semiconductor.

Thus, the ionization of electron donors (acceptors) levels can send an extra electron (hole) in the CB (VB).
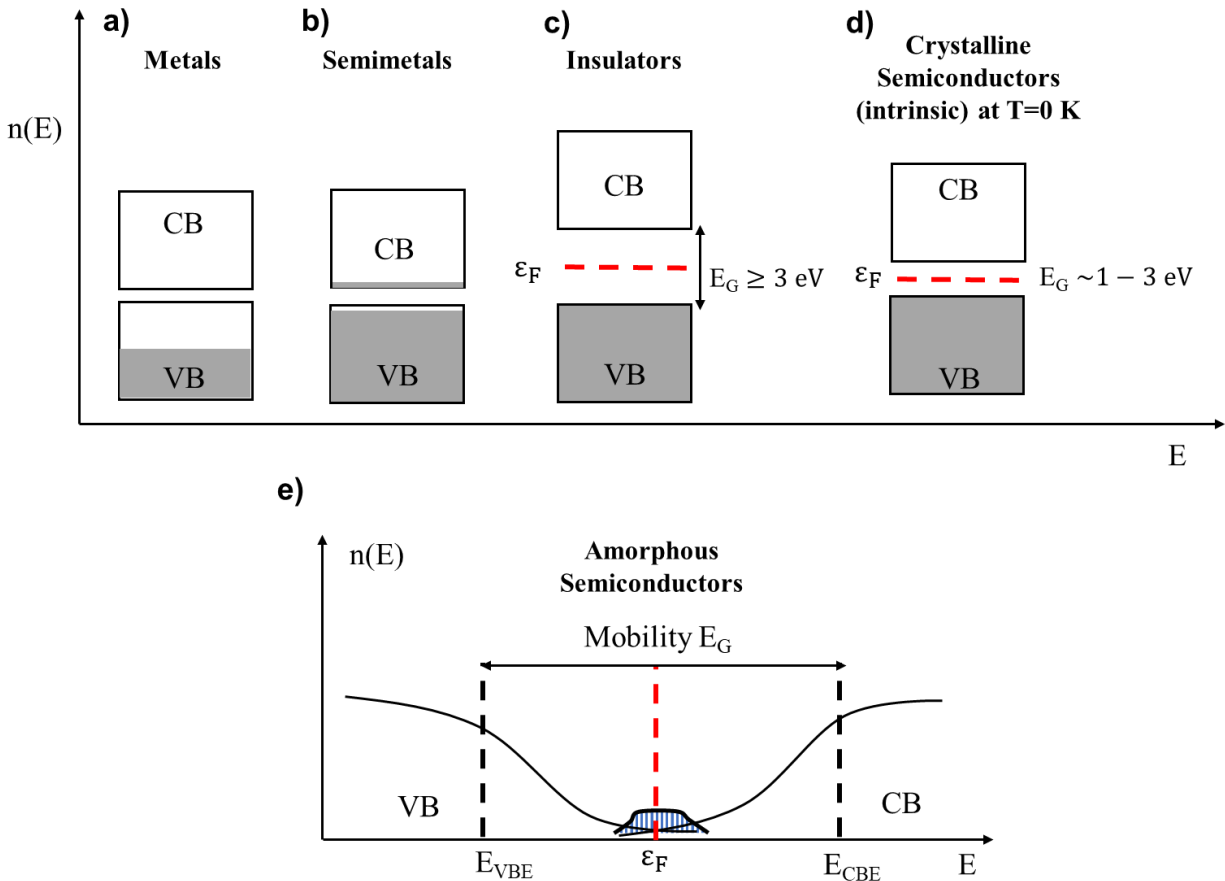
Figure 3.1 Density of electronic states in the energy landscape for (a) metals, (b) semimetals, (c) insulators, (d) crystalline intrinsic semiconductors, and (e) amorphous semiconductors (permission granted by authorship from Ref. [46]). The red dashed line shows the Fermi level in (c) and (d). The grey areas in (a) to (d) indicate the region filled with electrons. The dashed blue area in (e) indicates the region of the space where VB and CB tails of states extend with a Gaussian distribution of in the energy gap as posited by the MD model.

The study of charge transport of any material consists in understanding the relationship between E_G and the density of intrinsic charge carriers' concentration (n). In intrinsic semiconductors, the

total density of electrons $n_0(T)$ and holes $p_0(T)$ as a function of the temperature in CB and VB are given by equations of the form $n_0(T) = N_C(T)e^{-\frac{E_C-\varepsilon_F}{k_BT}}$ and $p_0(T) = N_V(T)e^{-\frac{\varepsilon_F-E_V}{k_BT}}$,where k_B is the Boltzmann constant, T the temperature, $N_C(T)$ and $N_V(T)$ the effective CB and VB density of states, respectively. The mass-action law posits that the intrinsic concentration of available charge carriers for conduction depends on E_G and T with a Maxwell-Boltzmann relation of the form $n = \sqrt{n_C(T)n_V(T)}e^{-E_G/2k_BT}$ [197]. As a result, the electric conductivity can be written as:

$$\sigma = q\mu\sqrt{N_C(T)N_V(T)}e^{-E_G/2k_BT} \qquad\qquad Eq.\,3.2$$

q and μ being the elementary charge and the total charge mobility (i.e., the sum of electron (μ_e) and hole mobility (μ_h)), respectively. Electron mobility is typically higher than hole mobility because in CB there is a much larger number of available empty states than in the VB. In semiconductors, σ is temperature-dependent and E_G is an activation energy barrier for charge carrier transport.

3.2.2 Modifications of Band Theory: the Mott-Davis (MD) Amorphous Semiconductor Model

The word *amorphous*, both for the case of inorganic and organic solids, refers to the presence of long-range (extended) disorder (or short-range order). For inorganic materials, structural disorder stems from fluctuations of bond length, presence of interstitial defects and vacancies. In organic amorphous materials, *positional disorder* originates for instance from shorter (or longer) than average conjugations lengths of molecular chains not arranged into periodic structures [38], [196]–[198]. Twists of molecular backbones cause additional source of disorder (i.e. *conformational* disorder) [199], [200].

A key aspect to understand the transport physics of amorphous systems is that disorder strongly localizes the electronic states. The electrical properties of amorphous semiconductors have been described by several models. In the Mott-Davis (MD) model [201], disorder confines Bloch's waves around a few lattice units and introduces band tails of states at the band edge of VB (E_{VBE}) and CB (E_{CBE}). These states extend in the gap around ε_F with a Gaussian distribution (shaded

blue area, Figure 3.1 (e)) such that only a mobility energy gap can be defined. In the MD model, such an electronic structure exhibiting a non-well-defined energy gap is responsible for the broadband optical absorption properties of amorphous semiconductors, like chalcogenide glasses [39].

We note that other models, such as the Brust model, the Penn-Philips model and the Thorpe model, admit the existence of a well-defined energy gap in the density of electronic of states as function of the energy [202].

In crystals, only band-like conduction is expected because E_G is the only activation energy appearing in the analytic expression for $\sigma(T)$. Conversely, for amorphous solids several activation energies exist, each one corresponding to a given transport mechanism. For instance, a localized electron can hop to its closest localized empty state (*nearest neighbor hopping* (NNH)) or to an empty localized state further away but within the energy landscape around the ε_F level (*variable range hopping* (VRH)). For an electron to hop from a fully occupied localized state to an unoccupied localized state, it requires an activation energy B such that the conductivity is described by the following equation:

$$\sigma = A\exp\left(-B/k_BT^k\right)$$ Eq. 3.3

where A is pre-exponential factor related to the electrical conductivity in localized electronic states and k is an exponent determined by the temperature (i.e. at room temperature k=1 and at lower temperatures k= ¼).

By applying strong electric fields (e.g. thousands of V cm^{-1} as in resistive switching experiments) and/or increasing temperature, electrons can hop from occupied localized states, located within E_{CBE} and ε_F, to empty delocalized states in CB (*band-like conduction,* Figure 3.1 (e)) [38]. The conductivity in band-like conduction regime is temperature-dependent through an exponential relation similar to eq. 3.3 but with the exception that k=1 and B indicates the minimum required energy for electrons to hop from localized to delocalized states. Same discussion holds for hopping of holes in localized states (NNH and VRH) and from localized to delocalized states beyond the VB (hole band-like conduction).

3.2.3 Relevance and Limitations of the MD Model to Bio-sourced Materials

The relevance of the MD model to bio-sourced materials is an open debate in the field of organic electronics. In biomaterials the presence of intrinsic and extrinsic (e.g., adsorbed water in the molecular structure) disorder impacts their charge transport properties. Particularly, it has been reported that the presence of adsorbed water perturbs the structural environment of these systems by locally changing dielectric constant and capacitance [203]. In addition, the interplay of hydration and temperature effects makes challenging the assignment of an exclusive temperature (or hydration)-dependent analytical expression for the electrical conductivity of bio-sourced materials. Several studies on proteins [204], dry and hydrated hemoglobin [205], and DNA [203], [206]–[209], showed that the conductivity in these systems is strongly temperature-dependent through hopping of electrons across activation energy barriers, in analogy to amorphous semiconductors. In accordance with these studies, the mobility for mixed electronic-protonic bio-molecular systems can be described as follows:

$$\mu = \mu_o \exp\left(-E_H/k_B T\right) \qquad\qquad\qquad \text{Eq. 3.4}$$

μ_o being a pre-exponential factor and E_H the average energy barrier height for a hopping event. It is worth noticing that there is no exponent behaviour at low temperature, as observed in amorphous semiconductors (Eq. 3.3). This appears to be a fundamental difference between localized hopping transport in disordered inorganic and organic materials. As mentioned above, in inorganic materials charge carrier mobility and density strongly depend on temperature. In bio-sourced materials the effects of hydration and temperature on the charge carrier transport properties are profoundly linked and therefore, difficult to disentangle. This is a fundamental aspect to considered when describing the electronic conduction properties of bio-sourced materials.

Although the direct application of the MD model to biological systems is quite rare, one of the most important exceptions is given by the case of eumelanin. The optical and hydration-dependent electrical properties of eumelanin were initially ascribed to the MD model, since the observation of broadband absorption (see section 2.3.1, chapter 2), paralleled by band-like conduction in resistive switching and temperature-activated conductivity experiments [23], [37], [203] (see section 3.3.1). Over the last ten years, the MD model for eumelanin has been

undermined by the "mixed protonic-electronic conductor model". This model posits that eumelanin is mainly a protonic conductor when it adsorbs water beyond a threshold of about 12% by weight (%w/w). Thus, adsorbed water would act as a "proton sink" increasing the density of available charge carriers (i.e. protons and electrons for conduction in the biopigment) [42], [44] (see section 3.3.2).

From these considerations, the question whether in bio-sourced materials the band theory of transport holds for ions and for the special case of protons, naturally arises. This is particularly true in the case of eumelanin, for which the role of protonic and electronic transport in conferring semiconducting properties has not been clarified, yet. In sections 3.2.4, 3.2.5 and 3.2.6 we show that studies on proton transport mechanisms in protonic biomaterials lead to the concept of protonic semiconductor. The existence of this model highlights, once more, the challenges of attempting to provide an appropriate description of the transport physics of bio-sourced materials, including eumelanin.

3.2.4 Protonic Transport in Bio-sourced Materials

Biomaterials are intrinsically wet and feature ionic transport. Biological signals naturally arise from the movement of ions (e.g., Na^+, K^+, Ca^{2+}, Cl^- etc.) and protons (H^+). In these systems, the presence of ionic species affects charge transport properties by locally modifying molecular environment, this last dependent upon the hydration/solvation conditions.

Protons are the most mobile charges among ionic species with close radius and similar mass [210]. Nature conveyed to protonic transport a pivotal role in several biological energy conversion processes, these lasts occurring via protonation/deprotonation reactions across hydrogen (H) bonds. The most common example is the formation of adenosine triphosphate (ATP) via oxidative phosphorylation of adenosine diphosphate (ADP), driven by proton gradients during the photosynthesis in mitochondria [211], [212]. Additional examples include proton gradients in rhodopsin [213], proton activated flagella in a few species of bacteria [214], pH regulation in cellular proton channels [215].

Aside from specific biological functions, protonic (ionic) transport attracts tremendous interest in the field of organic bio-sourced iontronics. Particularly, protonic (ionic) and mixed conductors can be integrated in logic circuits to mimic, register and stimulate biological functionalities [216], [217]. Beside converting biochemical (ionic) into electronic signals [27], they can be active components in bioprotonic FETs [218], LEDs [14] and switching memory devices [219], [220]. Therefore, understanding role and impact of mixed transport on the mesoscopic properties of bio-sourced materials (i.e., physicochemical properties of matter at the nano- and micron-scale) is the underpinning to design and develop high performance bioelectronic devices. In protonic and mixed protonic-electronic biomaterials H-bonds build up molecular chains that serve as *pathways* for protons.

3.2.5 Proton Transport Mechanisms

The H-bond is a noncovalent and directional interaction where a H atom is shared between two electronegative atoms that take part to a covalent bond. Due to different bonding configurations, many types of H-bonds exist, approaching typical energy range from 0.05 eV (i.e. van der Waals bonds) to about 0.7 eV (i.e. covalent bonds) [221]. In several hydrated bio-sourced materials, molecular chains known *as proton wires* form via H-bonding between water molecules and between water molecules and proton donors (e.g. N-H, NH_2) and/or proton acceptors (e.g. O-H, =O) functional groups. The acidity increases with the content of proton donors and basicity with the content of proton acceptors [222]. The acidity and basicity can be also increased by hydration, i.e. the increase of water %w/w via water absorption in the molecular backbone.

Depending on the level of acidity/basicity (and/or hydration), two hopping mechanisms are possible for protonic transport along the proton wires. At low acidity/basicity (and/or hydration), sequential hops take place via diffusion processes induced by local charge gradient concentration (*vehicle mechanisms*). In vehicle mechanisms, the diffusion coefficient (D) depends on the frequency of proton hopping; proton mobility (μ) and conductivity (σ) are given by the Einstein-Stokes relations [223]:

$$\mu = qD/k_B T \qquad\qquad\qquad \text{Eq. 3.5}$$

$$\sigma = nq\mu = nq^2 D/k_B T \qquad\qquad\qquad \text{Eq. 3.6}$$

where q is the proton charge and D the diffusion coefficient. Thus, in vehicle mechanisms, protons can be thought as *localized charges* diffusing across proton wires featuring short H-bond networks.

At high acidity/basicity (and/or hydration), proton wires form continuous pathways such that cooperative proton transport via *Grotthus mechanism* takes place (Figure 3.2 (a)) [224]. In the Grotthus mechanisms, injected protons (H^+) and hydroxyl ions (OH^-) (considered as ionic defects, with respect to *conventional* electronic charge carriers) can hop from one molecular site to another (Figure 3.2 (a) and (b)). Each hopping event locally modifies the charge neutrality along the chain. Consequently, a sequence of hopping events can occur only if the molecule donating (receiving) the ionic defect rotates to reverse the direction of its dipole moment. As soon as a rotation occurs, the H-bond losing (receiving) a proton generates an orientational negatively (positively) charged defect, *i.e. Bjerrum L* (*Bjerrum D*) in which no protons (two protons) are shared in the H-bond (Figure 3.2 (c)). In this framework, a fast-cooperative proton transport is driven by the sequential motion of ionic and orientational defects along the proton wires. The generation and translation of ionic and orientational defects requires energy that can be provided to the system by applying an electric field and/or by raising the temperature. Considering the contribution of the Grotthus transport and vehicle mechanism together, the protonic conductivity can be written as follows:

$$\sigma = nq\mu = (C/k_BT)\exp(-E_a/k_BT) \qquad\qquad \text{Eq. 3.7}$$

where C is a constant including the diffusion coefficient (D) and the elementary charge (q), E_a the activation energy barrier for protonic hopping, this last approximatively equal to the energy required to break a H-bond (i.e. 0.1 eV) [225]. It is worth noticing the similarity between equation 3.7 and equation 3.3 for the transport physics of amorphous semiconductors, experimentally verified for a wide range of biological systems and bio-sourced materials, including mixed conductors [203], [205], [208], [226], [227].

3.2.6 Protonic Semiconductor Model

The concept of protonic semiconductivity was formulated for the first time in 1958 after the experimental observation of p-n rectification effects in ice crystals doped with donor-acceptor

functional groups [228]. P-n rectification effects as well as p and n-type field-effect behavior of chitosan films have been recently reported by M. Rolandi's group [15]. These observations, paralleled by recent quantum mechanical models [227]–[230], led to describe the protonic transport in proton wires by considering H^+ and OH^- respectively as the electron and the hole counterparts of electronic semiconductors. In this framework, protons occupy the protonic valence band leaving the protonic conduction band empty, in analogy to the case of intrinsic electronic semiconductors. The *protonic band gap* corresponds to the energy required to generate a *proton - proton hole* pair. As in the case of electronic intrinsic semiconductors, such an ensemble of proton wires is poorly conductive because the energy required to excite a proton to the conduction band is about two orders of magnitude higher than the room temperature thermal energy ($k_BT\sim25$ meV). However, the conductivity of proton wires can be enhanced by injecting ionic defects into them. This process is in analogy with the case of electronic semiconductors, where the addition of electron donor or electron acceptor groups transforms intrinsic semiconductors into n or p type extrinsic ones (i.e. doped) [197]. In a similar fashion, a proton wire is *doped* with proton donor-proton acceptor groups to obtain n-p type wires. Upon n (p) doping, the proto chemical potential, conceptually equivalent to the electronic Fermi energy level, shifts from mid gap toward the protonic conduction (valence) band edge.

As previously mentioned, this phenomenological description of protonic transport is well explained by quantum mechanics, as for electronic transport in band theory [201]. In this context, the protonic energy levels are determined by considering the proton in the potential of the lattice made of H-bonded water molecules (Figure 3.2 (d)). The problem considers the displacement of protons and water molecules as well as mutual interactions in the system (i.e., proton-water molecule, water molecule-water molecule interactions, including dipole-dipole interactions generated by the perturbation of charge neutrality in the chain).

Intuitively, the range of periodicity and the spatial coherence of the lattice potential strongly depends on the total concentration of proton wires available for transport. The proton can be found in two degenerate ground states of a double-well potential separated by a barrier which represents the energy required for the proton to hop across two equilibrium positions in the H-bond (*intra-bond barrier,* black arrow, Figure 3.2 (d)).
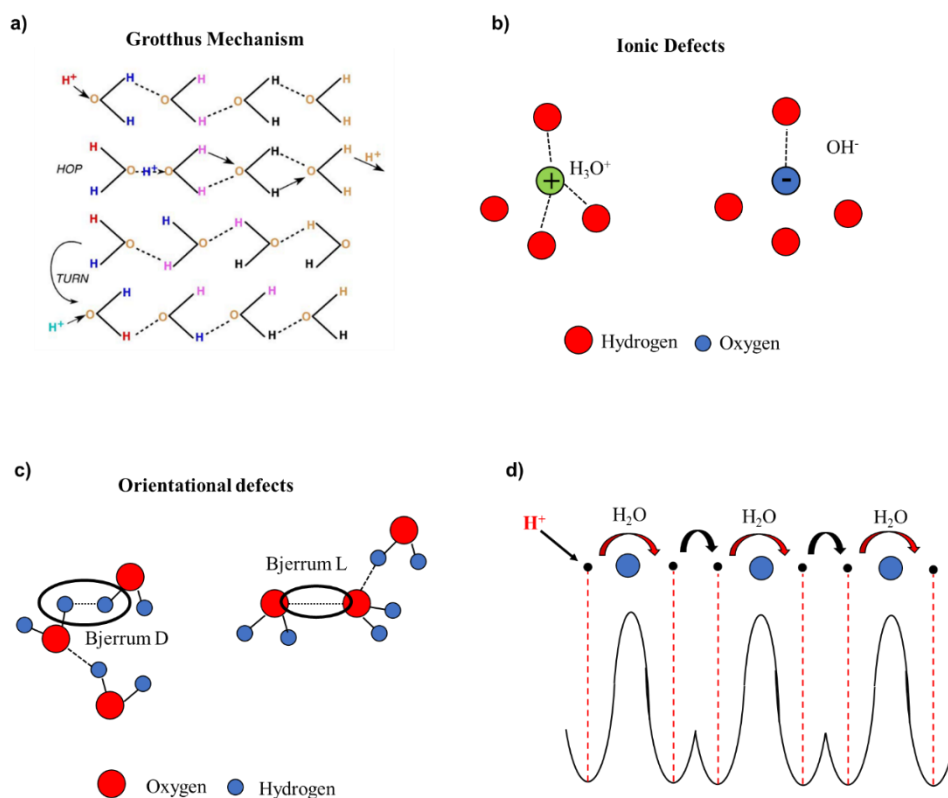
Figure 3.2 (a) Hopping and reorientation of H-bonded chains in Grotthus's theory of transport, (b) ionic and (c) orientational defects in H-bonded proton wires containing water molecules, (d) schematic representation showing the double-well potential of quantum model for Grotthus transport and the sequence of proton hopping events between H-bonded molecules in chains forming the proton wires. Protons and water molecules are represented by black and blue circles respectively. Permission granted by authorship from Ref. [46].

A second barrier represents the energy required to rotate the molecule and reverse its polarity to eventually generate a Bjerrum defect (*inter-bond barrier,* red arrow, Figure 3.2 (d)). Therefore, the protonic valence band is equivalent to the ensemble of energy levels (i.e. potential wells) generated by the H-bonded water molecules. If no energy is provided to the system, these levels are fully occupied by protons sitting in the double-well. On the other hand, by applying an electric field, the Hamiltonian of the quantum system admits the propagation of two delocalized wavefunctions. Depending on the direction of the electric field, a delocalized positive (negative) wavefunction is generated by the overlap between the wavefunctions of positive (negative) ionic

and orientational charge defects [229], [231]. In this view, the definition of protonic conduction band given by M. Rolandi's group [218] as the "*excess of protons fluctuating between hydrogen bonds*", naturally arises from the *delocalized character* of the protonic wavefunction.

In conclusion, the protonic semiconductor model can be potentially extended to any bio-sourced materials featuring significant presence of H-bonded molecular chains, e.g. by absorbing water molecules through hydration [225], [232]–[234].

3.3   Electrical Properties of Eumelanin

3.3.1 Resistive Switching Behavior, Amorphous Semiconductor Model and Electronic Transport

In section 3.2.3, we raised the question whether the MD amorphous model, based on the modified band theory (section 3.2.2), is an accurate description of the transport physics of bio-sourced materials. In this context, the case of eumelanin is unique and inspiring. For decades the biopigment has been considered an amorphous semiconductor for manifold reasons.

Firstly, eumelanin features broadband UV-Visible absorption, which in amorphous semiconductors is the consequence of the peculiar density of electronic states (Figure 3.1 (d)) [39]. Secondly, McGinness *et al*. observed, for synthetic and natural melanin pressed pellets, a reversible electrical resistive switching behavior (Figure 3.3) [37], commonly observed in inorganic amorphous semiconductors (e.g. a-Si, a-Ge, a-Se and a-Te) [38]–[40].

3.3.1.1   Electrical Resistive Switching in Eumelanin

Amorphous semiconductors exhibit several charge transport mechanisms depending on the population of charge carriers that can be eventually promoted to the band states (i.e., NNH, VRH and band like conduction, section 3.2.2). Ultimately, the peculiar density of electronic states in the energy landscape of amorphous semiconductors (Figure 3.1 (e)) has been ascribed as the underlying cause of the resistive switching. In most materials biased with as high as 10^5-10^6 V cm^{-1} electric fields, a disruptive breakdown is observed. Conversely, some crystalline and amorphous materials, if such high electric fields are applied, do not experience a disruptive

breakdown but they instead switch from high to low resistance states, respectively called OFF and ON states. This is, for example, the case of amorphous semiconductors. In these systems, the threshold voltage (V_T) is defined as the voltage beyond which the switching takes place.

The practical interest of amorphous semiconductors is that they set up a self-sustained high conducting state that prevents breakdown and make them suitable for applications in memory and switching devices.
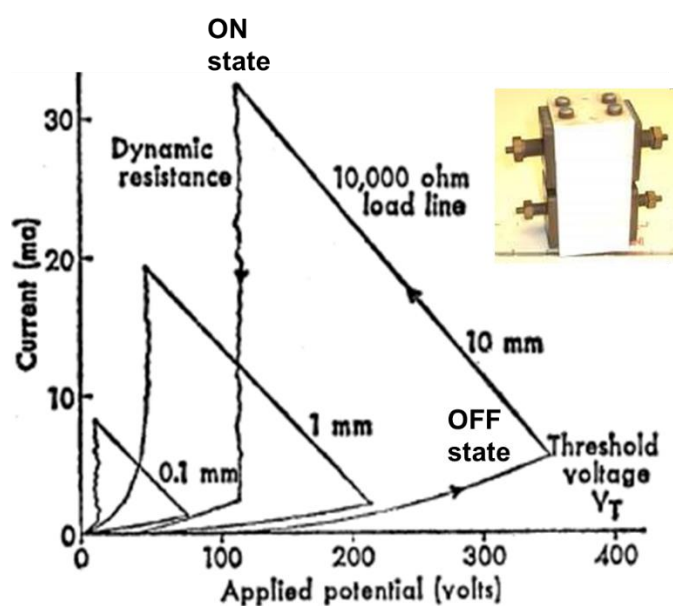
Figure 3.3 Resistive switching behavior of the current-voltage response of natural and synthetic hydrated eumelanin pellets featuring thickness of 0.1 mm, 1 mm, and 10 mm. The inset shows the original experimental apparatus which now belongs to the collection of the Smithsonian Museum in Washington. Reproduced and adapted from Ref. [37].

It is noteworthy that in McGinness 'experiment the resistive switching was observed in sandwich configuration, regardless the type of electrical contact (C, Al, Cu) but only with eumelanin powders hydrated prior the electrical tests. Pellets obtained from dried powders did not switch. McGinness's results were interpreted with the *modified dielectric constant theory* formulated by Powell and Rosenberg [203]. The theory posits that the presence of water increases the dielectric

constant of the material (i.e., by ionizing acid groups). Such an increase lowers the activation energy barrier for charge transport, leading to the resistive switching. Accordingly, the effect of water absorption on the electrical conductivity of eumelanin was modeled by the following equation:

$$\sigma = \sigma_0 e^{-\frac{E_D}{K_B T}} e^{-\frac{q^2}{2K_B TR}\left(\frac{1}{\epsilon_d}-\frac{1}{\epsilon_w}\right)} \qquad \text{Eq. 3.8}$$

with E_D activation energy in dry conditions, R the effective screening radius of absorbed water molecules (about 1 Å), ϵ_d and ϵ_w the dry and hydrated state dielectric constants, respectively.

These results triggered a series of quantum chemical studies, electrical measurements, temperature-resolved conductivity and photoconductivity experiments, looking for evidence in support of the amorphous semiconductor model for eumelanin.

3.3.1.2 Quantum Chemical Studies

In 1960, Longuet-Higgins showed that a fully oxidized quinone molecule has a closed electron shell and applied Huckel's theory to a eumelanin structure model made of only quinone units. Results indicated that an addition of surplus electrons would populate delocalized molecular orbitals formed by the combination of individual quinone lowest unoccupied molecular orbital (LUMO) levels [235]. In 1961, Pullman and Pullman computed the energies of molecular orbitals of monomers and dimers made of quinone units [236]. Their findings can be summarized as follows: (i) the monomer unit features low-lying energy LUMO level, (ii) the LUMO level of the dimer is a good electron acceptor orbital; (iii) a eumelanin structure made of quinone dimers brings about the formation of energy bands akin to semiconductors.

In 1988, Galvão and Caldas investigated the electronic properties of an ideal eumelanin structure made of five-six oligomeric units. Results suggested that a short-range ordered structure made of a few subunits may predominate on the overall structural disorder of the biopigment to eventually conveying it semiconducting properties [237].

Between 2003 and 2005, Stark *et al*. applied both steady-state and time dependent density functional theory to stacked H2Q, SQ, Q-based dimers, tetramers and hexamers and predicted the corresponding absorption spectra and HOMO-LUMO band gaps [89], [90].

3.3.1.3 Temperature-Resolved and Photoconductivity Studies

Between 1995 and 2002, Jastrzebska *et al.* studied the electrical response of eumelanin pellets as a function of hydration (0% RH-100% RH) and temperature (273 K-343 K) [238], [239]. In vacuum, authors reported an increase of the room temperature electrical conductivity with water absorption, from about 10^{-13} S cm^{-1} at 0% RH to 10^{-5} S cm^{-1} at 100% RH (Figure 3.4 (a)). Furthermore, they observed an increase of conductivity of about two orders of magnitude when the temperature was raised in vacuum, akin to semiconductors (Figure 3.4 (b)). Thermal activation energies of 0.76 eV and 0.69 eV were computed for heating and cooling cycles, respectively. In 2005, the same authors studied the alternate current response of natural and synthetic eumelanin. Authors showed that the dielectric response of eumelanin is modulated by clusters of percolating water.
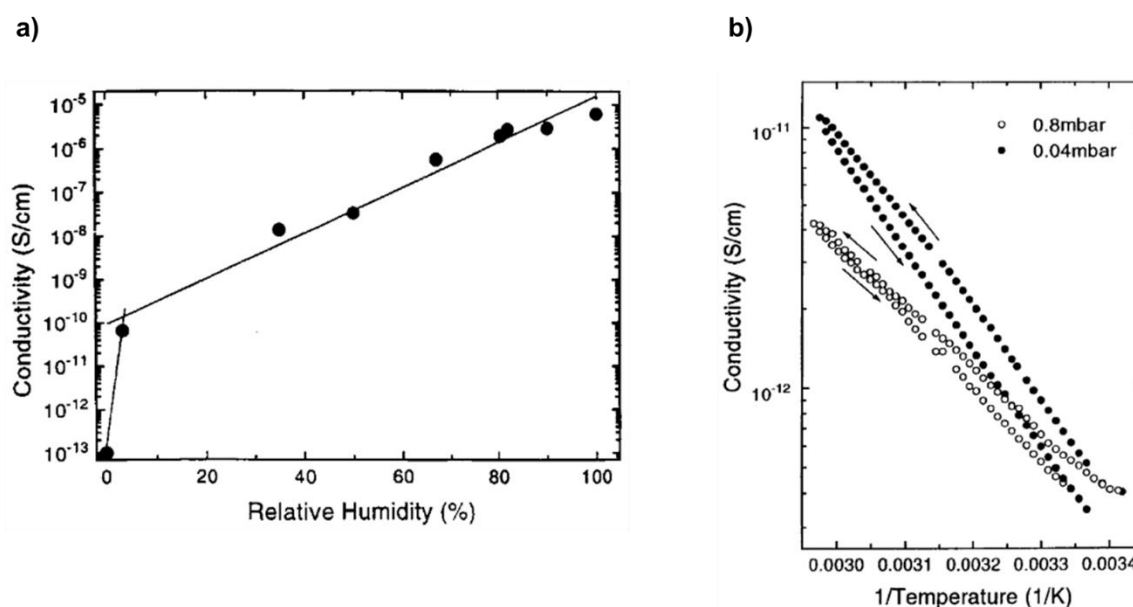
Figure 3.4 (a) Moisture (%RH)- and (b) temperature-dependent electrical conductivity of synthetic eumelanin pellets performed in vacuum atmosphere (0.8 mbar to 0.04 mbar). Reproduced and adapded with permission from Ref. [238].

These clusters contribute to decrease the charge carrier hopping distance by increasing the Coulombic screen [239], as proposed by Powell and Rosenberg (see Eq. 3.8).

A series of landmarks works, published between 1978 and 2006, showed that eumelanin is a photoconductor under UV and visible light [45], [73], [240], [241]. Interestingly, negative photoconductivity was reported for eumelanin pellets (the photoconductivity being broadly defined as the change of the current under illumination $(I_L - I_D)$ normalized to the value of the current in dark conditions (I_d)). The presence of shallow and deep trap states in the band gap of eumelanin, as in the case of amorphous semiconductors, was invoked to explain the observed negative photoconductivity.

3.3.2 Hydration-Dependent Electrical Response of Eumelanin Pellets: Mixed Protonic-Electronic Conductor Model

The application of the MD amorphous semiconductor model to eumelanin has been questioned in a series of studies published mainly by Meredith's group [27], [41]–[45] between 2010 and 2018. In these works, the authors investigated the impact of absorbed water on the transport physics of eumelanin, by studying the water adsorption isotherms of the synthetic eumelanin pellets (i.e. the effective amount of water adsorbed by weight as a function of atmospheric RH) [41], [43], [172] They measured the electrical conductivity of eumelanin pellets in sandwich and van der Pauw (vdP) configurations using Au electrodes. Pellets were hydrated in water atmosphere with values of relative humidity from 0% RH to 90% RH, corresponding to a water content of about 0%-20% by weight. For the two configurations, eumelanin's conductivity increased rapidly if the water content was greater than about 12% by weight (hydration threshold). Particularly, the conductivity vs water content in the sandwich geometry (Figure 3.5 (a)) fitted the MD model whilst the vdP one did not (Figure 3.5 (b)). Such a discrepancy was explained assuming that in the sandwich geometry, eumelanin pellets did not reach the hydration equilibrium because only the sides of the pellets were exposed to water vapors.

3.3.2.1 Muon-spin Relaxation Spectroscopy Studies

Afterwards, focus was given on probing the microscopic nature of the charge carriers in eumelanin pellets as a function of hydration and illumination. To this purpose, Mostert *et al.*

performed muon-spin relaxation spectroscopy (μSR) on hydrated eumelanin pellets [42]. Muons are fundamental particles that can be obtained from proton sources and have semi-integer spin. In μSR a beam of spin-polarized muons is sent to the sample in presence of a magnetic field ($\vec{B}$). Muons are expected to simulate the interaction of protons and their diffusion in the sample. Indeed, the interaction between the muons beam and the sample causes the muons to relax and decay into positrons that are eventually emitted in a direction parallel to the muon spin at the time of decay. The μSR technique provides a measure of the so called "decay asymmetry" ($A_T(\vec{B}, t)$), broadly defined as the relative number of positrons detected in front of and behind the plane of the sample, relative to the direction of propagation of the beam. The decay asymmetry is a function of the magnetic field and decay time (t) and is given by the sum of diamagnetic (A_D) and paramagnetic (A_P) asymmetry components. Particularly, the signal of paramagnetic component is strongly related to local unpaired electrons spin (radicals, see section 2.3.4 chapter 2). Accordingly, the measurement of $A_T(\vec{B}, t)$ provides details on the interaction of muons (and hence protons) with diamagnetic and paramagnetic species in the sample [242].

Mostert and co-workers modeled the total μSR decay asymmetry of hydrated synthetic eumelanin pellets as it follows:

$$A_T(\vec{B}, t) = A_D(|\vec{B}|, 0)K(\Delta, |\vec{B}|, t, \nu) + A_P(|\vec{B}|, 0)e^{-\lambda t} \hspace{2cm} \text{Eq. 3.9}$$

where K is the Kubo-Toyabe diamagnetic relaxation function, ν muon hopping rate, Δ and λ the relaxation rate of diamagnetic and paramagnetic muons, respectively.

Mostert's results evidenced that (i) μSR spectra were mainly associable to proton signature at higher water content; (ii) both proton and SQ populations (i.e., electronic charge carriers) increased with the increase of water content; (iii) protonic and electronic charge carriers hopping rate did not change with the increase of water content (Figure 3.5 (c)). In accordance with that, the increase in conductivity with hydration would be due to the increase of charge carriers' density and not to the decrease of the activation energy barrier for hopping.
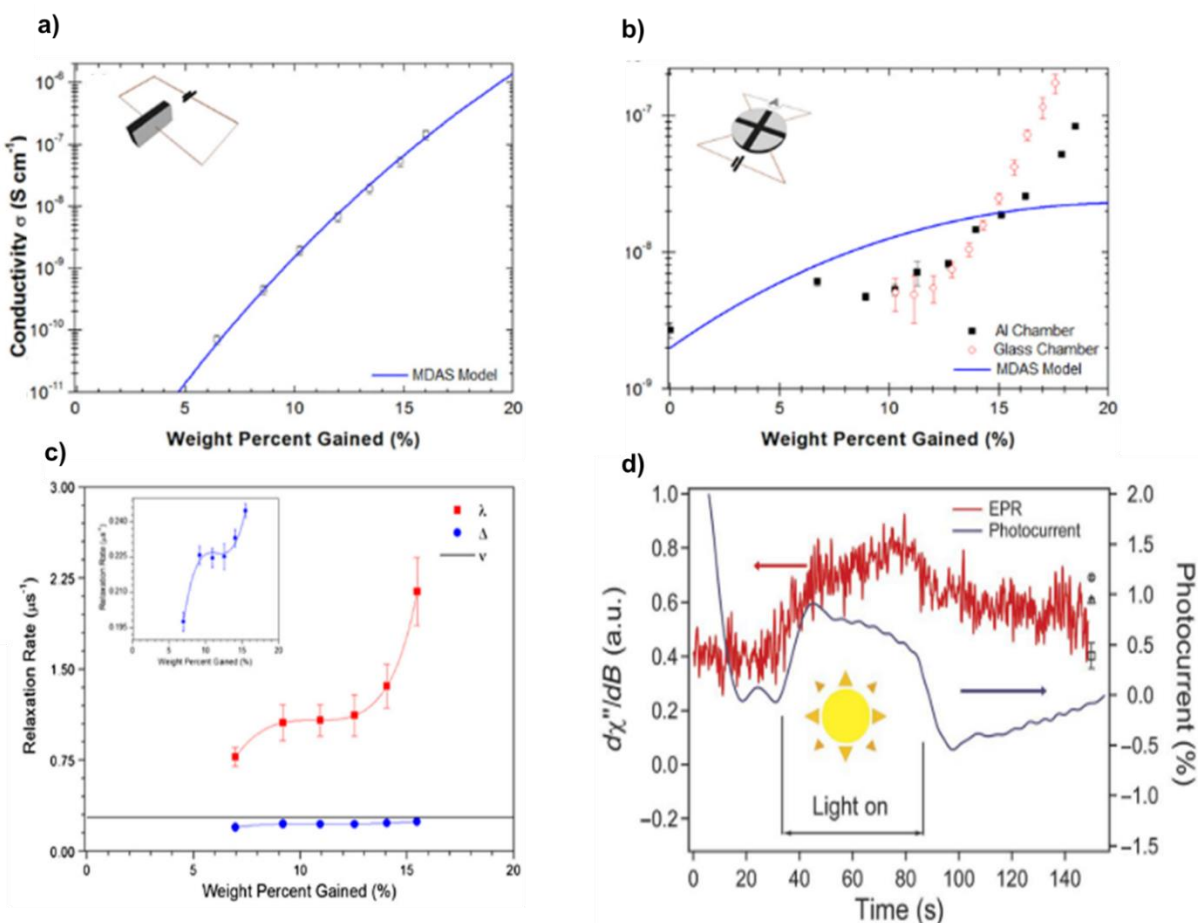
Figure 3.5 Conductivity as a function of water content by weight for eumelanin pellets (a) in sandwich and (b) van der Pauw geometry (respectively insets in (a) and (b)). The solid blue line shows the corresponding MD model. Reproduced and adapted with permission from Ref. [43]. In (c) paramagnetic and diamagnetic µSR relaxation rates for eumelanin pellets as a function of water content. In (d) p-EPR time response and corresponding photocurrent response of eumelanin pellets featuring water content of about 11.6 % by weight. Reproduced and adapted with permission from Refs. [42] and [45].

3.3.2.2 Electron Paramagnetic Resonance Spectroscopy Studies

The same authors performed photoinduced electron paramagnetic resonance spectroscopy (p-EPR) surveys on hydrated eumelanin pellets to monitor the population of intrinsic and extrinsic radicals as a function of hydration and illumination (CCR and SQR, respectively, section 2.3.4 chapter 2) [45]. They reported on comparable transient photocurrent and SQR photo-EPR time

response of hydrated eumelanin pellets (Figure 3.5 (d)). This similarity led the authors to conclude that protonic transport and increase of SQR density (through hydration and/or illumination) were profoundly connected in hydrated eumelanin. Mostert *et al.* offered an interpretation of eumelanin's electrical properties by which electrons and/or protons are released during a comproportionation equilibrium reaction in presence of water and/or light (the reaction takes place between hydroquinone and quinone moieties with water molecules, Figure 2.4, chapter 2).

3.3.2.3 Studies on the Electrical Response of Hydrated Eumelanin Films

In a sequence of papers published from 2013 and 2015, Wünsche *et al.* confirmed the predominance of protonic over electronic transport for highly hydrated eumelanin films spin coated on coplanar platinum (Pt) and Palladium-hydride (PdH$_x$) electrode-patterned substrates [243], [244] (Figure 3.6). The I-V response of hydrated films as a function of the voltage scan rate showed a capacitive behavior for |V| < 0.2 V. From a linear fit of the voltage rate dependence, the authors extracted a capacitance value much higher than that expected in dielectric polarization processes, an indication of bulk ionic conductivity. For |V| > 0.2 V, the increase of the current with the voltage was exponential, suggesting a non-capacitive behavior with redox processes taking place at Pt/eumelanin interfaces (Figure 3.6 (a)).

The contribution of protonic transport compared to the electronic transport was assessed in planar configuration by studying transient current measurements on synthetic eumelanin films, making use of Pd and PdH$_x$ contacts (*protodes*) (Figure 3.6 (b)). Indeed, the exposure of Pd to molecular hydrogen (H$_2$) forms PdH$_x$ electrodes that can inject both electrons and protons (for further details, see section 4.3, chapter 4). At the same % RH conditions, authors measured higher steady state current with PdHx contacts than that Pd ones. Furthermore, this difference increased with the increase of % RH, suggesting that the protonic contribution to the total conductivity becomes more and more prominent with the content of absorbed water.

Based on all these observations, the MD model for eumelanin was essentially ruled out because of the predominant protonic nature of the transport physics of eumelanin at high water content. In Mostert's frame, water absorption causes, quoting the authors, a "*chemical self-doping*" where electrons (in the form of SQ) and protons are released by shifting the comproportionation

equilibrium. Beyond the hydration threshold, water dopes eumelanin and significantly increases the density of charge carriers (protons and electrons). In turn, protons are transported across protonic pathways (proton wires) via Grotthus mechanism (see sections 3.2.4, 3.2.5 and 3.2.6).
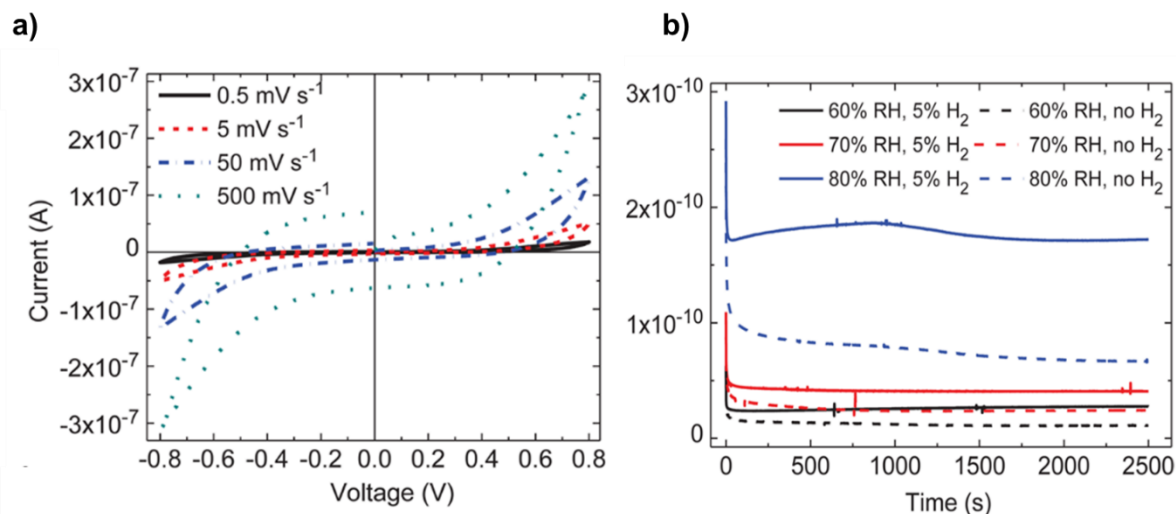
Figure 3.6 (a) I-V characteristics as a function of voltage scan rate of hydrated eumelanin films (90% RH) on coplanar Pt electrodes (W=24.5 mm, L=10 μm), (b) transient current measurements (0.5 V) of eumelanin films on Pd electrodes and PdHx contacts at 60% RH, 70% RH and 80% RH. Reproduced and adapted with permission from Ref. [244].

These studies herein reviewed considerably advanced the knowledge on the impact of adsorbed water on the mesoscopic properties of eumelanin by clarifying the relationship between microscopic and macroscopic conductivity. Remarkably, by recalling the fundamentals of the protonic semiconductor model for bio-sourced conductors (section 3.2.6), it appears that Mostert's conclusion on the electrical properties of highly hydrated eumelanin, describes a doped protonic semiconductor.

In conclusion for this section, it should be now clear that the physical description of the charge transport properties of eumelanin is only partly understood and deserves more attention, as several reliable works point to different interpretations.

3.4 **Organic Electronic and Bioelectronic Applications of Eumelanin**

The unique physicochemical properties of eumelanin make it an ideal candidate for a wide variety of organic electronic applications [26]–[28].

Owing to its broadband optical absorption matching the solar spectrum, eumelanin has been considered for photovoltaic applications. In this regard, Antidormi *et al.* focused on the band alignment as well as adhesion properties of eumelanin (electron donor)/Si (electron acceptor) interfaces [29]. They performed *ab initio* calculations on five tetrameric eumelanin structures differing in the binding sites and electronic configurations (e.g., number and positions of carbonyl terminations ($=O$) of the monomers in each tetramer). Authors found suitable band alignment only for the case of molecular structures with high degree of planarity. Furthermore, eumelanin structures with a higher number of carbonyl terminations featured stronger adhesion on Si than their counterparts.

Eumelanin/porous Si interfaces have been experimentally fabricated by Mula *et al*. [30] for solar cells applications. DHI-eumelanin methanol and methanol/water solutions were casted on etched Si substrates to form p-n eumelanin/porous silicon donor-acceptor bulk heterojunctions, sandwiched between top and bottom Au sputtered electrodes. The device, featuring a square active area of 1 mm^2, was illuminated with an irradiance of 0.2 Sun (ca. 20 mW cm^{-2}) in the UV-Vis range and delivered a photocurrent and an open circuit voltage of about 2 mA and 0.15 V, respectively. Lee *et al.* used eumelanin from purified squid ink as a dye in dye-sensitized solar cells (DSSCs) based on TiO$_2$ nanocomposites electrodes [245]. Authors showed the ability of eumelanin to sensitized TiO$_2$ nanotubes. Despite these interesting outcomes, the use of eumelanin in photovoltaic applications is still at the early stages as it entails several challenges, among them the unknown position in energy of its HOMO and LUMO levels is of great concern.

Migliaccio *et al.* demonstrated superior water stability and visible optical transmission of DHI-eumelanin/poly(3,4-ethylenedioxythiophene):poly(4-styrenesulfonate) (PEDOT:PSS) films compared with PEDOT:PSS [246]. Eumelanin/PEDOT:PSS films were subsequently integrated in ITO anodes of organic light emitting diodes (OLEDs [247]). The efficiency-luminance and the efficiency-voltage curves of eumelanin/PEDOT:PSS anodes (referred in the article as Eu:PH)

were compared to that of an ITO electrode and a PEDOT:PSS ITO-free electrode (referred as PH1000). It was found that the OLED efficiency of eumelanin/PEDOT:PSS anodes was comparable to that of ITO-free anodes. The authors reported on a lower turn-on voltage of eumelanin/PEDOT:PSS anodes compared to ITO and ITO-free anodes (Figure 3.7 (a)). This result not only showed that the addition of eumelanin into PEDOT:PSS improves its hole injection properties, but also set the basis toward the use of eumelanin in OLEDs technology.

The hydration-dependent electrical response of the biopigment inspired the fabrication of eumelanin-based organic electrochemical transistors (OECTs) [27], and humidity and pH sensors [248], [249]. Sheliakina *et al.* tested the ion-to-electron transducing properties of eumelanin in a top-gated PEDOT:PSS-based OECT (Figure 3.7 (b)) [27]. The transistor architecture was obtained by the deposition of a PEDOT:PSS channel between source(S) and drain (D) Au electrodes, followed by the spin coating of hydrated DHI-eumelanin. Then, a Au gate electrode (G) was thermally evaporated on the eumelanin film (inset, Figure 3.7 (b)). From the analysis of the output and the transfer curves (S-D current (I_{SD}) plot for constant S-D (V_{DS}) and G-S voltage (V_{GS}), respectively) it was inferred that (i) the device was in the ON state at V_{GS}=0 V and (ii) it was sufficient to apply a small positive V_{GS} to turn the device OFF (Figure 3.7 (b)). These results pointed to the ability of eumelanin to modulate the conductivity of a p-type PEDOT:PSS channel by injecting protons (as per comproportionation equilibrium) upon the application of a positive V_{GS}.

Hong's group studied the static and dynamic moisture sensitivity of eumelanin films deposited on Au electrodes [174]. In the static sensitivity test, film resistance was found to decrease of about six orders of magnitude with the increase of hydration from 0%RH to 100% RH. Furthermore, by performing dynamic sensitivity tests, the authors evaluated a response time for moisture detection and recovery of about 5s and 9s, respectively. Piacenti da Silva *et al.* studied the pH sensing capability of eumelanin films in extended gate field-effect transistors (EGFETs) [250]. Typically, EGFETs consist of an-ion sensing film deposited on a conducting substrate (e.g., Au or ITO) connected to the gate of a standard metal oxide semiconductor FET (MOSFET). In this regard, the authors fabricated EGFETs comprising a eumelanin film deposited on a Au substrate immersed in phosphate/citrate buffer solutions (0.1 mol/L, pH range from 2 to 12, the device architecture is shown in Figure 3.7 (c)). The authors studied the influence of V_{DS} and V_{GS} on the

total I_{DS} as a function of the pH. The output and transfer curves of films immersed in low pH buffer solutions displayed higher I_{SD} with respect to films immersed in high pH ones (Figure 3.7 (c)). Based on these results, the authors proposed that the sensor response depends on the pH values of the buffer solutions and on the acid dissociation potential (pK_a) of hydroxyl groups of the aromatic rings of eumelanin structure. In this framework, the pK_a provides information on the ability of hydroxyl and carboxylic acid groups to bind or release ions in solution (and, in turn, on the protonation/deprotonation of eumelanin structure). Thus, when the pH of the buffer solution is lower (higher) than the pK_a of eumelanin hydroxyl groups, the transistor's I_{DS} is higher (lower) because the functional groups are protonated (deprotonated).

Dopamine films have also been explored as active layers in organic phototransistors (OPTs) exhibiting remarkable photo-conducting response at relatively low applied voltage [31]. Eumelanin films were deposited on SiO_2/Si substrates patterned with Ag planar electrodes (interelectrode distance L=90 µm). When biased with variable V_{GS} (from V_{GS}=-12 V to V_{GS}=-2 V) in presence of light (irradiance of 0.2 Sun), the best device featured photo-responsivity (defined as $P_R = \frac{I_L - I_D}{P_I}$, where P_I is the power of the incident light, I_L the photocurrent and I_D the dark current) and photoconductivity (broadly defined as the change of the current under illumination ($I_L - I_D$) normalized to the value of I_D) of 9 A W^{-1} and 7×10^4, respectively.

The combined effects of metal-ion binding properties and redox activity of DHI and DHICA building blocks (see sections 2.3.2 and 2.3.5, chapter 2) paved the way towards the use of eumelanin in energy storage applications. Natural and synthetic eumelanin films have been explored as anodes and cathodes in sodium-ion [102] and magnesium-ion batteries [131], respectively. Kumar *et al.* fabricated eumelanin electrodes for flexible micro-supercapacitors featuring specific capacitance (i.e., defined as $C_S = \frac{\Delta Q}{\Delta V \times m}$, where ΔQ is the electrical charge, ΔV the potential change and m the electrode mass) of 167 Fg^{-1} and capacitance retention of 75% after 1000 cycles [25].

Recently, Xu *et al.* combined solar energy conversion and energy storage properties of eumelanin to develop light-assisted eumelanin-based supercapacitors [32] (Figure 3.7 (d)). Eumelanin electrodes were fabricated by drop casting of DHI- and DHICA-eumelanin films on activated carbon paper.
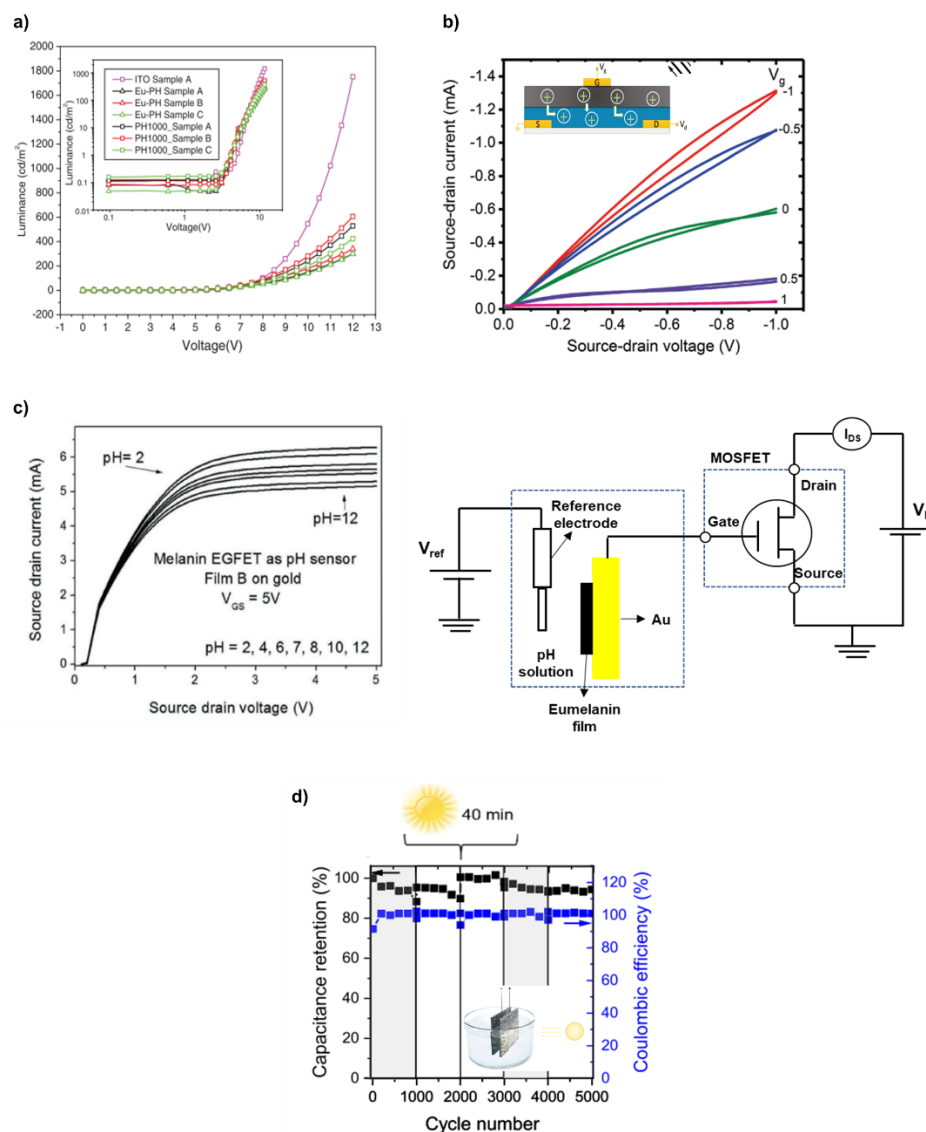
Figure 3.7 (a) Luminance of eumelanin/PEDOT:PSS (Eu:PH), ITO and ITO-free (PH1000) anodes for OLEDs; (b) output characteristics of a PEDOT:PSS channel (thickness 100 nm, length 100 μm), eumelanin top gate and Au gate electrode, solid state OECT. Inset shows the transistor's architecture; (c) output characteristics of an EGFET comprising a eumelanin film on a conductive substrate that is immersed in buffer solutions with variable pH (the device architecture is shown on the right side of the figure); (d) capacitance rated to the initial value and Coulombic efficiency for 5000 cycles of galvanostatic charge and discharge in light assisted eumelanin-based supercapacitors. In the inset a schematic representation of the device. Reproduced and adapted with permission from Refs. [246], [27], [250] and [32], respectively.

Under illumination (incident irradiance ca. 1 Sun), the specific capacitance of eumelanin electrodes increased of 39 %. In supercapacitor configuration (inset, Figure 3.7 (d)) and under prolonged illumination (about 40 min), eumelanin electrodes featured a capacitance retention of about 100% over 5000 cycles of galvanostatic charge and discharge and higher maximum power density (defined as $P_D = \frac{V_{max}^2}{4 ESR \times \Pi}$ where V_{max}^2 is the upper limit of the potential while charging [operating voltage], Π is the mass loading and ESR is the equivalent series resistance with respect to the initial values).

Finally, eumelanin has been recognized as a good candidate for biomedical and biotechnological applications, including drug-delivery [251], [252], melanoma detection [253], protection of the liver from alcohol-induced stress [252], growth of biocompatible stem cells [36] and many others [254], [255].

CHAPTER 4   METHODOLOGY

The theoretical physicist Wolfgang Pauli, Nobel Prize in physics in 1945 for "his decisive contribution through his discovery of a law of Nature, the exclusion principle" (cit. Einstein), once said: "*God made the bulk; the devil made the surface*". As a matter of fact, surfaces occur as structural defects in nature since they intrinsically are interfaces between the bulk and its surrounding environment.

The investigation of surface topography is essential to carry out fundamental studies of inorganic and organic electronics materials in view of practical applications. This study involves the qualitative and quantitative evaluation, possibly at the atomic and subatomic scale, of surface coverage and continuity (i.e. presence of voids, holes, terraces and steps), surface roughness as well as its morphology type (e.g. isomorphism versus polymorphism, this last being the lack of a unique surface morphology due to different degrees of supramolecular aggregation in molecular materials).

4.1 **Microscopy**

Microscopy is the technical field to get a visible image of an object otherwise too small to be seen at bare eye. The two basic parameters of microscopy are magnification and resolution. The former is the ratio between the angle at which an object is seen without the instrument and the angle at which the same object is seen with the instrument. The latter is the smallest distance at which two-point sources of an object can be seen as separate entities by the observer.

In the case of optical microscopy (OM), the Abbè's theory posits that optical resolution (R_{opt}) depends on the wavelength of the light source (λ), the index of refraction of the optical lenses (n) and the angle at which an object is seen by the microscope (α), according to the following relation:

$$R_{opt} = \frac{\lambda}{2n \sin \alpha} \qquad \text{Eq. 4.1}$$

In a typical optical microscope, $400\ nm \leq \lambda \leq 700\ nm$, $\sin \alpha \approx 1$ and $n \sim 1.5$. Thus, the highest achievable resolution is about 133 nm (Table 4.1).

The characterization of thin films of device quality requires much higher resolution than the optical one. Atomic Force Microscopy (AFM) and Scanning Electron Microscopy (SEM) are two advanced microscopy techniques providing resolution at the subatomic and atomic scale (Table 4.1) [256]–[258]. In paragraphs 4.1.1 and 4.1.2 we give a short overview of the basic principles of AFM and SEM, respectively.

Table 4.1 Comparison between analytical performance of OM, AFM and SEM.

	Optical Microscopy	Atomic Force Microscopy	Scanning Electron Microscopy
Magnification	1X-10^3X	10^2 X-10^8X	10X-10^4X
Resolution limit	133 nm	• 0.02 nm (vertical resolution) • 0.1 nm-10 nm (lateral resolution)	1 nm-5 nm

4.1.1 Atomic Force Microscopy (AFM)

AFM is an advanced microscopy technique conceived to obtain three-dimensional (3D) surface morphologies with atomic and subatomic resolution [259]. The atomic force microscope allows the acquisition of the surface morphology in air, in controlled atmosphere for environmentally sensitive surfaces (e.g., N_2, Ar glovebox with minimal content of O_2 and H_2O), in liquids and, in some cases, vacuum.

The atomic force microscope is based on a movable stage on top of which the sample is loaded in. A sharp silicon (Si) tip, mounted underneath the apex of a cantilever arm, scans the sample's topography. In turns, the cantilever is mounted onto a piezoelectric crystal which allows to scan the tip on top of different regions of the analyte's surface. A laser beam impinges the uppermost side of the cantilever to be reflected to a photodetector. During the scan of the surface, the deflection of the cantilever translates into a change of the position of the laser beam on the photodetector (Figure 4.1). By continuously monitoring the changes in the position of the laser

spot, the AFM software generates a height image of the surface. Typically, a height image is displayed using a dark-brown-light brown color gradient for small and high topographical features, respectively. As the image arises from height data, AFM allows to study the distribution of height, steps, hills and slopes along with their corresponding standard deviations [260], [261]. AFM also permits to perform the Fourier analysis of the topography for the identification of periodic features.

Atomic force microscopy can be performed in static (contact) and dynamic (tapping) mode. In static mode, the tip is always in contact with the sample's surface during the scan. Static mode can be performed in constant height mode or in constant force mode. In the former case, the tip is kept at a fixed distance from the sample. In the latter, the cantilever deflection is set as a feedback parameter in a way to control the intensity of the force applied by the tip on the surface [257], [259], [260], [262]. The static mode with constant force is usually performed on robust samples capable to resist to high lateral and torsional forces. In the dynamic mode, the cantilever oscillates at high frequency at about the frequency of resonance, typically in the kHz range. In amplitude modulation and phase modulation modes, the amplitude and phase of oscillations are the feedback parameters, respectively. During operation in dynamic mode, the AFM tip continuously engages and disengages from the sample surface. As the interaction tip-sample is very gentle, the impact of lateral and torsional forces is minimum. Beside preserving the tip sharpness, this condition allows to study the morphology of soft materials such as polymers and biomaterials, otherwise very challenging in static force mode.

The AFM vertical resolution (R_z) also known as z-resolution, is affected by the thermal noise of the deflection of the cantilever of spring constant k, according to the following equation:

$$R_z = 2\left(\frac{K_B T}{k}\right)^{\frac{1}{2}}$$

Eq. 4.2

where k is the cantilever spring constant (typically 1 N m^{-1} to 50 N m^{-1}), K_B the Boltzmann constant (1.38×10^{-23} J K^{-1}) and T the temperature (K). From equation 4.1, the best achievable vertical resolution of an AFM at room temperature is about 0.02 nm (Table 4.1)[257].

The AFM lateral resolution (R_{lat}) is the smallest detectable distance between two topographical features of small relative height (Δh). The lateral resolution depends on the radius of the tip (r), on R_z and Δh according to the following equation [257]:

$$R_{lat} = (2r)^{\frac{1}{2}}\left(\sqrt{R_z} + \sqrt{R_z + \Delta h}\right) \qquad Eq.\,4.3$$

Depending on Δh, for a vertical resolution of 0.02 nm and a standard tip radius of 10 nm, the AFM lateral resolution varies from 1 nm to 10 nm (Table 4.1).

The main artifacts occurring in AFM imaging are tip-related and feedback-related [256]. The geometry and sharpness of the tip affect the quality of the images: morphological features with smaller radius of curvature than the radius of the tip will be inaccurately imaged. Typically, tip-related artifacts give an image where the lateral dimension of the apparent structure is larger than the actual one. Furthermore, the majority (if not all) the topographic features appear with similar shape (usually pyramidal facets). Tip-related artifacts can be avoided by choosing a cantilever tip with aspect ratio larger than that of the morphological features of the samples.
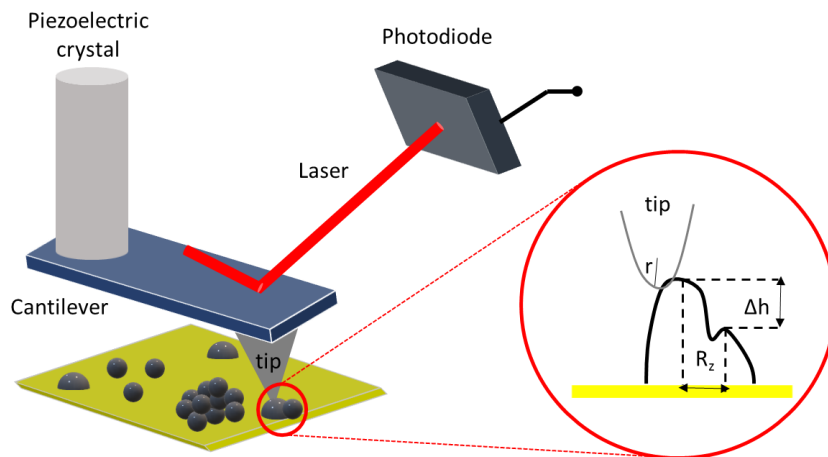
Figure 4.1 Basic set up of an atomic force microscope. The tip-sample interaction region is magnified to provide a simplified schematics of AFM lateral resolution.

Feedback-related artifacts occur when there is a difference between the value setpoint (e.g., force intensity in static mode, amplitude of oscillation in dynamic mode) and the actual value. Whenever a feedback-related artifact is produced, the edge of a topographic feature is oversmoothed. The asymmetry between the trace and retrace signals is an indication of the occurrence of these artifacts during the scan. Feedback-related artifacts can be avoided by decreasing the scan speed and by performing an optimization of the feedback parameters, for instance by retuning the deflection force of the cantilever in static mode and the frequency of the oscillations in dynamic mode.

In this PhD work, we used AFM to study the morphological changes occurring in DHI and DHICA films during their formation at ambient conditions (Article 1, chapter 5).

4.1.2 Scanning Electron Microscopy (SEM) and Energy Dispersive X-Ray (EDX) Spectrometry

SEM relies on the interaction between electrons and matter. When an incident electron beam penetrates the matter, elastic and inelastic scattering events occur. The volume of the primary excitation region (i.e., the region of the space in the sample interacting with the electron beam) and the type of scattering event depend on (i) the angle of incidence and initial energy of the electron beam (typically from 5 keV to 50 keV)), (ii) the mean free path of the electrons in the sample, (iii) the sample's atomic number (Z) and density. For a fixed Z, the higher the energy of the beam the larger the volume of interaction; for the same electron beam energy, the higher Z the smaller the volume of interaction [263].

Elastic scattering events between the electron beam and the atoms of the target are such that electrons are deflected with negligible energy loss (typically a few eV). This process generates a signal of high-energy backscattered electrons (BSEs). Conversely, during inelastic scattering events, the electron beam transfers part of its energy to the atoms of the target to generate low energy secondary electrons (SEs), Auger electrons and X-rays signals (Figure 4.2 (a)).

The detection and decoding of either BSEs or SEs signals form the sample's SEM image in a display. These images provide different information based on the intrinsic differences between the physical processes involving the emission of BSEs and SEs.

For BSEs, the diffusion angle rescales with the sample's atomic number (about 1°-2° for small Z to and close 180° for large Z). Moreover, the emission coefficient of BSEs, broadly defined as the number of reflected electrons over the total number of incident electrons, depends on Z: the higher Z, the higher emission coefficient [263]–[265]. Therefore, BSEs signals form contrast images where elements of higher Z appear brighter than those of smaller Z. The analysis of contrast images provides information on sample's composition.

SEs are emitted at small diffusion angles and from a small volume of interaction. As opposed to the case of BSEs, the emission coefficient of SEs is affected by surface orientation and morphology, but it does not depend on Z. Thus, for a given surface orientation, the emission of SEs is very stable, and the SEs signals form a reliable topographic image of the sample [265], [266].

The highest resolution achievable by SEM is about 1 nm-5 nm (Table 4.1), depending on the dimensions of the interaction volume, the electron beam spot-size and the yield of electron emission. The basic components of a scanning electron microscope are a vacuum chamber, an electron beam gun, a system of electromagnetic lenses and deflection coils, an electron detector, and a display (Figure 4.2 (b)). An Energy-Dispersive X-ray (EDX) spectrometer is often coupled to the electron microscope to get a chemical fingerprint of the sample. When the electron beam is sufficiently energetic, the sample bombardment can bring about the ejection of an inner shell paralleled by the creation of a vacancy. To stabilize the atom and fill the vacancy, an electron from an outer shell spontaneously decays in the inner shell. This process causes the emission of an X-ray photon with energy equal to the difference between the outer and the inner shell energies. As this energy difference is characteristic of each element, the analysis of the X-ray signal gives a unique footprint of the local chemical composition of the sample.

In this thesis, we collected the SEM images and EDX spectra of Sepia melanin pellets metal electrodes after the electrical resistive switching (Article 2, chapter 6). The objective was to exclude the occurrence of electrodes' dissolution processes which could lead to the formation of metallic filaments bridging the electrodes during the electrical tests.
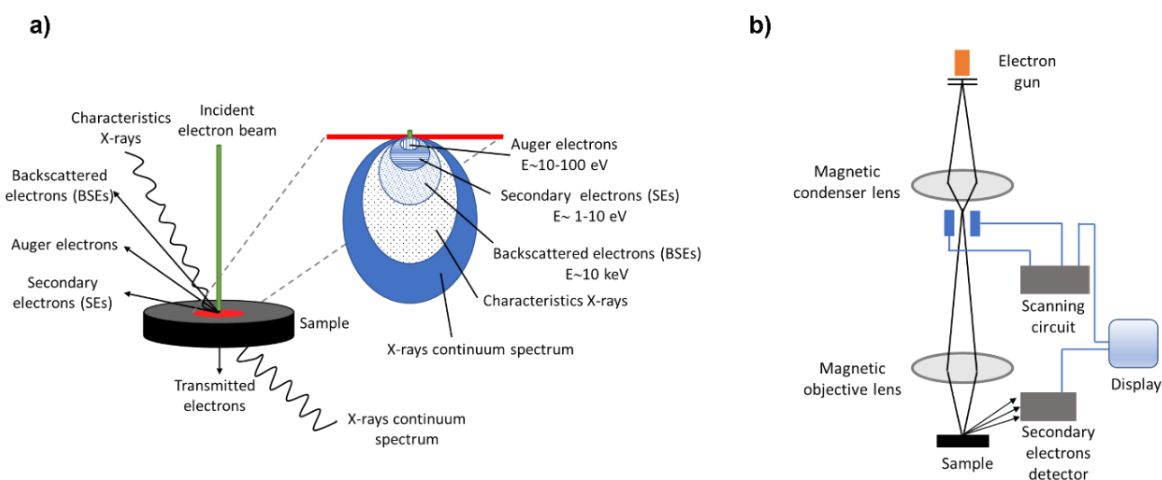
Figure 4.2 (a) Sketch of the interaction between the electrons and the matter generating backscattered electrons (BSEs), secondary electrons (SEs), Auger electrons, characteristic X-rays, and the continuum X-ray spectrum during scanning electron microscopy. In (b) basic set up of a scanning electron microscope.

4.2 Spectroscopy

4.2.1 UV-Vis-NIR Absorption Spectroscopy

Optical spectroscopy relies on interactions between UV-Vis and NIR light with electrons of atoms and molecules and is used to probe the fundamental properties of the matter, e.g., the optical extinction coefficient.

Such an interaction is explained by quantum mechanics. Briefly, the energy ground state of a molecule is determined assuming the nuclear (rotations and vibrations) and the electronic motion as separated motions (*Born-Oppenheimer* approximation). Indeed, the nucleus to electron mass ratio goes from 10^3 to 10^5, i.e., the period of motion of the nucleus is very small with respect to that of electrons. Therefore, the nucleus rotates and vibrates around a nearly fixed equilibrium position within the molecule. In this framework, the electronic and the nuclear wavefunctions are independent (separable) and the rotational (E_{rot}), vibrational (E_{vib}) and electronic (E_e) energies are additive:

$$E_T = E_e + E_{rot} + E_{vib} \qquad\qquad\qquad Eq.\,4.4$$

As $E_{rot} \approx 10^{-4}E_e$ and $E_{vib} \approx 10^{-2}E_e$, E_e being of a few electron volt (eV), rotational and vibrational states are quantized energy levels within the same electronic state [267]. The interaction of the UV-Vis-NIR radiation with matter brings about the transition of electrons from the ground state energy (S_0) to an excited state energy (S_*). According to the Bohr-Einstein relation, the energy difference during the electronic transition is:

$$\Delta E = S_* - S_0 = \frac{hc}{\lambda} \qquad \text{Eq. 4.5}$$

where h is the Planck's constant (6.6×10^{-34} J s), c the speed of light (3×10^8 m s^{-1}) and λ the absorbed wavelength. In the case of molecules, quantum mechanics predict that the individual energy levels correspond to electrons in singlet (S) and triplet (T) spin states (Figure 4.1). The S_0-S_1, S_0-S_2, S_0-S_3 and S_0-S_4 transitions generate the absorption spectrum of a material in the ultraviolet (UV, 220 nm-400 nm), visible (Vis, 400 nm-700 nm) and near infrared (NIR, 700 nm -2500 nm) regions (Figure 4.3). Since the electronic states of a molecule depend on the number of electrons as well as molecule's geometry (i.e., symmetry) and structure, UV-VIS-NIR spectroscopy is an efficient technique to unravel the structural properties of the molecules.

The physical principles of light absorption in the UV-VIS-NIR region are given by the empirical Beer-Lamber law [268]. This law posits that the analyte's absorbance (unitless, A_λ) is given by:

$$A_\lambda = \varepsilon_\lambda \tilde{c} d = \log\left(\frac{I_0}{I}\right) = \log\left(\frac{100}{T(\%)}\right) \qquad \text{Eq. 4.6}$$

where I_0 is the intensity of the incident light (power per unit area), I the intensity of the light emerging from the analyte (power per unit area), ε_λ the molar extinction coefficient (M^{-1} cm^{-1}), $\tilde{c}$ the concentration of the analyte (M), T (%) the transmittance and d the optical pathlength (cm). Owing to light scattering effects taking place in solid samples and thin films, UV-Vis-NIR spectroscopy is more accurate in the case of liquid samples or solutions than solid state ones.
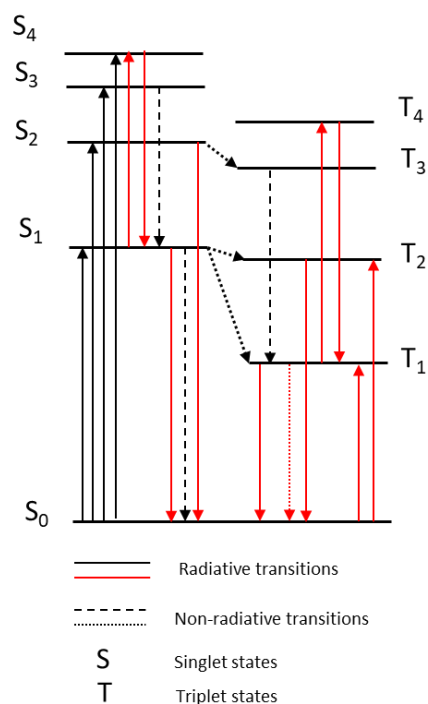
Figure 4.3 Energy level diagram of the electronic excitations arising from the interaction between the UV-Vis-NIR photons and matter. The black solid arrows represent the singlet-singlet radiative transitions generating the UV-Vis-NIR spectrum of the analyte. The red solid arrows show all the other radiative transitions. Black dotted and dashed arrows indicate the ensemble of all singlet-singlet and singlet-triplet non-radiative transitions.

UV-Vis-NIR spectra are collected using a spectrophotometer comprising a monochromatic light source (usually a deuterium lamp for the UV spectrum and a tungsten-halogen lamp for the Vis-NIR spectrum), a detector and a sample holder. Most of modern spectrophotometers are double beam, that is the path of the light source is such that the 50% of the beam goes to the analyte and 50% goes to the detector (analyte-free path). This configuration allows to compare the two beams during the acquisition of the spectra avoiding that any undesired effects (e.g. change of light source intensity) affect the actual analyte's spectrum [269].

In this thesis, we used a Cary 7000 universal measurement double-beam spectrophotometer to study the change in absorption spectra of DHI and DHICA films as a function of different environmental conditions and time (Article 1). Since light scattering constitutes up to 6% of the

overall light absorption in eumelanin [105], we collected the total optical absorption of eumelanin by acquiring the total diffusely transmitted and reflected radiation.

4.2.2 Vibrational Spectroscopy

Vibrational spectroscopy relies on the interaction between the visible light as well as the mid infrared (IR) radiation (i.e., photons in the frequency range 10^4 cm^{-1}-10^2 cm^{-1}, Table 4.2) and the molecules of matter.

Beside electronic transitions, the absorption of photons by the molecules can cause transitions between quantized roto-vibrational energy levels within the same electronic state (see paragraph 4.3). Roto-vibrational modes include symmetric-antisymmetric stretching, bending, twisting along specific the axis of a chemical bond and torsions.

An IR spectrum shows the absorption bands as a function of the frequencies of excitations of vibrational modes. The IR bands represent a unique chemical fingerprint of the material under analysis. Indeed, the frequency of IR bands depends on molecular structure, mass, and strength of chemical bonds, whereas the intensity and shape depend on concentration of functional groups and their chemical environment, respectively. Remarkably, vibrational spectroscopy allows the collection of high-resolution IR spectra using small quantities of the analyte in different physical states (e.g., gasses, solutions, powders, and films) [270].

The two prevalent vibrational spectroscopy techniques are Raman spectroscopy and Fourier transform infrared spectroscopy (FT-IR). These techniques are complementary since some Raman active molecular vibrations are FT-IR inactive and vice versa. For instance, symmetric vibrations of non-polar functional groups are Raman active whilst asymmetric vibrations of polar functional groups are FT-IR active [271].

The complementarity of the two techniques stems from the different ways in which the IR photon energy is transferred to the molecules to change their vibrational and rotational energy state.

In Raman spectroscopy, the sample is irradiated by a laser beam in the UV-Vis region and the scattered light is collected in the direction perpendicular to that of the incident light. The interaction between the UV-Vis laser beam and the sample induces a deformation of the electronic cloud surrounding the molecule of the sample. This deformation forms temporary

(induced) dipole moments causing a change in the polarizability of the molecule. In this process, the incident photon ($h\nu_0$) transfers part of its energy to the vibrational energy of the molecule ($h\nu_m$) and the remaining energy is scattered as a second photon. The scattered light is of two types: (i) Rayleigh, where the frequency of the scattered photon (ν_s) is equal to incident one and (ii) Raman, where the scattered photon has frequencies $\nu_s = \nu_0 \pm \nu_m$. The $\nu_0 - \nu_m$ and $\nu_0 + \nu_m$ lines are called Stokes and anti-Stokes lines, respectively (Figure 4.4 (a)). The Stokes lines are associated to quantized transitions from the lowest vibrational ground state to a virtual ground state, anti-Stokes lines to the opposite process [272].

Conversely, in FT-IR the absorption of the incident mid-IR light by the molecules of the analyte causes a change in the electric dipole moment of the molecules [271]. Thus, the corresponding IR band intensity is proportional to the square of the change in the dipole moment [273]. As in the case of UV-Vis spectroscopy, the intensity of the absorbed IR light is given by the Beer-Lamber law (see Eq. 4.6, section 4.3).

The substantial difference between Raman and FT-IR spectroscopies brings about different types of instrumentation to collect their spectra. As mentioned above, in the Raman spectrophotometer a monochromatic laser beam excites the sample. Subsequently, the scattered light goes to a notch filter which collects the Stokes and anti-Stokes scattering light and filter out the Raleigh light. A diffraction spectrograph grating bends the Raman light according to the wavelength and sends it to a detector for decoding (Figure 4.2 (b)).

The FT-IR spectrometer uses a Michelson interferometer to split the light into individual components. A Michelson's interferometer is composed of a light source, a beam splitter, a fixed and a movable mirror and a detector. The beam splitter transmits 50% of the incident light intensity to the fixed mirror and reflects off the remaining 50% to the movable mirror. The two beams are then back reflected from the mirrors to the beam splitter where, once again, 50% of the radiation is transmitted and 50% is reflected. As a result, one beam goes to the detector and one back to the light source (Figure 4.4. (c)).

The working principles of the interferometer are based on the laws of interference between the two beams at the beam splitter. Specifically, when the distance beam splitter-movable mirror and beam splitter-fixed mirror are identical, the two beams arrive in phase on the beam splitter

resulting into constructing interference for the beam going to the detector (maximum of interference). This situation occurs whenever the optical path difference between the two beams is an integer number of wavelengths. On the other hand, if the optical path difference is a semi-integer number of wavelengths, the detector will detect a minimum of interference. Such an alternance of maxima and minima of interference with the motion of the movable mirror, generates a sine (or cosine) signal at the detector called interferogram. The Fourier transform of the interferogram is then performed by the FT-IR spectrometer to obtain the IR spectrum.

In this PhD thesis, we collected the Raman spectra of Sepia melanin pellets to exclude that a Joule heating-induced phase transition from amorphous to graphitic carbon could explain the resistive switching behavior of Sepia melanin pellets (Article 2, chapter 6).

We used FT-IR spectroscopy to systematically investigate the change of physical and chemical interactions occurring in DHI and DHICA films in different conditions (e.g., ambient conditions versus an ammonia (polymerization catalyst) enriched atmosphere [36], [187], stored in the dark or in presence of laboratory daylight, Article 1, chapter 5).
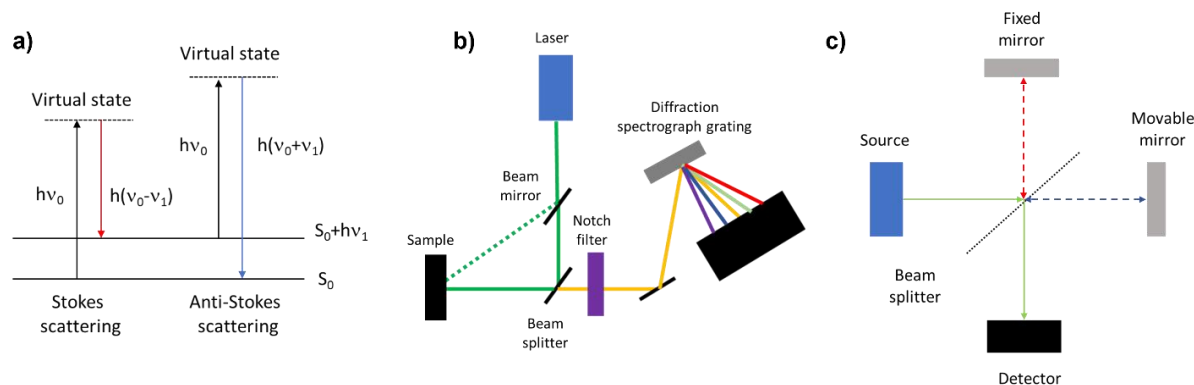
Figure 4.4 (a) Schematics of Stokes and anti-Stokes inelastic scattering events that generate the Raman spectra of molecular vibrational energy states. In (b) and (c) a simplified sketch of Raman and FT-IR spectrometer, respectively.

Table 4.2 Frequency, wavelength regions and origin of UV-Vis, IR and Raman spectroscopies.

Technique	Frequency (cm^{-1})	Wavelength (cm)	Origin
UV-Vis spectroscopy	10^6-10^4	10^{-6}-10^{-4}	Transition between electronic energy levels of valence atoms and molecules
Raman and IR spectroscopies	10^4-10^2	10^{-2}-10^{-4}	Transition between roto vibrational energy levels within the same electronic state of molecules

4.2.3 X-Ray Photoelectron Spectroscopy (XPS)

XPS is one of the most popular surface analysis techniques. XPS allows to identify and quantify the elemental composition of a solid with a depth resolution of about 10 nm [274]. XPS also provides the relative atomic percent of elements along with useful information on the chemical state and valence band structure. This information can be easily obtained as sample preparation requires minimal effort. Furthermore, XPS can analyze practically any kind of surface, from organic to inorganic, from conducting to insulating and in different physical states (e.g., powders, pellets and thin films).

An XPS spectrometer comprises an ultra high-vacuum (UHV) chamber, a monochromatic X-ray source (e.g., Mg or Al Kα lines, 1253.6 eV and 1486.6 eV, respectively), a sample holder, a system of electromagnetic lens to focus the photoemitted electrons to an electron energy analyzer and a detector.

The physical principle of XPS is the photoelectric effect. Briefly, an X-ray photon impacts the analyte's surface and transfers its energy to an electron initially bound to an atom of the surface. If the photon energy is higher than the surface electron binding energy (BE), the surface electron is emitted with a discrete kinetic energy (KE) given by the following equation:

$$KE = E_{ph} - BE - \varphi$$
Eq. 4.7

where E_{ph} is the energy of the photon and φ fixed the work function of the instrument. The electron KE is the physical quantity recorded by the XPS spectrometer. However, the XPS spectrum is derived by calculating the electron BE, which is element- and environment-specific, as well as independent on the initial X-ray photon energy. Since the photoelectron emission is a discrete process, to each value of KE corresponds an ejected electron. As a result, the XPS spectrum shows the counts of electrons per seconds as a function of the electron BE [274], [275].

In this work we compared the high-resolution C_{1s} XPS spectra of dry and wet Sepia melanin pellets, before and after the electrical tests, to find the presence of graphitic carbon domains in the structure that could explain the observed electrical resistive switching (Article 2, chapter 6).

4.2.4 Impedance Spectroscopy (IS)

Impedance spectroscopy is a non-invasive technique where the system is probed with a sinusoidal potential of given amplitude, frequency and phase (typically small amplitude excitation of 1-10 mV and frequency range from MHz to mHz). The differences of amplitude and phase between the input and the output signal provide useful information on a specific protonic(ionic)/electronic process occurring in the material under analysis (bulk) and at the interface between the metal contact and the material [276], [277]. IS measurements can in principle distinguish protonic (ionic) and or electronic contributions to the conductivity of a mixed protonic/electronic conductor between ion-blocking electrodes (see section 4.3). The experimental results are usually given in terms of *Nyquist plot*, where the negative imaginary part of the impedance (-Im (Z)) is plotted against its positive real counterpart (Re (Z)). From the difference in amplitude and phase between the input and output signals it is possible to measure electronic, ionic and dielectric relaxation times that can be signature of charge transfer processes at the interface, charge transport in the bulk of the active layer and diffusion processes (electronic and ionic). To each process corresponds a different value of the impedance such that the system can be often described with different circuit models [278], [279]. We note that it is challenging to provide an accurate description of the electrical properties of a material using solely IS: Nyquist plot themselves can correspond to different circuit configuration models [279]. For this reason, the investigation of the charge carrier transport properties of matter should be carried out performing both IS and direct current (DC) measurements.

In this PhD work, we collected the IS spectra of dry and wet Sepia melanin pellets to shed light on the different electronic and ionic processes taking place in the bulk and at the Sepia melanin/metal interfaces, before and after switching (Article 2, chapter 6).

4.3 Measuring Electronic and Protonic Currents in Bio-sourced Materials

> In this section we considered as a reference a paragraph of my first author work "Electronic and Protonic Transport in Bio-sourced Materials: A new Perspective on Semiconductivity", by Manuel Reali, Pooja Saini, and Clara Santato, published as a review article on October 13th, 2021, in Materials Advances, 2(1), 15-31.

Good contacts and efficient charge transfer processes (injection) at the electrode/active layer interface are essential requirements for carrying out reliable charge transport studies and developing optimized architectures for high-performance devices. For electronic conductors, electron/hole injection at metal electrodes (e.g. gold (Au), aluminum (Al), copper (Cu), platinum (Pt), palladium (Pd) and silver (Ag)) is affected by energy band-bending [197]. In other words, an offset exists between the metal work function and the valence (highest occupied molecular orbital (HOMO))-conduction band (lowest unoccupied molecular orbital (LUMO)) edge levels of the electronic conductor. This energy mismatch causes the formation of energy barriers for electron/hole injection, known as *Schottky barrier* [197]. Schottky barriers effects can be considerably reduced by tuning the metal work function e.g. via chemical functionalization [280] or, as recently demonstrated, by using carbon nanotubes (CNTs)-based electrodes [281].

The choice of using metal electrodes to measure protonic currents, both for protonic and mixed conductors, entails several challenges. Indeed, metal electrodes do not effectively transfer protons at the contact/active layer interface; they are known as *ion(proton)-blocking electrodes*. The electron and proton transfer across this type of interface occurs with variable efficiency, i.e. from complete blocking (lowest efficiency) to ohmic injection (highest efficiency) [225]. During charge carrier injection, chemical reactions may occur at the metal/active layer interface, causing

blocking effects and unbalanced charge injection rates. These two effects cause the polarization of the metal electrodes and the formation of space charge layers at the interface (defined as an accumulation of charge carriers in a region of the space). The application of moderate or high electric fields can cause discharge effects in the form of space charge currents in the protonic (ionic) conductor.

Thus, at least for mixed conductors, the formation of space charge layers during DC measurements is not conclusive to disentangling the single contribution of different carrier types (e.g., protonic/ionic versus electronic) to the total electrical conductivity. DC measurements of protonic conductors between blocking electrodes should be accompanied by alternate current (AC) measurements i.e. impedance spectroscopy (IS) [210], [225]. It is important to notice that space charge currents can also flow in amorphous electronic conductors between metal electrodes because their disordered nature favors charge trapping phenomena facilitating injection at the interface [38].

Over the last four decades, researchers evaluated protonic and electronic conductivity of biomaterials [204], [205], [219], [227], [234], [282], [283], bio-sourced and mixed protonic-electronic conductors using metal electrodes. In this regard, it was demonstrated that protonic currents can be efficiently detected by Cu, Au and Pd partially ion-blocking electrodes, especially at high hydration (high relative humidity (RH) atmosphere) [284].

To get rid of ion-blocking effects when acquiring DC in bio-sourced protonic devices, the use of contacts capable to (i) inject protons (H^+) at the source (drain) active layer/contact interface and (ii) transport electrons towards the external circuit, is paramount. These types of contacts are often referred as *protodes*. Palladium has been widely used as proton source because of its ability to inject and extract protons as well as conduct electronically [15], [218], [225], [285]. Palladium forms proton conducting palladium hydride (PdH_x) protodes upon exposure to molecular hydrogen atmosphere. Protonic and electronic transport across the PdH_x /active layer interface and in the bulk is monitored by keeping the protodes under constant H_2 atmosphere during the acquisition. This operation ensures the presence of a *pool of protons* during the measurements. Therefore, palladium hydride protodes act as a proton source (or proton sinks) in hydrogen atmosphere. Accordingly, PdH_x injects protons into the active layer at the source terminal and extract protons from the channel at the drain terminal.

Several studies already exist on protonic transport in eumelanin films and pellets, interfaced both with protodes and ion-blocking electrodes [27], [42]–[44], [182], [184], [186], [243], [244], [286] (see chapter 3).

In this PhD work we were interested in finding evidence of exclusive electronic transport in eumelanin (see section 1.2, chapter 1). Thus, we studied the charge carrier transport physics of chemically controlled DHI and DHICA films (Article 1, chapter 5) and Sepia melanin pellets (Article 2, chapter 6) by using ion-blocking electrodes.

In Article 2, DC measurements were coupled to IS measurements to study the charge transfer and transport properties taking place at the interface and in the bulk of Sepia melanin pellets.

CHAPTER 5   ARTICLE 1: EUMELANIN: FROM MOLECULAR STATE TO FILM

Article 1 has been published in The Journal of Physical Chemistry C on February 3rd, 2021. The Supplementary Information is provided in Appendix A.

5.1 Authors

Manuel Reali[1], Anthony Camus[1], Guillaume Beaulieu[1], Jordan De Angelis[2], Christian Pellerin[3], Alessandro Pezzella[4], Clara Santato[*1]

[1]Department of Engineering Physics, Polytechnique Montreal, C.P. 6079, Succ. Centre-ville, Montréal, QC, H3C 3A7, Canada

[2]Department of Electronic, Electrical and Information Engineering (DEI), University of Bologna, Viale del Risorgimento 2, 40136, Italy

[3]Département de chimie, Université de Montréal, C.P. 6128, Succ. Centre-ville, Montréal, QC, H3C 3J7, Canada

[4]Department of Physics "Ettore Pancini", University of Naples "Federico II", Complesso Universitario Monte S. Angelo, Via Cintia 1, 80126, Naples, Italy.

[*]Clara Santato (Email:clara.santato@polymtl.ca)

5.2 **Abstract**

Eumelanin, a macromolecular biopigment, is an attractive candidate for Sustainable (Green) Organic Electronics. Establishing structure-property relationships in eumelanin films is an essential step to exploit its technological potential. We report on the evolution from the molecular state to film after spin coating on silicon dioxide solutions of (5,6)-dihydroxyindole (DHI) and (5,6)-dihydroxyindole-2-carboxylic acid (DHICA) eumelanin building blocks (monomers). The evolution of the spin-coated films was followed under various environmental conditions, such as ambient vs ammonia atmosphere which catalyzes polymerization. Atomic force microscopy images reveal dramatic morphological changes as a function of the environmental conditions. Infrared and UV-Vis spectroscopies indicate these changes are due to a combination of physical (self-assembly) and chemical (polymerization) processes. Preliminary electrical measurements on films were also carried out.

5.3 **Introduction**

The expansion of consumer electronics has generated unsustainable amounts of Waste Electric & Electronic Equipment (WEEE), posing serious environmental and health concerns[1]. Sustainable Organic Electronics, based on the use of abundant, bio-sourced and biodegradable organic electronic materials, are an emerging route to design low eco- and human-toxicity technologies and alleviate the environmental footprint of electronics[4], [5]. Despite their interest, enormous challenges have to be overcome before applying bio-sourced organic materials in electronics.

The charge transfer and transport properties of bio-sourced organic materials are complex, due to the materials' chemical composition and structure. Indeed, they are usually immersed in aqueous saline media, such that their composition includes water and salts. Furthermore, their biosynthesis brings about a certain amount of chemical disorder (chemical heterogeneity), e.g. macromolecules resulting from more than one building block (monomer), and physical disorder, e.g. π-π stacked regions with different extension and orientation coexisting in the supramolecular structure of the materials[83], [182], [184], [243]. Intrinsic chemical and physical disorder (that we qualify as intermediate since these materials are not well ordered , yet not amorphous either

[287]), are among the key factors limiting the performance of corresponding devices (e.g. in terms of charge carrier mobility).

Considering the weak van der Waals interactions that bind organic molecules together into films, polymorphism (i.e. lack of a unique structure due to different types of molecular arrangements) has always been a challenge when attempting to establish sound structure-property relationships in organic electronic materials and optimize device performance[288], [289].

Among bio-sourced materials, eumelanin, a black-brown bio-pigment belonging to the melanin family, is an interesting candidate for study[31], [34], [42], [290]. Eumelanin is a redox-active quinone-based bio-macromolecule that features an electronically conjugated molecular structure (alternating single and double bonds). It is derived from the oxidative polymerization of 5,6-dihydroxyindole (DHI) and 5,6-dihydroxyindole-2-carboxylic acid (DHICA) monomers (building blocks)[93] (Figure 5.1). The building blocks have several polymerization sites and co-exist in different redox states (fully reduced hydroquinone (HQ), semi-reduced semiquinone (SQ), and fully oxidized quinone (Q)). It, therefore, features chemical heterogeneity. Considering the different supramolecular structures that can be generated from different monomers and oligomers, eumelanin also features physical (structural) disorder [22], [92], [107]. A few models predict that ensembles of oligomers of the two building blocks hierarchically build up via π-π stacking with inter-plane distance of about 3.4 Å and lateral extension of about 20 Å [85], [87], [88], [95], [291], [292].

Recently, chemically controlled films obtained from eumelanin building blocks have been fabricated using an ammonia-induced (catalyzed) solid-state polymerization (AISSP)[36], [187].

Understanding the formation of DHI- and DHICA-based films, as determined by both chemical (covalent) and physical (self-assembly) interactions, is needed to establish structure-functional properties relationships, a crucial piece of knowledge in view of the practical applications of eumelanin films in electronics.

In this work, we report on the early stages of the formation of films obtained from eumelanin building blocks under different environmental conditions (ambient conditions vs ammonia atmosphere, laboratory daylight vs dark). Atomic force microscopy (AFM) and optical microscopy (OM) images were acquired at different stages of film formation. Infrared

spectroscopy (IR) and UV-Vis spectroscopy surveys showed that the formation of DHI- and DHICA-based films is driven by the interplay of physical (self-assembly) and chemical (covalent) interactions. Preliminary investigations into the electrical properties of the films were also carried out.
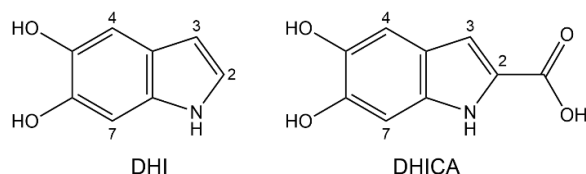
Figure 5.1 Molecular structure of 5,6-dihydroxyindole (DHI) and 5,6-dihydroxyindole-2-carboxylic acid (DHICA) eumelanin building blocks.

5.4 Experimental Section

Preparation of Chemically Controlled DHI- and DHICA-based Films. DHI and DHICA powders were synthesized as previously reported [293]. Ten milligrams of DHI and DHICA powders were dissolved in 1 ml anhydrous methanol in controlled atmosphere (N$_2$ with O_2 and $H_2O < 5$ ppm). DHI and DHICA solutions were spin-coated (40 μL, 30 s at 2000 rpm) on SiO2 /Si (1 cm × 1 cm, (1-0-0) n-doped Si, SiO2 thickness of 200 ± 10 nm) for morphological and electrical characterization, on fused silica substrates (pre-cleaned, area 1 cm × 1 cm, thickness 0.96-1.06 mm) for optical characterization and BaF2 windows for IR characterization. Prior to spin coating, substrates were cleaned by sequential sonication in acetone, isopropanol and deionized water, followed by 10 min UV-ozone treatment. Films were exposed to different environmental conditions after spin coating: (i) AC-L-DHI and AC-L-DHICA films stored in ambient conditions (relative humidity (RH) between 30% and 50%) and exposed to ambient laboratory daylight (Philips, F32T8/TL841 model, 32 W); (ii) AC-D-DHI and AC-D-DHICA films stored at ambient conditions in the dark (between 30 %RH and 50 %RH). AC-L films were kept in open sample holders whereas AC-D films were kept in closed sample holders, wrapped up in aluminum foil; (iii) AISSP-L-DHI, AISSP-D-DHI, AISSP-L-DHICA and AISSP-D-DHICA

films exposed to ammonia vapors (Sigma Aldrich, 28-30% w/v) at ambient conditions for 24 h. AISSP-L- and AISSP-D- films were exposed to ammonia vapors in a glass bell respectively unprotected and protected from laboratory daylight. To protect AISSP-D- samples from laboratory daylight, an aluminum foil was used to cover the glass bell.

Powders were synthesized in the Department of Chemical Sciences of the University of Naples, "Federico II" (Italy) and stored in closed vials (under N2, protected by Parafilm®) during shipping to Polytechnique Montreal. After shipping vials were stored at -25 ∘C.

Morphology. Morphology of DHI and DHICA films on SiO2/Si substrates was investigated at ambient conditions using AFM in tapping mode (AFM Digital Instruments Dimensions 3100, aluminum-coated silicon cantilever (radius 10 nm, spring constant 42 N m^{-1})). AFM images were analyzed using NanoScope Analysis software.

In the case of DHI films, the formation rate of the fern front was evaluated by taking the difference between two sequential front positions of a forming fern along its $\hat{\mathbf{x}}$ direction (yellow arrow, Figure 5.2 (a)). The width of the ferns' branches as a function of time was evaluated by taking the average width of a fern along its $\hat{\mathbf{y}}$ direction (blue arrow, Figure 5.2 (a)). Our fabrication protocol enables a well reproducible morphology of AC-DHI films (90% over 100 experiments). Furthermore, our protocol gives an average of about 10 spiral-like shapes of AC-DHI films on SiO2.

For AC-L-DHICA, the formation rate of rod-shaped structures along the $\hat{\mathbf{z}}$ direction ($v_{\mathbf{z}}(t)$, Table A.2, SI) was evaluated from the time derivative of the average height profile of the rods (z(t), Table A.2, SI). The fabrication protocol provides a well reproducible morphology and surface coverage of AC-L-DHICA films (90% over 50 experiments).

Fourier Transform Infrared Spectroscopy. IR spectra were acquired in inert dry air in transmission mode using a Vertex 70 FT-IR spectrometer (Bruker Optics) equipped with a DLaTGS detector. The background spectra of the atmosphere were automatically removed from the actual spectra during the measurements. Spectra were recorded with 4 cm^{-1} resolution by averaging 200 scans.

UV-Visible Absorption Spectroscopy. UV-Vis spectra of DHI and DHICA were collected using a Cary 7000 Universal Measurement Spectrophotometer (Agilent, UMS). The total transmitted

(%T) and reflected (%R) radiation was collected to evaluate the total resulting absorption of the films by posing $\%A = 100 - (\%T + \%R)$. The Tauc plot model was used to extract the optical absorption gap of DHI and DHICA films from the linear extrapolation of the plot $(\alpha h\nu)^{1/2}$ vs hν, where α is the absorption coefficient, h the Planck's constant and ν the frequency of the light. The wavelength-dependent absorption coefficient was computed by posing $\alpha(\lambda) = \%A/t$, where t is the thickness of the film. The thickness was evaluated by means of a profilometer tip after gently scratching the films.

IR and UV-Vis spectra were acquired on different films prepared under similar conditions at least in duplicate.

Electrical characterization. Organic films were deposited on SiO$_2$/Si substrates photolithographically patterned with interdigitated circular electrodes (5 nm of Ti adhesion layer, 40 nm of Au) with interelectrode distance $L = 10\ \mu$m and electrode width $W = 24.5$ mm and total in-plane area $A = 0.8$ mm^2 (Figure 5.6 (a)). Films were transferred in a manipulated cryogenic optoelectronic probe station (CXP, Lakeshore). Current-voltage measurements were acquired using Agilent B1500 in vacuum (10^{-7}-10^{-8} Torr, 295 K).

The electrical conductivity as a function of voltage scan rate was evaluated as follows:

$$\sigma = \frac{L}{A * R}$$

where R is the film resistance (including the contact resistance) evaluated at a voltage $V = 1.5\ V$. The charge stored vs. voltage scan rates was calculated as follows:

$$q = \frac{\int_{V_m}^{V_M} I(V')dV'}{\left(\dfrac{dV}{dt}\right)}$$

where V_M and V_m are voltage extremities of the hysteresis characteristics, $\Delta V = V_M - (-V_m)$ the voltage window and $\dfrac{dV}{dt}$ the voltage scan rate.

The ρ-V characteristics of AC-L-DHICA and AC-L-DHI films were obtained by evaluating the differential resistance $R(V) = \left(\dfrac{dI}{dV}\right)^{-1}$ (namely the inverse of the derivative of the hysteresis

current with respect to the hysteresis voltage) and then by plotting the resistivity $\boldsymbol{\rho(V)} = \frac{\boldsymbol{A*L}}{\boldsymbol{R(V)}}$ as a function of the voltage.

5.5   Results and Discussion

5.5.1 Atomic Force Microscopy Characterization

5.5.1.1   DHI-Based Films in Dark Conditions: Changes during the First Few Hours.

AFM images of spin-coated DHI samples exposed to ambient conditions (indicated as AC, Table 5.1) in the dark (indicated as D) reveal the formation of *fern-like* structures (green dashed lines in region A, Figure 5.2 (a)), within a few hours of deposition.

We followed the growth of the ferns in the $\hat{x}$ direction and found that the growth rate is about 5 µm min^{-1} during the first hour, decreasing to about 0.5 µm min^{-1} in 3 h (see Experimental). Within this time, the fern-like structures are about 120 nm high, and branches are about 400 nm wide (Figure 5.2 (a), red and blue crosses). Optical microscopy images, acquired a few hours after preparation, show that fern-like structures are part of spiral-like shapes forming on the surface (Figure A.1 (a) supplementary information, SI). After about 3 h, spiral-like shapes are approximately 200 µm×150 µm (e.g., Figure A.1 (a) and (f), SI). The density of the ferns depends on the distance from the center of the spiral. Denser branches are observed close to the center (Figure A.1 (b) and (c), SI).

The formation of fern-like structures likely results from diffusion-limited aggregation (DLA)[294] paralleled by the coffee ring effect[295]. Indeed, DLA has already been observed during the self-assembly of natural and synthetic melanin particles in aqueous solutions[296], [297]. During DLA, particles follow a Brownian motion with the probability to stick on the first encountered cluster being higher than that of sticking on the inner portions. Thus, the outermost portions of the clusters screen the innermost ones, leading to the formation of branched structures. In the coffee ring effect, ring-like structures (like our spiral-like shapes) generate at the micrometric scale after the evaporation of solvent drops. Different evaporation rates across the spin-coated sample cause an outward flow of solvent to minimize surface tension bringing about accumulation of particles at the edge of the forming structures.

5.5.1.2 DHI-Based Films Stored in Open Sample Holders in the Presence of Laboratory Daylight: Changes during the First Few Hours.

AFM images of DHI films exposed to ambient conditions, stored in open sample holders in the presence of laboratory daylight (indicated as L, Table 5.1 and Experimental) show, during the first few hours after deposition, the formation of fern-like structures as did their dark counterparts. On top of fern-like structures, *pillar-like aggregates* form (Figure 5.2 (b), region B and Figure A.2, SI). The density of the pillar-like aggregates is between 0.5 and 1 μm^{-2}. These aggregates grow in the $\hat{z}$ direction at a rate of about 70 nm h^{-1}. Within 1-2 h of exposure to laboratory daylight, pillar-like aggregates reach a height and width of about 150 nm and 400 nm, respectively. Heights and widths of pillar-like aggregates did not significantly change after about 2 h from the exposure to laboratory daylight.

5.5.1.3 DHI-Based Films Stored in Open Sample Holders in The Presence of Laboratory Daylight: Changes from 1 Day to 1 Month

After about one day at ambient conditions, in open sample holders, under laboratory daylight, well-defined structures (*crystal-like aggregates)* are observable on the ferns (Figure 5.2 (c), regions C_1 and C_2). These aggregates, possibly developing from pre-existing pillar-like aggregates, grow in the $\hat{z}$ direction at an initial rate of about 25 nm h^{-1}.

The process is considered completed about 30 h after deposition (Table A.1, SI). No further drastic morphological changes were observed during the following month. Our films were processed from anhydrous methanol solutions, in dry nitrogen. Other morphologies have been reported in the literature for non-anhydrous processing conditions[36], [187]. This observation points to the potentially relevant role played by moisture in affecting film morphologies.

5.5.1.4 Ammonia-Induced Solid State Polymerized-DHI-Based (AISSP-DHI) Films

AISSP-L-DHI films feature remarkable polymorphism. AFM images show that films feature fibrous morphology with a small population of *small spheres* and *flat rings* (Figure 5.2 (d), regions D_1, D_2 and D_3 respectively, Table 5.1 and Experimental). These structures reach a height of about 100 nm after one day. Upon exposure to ambient conditions, the height of these

structures did not significantly increase. While following the sample for a month, we did not observe any further morphological changes.

AFM images of AISSP-D-DHI films (Figure A.3, SI), show spontaneous segregation into spherical aggregates confined by rims (Figure A.3 (a) and (b), SI). These structures could result from the interplay of intermolecular and film-substrate van der Waals interactions possibly associated to thermodynamic instabilities in the films, leading to de-wetting-like processes[298].
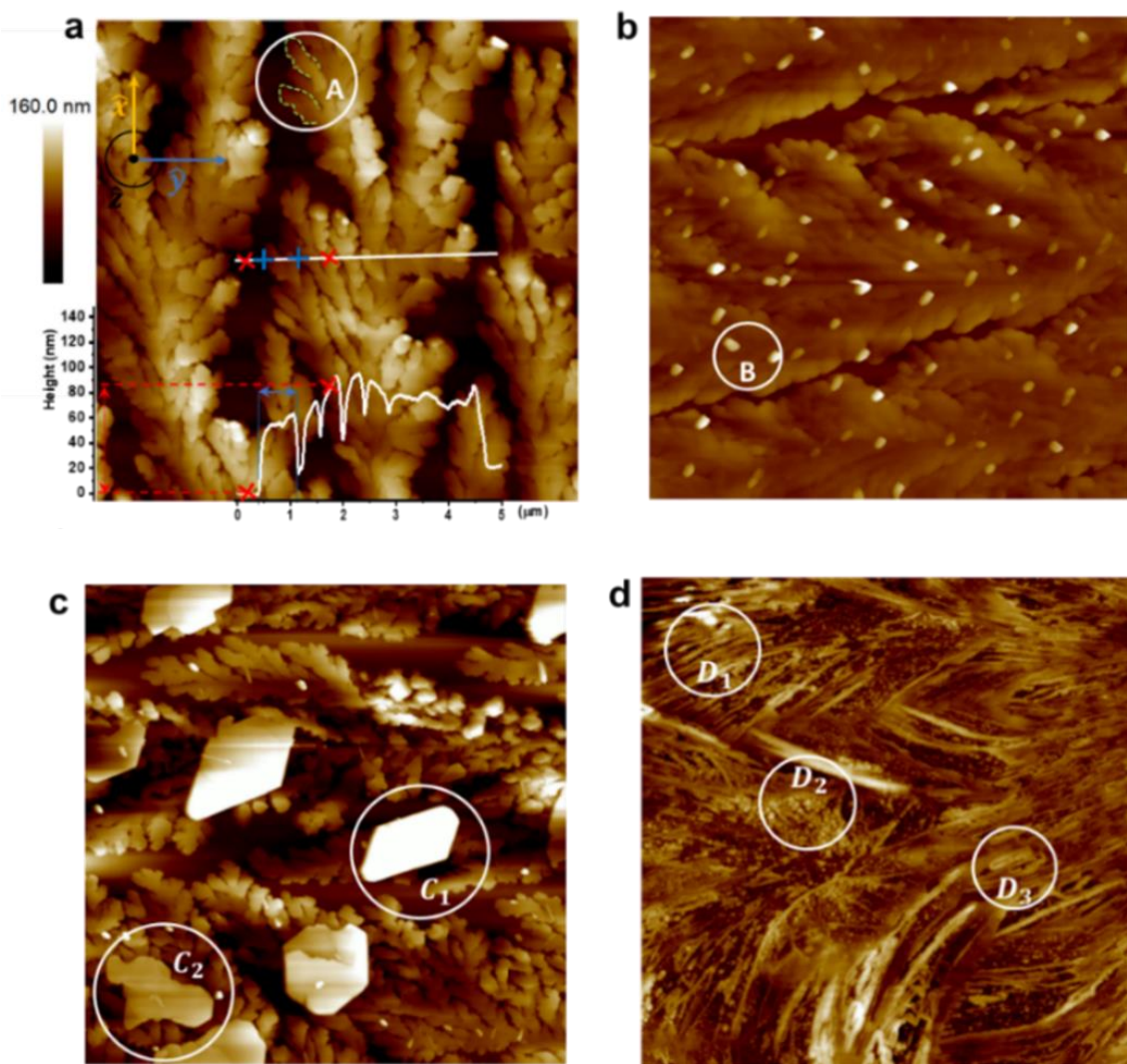
Figure 5.2 10 µm×10 µm AFM height images of (a) AC-D-DHI films acquired after 3 h (b) AC-L-DHI after a few minutes and (c) AC-L-DHI after one day. In (d) AISSP-L-DHI film after one day.

Table 5.1 Experimental conditions for the study of DHI- and DHICA-based samples on SiO_2. The abbreviations AC-L and AC-D respectively indicate films formed at ambient conditions with and without exposure to laboratory daylight, while AISSP-L and AISSP-D represent their counterparts exposed to ammonia vapors.

Name	Storage environment		Light conditions		Morphology observed	Time of observation
	Air	Ammonia vapors	Light	Dark		
DHI						
AC-L-DHI	×		×		Fern-like	0-3 h
					Pillar-like	1-3 h
					Crystal-like	20-30 h
AC-D-DHI	×			×	Fern-like	0-3 h
AISSP-L-DHI		×	×		Fibers, sphere-like, continuous flat regions	24-26 h
AISSP-D-DHI		×		×	Spherical-like shapes confined by rims	
DHICA						
AC-L-DHICA	×		×		Rod-shaped	0-3 h

AC-D-DHICA	×			×	Rod-shaped	0-3 h
AISSP-L-DHICA		×	×		Small spheres, shell-like and rods	24-26 h
AISSP-D-DHICA		×		×	Dense aggregates	24-26 h
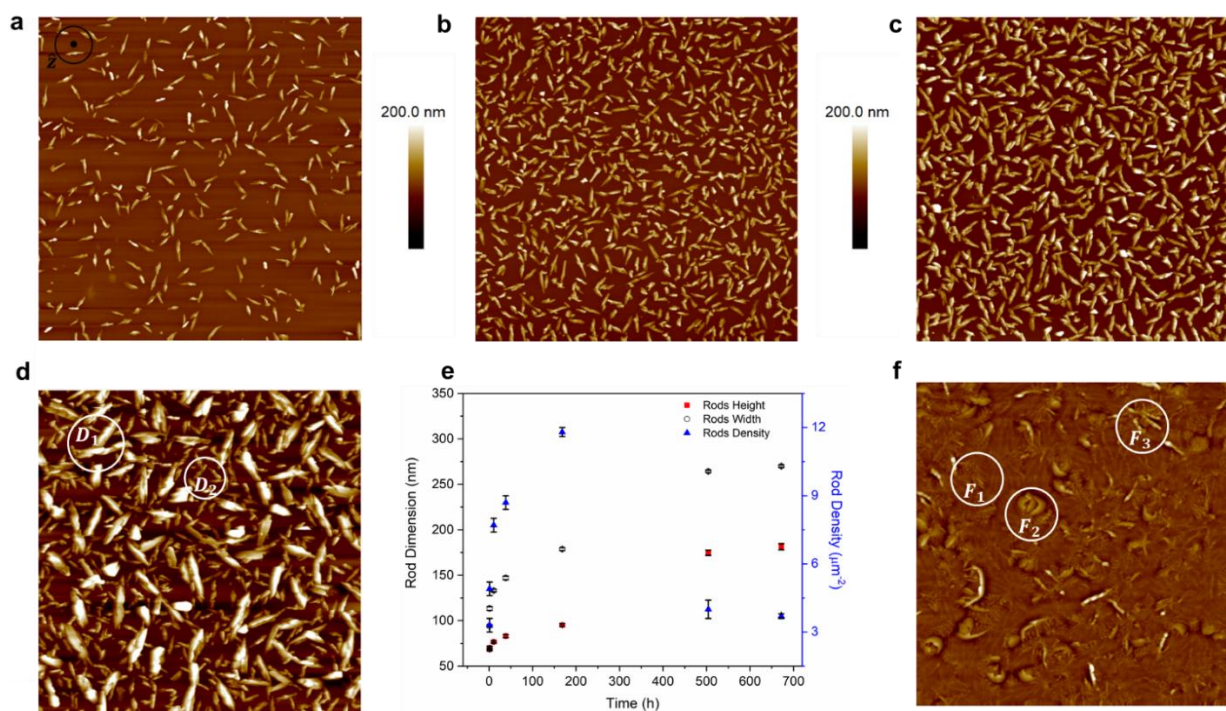
Figure 5.3 10 µm×10 µm AFM height images of AC-L-DHICA samples acquired at about (a) 1 h, (b) 1 d, (c) 3 d and (d) 1 week. In (e) Rod Dimension (average Rod Height and Rod Width) and Rod Density of AC-L-DHICA samples as a function of time. In (f), AISSP-L-DHICA sample after one day.

5.5.1.5 DHICA-Based Films Stored in Open Sample Holders in the Presence of Laboratory Daylight: Changes during the First Few Hours

AFM images of DHICA spin-coated samples exposed to ambient conditions and laboratory daylight show rod-shaped structures [93], which form on the surface already in the early stages of formation (about 1 h from fabrication, Figure 5.3 (a)). After about 1 h, rod height and width are about 70 nm and 180 nm, respectively. Over one month, rod height and width increase to about 100 nm and 300 nm, respectively (Figure 5.3, Figure A.4 (red and blue crosses) and Table A.2, SI). Rod density reaches a maximum after about one week and a minimum after about one month (Figure 5.3 (e)), likely due to Ostwald ripening[299]. The formation of larger rods ((Figure 5.3 (d) region D1, D2) is paralleled by a change in the root mean square roughness (RMS) of the films from about 15 nm to about 65 nm (Table A.2, SI)[300]. The decrease of the rods' density does not affect the homogeneity of the rods on the surface; substrate coverage is still very uniform even one month from fabrication. It is worth noticing that AFM images of DHICA films spin-coated at ambient conditions in dark (AC-D-DHICA, Table 5.1) feature the same morphology of their counterparts exposed to laboratory daylight (Figure A.5 (a), SI).

5.5.1.6 Ammonia-Induced Solid-State Polymerized-DHICA-Based (AISSP-DHICA) Films

AISSP-L-DHICA films are polymorphic as were their DHI counterparts. AFM images show that films feature layers made of *small spheres* on which *rods* and *shell-like structures* developed at high density (Figure 5.3 (f), regions F_1, F_2 and F_3 respectively). The morphology of AISSP-L-DHICA films does not evolve over time, as we also observed for AISSP-DHI films (Figure 5.2 (d)).

DHICA films exposed to ammonia vapors in dark (AISSP-D-DHICA, Table 5.1) are not polymorphic as were their counterparts exposed to laboratory daylight. AFM images of AISSP-D-DHICA samples show dense aggregates, about 50 nm high (Figure A.5 (b), SI). Likely, the exposure of AISSP-DHICA samples to light favors the formation of different molecular aggregates that generate the observed polymorphism.

5.5.2 Chemical Characterization

The changes in DHI-and DHICA-based samples was observed by IR spectroscopy. Indeed, molecular vibrational modes can provide information about the physical (self-assembled) state and chemical (monomeric or polymerized) state in the films[301], [302].

5.5.2.1 AC-DHI-Based Films: Changes in IR Spectra

The IR spectrum of AC-L-DHI films about 1 h after fabrication is characteristic of the monomeric form of DHI [301], [302]. It features a strong broadband around 3400 cm^{-1} due to O-H stretching vibrations (Figure 5.4 (a)) that overlap with the N-H stretching with various levels of hydrogen bonding. The aliphatic C-H stretching modes expected within 2934-2837 cm^{-1} are mostly obscured. Two peaks, at 1636 cm^{-1} and at 1595 cm^{-1}, stem from C=C vibrations in the phenyl and pyrrole rings, while two features at 1507 cm^{-1} and 1473 cm^{-1} are due to coupled in-plane ring and C-H deformation modes (Figure 5.4 (a), blue solid and dashed arrows respectively). Additional groups of peaks attributed mainly to C-H and O-H deformations, are present at 1380-1120 cm^{-1}. We do not observe any band in the carbonyl stretching region (1715-1660 cm^{-1}) of the spectrum at 1 h.

After 4 days (4 d, indicated in red), two shoulders appear at around 3460 cm^{-1} and 3430 cm^{-1} (Figure 5.4 (a), red dashed arrows). This points to a possible preferential supramolecular arrangement developing in the samples. Indeed, band splitting is an indication of the existence of specific molecular environments within the sample and is typically observed upon crystallization of initially amorphous materials. There is also a small increase of the intensity of the background around 1750-1600 cm^{-1} that can be associated with the formation of carbonyl groups by oxidation.

The formation of carbonyl bands in DHI melanin is attributable to the oxidation of the hydroquinone form into the semiquinone and quinone forms[35],[303].

Thus, the observed slight increase of intensity in the carbonyl region of the 4 d spectrum suggests slow oxidation of DHI films at ambient conditions. All in all, a reorganization of DHI via noncovalent interactions (supramolecular assembly) is observed as a function of time. It is possible that the formation of pillar-like and crystal-like aggregates, observed by AFM (Figure

5.2 (b) and (c)), is related to supramolecular self-assembly manifested by the splitting of the 3400 cm^{-1} band. The IR spectrum of AC-D-DHI films after one day is akin to that of AC-L-DHI, except for a slightly broader O-H stretching band (Figure 5.4 (b)).

5.5.2.2 AISSP-DHI Based Films: Changes in IR Spectra

The IR spectrum of AISSP-L-DHI films after one day (1 d) displays a much broader O-H and N-H stretching band compared to AC-L-DHI (Figure 5.4 (c)). The absorption of AISSP-L-DHI films in the carbonyl region is also stronger than that of AC-L-DHI films. These observations indicate that samples exposed to ammonia are more oxidized than those stored at ambient conditions. Oxidation of hydroquinone (HQ) is a fundamental step towards achieving the polymerization of DHI[93],[19],[304], [305].

It is worth noticing that the absence of splitting around 3400 cm^{-1} in the IR spectrum of AISSP-L-DHI could be linked to the lack of pillar-like and crystal-like aggregates in their AFM morphology (Figure 5.2 (d)).

The spectrum of AISSP-D-DHI after one day is quite different from that of AISSP-L-DHI (Figure 5.4 (d)). In particular, the strong band around 3400 cm^{-1} is narrower and the broad absorption in the carbonyl region is lower than for its counterpart exposed to laboratory daylight (AISSP-L-DHI), pointing to a lower extent of the oxidation. Furthermore, the band around 3400 cm^{-1} shows the same shoulders as noted in Figure 5.4 (a) for the AC-L-DHI films prepared in absence of ammonia and attributed to a preferential supramolecular arrangement.

5.5.2.3 DHICA-Based Films: Changes in IR Spectra

The IR spectrum of AC-L-DHICA shows an O-H band at 3437 cm^{-1} a shoulder at around 3346 cm^{-1} as well as a strong C=O band at 1660 cm^{-1}. Furthermore, the IR spectrum of DHICA samples feature more intense absorption around 1200 cm^{-1} than does AC-L-DHI, this last attributable to additional C-O stretching (Figure A.6 (a), SI). The appearance of these bands in the IR spectrum of AC-L-DHICA stems from the anticipated presence of carboxylic acid groups in DHICA. The IR spectra of AC-L-DHICA, recorded after 1 h and 4 d, do not significantly change, except for the appearance of a more defined shoulder at 3346 cm^{-1} (Figure 5.4 (e)).

The IR spectrum of AC-D-DHICA films after one day is akin to that of AC-L-DHICA, except for a more intense band at 3437 cm^{-1} and a broader O-H shoulder at about 3346 cm^{-1} (Figure A.6 (b), SI). The region of the carbonyl band, for both AC-L-and AC-D-DHICA samples, is almost unchanged after 4 d, *indicating very limited oxidation* within this time (respectively Figure 5.4 (e) and Figure A.6 (c), SI).

The spectrum of AISSP-L-DHICA films after 1 d, is considerably different from that of AC-L-DHICA counterparts. We observe the appearance of a new band in the spectrum of AISSP-L-DHICA at 3151 cm^{-1} (red solid arrow, Figure 5.4 (f)). The C=O peak at 1660 cm^{-1} of carboxylic acid groups, found for AC-L-DHICA, is absent in the spectrum of AISSP-L-DHICA. In the region of C=C vibrations of AISSP-L-DHICA spectrum, the peak at 1545 cm^{-1} is replaced by two peaks located at 1557 cm^{-1} and 1529 cm^{-1}. This process is paralleled by the appearance of strong peaks at about 1300 cm^{-1} and 1400 cm^{-1} and the weakening of the peaks at 1253 cm^{-1} and 1222 cm^{-1}.

The IR spectrum of AISSP-D-DHICA after 1 d is similar to that of AISSP-L-DHICA, except for a slightly broader band at 3151 cm^{-1}, a weaker peak at about 1300 cm^{-1} and two stronger ones at about 1557 cm^{-1} and 1529 cm^{-1} (Figure A.6 (d), SI).

One plausible explanation for these observations is an acid-base reaction between ammonia and the carboxylic group of DHICA. Ammonia can act as proton acceptor when in proximity with the carboxylic acid groups of DHICA in AISSP-DHICA samples. The formation of an ammonium salt could explain the appearance of the broad absorption band at 3150 cm^{-1}, the new intense band at 1400 cm^{-1} (Figure 5.4 (f) and Figure A.6 (d), red and blue solid arrows respectively, SI) and the shift of the C=O stretching band to lower frequencies in the carboxylate form.

The deprotonation process reveals the different role played by ammonia in film formation from DHI and DHICA. AISSP-DHI films are more oxidized than their ambient conditions counterparts. Our results suggest that, for L- and D-DHICA, ammonia plays a predominant role as acid-base agent, not catalyst.
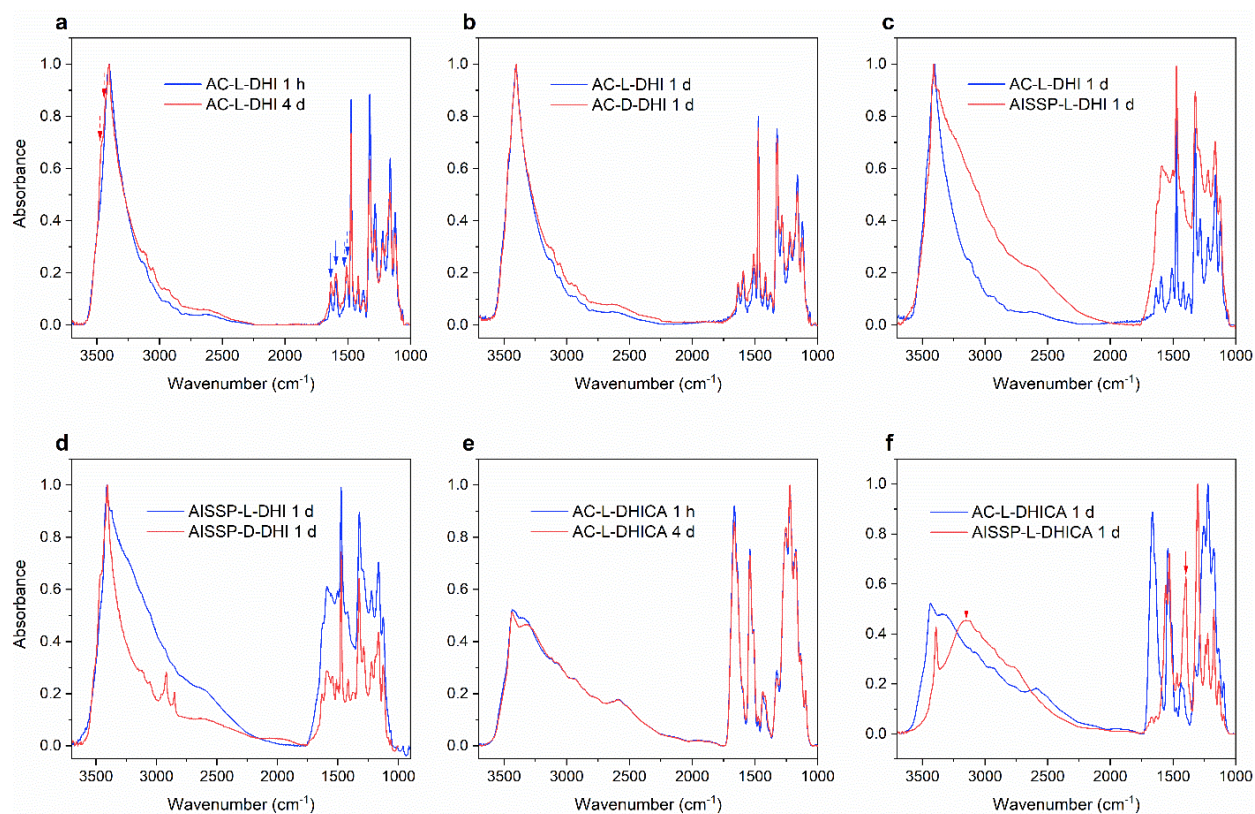
Figure 5.4 IR spectra of (a) AC-L-DHI films at different stages of formation. IR spectra of (b) AC-L-DHI and AC-D-DHI, (c) AC-L-DHI and AISSP-L-DHI and (d) AISSP-L-DHI and AISSP-D-DHI after one day. IR spectra of (e) AC-L-DHICA films at different stages of formation.

5.5.3 UV-Vis Spectra of DHI and DHICA-Based Films

The UV-Vis spectrum of AC-L-DHI films after about 1 h from fabrication shows a broad peak with lambda max of about 307 nm (Figure 5.5 (a)). In a timescale of one week (7 d) at ambient conditions, the peak at 307 nm is more intense than after 1 h and 1 d. The UV-Vis spectrum of AC-L-DHICA films after 1 h shows a broad peak located at lambda max of 364 nm (Figure 5.5 (b)). The UV-Vis spectra of AC-L-DHICA films also undergo changes over time. After one week at ambient conditions, the peak shifts to lambda max of 359 nm and its width increases. The UV-Vis spectra of AISSP-L-DHI films are broadband and do not significantly change within one week of observation (Figure 5.5 (c), Table A.3, SI). Conversely, spectra of AISSP-L-DHICA show a small feature at around 351 nm (Figure 5.5 (d) and Table A.3, SI). As in the case of

AISSP-L-DHI, we did not observe any remarkable variation of the absorption spectra of AISSP-L-DHICA in the timeframe of one week.

The progressive increase of optical absorption in the visible region of the spectrum, for both AC-L-DHI and AC-DHICA, might stem from an improvement of π-electron delocalization through self-assembly[306]–[308]. To validate this conjecture, we evaluated the highest occupied molecular orbital (HOMO)-lowest unoccupied molecular orbital (LUMO) optical energy gap of our films using the *Tauc Plot model* [34] (see Experimental and Table A.3, SI). The evolution of the optical HOMO-LUMO energy gap of both AC-L-DHI and AC-L-DHICA films, after one week at ambient conditions, cannot exclude the hypothesis of π-electron delocalization. The UV-Vis spectrum of AISSP-L-DHI is characteristic of the polymerized form (i.e., broadband) already after 1 h from fabrication. On the other hand, in AISSP-L-DHICA spectra, the presence of a small feature at around 351 nm after one week at ambient conditions, suggests a slower polymerization rate than that of AISSP-L-DHI films.
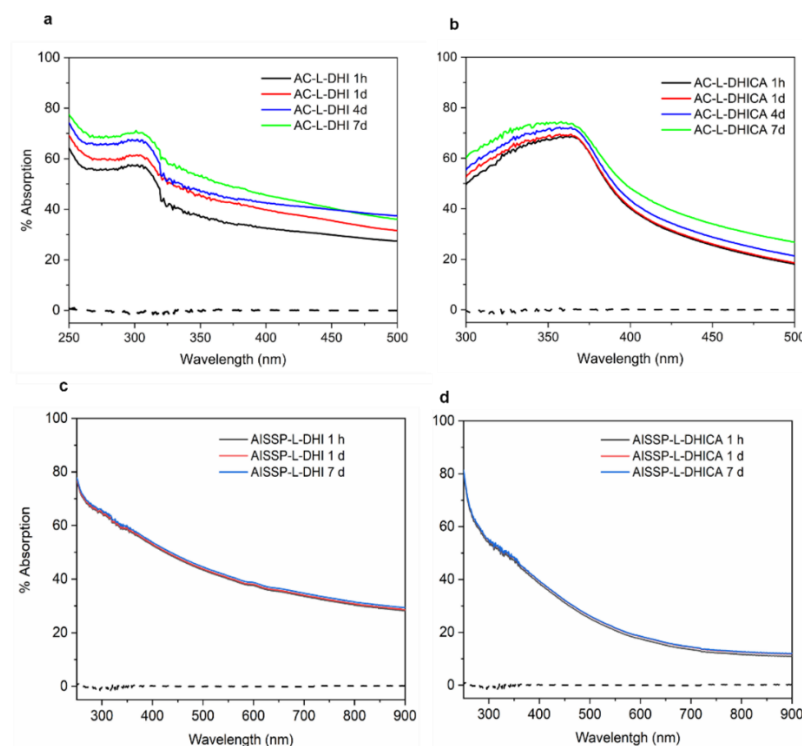
Figure 5.5 UV-Vis absorption spectra of (a) AC-L-DHI, (c) AISSP-L, (b) AC-L-DHICA and (d) AISSP-L-DHICA films respectively. The dotted black line shows the UV-Vis absorption spectrum of fused silica (background substrate).

5.5.4 Electrical Characterization of DHICA-and DHI-Based Films

The electrical response of AC-L-DHICA and AC-L-DHI films (respectively Figure 5.6 (a) and Figure A.7, SI) features hysteresis behavior in the current density voltage curves (J-V) obtained sweeping the voltage at 25 mVs^{-1} and 50 mVs^{-1} in vacuum conditions (see Experimental). Hysteresis curves, akin to those we report here, were also observed in a few conjugated organic polymer-based memory devices (e.g. 3-(6-methoxylhexyl) thiophene (P6Ome)[309], poly (3,4-ethylenedioxythiophene):poly(4-styrenesulfonate)[310] (PEDOT:PSS), and synthetic eumelanin films[290]).

We observe that hysteresis area and parameters $J_+(V=0)$, $J_-(V=0)$, $V_+(J=0)$, $V_-(J=0)$ depend on voltage scan rate (Figure 5.6 (a), Figure A.7 (a) and Table A.4, SI). Indeed, when changing the voltage scan rate from 25 mVs^{-1} to 50 mVs^{-1} we observe an increase of the hysteresis areas, paralleled by a decrease of $V_+(J=0)$ and $V_-(J=0)$ (Table A.4, SI). Regardless of the voltage scan rate, the hysteresis curves are asymmetrical (i.e., current density is higher in the negative voltage region than in the positive one). Furthermore, AC-L-DHICA hysteresis exhibits a broad peak centered around -1.1 V at 50 mVs^{-1} not observable at 25 mVs^{-1} which could be due to diffusion limited proton-related phenomena. This peak is absent for the hysteresis of AC-L-DHI at any voltage scan rate (Figure 5.6 (a) and Figure A.7, SI).

The formation of *space charge layers* (i.e. excess of electrons and/or holes in a region of space) in presence of an electric field, followed by de-trapping of charge carriers from traps at structural defect sites, may explain the electrical hysteresis of our films[290]. Structural defects originate from disruption of hydrogen bond networks, steric hindrance, weaker-than-average interchain interactions, higher (lower)-than-average conjugated molecular segments (i.e. electronic coupling)[200], [311]. The build-up of space charge layers of different densities at the metal electrodes/film interfaces would justify the asymmetry of the hysteresis. The higher amount of charge stored in our films at 25 mVs^{-1} than at 50 mVs^{-1} supports the build-up of denser space charge layers at slower voltage scan rates (Table A.4, SI and Experimental). Assuming space charge layer formation in the presence of an electric field, charge carriers could hop from one defect to another via charge trapping/releasing mechanisms. The resistivity-voltage characteristics (ρ-V) of our films show significant variations in the region of the plot where

$V_-(J = 0) \leq V \leq V_+(J = 0)$ (blue shaded region, Figure 5(b)). This region corresponds to the portion of the plot where $J_-(V = 0)$ and $J_+(V = 0)$ are detected (Figure 5(b) and Figure A.7 (b), SI). The presence of oscillations in the ρ-V characteristics of a few organic conjugated polymers, has been considered as evidence of charge transport taking place via trapping/releasing mechanisms[290], [310]. These observations suggest that the current densities $J_-(V = 0)$ and $J_+(V = 0)$ would originate from combined effects of charge carrier trapping/releasing mechanisms.
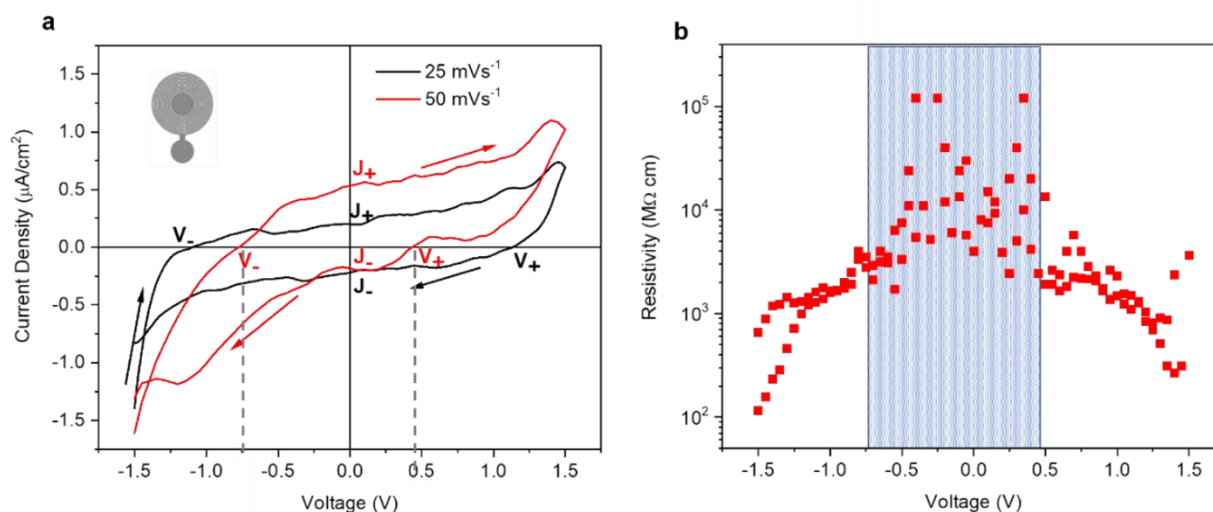
Figure 5.6 AC-L-DHICA films (a) J-V hysteresis at different scan rates on circular interdigitated Ti/Au electrodes (schematic of electrodes geometry is in inset of (a)). In (a) the third J-V cycle is shown. In (b) Resistivity at 50 mVs^{-1}.

5.6 Conclusions

In conclusion, we show that films spin-coated on SiO$_2$ from solutions of eumelanin DHI and DHICA building blocks (monomers) dramatically *evolve over time* as a function of the environmental conditions. Atomic force microscopy (AFM) images of DHI-based films kept in the dark show the formation of fern-like structures, explained by diffusion-limited aggregation.

Further, if samples are not protected from light, pillar-like and crystal-like aggregates form on ferns over different time scales.

On the other hand, AFM images of DHICA-based films show the formation of rod-shaped structures, attributed to Ostwald ripening.

When *exposed to ammonia (catalyst for the solid-state polymerization), DHI- and DHICA-based films feature polymorphism*: in the case of DHI, we observe fibers, sphere-like structures and flat regions, whereas in the case of DHICA-based films sphere-like and shell-like structures as well as rods.

Infrared spectroscopy suggests a combination of physical (π-π stacking and hydrogen bonding) and chemical (new covalent bonds) interactions occurring as a function of time, after deposition. The *exposure to ammonia vapors* of *DHI* causes the *oxidation* of the films, a crucial step to form new covalent bonds (polymerization). Conversely, there are indications that ammonia does not oxidize DHICA to the same extent as DHI.

The evolution of the optical HOMO-LUMO gap of both DHI and DHICA films, evaluated from the UV-Vis spectra at different stages after deposition, cannot exclude the hypothesis of π-electron delocalization.

After the physicochemical surveys we explored the electrical response of DHI and DHICA-based films. We show that the current-voltage response, in vacuum atmosphere, is an electrical *hysteresis* which we attribute to charge carrier trapping/de-trapping mechanisms, expected in organic electronic materials.

 Work is in progress to shed light onto a possible further degree of freedom in our study, namely the aging of the DHI and DHICA powders.

All in all, our results are paramount for understanding the structure-property relationships in eumelanin, which is a fundamental step to achieve eumelanin films of device quality. Our study is a step in the establishment of a *phase diagram* that correlates eumelanin film processing parameters, morphology, and functional properties. The creation of this diagram is necessary for exploitation of the full technological potential of usually disordered bio-sourced organic electronic materials, well beyond eumelanin.

5.7 **Acknowledgments**

CHAPTER 6   ARTICLE 2: ELECTRONIC TRANSPORT IN THE BIOPIGMENT SEPIA MELANIN

Article 2 has been published in ACS Applied Bio Materials on July 6th, 2020. The Supplementary Information is provided in Appendix B.

6.1   Authors

Manuel Reali[1], Abdelaziz Gouda[1], Jonathan Bellemare[1], David Ménard[1], Jean-Michel Nunzi[2,3], Francesca Soavi[4], Clara Santato[1*]

[1]Department of Engineering Physics, Polytechnique Montreal, Montreal, H3C 3A7, Canada

[2]Department of Physics, Engineering Physics & Astronomy, Queen's University, Kingston, K7L 3N6, Canada

[3]Department of Chemistry, Queen's University, Kingston, K7L 3N6, Canada

[4]Department of Chemistry "Giacomo Ciamician", Alma Mater Studiorum Università di Bologna, Bologna, 40126, Italy

*email address: clara.santato@polymtl.ca

KEYWORDS. Sepia melanin, electronic transport, reversible resistive switching, bio-sourced materials, sustainable (green) organic electronics

6.2   Abstract

Eumelanin is the most common form of the pigment melanin in the human body, with diverse functions including photoprotection, antioxidant behavior, metal chelation, and free radical scavenging. Melanin also plays a role in melanoma skin cancer and Parkinson's disease. *Sepia Melanin* is a natural eumelanin extracted from the ink sac of cuttlefish.

Eumelanin is an ideal candidate to eco-design technologies based on abundant, biosourced and biodegradable organic electronic materials, to alleviate the environmental footprint of the electronics sector.

Herein, the focus is on the reversible electrical resistive switching in dry and wet Sepia eumelanin pellets, pointing to the possibility of predominant electronic transport a *conditio sine qua non* to develop melanin-based electronic devices. These findings shed light on the possibility to describe the transport physics of dry eumelanin by the amorphous semiconductor model. Results are of tremendous importance for the development of sustainable organic electronics.

6.3 Introduction

The rapidly growing demand for consumer electronics, one of the most ubiquitous technologies, has led to unsustainable amounts of waste of electrical & electronic equipment (WEEE). On a global scale, WEEE amounts approximately to 45 megatons per year[1]. WEEE contains hazardous substances that pose health and environmental concerns[1]. Refurbishment, recycling and recovery in conventional (inorganic) electronics are viable routes to limit the environmental footprint of consumer electronics[2]. In parallel, the eco-design of electronic devices based on the use of abundant organic bio-sourced materials that are potentially biodegradable, a field that we call organic green (sustainable) electronics, is of the utmost importance, e.g., for the development of low human- and eco-toxicity technologies for the Internet of Things.

In the melanin biopigment family, eumelanin is a brown-black subgroup found in the human body, other mammals, birds, reptiles, amphibians and fishes as well as in lower invertebrates, such as cuttlefish and insects[63]. In humans, aside from photo-protection, eumelanin is involved in a variety of processes, e.g. the accumulation and release of metal cations in the body[45], [312]. It is noteworthy that the interactions between iron and neuromelanin, a pigment made of eumelanin and red-yellow pheomelanin, present in the brain of humans and primates, have been related to Parkinson's disease[53]. The remarkable adhesion of melanin-like materials on surfaces is the underpinning for emerging applications in the biomedical and water treatment fields[185], [313], [314].

Sepia melanin is a natural eumelanin extracted from the ink sac of cuttlefish (Sepia officinalis)[315]. Eumelanin is an ideal bio-sourced candidate for the exploration of the potential

of sustainable organic electronics. Indeed, its molecular structure features electronic conjugation (alternance of single and double bonds), which is a peculiar structural feature of organic semiconductors[9]. At the same time, beyond its ubiquity among flora and fauna, eumelanin is biocompatible, edible and potentially biodegradable[65], [185]. Considering the presence of redox active quinone groups in the molecular structure[185], electronics powered by eumelanin-based electrochemical energy storage devices can also be conceived. Indeed, the redox activity of eumelanin has recently enabled a number of technologies, such as melanin-based biological electrodes as well as flexible and light-assisted (micro)supercapacitors[32], [102]. Eumelanin is made up of two building blocks, 5,6-dihydroxyindole (DHI) and 5,6-dihydroxyindole-2-carboxylic acid (DHICA), coexisting in different redox states. Hydroquinone (H2Q) is the reduced state, semiquinone (SQ) the intermediate redox state and quinone (Q) the oxidized state, with its tautomer quinone imine (QI) (Figure 6.1). The presence of water shifts towards the right the comproportionation equilibrium where H2Q and Q react to give SQ extrinsic radicals and protons. The latter are the mobile electronic charge carriers in eumelanin[162] (Figure 6.2).

DHI and DHICA have several polymerization sites making eumelanin a chemically heterogeneous macromolecule[93], [107]. This heterogeneity explains the short-range order in the material that can therefore be defined, to a certain extent, as amorphous. Nevertheless, self-assembled π-π stacked supramolecular structures with a characteristic inter-plane spacing of ~3.7 Å have been observed both with natural and synthetic eumelanin[91].

In the 1970s, McGinness *et al*. reported on the reversible electrical resistive switching from a high (OFF) to a low (ON) resistive state observable beyond a threshold voltage (V_T) for hydrated eumelanin pressed pellets[37]. At that time, resistive switching had been experimentally observed in amorphous Si, amorphous Ge and chalcogenide glasses (e.g. amorphous Te and amorphous Se)[38]. As a result, the resistive switching behavior shown by eumelanin pellets was interpreted within the Mott-Davis amorphous semiconductor model (ASM)[37], [235]. This model also provided an explanation for the broadband UV-Vis absorption of the biopigment [39]. A crucial element in the work of McGinness *et al*. was the observation that only hydrated eumelanin pellets exhibited electrical resistive switching, i.e., dry pellets did not. The lack of switching of dry pellets was explained by the modified dielectric constant theory, which posits that the adsorbed water increases the dielectric constant of the material, lowering the activation energy for charge transfer processes[203]. Recent publications on the electrical response of hydrated

eumelanin[186], [244], [286] questioned the ASM and proposed the mixed ionic-electronic conductor model (Figure 6.2 and Table 6.1)[27], [42], [44].

Here, we report on the observation of predominant electronic transport in dry pellets of natural Sepia melanin, processed at room temperature. Pellets exhibit room temperature conductivity of about 10^{-3} S·cm^{-1}, after switching. Our observation has profound implications for the development of the field of sustainable organic electronics. Indeed, the observation of pure electronic transport paves the way towards the development of Sepia melanin-based transistors and memory devices. Further, long-term implications are also foreseen in the medical and biomedical fields.
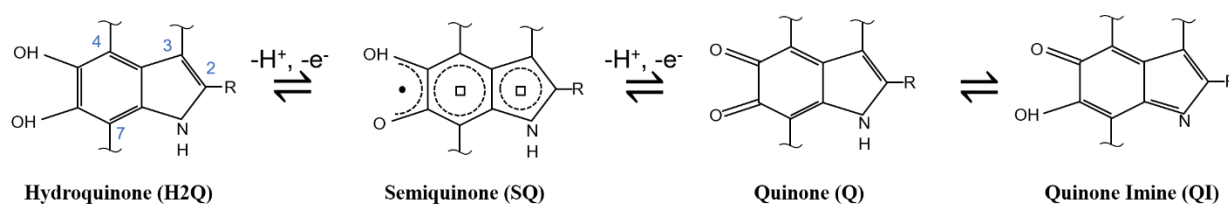
Figure 6.1 Hydroquinone (H2Q), semiquinone (SQ) and quinone (Q) redox forms of the building blocks of eumelanin: 5,6-dihydroxyindole (DHI) and 5,6-dihydroxyindole-2-carboxylic acid (DHICA). R is –H in DHI whereas R is the –COOH group in DHICA. The quinone imine form the tautomer of Q.
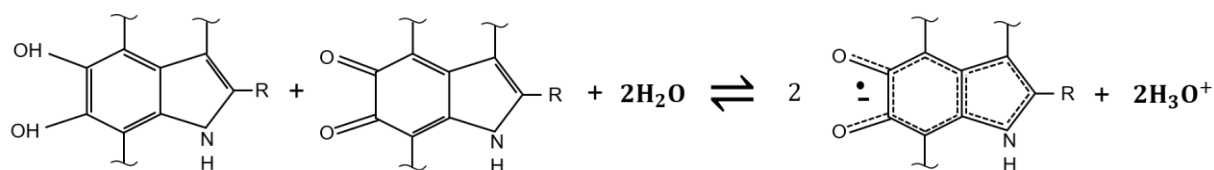
Figure 6.2 The comproportionation equilibrium that regulates the relative concentrations of hydroquinone (H2Q), semiquinone (SQ) and quinone (Q) redox forms of the building blocks of eumelanin in the presence of water. Specifically, H2Q and Q react to form protons and SQ free radicals.

Table 6.1 Literature on the charge carrier transport properties of eumelanin in the form of wet and dry pellets and thin films.

Ref.	Type of Eumelanin (Form Factor, Dry versus Wet)	Metal Contact	Ion Content	Interelectrode Distance	Applied Voltage	Charge Carrier Transport Properties
[37]	Enzymatic action on tyrosinase, autooxidation of L-dopa, extracted from melanoma tumor material, homogenized tumor (pellets, wet)	Cu, C, Al	-	0.1, 1, 10 mm	Interval 0 V – 400 V	Electronic Conductor with Local Modification of the Dielectric Constant
[42]	From solutions of DL-dopa oxidized in air (pellet, 7- 16% water content)	Au	-	2 mm	15 V	Mixed Ionic-Electronic Conductor
[27]	From solutions of DL-dopa oxidized in air (film used as ion gating medium, wet)	Au	-	-	-	Predominantly Ionic Conductor
[316]	Sigma melanin (film, 40% RH in	p- or n-Si	-	50 nm (diode)	ca 3 V	Predominantly

	air and vacuum)	and Au				Electronic Conductor
[290]	Sigma melanin (film, ambient conditions and vacuum)	ITO and Au	-	400 nm (diode)	ca 1.5 V	Predominantly Electronic Conductor
[186]	Sigma melanin (film, interval included between 50% and 90% RH)	Pt	-	10 µm (planar configuration)	ca 1 V	Predominantly Ionic Conductor
[244]	Sigma melanin obtained by oxidation of tyrosine by H_2O_2 (film, 12% and 17% water content)	Pt, Pd, PdH	-	10 µm (planar configuration)	ca 1 V	Predominantly Ionic Conductor
[286]	Sigma melanin and Sepia melanin purchased from Sigma (film, 90% RH)	Au	Cl ca 7.0 mg/g Na ca 64 mg/g	6 or 10 µm (planar configuration)	ca 1 V	Ionic Conductor with Formation of Metallic Filaments
This work	Purified natural Sepia melanin (pellet, dry and 14% and 19%	Cu and stainless steel	Cl ca 0.87 mg/g Na ca	2 mm	Interval 0 V – 160 V	Dry Pellets: Electronic Conductors Wet Pellets:

					Ionic and
water content)		3.9 mg/g			Electronic Conductors

6.4 **Experimental Section**

Sepia Melanin Extraction. Sepia melanin was extracted from the ink sac of the cuttlefish Sepia officinalis. First 100 g of ink were suspended in 200 mL of HCl 2M and stirred for 24 hr at 10 °C. The suspension was centrifuged in a planetary mixer (THINKY ARM-310) and washed several times with 0.5M HCl, ethanol, DI water, ethyl acetate and a buffer solution (0.95 v/v of monobasic sodium phosphate 200 mM, 40.5 v/v of dibasic sodium phosphate 200 mM, 50 v/v of DI water). For each step, the suspension was weighed, and the pH measured. Centrifugation was performed at 10000 rpm at 5 °C (25 min for DI water and buffer solution, 15 min for HCl 0.5M, ethanol and ethyl acetate). After stirring, the centrifugate was sequentially washed with HCl 0.5M, DI water, the buffer, and ethanol, and centrifuged at each washing step. Subsequently, the suspension was washed again with DI water and centrifuged three times. The final product was lyophilized for 24 hr to remove solvents. A fine black powder was finally obtained.

Fabrication of Wet Pellets. The Sepia melanin powder was ground to remove large agglomerates and subsequently weighed (analytical balance, accuracy 10^{-5} g). For the hydrated pellets, we measured the weight percent gained by the pellets after 24 hr hydration (% wt), at different percentages of relative humidity in the atmosphere (Table B.1). The percentage of weight gained after hydration was calculated using the following relation: $\%wt = \frac{W_2 - W_1}{W_1} \times 100$, where W_2 and W_1 are the weight after and before hydration respectively. The hydration was performed in a Cole-Parmer Mini Humidity Chamber (03323-14) equipped with an automatic humidity controller and an ultrasonic humidification system (control humidity levels from 20% to 90% with programmable set points).

A cylindrical stainless-steel coin cell (inner diameter 15.5 mm, outer diameter 19.5 mm, thickness prior pressing 2.6 mm) was used as protective gasket to assemble and seal the pellet. The coin cell was assembled as follows. A pre-cleaned 99% purity Cu foil (dimensions of the

inner diameter of the coin cell, 0.1 mm thickness), from Goodfellow Cambridge Limited, was placed inside the coin cell and the hydrated powder gently transferred on the Cu surface. The top contact was then made by placing the top stainless-steel disk (0.1 mm thickness, SUS316L from SteelJIS) on the powder and the sandwich structure sealed with the upper cap (Figure 6.3 B and C). The coin cell was then manually pressed into 2 mm thick pellets by applying a pressure of 3 tons for 60 s by means of a manual hydraulic press machine (Specac's Atlas Series).

Fabrication of Dry Pellets. Sepia melanin powder was ground to remove large agglomerates and transferred with the coin cell and the pre-cleaned contacts to an argon glovebox (H2O<0.1 ppm, equipped with a manual hydraulic press machine where it was kept for 24 hr prior to pressing it into pellets. The powder was weighed (analytical balance, accuracy 10^{-5} g) and the coin cell assembled following the same fabrication procedure as the hydrated samples. The structure was then pressed into 2 mm thick pellets (3 tons for 60 s).

Electrical. The pellets were clamped to ensure the stability of the contacts during the electrical measurements. Then, they were connected to an amperometer at the terminals of which the current was recorded. The pellets were modeled with an electrical resistance ($R_P = R_{eu} + R_c$ where R_{eu} and R_c are the intrinsic eumelanin resistance and the contact resistance, respectively) in series with the internal resistance of the voltage source R_S. At the threshold voltage (V_T), RP can be calculated as $R_P = \frac{V}{I} - R_S$, where V is the applied voltage and I the measured current (Figure 6.3 A). At least five dry and wet Sepia melanin pellets were tested. The reported values of resistances (Figure B.2 and Table B.3) are average with an error of $\pm$ 0.5 %. The electrical response of the pellets was acquired using a Genesys^{TM} Lambda-TDK 600-2.6 DC power supply (output voltage 600 V, maximum output current 2.6 A). *LabView I-V Software* was used for data recording and programmed to limit the current of the power supply (output current) to the maximum value supported by the resistor (about 150 mA, **Scheme 3A**). The room temperature electrical conductivity of the pellets can be calculated using the following equation:

$$\sigma(295K) = \frac{t}{A \times R_p} \qquad (1)$$

where t is the thickness, A is the inner surface area and R_p is the resistance of the pellets.

Chemical. Before and after the electrical tests, the chemical properties of the hydrated and dry pellets were characterized via Raman Spectroscopy and X-ray Photoelectron Spectroscopy

(XPS). For the former, we used a Renishaw InVia Raman spectrometer (λ=514 nm, 100 nm s^{-1} scanning rate, 5% of the total power to prevent overheating effects). XPS was performed with a VG ESCALAB 3 MKII apparatus (source Mg Kα, power 300 W [15 kV, 20 mA], pressure in analysis chamber ca. 10^{-9} Torr, electron take off angle 0 deg, analyzed depth less than 10 nm, detection limit 0.1% at). Survey scans and high-resolution scans were carried out with 1 eV and 0.05 eV energy steps. Background subtraction was performed via the *Shirley method* and charge correction with respect to C$_{1s}$ set at 284.7 eV.
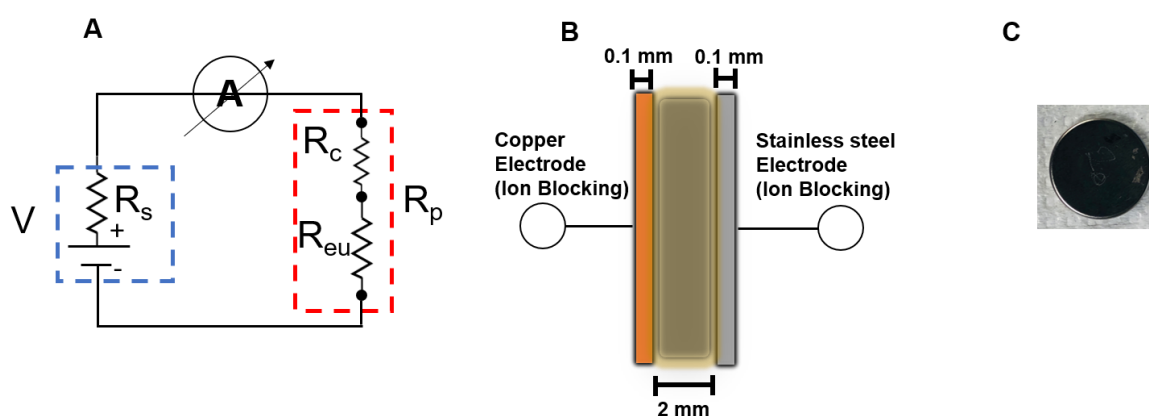
Figure 6.3 Schematic representation of (A) the electrical circuit used in this work to acquire the electrical response of the pellets (B) the sandwich configuration of our Sepia melanin pellets (C) top view of Sepia melanin powders in a half coin cell. In (A) V is the voltage source, A is the amperometer in series with the resistance of the voltage source R$_s$ and the pellet resistance R$_p$ = R$_{eu}$ + R$_c$, where R$_{eu}$ and R$_c$ are the intrinsic eumelanin resistance and the contact resistance respectively.

Electrochemical Impedance Spectroscopy. EIS measurements were performed at ambient conditions with a BioLogic bipotentiostat (SP-300). Data were acquired at open circuit potentials (OCP), within the frequency range 3 MHz - 0.1 Hz, 20 points per decade, 10 mV oscillation amplitude.

Scanning Electron Microscopy and Energy-Dispersive X-Ray. A JEOL JSM7600F microscope was used. EDX was carried out using the same microscope with Aztec (Oxford) software, detector x-Max (80 mm^2, Oxford), at 5 kV.

6.5   Results

6.5.1 Electrical Response of Sepia Melanin Pellets

The current-voltage characteristics of dry and wet Sepia melanin pellets, placed between Cu and stainless-steel electrodes, show that for dry pellets, during the first current-voltage scan, the current monotonically increases with the increase of the voltage up to the threshold voltage VT, where the electrical resistive switching takes place (Figure 6.4 A). The resistance across the pellets in the ON and OFF states is about 100 Ω and 550 Ω (the ON resistance, R_{ON}, is calculated at the maximum value of the current after switching, whereas the OFF resistance, R_{OFF}, is calculated at V$_T$ right before switching (see experimental section and Table B.2). For an ON resistance of 100 Ω, dry pellets feature a room temperature electrical conductivity of about 1×10^{-3} S·cm^{-1}, a value falling within the range of electrical conductivity of semiconductors.

From the second current-voltage cycle, the electrical response is significantly different from that of the first. Indeed, the response from the second cycle fits a current-voltage power law of the form $I \propto V^a$, with values of a close to or higher than unity (Figures B.1 A and C and Table B.3). The electrical response of dry pellets features the same current-voltage power law at different voltage scan rates, after the first scan (Figure 6.4 C). The independence of the electrical response on the voltage scan rate suggests predominant electronic conduction in the dry pellets. Values of $a \geq 1$ in the power law indicate that, under the effect of an electric field, electronic space charge layers, broadly defined as an excess of electrons or holes over a region of space, form at the Sepia melanin/metal interface. Amorphous materials, such as eumelanin, are prone to host space charge layers due to the presence of structural defects acting as charge carrier traps[200], [241]. To validate this hypothesis, we converted our I-V curves into log (J)-log (V) plots, J being the current density, namely the total current per unit area. Our log (J)-log (V) plot shows the change of slope between the Ohmic regime and the Space Charge Limited Current (SCLC) regime (Figure B.1 E, red and blue solid lines with slope of 0.93±0.06 and 2.09±0.02 respectively). This

change of slope can be attributed to the flow of space charge currents in the presence of a distribution of shallow trap states in organic semiconductors[317].

Wet Sepia melanin pellets also feature electrical resistive switching (Figures 6.4 B, B.1 B and D). No considerable difference is observable between the first and the following scans apart from V_T (Figure B.1 D). The scan rate has a dramatic effect on the current-voltage characteristics of wet pellets. At 2000 mVs^{-1} the current starts to increase at about 12 V to reach a maximum at about 40 V. This maximum likely results from the increase of the electronic component of the current and the (exponential) decrease of the ionic component, at this rate. In addition, the electrical response for the whole interval 0 V to 180 V shows that, beyond 2000 mVs^{-1}, the resistive switching is not observable, and the electrical response fits a power law (Figures B.1 D, B.2 and Table B.3). From these results, we infer that conduction in wet pellets is predominantly electronic at high voltage scan rates.

After the resistive switching, we followed the evolution of the resistance with time, for dry and wet pellets (Figure B.3). Dry and wet pellets have an initial resistance of 130 Ω and 225 Ω. The resistance of dry and wet pellets increases up to about 1200 Ω in 10 hr (in the first 5 hr the resistance of the dry pellets increases by ca. 27 Ω hr^{-1} while the resistance of the wet counterparts by ca. 155 Ω hr^{-1}). Such an increase of resistance with time points to volatile memory behavior of both dry and wet Sepia melanin pellets, analogous to organic polymer-based memory devices[17].

To gain insights into the relaxation processes taking place after resistive switching, we measured the current-time characteristics at constant electrical bias. Dry pellets show a plateau-like behavior after an initial increase of the current, most likely attributable to an electric field-induced supramolecular arrangement favorable to electronic transport (Figure 6.5). On the other hand, the transient current characteristics of wet pellets show an exponential decay likely due to the formation of ionic double layers, followed by a plateau-like behavior attributable to electronic transport (Figure 6.5 and Table B.4).
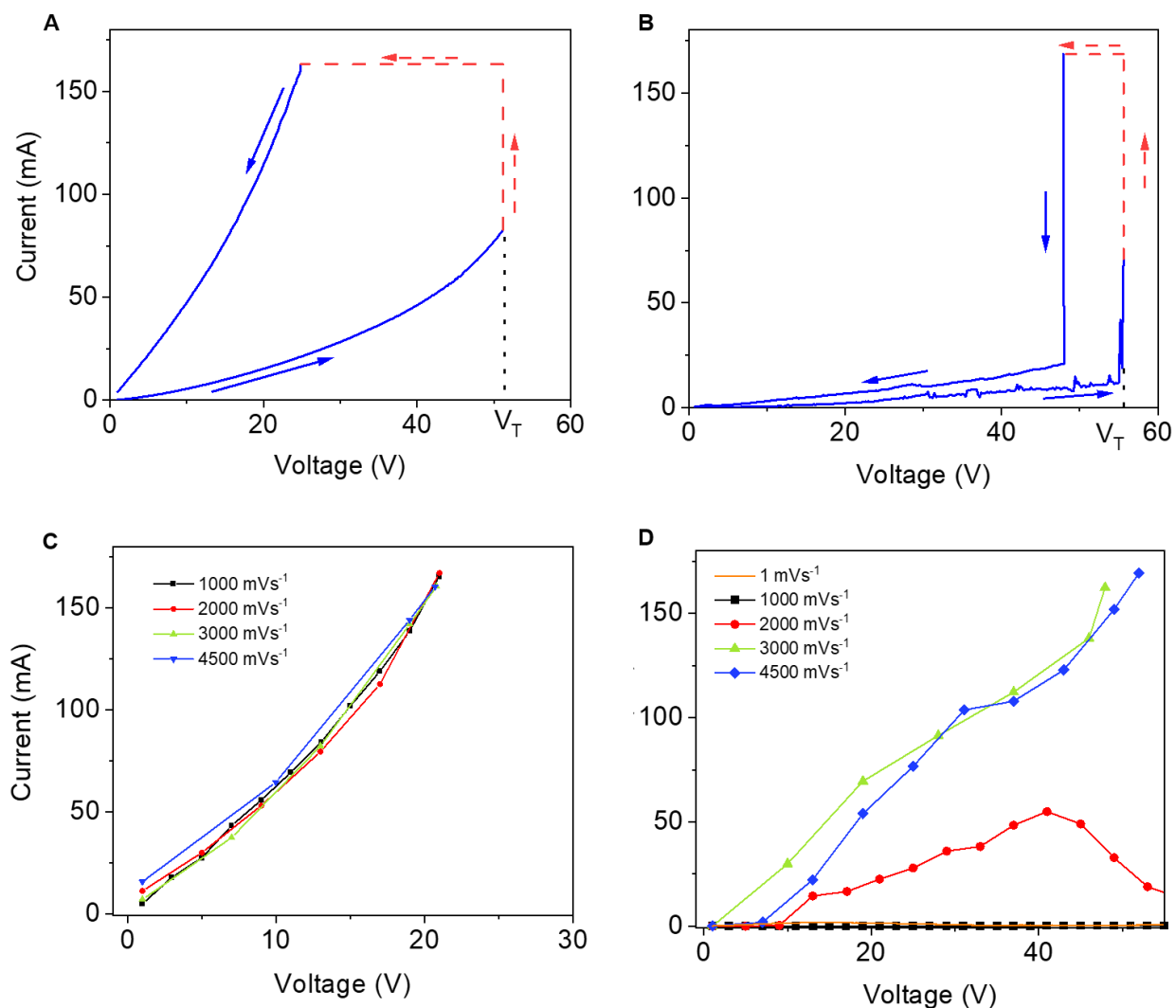
Figure 6.4 Current-voltage response at 100 mVs^{-1} for (A) dry and (B) wet pellets; sequential current-voltage acquisitions from low to high scan rates for (C) dry and (D) wet pellets (beyond 2000 mVs^{-1}, see also Figure B.2). When the voltage source increases, the current monotonically increases up to the threshold voltage (V_T). At V_T, because of the switching, the resistance of the pellet drops and the current increases non-monotonically up to the maximum current (maximum value of the current tolerated by the amperometer (Figure 6.3 A). Thus, from the portion of the plot where the source voltage increases to where the source voltage decreases a transition takes place. Since this transition is fast, only its start and end points can be measured. The real transition should appear as the contribution of a first line at constant voltage and of a second line at the constant maximum current (dash red lines and arrows).
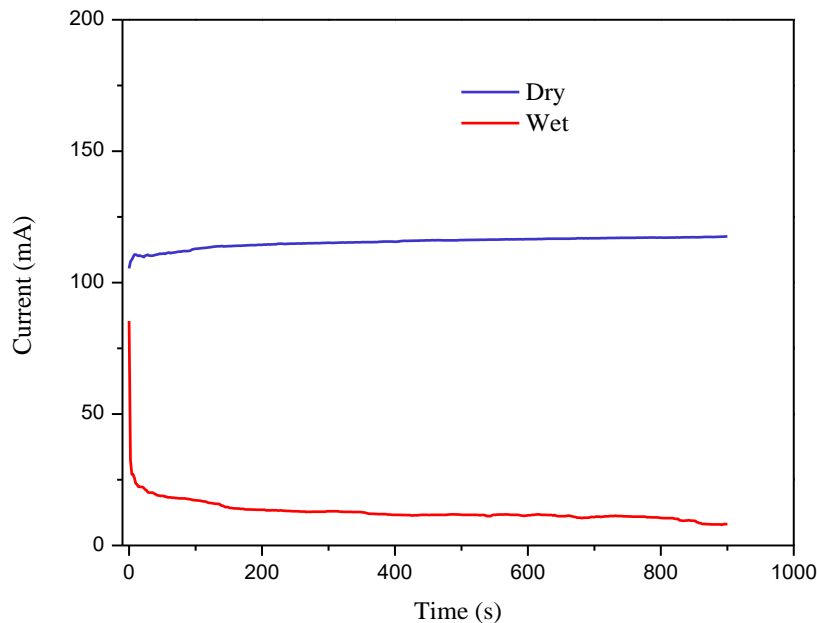
Figure 6.5 Current-time characteristics of wet and dry Sepia melanin pellets after resistive switching for dry (V is about 25 V, close to V_T) and wet Sepia melanin pellets (V is about 45 V, close to V_T).

6.5.2 Electrochemical Impedance Spectroscopy

To shed light on ionic and electronic processes featuring different relaxation times, as well as possible interfacial processes at Sepia melanin/metal interfaces, we performed an Electrochemical Impedance Spectroscopy (EIS) study with frequency ranging from 3 MHz down to 0.1 Hz. Nyquist plots (imaginary vs real components of the complex impedance) obtained from dry pellets before resistive switching feature one semicircle and a low-frequency diffusion tail (Figure 6.6 A). We associate the high-frequency semicircle with the electronic impedance of the dry pellet and the Sepia melanin/metal electrode interfacial impedance. The low-frequency tail describes electronic diffusion processes in dry Sepia melanin (suggesting the hypothesis that ionic contribution can be excluded). Assuming a simple resistor-capacitor behavior (RC) with a semicircle, a relaxation time of 17.4 ms is obtained (this is the $1/f_{max}$ value where f_{max} is the frequency of the top of the semicircle, about 57.5 Hz). On the other hand, Nyquist plots of the wet pellets before resistive switching exhibit three semicircles with relaxation times of 1.33 µs, 0.31 ms, 6.14 ms (Figure 6.6 C). We propose that the two high-frequency semicircles are

attributable to the ionic and electronic impedance in the bulk whereas the low-frequency one is attributable to the charge transfer impedance at the Sepia melanin/metal interfaces. The presence of three semicircles suggests electronic conduction in parallel with ionic conduction[279], [318]. The overall impedance should include the capacitance developing at the interface. Nyquist plots of wet and dry pellets do not show any low-frequency capacitive line. Considering the thickness of the pellets (ca. 2 mm, see experimental section), the capacitance is expected to be insignificant. Before the electrical resistive switching, wet pellets show lower impedance than their dry counterparts. This observation can be rationalized in terms of the comproportionation equilibrium, which induces a high density of SQ extrinsic radicals (mobile charge carriers) and protons in wet pellets with respect to dry ones, and leads to the decrease of ionic and electronic impedance[42].

After the electrical resistive switching, we observe that dry and wet pellets exhibit only one semicircle in the EIS spectra (Figures 6.6 B and D). The buildup of an electrical double layer under the action of the electric field, expected to be electronic for dry pellets and predominantly ionic for their wet counterparts, likely facilitates charge carrier injection in the two types of pellets. We also observe that the real part of the total impedance of wet pellets, after the electrical resistive switching, is higher than that of dry pellets. This observation could be attributed to possible side reactions at the wet Sepia melanin/metal interface that passivate the metal contacts.

To better quantify the impedance changes before and after the electrical resistive switching, for both dry and wet Sepia melanin pellets, we fitted the EIS with a simplified R_{tot} Q circuit where R_{tot} is the total resistance in series with the constant phase element Q (Table B.5). The total resistance includes the electronic (R_e), ionic (R_i) and interface resistance (R_{if}) such that $R_{tot}=R_e+R_i+R_{if}$. The constant phase element is the series combination of the melanin's geometrical capacitance and the capacitance at the Sepia melanin/metal interface that describes any deviation from an ideal capacitive response. The fitting parameters indicate that the value of Q (the capacitive element) for dry pellets increases from ca. $6.70\times 10^{-12}\,F.s^{n-1}$, before switching to $6.77\times 10^{-9}\,F.s^{n-1}$, after switching (Table B.5). This increase in capacitance after switching for the dry pellet confirms the formation of a space charge layer that facilitates the charge carrier injection. Considering that the thickness and the section of the pellet do not change before and after switching, the dielectric constant of melanin increases too after switching.

On the other hand, the total capacitance of the wet pellet decreases from ca. 2.60×10^{-8} $F.s^{n-1}$, before switching to 3.80×10^{-10} $F.s^{n-1}$, after switching. The aforementioned decrease in capacitance of the dry pellet, is in agreement with the hypothesis of the formation of a passivating layer at the wet Sepia melanin/metal interfaces (Table B.5).
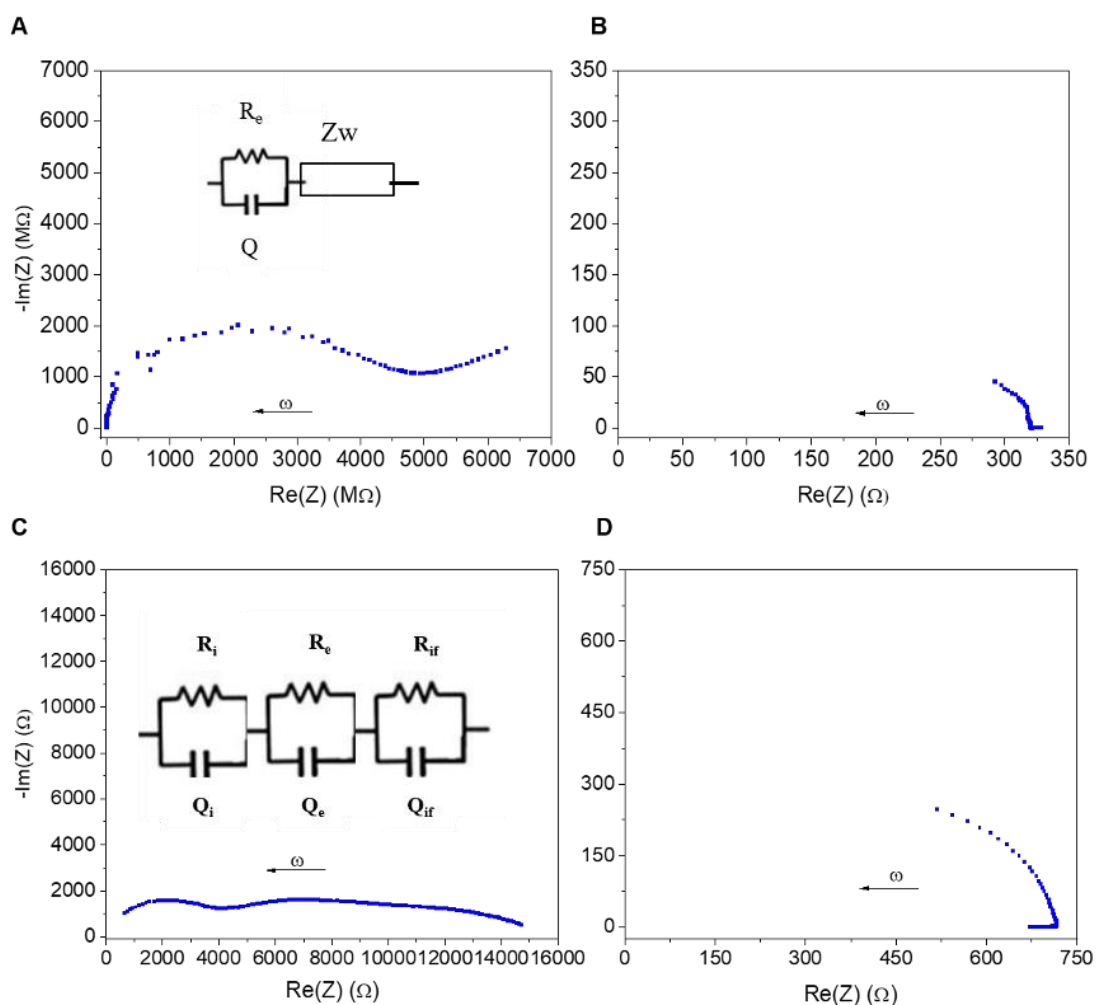
Figure 6.6 Electrochemical impedance spectroscopy of dry and wet Sepia melanin pellets. Nyquist plots of dry, (A) and (B), and wet, (C) and (D), pellets; (A) and (C) before and (B) and (D) after resistive switching. Insets of figures (A) and (C) corresponding to equivalent circuits where R_e is the electronic resistance, R_i the ionic resistance, R_{if} the interface resistance, Q is the constant phase element (the series combination of melanin's geometrical capacitance and the capacitance at melanin/metal interface that describes any deviation from an ideal capacitive response) and Z_w the diffusion hindered impedance.

6.5.3 Scanning Electron Microscopy

To evaluate the possibility of explaining the resistive switching by the formation of metallic conductive filaments bridging the interelectrode distance by electrode dissolution [38], [286], we investigated the surface of the electrodes after switching by Scanning Electron Microscopy (SEM). SEM images and Energy Dispersive X-ray spectra (EDX) do not show any trace of metallic filaments (Figures B.4 and B.5). Therefore, we tentatively exclude the formation of metallic filaments as the cause of the resistive switching.

6.5.4 Raman Spectroscopy

We evaluated the possibility of attributing the resistive switching to a phase transition from amorphous to graphitic carbon by Joule heating [38] To this end, we performed Raman spectroscopy surveys of dry and wet Sepia melanin powder samples obtained from pellets before and after resistive switching (Figures B.6 A, B, C and Table B.6). Raman spectra of dry and wet Sepia melanin do not show any change before and after switching. We did not observe any peak or shoulder attributable to ordered sp2 carbon expected at 2750 cm^{-1} (2D$_2$ band) and at 2700 cm^{-1} (2D$_1$ shoulder) [319].

6.5.5 X-ray Photoemission Spectroscopy and X-ray Diffraction

In agreement with the results of Raman spectroscopy, the high-resolution C1s X-ray photoemission (XPS) spectra of dry Sepia melanin powders, acquired before and after the current-voltage measurements, do not show evidence of graphitic carbon (Figures B.6 D and E, Tables B.7 and B.8). Typical signatures of graphitic carbon are a C$_{1s}$ peak at BE=291.4 eV and an unusually thin C$_{1s}$ component at BE=284.6 eV. The high-resolution C$_{1s}$ XPS spectra of dry Sepia melanin powders show a satellite peak at BE=291.4 eV; this is expected in eumelanin because of the cyclic carbon structure. The C$_{1s}$ component at BE=284.7 eV is broad and not as sharp as expected in graphitic carbon (Figure B.6 E). The concentration of C-O, C-OH, or C-O-C groups (BE=286.7 eV) is high compared to the other chemical groups observed (Tables B.7 and B.8). The concentration of C-O groups, compared to C-N and C=C groups, is also higher than expected. Nevertheless, the C$_{1s}$ spectra before and after switching of Sepia melanin powders are similar, except for a slight increase in C-O and decrease in C-N after switching. X-ray Diffraction (XRD) patterns of dry Sepia melanin powders before and after the electrical resistive switching

do not show any signature of graphitic planes (Figure B.7), expected as sharp peaks located at $2\theta \sim 27°$ and $2\theta \sim 54°$ [320].

6.6 Discussion

We propose a tentative model to explain our results, based on the hypothesis that in dry pellets charge carrier injection takes place at sufficiently high applied voltages causing the formation of space charge layers namely *electronic* double layers at the Sepia melanin/metal interface (Figure 6.7). A further increase of the voltage leads to traps filling[200], [241], and to the effective overlap of the tails of the functions describing the density of energy states of the valence and conduction bands, eventually leading to the resistive switching[38]. In our model, the tails stem from the amorphous nature of the Sepia melanin material. From the second current-voltage scan, dry pellets are in a trap-free regime and the current-voltage characteristics can be described by a power law[38]. For the wet pellets, space charge layers with ionic nature at the Sepia melanin/metal interfaces would lead to the electrical resistive switching (Figure 6.7). The mixed protonic-electronic conductor model for the wet pellets is supported by the linearization of the current-voltage characteristics at voltage scan rates higher than 2000 mVs^{-1}. Work is in progress to locate the Highest Occupied Molecular Orbital (HOMO) and Lowest Unoccupied Molecular Orbital (LUMO) energy levels of Sepia melanin, by Ultraviolet Photoelectron Spectroscopy (UPS) and Inverse Photoemission Spectroscopy (IPES), with the aim to optimize the charge carrier injection process.
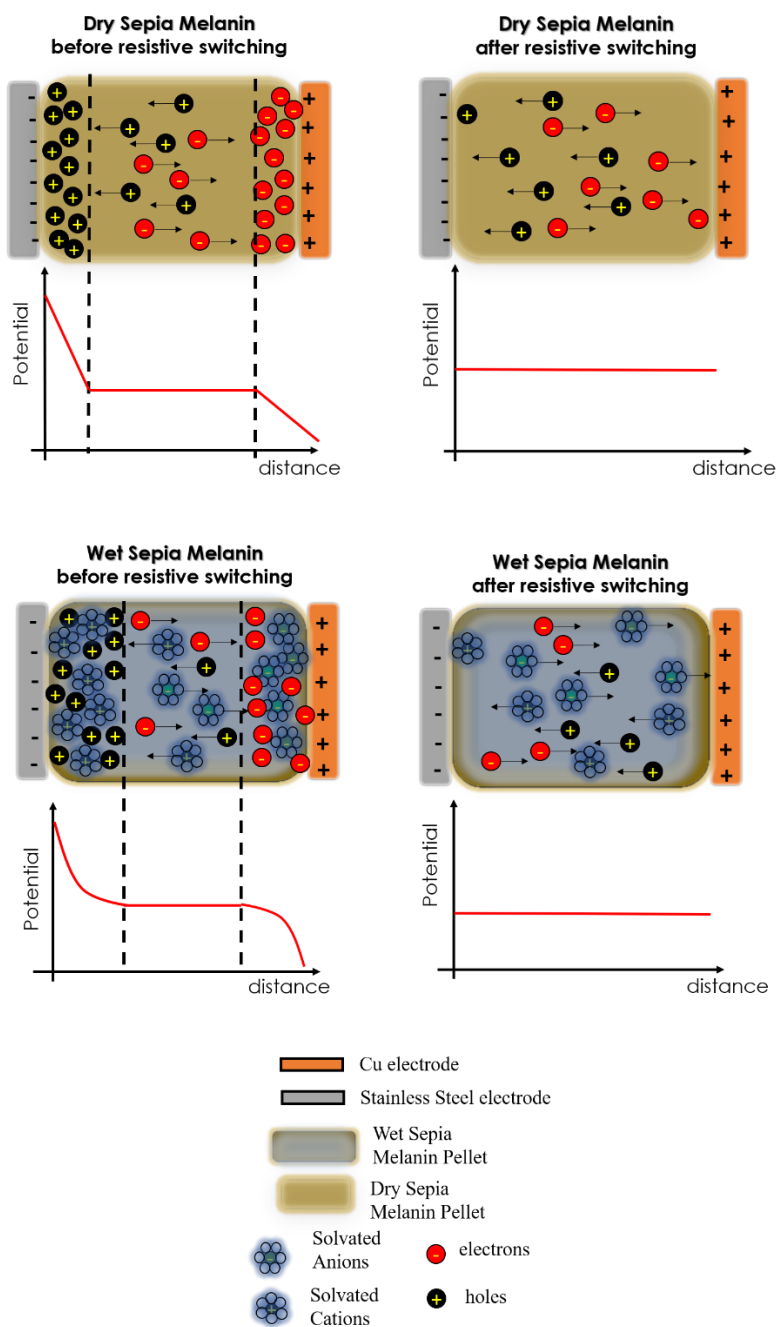
Figure 6.7 Tentative model to describe the phenomenon of electrical resistive switching observed in dry and wet pellets of Sepia melanin, reported in this work. A key role in the model is played by the formation of electrical double layers (predominantly electronic when the pellets are dry and predominantly ionic when the pellets are wet) at the Sepia melanin /metal interfaces.

6.7 **Conclusions**

In conclusion, dry and wet Sepia melanin pellets included between metal electrodes feature reversible electrical resistive switching. Our dry and wet pellets feature a conductivity of about 10^{-3} S·cm^{-1} after switching. This value refers to natural eumelanin pellets processed at room temperature. We propose that in *dry* Sepia melanin pellets, under bias, the effective overlap of the density of energy states of valence and conduction band leads to the electrical resistive switching. Electrical double layers (expected to be electronic in dry pellets and ionic in wet ones) enable charge carrier injection at the Sepia melanin/metal interface. This behavior points to the validity of the amorphous semiconductor model to describe the transport physics of dry Sepia melanin. The linearization of the current-voltage characteristics after switching and at different voltage scan rates is a strong indication of predominantly electronic conduction. However, the buildup of ionic double layers at voltage scan rates below 2000 mVs^{-1} and the linearization of the current-voltage characteristics at higher voltage scan rates support the mixed protonic-electronic conduction model to describe the transport physics of *wet* Sepia melanin pellets, in agreement with the literature.

The observation of predominant electronic transport in Sepia melanin satisfies the *conditio sine qua non* to start designing and developing Sepia melanin-based devices. Our results are of the highest importance for the development of the field of sustainable organic electronics that aims at alleviating the environmental footprint of the electronics sector using abundant, solution processable, possibly biodegradable electronic materials, including biomolecules extracted from agri-waste and biomass feedstock.

6.8 **Author Contributions**

C. Santato and M. Reali designed the experiments. M. Reali and A. Gouda fabricated dry and wet Sepia melanin pellets. J. Bellemare designed the electrical circuit and programmed the software to measure the current-voltage characteristics of Sepia melanin pellets. M. Reali performed the current-voltage and the transient current measurements. A. Gouda acquired the electrochemical impedance spectroscopy response. C. Santato supervised the experiments. All authors gave their

critical contribution to data interpretation. M. Reali and A. Gouda drafted the manuscript. All authors made comments and proofread the manuscript.

6.9 **Acknowledgements**

CHAPTER 7   GENERAL DISCUSSION

In this thesis, we chose eumelanin as the study case material for several reasons. First and foremost, as presented in chapter 2 and chapter 3, beside playing fundamental roles in flora and fauna (e.g., photoprotection, antioxidant, camouflage etc. etc.) eumelanin is edible, biocompatible, and potentially biodegradable. Its unique set of physicochemical properties makes eumelanin an exciting material to be studied in several fields: medicine (e.g., dermatology and oncology for melanoma skin cancer), neurology for Parkinson's disease, drug binding), physics, chemistry, electrochemistry, materials science, and engineering (e.g., structural properties, charge transfer and charge carrier transport properties, etc.).

Thin films are the core organic electronic devices and enable the investigation of the physicochemical properties of matter using plenty of techniques. The development of high-performance organic electronic devices based on eumelanin relies on the fabrication of smooth, uniformly thick, and continuous films as well as on the study of their physicochemical properties, both at the microscopic and macroscopic scale. The accomplishment of this task requires the construction of structure-property relationships correlating eumelanin film processing, morphology, and functional properties. As discussed in chapter 2 and chapter 3, several poorly understood physicochemical properties of eumelanin are limiting the potential of its applications in green organic electronics and bioelectronics.

In this chapter, the results of Chapter 5 and 6 are discussed with reference to the literature discussed in chapter 2 and chapter 3. While in this PhD thesis we could investigate only a few physicochemical properties of eumelanin, we gained exceptional insights. We discuss these insights with respect to eumelanin film formation (as governed by physical interactions (self-assembly) and covalent bonding) and transport physics.

7.1   Eumelanin film Formation

Because of the high degree of chemical heterogeneity and structural disorder, little is known about the underlying mechanisms of eumelanin aggregation (supramolecular buildup) and polymerization (covalent bonding) in solid state. Despite the body work of the last twenty years, eumelanin filmability has not been investigated under the lens of supramolecular self-assembly (physical interactions through π-π stacking) and covalent bonding. Indeed, the limited solubility

of eumelanin in most common solvents *de facto* prevented to unravel these mechanisms during film formation (solubilization requires partial interruption of supramolecular buildup). In this context, Pezzella's group at the University of Naples "Federico II" (Italy), recently demonstrated the fabrication of synthetic eumelanin films (i.e., films expected to mimic the natural pigment and obtained from powders of only one of the two building blocks, DHI and DHICA) through an ammonia-induced solid state polymerization protocol (AISSP). The AISSP protocol involves the fabrication of eumelanin films by (i) spin-coating or drop casting solutions of DHI and DHICA powders dissolved in methanol and (ii) exposing the films to an ammonia enriched atmosphere (polymerization-catalyst, see chapter 3).

In <u>Article 1</u> (chapter 5), we built from these findings to follow the early stages of formation of DHI- and DHICA-eumelanin films under different environmental conditions, including ambient conditions versus ammonia atmosphere, dark versus laboratory daylight. Our investigations led us to unravel the dramatic morphological and chemical changes undergone by DHI, DHICA, AISSP-DHI and AISSP-DHICA films from the first few hours to months after deposition.

AFM images of DHI films in dark conditions revealed the formation fern-like structures. When exposed to laboratory daylight, pillar-like structures grow on top of the ferns and eventually evolve into micron-sized crystal-like structures after one month from deposition. In the case of DHICA films we observed the formation rod-shaped like structures with density, length and width increasing over time at ambient conditions. We attributed the formation of ferns in DHI and rods in DHICA films to diffusion-limited aggregation (DLA) and Ostwald ripening mechanisms, respectively. These processes are associated to the change of physical interactions (self-assembly) during the supramolecular buildup of DHI and DHICA. Furthermore, in presence of laboratory daylight the formation of pillar-like structures in DHI films suggests the coexistence of various molecular arrangements responsible for structural and morphological polymorphism. In this regard, we also found that the exposure to an ammonia enriched environment for 24 h after deposition brings about marked polymorphism both in AISSP-DHI and AISSP-DHICA films.

The IR spectra of DHI and DHICA-based films, collected over time after film deposition, were twofold relevant as they enable us to provide important insights into: (i) the change of and

chemical interactions in the films and (ii) the effectiveness of the AISSP protocol in achieving film polymerization.

Particularly, in DHI-based films the observation of band splitting in the O-H stretching vibrations (expected at 3400 cm^{-1}) paralleled by the slight increase of the absorption in the carbonyl region (expected at 1660-1715 cm^{-1}) from 1 h to 4 d after deposition, suggested (i) prevalent reorganization through noncovalent interactions and (ii) slow oxidation at ambient conditions. The IR absorption in the carbonyl region of AISSP-DHI films revealed higher film oxidation with respect to DHI films processed at ambient conditions. As we discussed in chapter 2, oxidation of hydroquinone (HQ) into semiquinone (SQ) and quinone (Q) is a key step to achieve the polymerization of eumelanin. Thus, we proposed that structural reorganization in AISSP-DHI films is prevalently governed by oxidation of HQ that can eventually favor the formation of new covalent bonds. On the other hand, the IR spectra of AISSP-DHICA films provided evidence of the occurrence of deprotonation of COOH groups in ammonia atmosphere. Our results casted doubts on the role of polymerization-catalyst of ammonia for DHICA.

All in all, these findings represent a very important step towards the achievement of a holistic structure-property relationship phase diagram for the correlation of processing parameters, morphological, chemical and functional properties of eumelanin films. The achievement of this diagram is paramount to engineer device-quality eumelanin films for its extensive exploitation in the field of green organic electronics.

7.2   **Eumelanin Transport Physics**

The degree of supramolecular self-assembly (π-π), H-bonding and covalent interactions profoundly impact the electrical properties of eumelanin, both in terms of charge carrier type (electronic/protonic) and transport mechanisms (electronic hopping, trapping-de trapping, protonic Grotthus transport). In this context, in chapter 3 we gave a detailed overview of the electrical properties of eumelanin with focus on the two models of transport physics formulated for the biopigment: the Mott-Davis amorphous semiconductor model and the mixed ionic (protonic) conductor model. Despite these two charge carrier transport models were based on solid and compelling evidence, they showed important limitations. The mixed-protonic-electronic conductor model has not been tested regarding the electrical resistive switching (only low electric

fields have been considered) and did not explain it [43]. On the other hand, crucial details were not reported during the electrical resistive switching experiments [37], i.e. the %RH, hydration time, I-V response of dry eumelanin pellets. Besides that, in most of the works published between the 1960s and the 1970s supporting the Mott-Davis amorphous semiconductor model, information on the quantitative water intake before and after tests is missing.

In <u>Article 2</u> (chapter 6), we reported on the reversible resistive switching behavior of dry and wet Sepia melanin pellets in a sandwich configuration between copper and stainless-steel electrodes. We focused on the electrical properties of eumelanin pellets at the opposite sides of the hydration scale (i.e., highly hydrated (19% w/w) vs. dry pellets). By combining I-V voltage sweeps at different voltage scan rates, transient current measurements, and impedance spectroscopy surveys before and after switching, we (i) found strong indications of predominant electronic and protonic transport, for dry and wet Sepia melanin pellets; (ii) reported on the increase of the electrical resistance of dry and wet pellets in unbiased conditions over a period of 10 h after switching. Such an increase of the resistance suggests a volatile-memory behavior of both dry and wet eumelanin pellets; (iii) provided a tentative model to explain the resistive switching behavior. We attributed the resistive switching behavior to the formation of electrical double layers of electronic and ionic (protonic) nature for dry and wet pellets, respectively. Assuming the Mott-Davis model for dry pellets, we proposed that, under the action of the electric field, electronic space charge layers help in charge carrier injection thus shifting eumelanin's Fermi level and consequently improving the overlap of the CB and VB energy states. Likewise for wet pellets, the formation under bias of ionic (protonic) double layers increases the proton and SQ radical density (as per comproportionation equilibrium), leading to resistive switching.

This thesis contains the first detailed investigation of the electrical properties as well as the first observation of resistive switching in dry Sepia melanin pellets.

All in all, when inserted in a broader context comprising both electronic and protonic transport models for bio-sourced materials (chapter 3), our results suggest that the mixed protonic–electronic conductivity of eumelanin is the signature of a *special* semiconducting behavior. Particularly, depending on the molecular characteristics of eumelanin, degree of supramolecular self-assembly and content of adsorbed water, eumelanin appears to ''switch'' from electronic to protonic semiconductivity.

CHAPTER 8 CONCLUSION AND PERSPECTIVES

In conclusion, the global objective of this PhD thesis was providing insights on eumelanin film formation and transport physics for its exploitation in green organic electronics and bioelectronics.

Based on the results collected during this PhD work, we can conclude the followings:

In Article 1, we reported on the evolution from the molecular state to film after spin coating of solutions of DHI and DHICA on SiO_2. The examination of film growth with atomic force microscopy (AFM), Fourier transform infrared (FTIR) and UV-Vis spectroscopy revealed that:

1) DHI-based films show fern-like structures resulting from diffusion-limited aggregation, whereas rod-shaped structures, attributable to Ostwald ripening, are observable for DHICA-based films. When exposed to ammonia (a catalyst for the polymerization of eumelanin building blocks in solid state), DHI- and DHICA-based films exhibit polymorphism.

2) A combination of physical (i.e., π-π stacking and H-bonding) and chemical (covalent) interactions occurs in the films as a function of time. As discussed in detail in chapter 5 and 7, the exposure to ammonia causes oxidation of the DHI building blocks, the oxidation being an initial step to the formation of new covalent bonds (polymerization). Conversely, ammonia does not oxidize DHICA to the same extent as DHI, bringing about a limited polymerization in DHICA-based films.

The remarkable insights we gained in Article 1 call for a number of future investigations.

a) Considering the hydrophilicity of eumelanin (section 2.3.6) and our findings on film oxidation at ambient conditions, we suggest studying the changes of morphology and chemical properties taking place in films (i) in inert atmosphere (e.g., low content of H_2O and O_2) and (ii) in controlled humidity conditions.

Furthermore, since the molecular mobility is affected by the evaporation rate of the solvent, (i) and (ii) should be performed by dissolving chemically controlled powders in suitable solvents featuring low, intermediate and high evaporation rate.

b) Considering the impact of DHI:DHICA ratio on the physicochemical properties of eumelanin (see chapter 2), we also recommend performing studies as in (i) and (ii) by exploring several ratios. In this regard, replicating the DHI:DHICA ratio of the natural biopigment in synthetic films, would open the opportunity to mimic the supramolecular aggregation of natural eumelanin.

c) Considering the high degree of chemical heterogeneity and reactivity of the building blocks, synthetic DHI and DHICA powders may not feature a monomeric character. Therefore, we also suggest studying film formation as a function of the *oligomerization* state of the powders.

In perspective, the combination between the results of this thesis and the investigations in (a), (b) and (c) will provide a complete description of the supramolecular buildup of eumelanin from DHI and DHICA by the AISSP protocol and enable the establishment of a structure-property relationship diagram for the biopigment.

In Article 2, we studied the electrical properties of dry and wet room temperature-processed Sepia melanin pellets, in sandwich configuration between Cu and stainless-steel electrodes. The acquisition of I-V response as a function of the voltage scan rate, transient current measurements and impedance spectroscopy led us to:

1) Finding evidence, for the first time, of predominant electronic transport in dry Sepia melanin pellets.

2) Confirming the prevalence of protonic transport in wet (highly hydrated) Sepia melanin pellets.

3) Reporting on the electrical resistive switching in dry and wet Sepia melanin pellets. After switching, pellets featured an electrical conductivity as high as 10^{-3} S cm^{-1}, this last falling within the range of electrical conductivity of organic semiconductors.

4) Reporting on the increase of the electrical resistance in unbiased conditions and after switching of dry and wet Sepia melanin pellets, suggesting volatile memory behavior. We observed that the resistance of wet Sepia melanin pellets increases faster than the resistance of dry counterparts.

5) Explaining the electrical resistive switching of dry and wet Sepia melanin pellets with the formation of electronic and ionic double layers at the Sepia melanin/metal interface, respectively.

The results achieved in <u>Article 2</u> open the door to future experiments:

a) Studying the electrical response of Sepia melanin pellets pressed using high work function (e.g., Cu, Au) and low-work function metal contacts (e.g., Zn, Y), expected to easily inject holes and electrons in the bulk of Sepia melanin pellets, respectively. Such a study will contribute to shed light on the nature of the polarity of electronic charge carrier in eumelanin pellets when electronic transport is dominant (as in dry Sepia melanin). We also recommend changing the pellet thickness to gain insights on the contribution of the contact resistance to (i) the mechanisms of charge carrier injection at the Sepia melanin/metal contact interfaces and (ii) the total resistance of system.

b) Studying the electrical response of Sepia melanin pellets using chemically inert metal electrodes such as Pt (i.e., metal electrodes exhibiting high resistance to the formation of passivation layers or corrosion in presence of adsorbed water). These investigations are expected to provide further insights into the mechanism of formation of ionic-double layers in wet Sepia melanin pellets in presence of an electric field.

c) Collecting sequentially the impedance spectroscopy characteristics of Sepia melanin pellets and the corresponding resistance in unbiased conditions until the pellet resistance reaches a stationary value (about 8 h for dry pellets and 6 h-10 h for wet pellets, Figure B.3, appendix B). Such an investigation is expected to shed light on the characteristic relaxation times of charge carriers in dry and wet pellets in unbiased conditions, several hours after the electrical resistive switching. These experiments are expected to answer a question that we left open in this PhD thesis, that is "why the resistance of wet pellets increases faster with respect to the resistance of dry pellets". Unraveling the different mechanisms of charge carrier relaxation in dry and wet eumelanin, after the occurrence of the electrical resistive switching, open the door to the design and characterization of volatile memory devices based on Sepia melanin.

In perspective, the unprecedented values of electrical conductivity reported in this thesis for Sepia melanin pellets, call for an in-depth study of the charge carrier transport properties of Sepia melanin films. Once again, the limited solubility of eumelanin in most common solvents remains a key challenge to face. The formulation of Sepia melanin-based inks is a promising route to circumvent the limited solubility issue. Conventional ink formulations make use of polymer binders (e.g., polyvinyl butyral (PVB), polyvinyl pyrrolidone (PVP)) that are soluble in organic solvents, to bind and stabilize insoluble pigments in the ink state.

In this regard, at the end of this PhD work, we succeeded in formulating a Sepia melanin ink optimized for large scale roll-to-roll printing. The ink includes Sepia melanin powders (extracted and purified from the raw ink of cuttlefish as in <u>Article 2</u>), PVB as a binder and 1-propanol as organic solvent. We successfully demonstrated proof-of-principle printability of Sepia melanin ink films on Kromekote® paper and flexible polyethylene terephthalate (PET) for low-cost, low embodied energy printable electronics. SEM images of printed and spin-coated Sepia melanin ink films show complete substrate coverage and exhibit homogeneity, continuity and thickness uniformity. Film morphology by SEM also shows the presence of aggregates of PVB that improve the contacts among the Sepia melanin granules, thus affecting the transport properties at their interfaces, eventually leading to inter-granule percolation phenomena.

The fabrication of uniform and continuous Sepia melanin ink films currently enables the investigation of a few fundamental aspects of the transport physics of eumelanin that we could not study in the pellet form during this PhD work. These aspects include:

a) Determining the nature of the predominant electronic charge carrier in dry Sepia melanin films by performing Hall effect measurements. Hall effect should be coupled with electron-paramagnetic resonance spectroscopy surveys to disentangle the contributions of unpaired electrons (semiquinone radicals (SQR)), electrons and holes to the overall electrical conductivity of eumelanin (see section 2.3.4, section 2.3.6 chapter 2 and section 3.3, chapter 3).

b) Finding characteristic values of activation energies for charge carrier transport by performing temperature-activated electrical conductivity measurements. Besides that,

the observation of a temperature-dependent electrical conductivity could set the basis toward the design of Sepia melanin-based temperature sensors.

c) Studying the behavior of Sepia melanin ink films as channel materials in field effect transistor (FET). Beside the intrinsic technological relevance, FETs would permit evaluation FET mobility as well as the contribution of the contact resistance and the channel resistance. Furthermore, the FET threshold voltage would provide an accurate evaluation of the density of shallow trap states of the channel.

d) Coupling the investigations in c) to photoconductivity experiment to estimate the density of deep charge carrier traps from the rise and decay of the transient-photocurrent intensity of Sepia melanin films.

In summary, we collected experimental evidence supporting the interest of eumelanin for technological applications in sustainable organic electronics. We have proposed a solid methodology for extending the eumelanin studies to other biosourced materials exhibiting high degrees of chemical and structural disorder.

REFERENCES

[1]   C. P. Balde, V. Forti, V. Gray, R. Kuehr, and P. Stegmann, *The Global E-waste Monitor 2017. Quantities, Flows and Resources.* United Nation University, 2017.

[2]   M. Meloni, F. Souchet, and D. Sturges, "Circular Consumer Electronics: an Initial Exploration," *Ellen MacArthur Found.*, pp. 1–17, 2018.

[3]   V. Forti, C. P. Baldé, R. Kuehr, and G. Bel, *The Global E-waste Monitor 2020: Quantities, Flows, and the Circular Economy Potential*. 2020.

[4]   M. Irimia-Vladu, "'Green' electronics: biodegradable and biocompatible materials and devices for sustainable future," *Chem. Soc. Rev.*, vol. 43, no. 2, pp. 588–610, 2014.

[5]   M. Irimia-Vladu, E. D. Glowacki, N. S. Sariciftci, and S. Bauer, *Green Materials for Electronics*. Wiley-VCH, Weinheim, Germany, 2018.

[6]   E. Davies, "Endangered Elements: Critical Thinking.," 2011.

[7]   J. P. de Cuéllar, "Report of the World Commission on Environment and Development: Our Common Future.," United Nations University, Oxford, UK, 1987.

[8]   H. Zhao *et al.*, "A New Circular Vision for Electronics Time for a Global Reboot," *World Econ. Forum*, no. January, pp. 1–24, 2019.

[9]   G. Malliaras and R. Friend, "An organic electronics primer," *Phys. Today*, vol. 58, no. 5, pp. 53–58, 2005.

[10]   M. Irimia-Vladu *et al.*, "Stability of Selected Hydrogen Bonded Semiconductors in Organic Electronic Devices," *Chem. Mater.*, vol. 31, no. 17, pp. 6315–6346, 2019.

[11]   A. Facchetti, "Semiconductors for organic transistors," *Mater. Today*, vol. 10, no. 3, pp. 28–37, 2007.

[12]   A. Facchetti, "π-Conjugated polymers for organic electronics and photovoltaic cell applications," *Chem. Mater.*, vol. 23, no. 3, pp. 733–758, 2011.

[13]   N. Thejo Kalyani and S. J. Dhoble, "Organic light emitting diodes: Energy saving lighting technology - A review," *Renew. Sustain. Energy Rev.*, vol. 16, no. 5, pp. 2696–2723, 2012.

[14]   J. J. Langer, E. Frąckowiak, and S. Golczak, "Electrically induced light emission from proton-conducting materials. Protonic light-emitting diodes," *J. Mater. Chem. C*, vol. 8, no. 3, pp. 943–951, 2020.

[15]   Y. Deng *et al.*, "H$^+$-type and OH$^-$-type biological protonic semiconductors and complementary devices," *Sci. Rep.*, vol. 3, no. 2481, pp. 1–7, 2013.

[16]   P. Meredith, C. J. Bettinger, M. Irimia-Vladu, A.B. Mostert, and P. E. Schwenn, "Electronic and optoelectronic materials and devices inspired by nature," *Reports Prog. Phys.*, vol. 76, no. 3, pp. 034501–034537, 2013.

[17]   W. Lin, W. P., Liu, S. J., Gong, T., Zhao, Q. , Huang, "Polymer-Based Resistive Memory Materials and Devices," *Adv. Mater.*, vol. 26, pp. 570–606, 2014.

[18]   S. Pradhan, A. K. Brooks, and V. K. Yadavalli, "Nature-derived materials for the fabrication of functional biodevices," *Mater. Today Bio*, vol. 7, no. June, p. 100065, 2020.

[19]   M. Wang, P. Baek, A. Akbarinejad, D. Barker, and J. Travas-Sejdic, "Conjugated polymers and composites for stretchable organic electronics," *J. Mater. Chem. C*, vol. 7, no. 19, pp. 5534–5552, 2019.

[20]   G. Nisato, D. Lupo, and S. Ganz, *Organic and Printed Electronics*, 2016.

[21]   S. Dubey and A. Roulin, "Evolutionary and biomedical consequences of internal melanins," *Pigment Cell Melanoma Res.*, vol. 27, no. 3, pp. 327–338, 2014.

[22]   M. L. Tran, B. J. Powell, and P. Meredith, "Chemical and structural disorder in eumelanins: A possible explanation for broadband absorbance," *Biophys. J.*, vol. 90, no. 3, pp. 743–752, 2006.

[23]   P. Meredith and T. Sarna, "The physical and chemical properties of eumelanin," *Pigment Cell Res.*, vol. 19, pp. 572–594, 2006.

[24]   M. R. Chedekel, B. L. Murr, and L. Zeise, "Melanin Standard Method: Empirical Formula," *Pigment Cell Res.*, vol. 5, no. 3, pp. 143–147, 1992.

[25]   P. Kumar *et al.*, "Melanin-based flexible supercapacitors," *J. Mater. Chem. C*, vol. 4, no. 40, pp. 9516–9525, 2016.

[26]   R. Kautz, D. D. Ordinario, V. Tyagi, P. Patel, T. N. Nguyen, and A. A. Gorodetsky,

"Cephalopod-Derived Biopolymers for Ionic and Protonic Transistors," *Adv. Mater.*, vol. 30, no. 19, pp. 1–15, 2018.

[27]   M. Sheliakina, A.B. Mostert, P. Meredith, "An all-solid-state biocompatible ion-to-electron transducer for bioelectronics," *Mater. Horizons*, vol. 5, no. 2, pp. 256–263, 2018.

[28]   E. Vahidzadeh, A. P. Kalra, and K. Shankar, "Melanin-based electronics: From proton conductors to photovoltaics and beyond," *Biosens. Bioelectron.*, vol. 122, pp. 127–139, 2018.

[29]   A. Antidormi, C. Melis, E. Canadell, and L. Colombo, "Assessing the Performance of Eumelanin/Si Interface for Photovoltaic Applications," *J. Phys. Chem. C*, vol. 121, no. 21, pp. 11576–11584, 2017.

[30]   G. Mula, L. Manca, S. Setzu, and A. Pezzella, "Photovoltaic properties of PSi impregnated with eumelanin," *Nanoscale Res. Lett.*, vol. 7, no. 1, p. 377, 2012.

[31]   H. J. Nam, J. Cha, S. H. Lee, W. J. Yoo, and D. Y. Jung, "A new mussel-inspired polydopamine phototransistor with high photosensitivity: Signal amplification and light-controlled switching properties," *Chem. Commun.*, vol. 50, no. 12, pp. 1458–1461, 2014.

[32]   R. Xu, A. Gouda, M. F. Caso, F. Soavi, and C. Santato, "Melanin: A Greener Route To Enhance Energy Storage under Solar Light," *ACS Omega*, vol. 4, no. 7, pp. 12244–12251, 2019.

[33]   A. B. Mostert, "Melanin , the What , the Why and the How : An Introductory Review for Materials Scientists Interested in Flexible and Versatile Polymers," *Polymers (Basel).*, vol. 13, p. 1670, 2021.

[34]   M. Reali and C. Santato, "Eumelanin: semiconductor, protonic conductor or mixed electronic-ionic conductor?," in *Handbook of Nanoengineering, Quantum Science and Nanotechnology*, 1st ed., S. E. Lyshevski, Ed. CRC Press, 2019, pp. 101–113.

[35]   E. Di Mauro, R. Xu, G. Soliveri, and C. Santato, "Natural melanin pigments and their interfaces with metal ions and oxides: Emerging concepts and technologies," *MRS Commun.*, vol. 7, pp. 141–151, 2017.

[36]   A. Pezzella *et al.*, "Stem cell-compatible eumelanin biointerface fabricated by chemically

controlled solid state polymerization," *Mater. Horizons*, vol. 2, no. 2, pp. 212–220, 2015.

[37]   J. McGinness, P. Corry, and P. Proctor, "Amorphous Semiconductor Switching in Melanins," *Science*, vol. 183, no. 4127, pp. 853–855, 1974.

[38]   H. Fritzsche, "Switching and Memory in Amorphous Semiconductors," in *Amorphous and Liquid Semiconductors*, J. Tauc, Ed. London and New York: Plenum Press, 1974, pp. 313–355.

[39]   J. Tauc, "Optical Properties of Amorphous Semiconductors" in *Amorphous and Liquid Semiconductors*, J. Tauc, Ed. London and New York: Plenum Press, 1974, pp. 159–214.

[40]   D. Kaplan, T., Adler, "Electrothermal switching in amorphous semiconductors," *J. Non. Cryst. Solids*, vol. 8, pp. 538–543, 1972.

[41]   A. B. Mostert, K. J. P. Davy, J. L. Ruggles, B. J. Powell, I. R. Gentle, and P. Meredith, "Gaseous adsorption in melanins: Hydrophilic biomacromolecules with high electrical conductivities," *Langmuir*, vol. 26, no. 1, pp. 412–416, 2010.

[42]   A. B. Mostert *et al.*, "Role of semiconductivity and ion transport in the electrical conduction of melanin," *Proc. Natl. Acad. Sci.*, vol. 109, no. 23, pp. 8943–8947, 2012.

[43]   A. B. Mostert, B. J. Powell, I. R. Gentle, and P. Meredith, "On the origin of electrical conductivity in the bio-electronic material melanin," *Appl. Phys. Lett*, vol. 100, no. 093701, pp. 1–3, 2012.

[44]   M. Sheliakina, A. B. Mostert, and P. Meredith, "Decoupling Ionic and Electronic Currents in Melanin," *Advanced Functional Materials*, p. 1805514, 2018.

[45]   A. B. Mostert, S. B. Rienecker, C. Noble, G. R. Hanson, and P. Meredith, "The photoreactive free radical in eumelanin," *Sci. Adv.*, vol. 4, no. 3, pp. 1–6, 2018.

[46]   M. Reali, P. Saini, and C. Santato, "Electronic and protonic transport in bio-sourced materials: a new perspective on semiconductivity," *Mater. Adv.*, vol. 2, no. 1, pp. 15–31, 2020.

[47]   M. D'Ischia *et al.*, "Melanins and melanogenesis: Methods, standards, protocols," *Pigment Cell and Melanoma Research*. pp. 616–633, 2013.

[48]   G. Prota, "The chemistry of melanins and melanogenesis.," *Prog. Chem. Org. Nat. Prod.*,

vol. 64, pp. 93–148, 1995.

[49] J. J. Berzelius, *Lehrbuch der Chemie,* 1837.

[50] R. A. Nicolaus, *Melanins*. Paris, FR: Hermann, 1969.

[51] M. D'Ischia *et al.*, "Melanins and melanogenesis: From pigment cells to human health and technological applications," *Pigment Cell Melanoma Res.*, vol. 28, no. 5, pp. 520–544, 2015.

[52] W. D. Bush *et al.*, "The surface oxidation potential of human neuromelanin reveals a spherical architecture with a pheomelanin core and a eumelanin surface," *Proc. Natl. Acad. Sci.*, vol. 103, no. 40, pp. 14785–14789, 2006.

[53] H. Fedorow, F. Tribl, G. Halliday, M. Gerlach, P. Riederer, and K. L. Double, "Neuromelanin in human dopamine neurons: Comparison with peripheral melanins and relevance to Parkinson's disease," *Prog. Neurobiol.*, vol. 75, no. 2, pp. 109–124, 2005.

[54] D. N. Peles and J. D. Simon, "The UV-absorption spectrum of human iridal Melanosomes: a new perspective on the relative absorption of eumelanin and pheomelanin and its consequences.," *Photochem. Photobiol.*, vol. 88, pp. 1378–1384, 2012.

[55] A. Biesemeier, U. Schaermeyer, and O. Eible, "Chemical composition of melanosomes, lipofuscin and melanolipofuscin granules of human RPE tissues. 93,29–39.," *Exp. Eye Res.*, vol. 93, pp. 29–39, 2011.

[56] S. Murillo-Cuesta *et al.*, "Melanin precursors prevent premature age-related and noise-induced hearing loss in albino mice.," *Pigment Cell Melanoma Res.*, vol. 23, pp. 72–83, 2010.

[57] G. R. Bortolotti, "Natural selection and coloration: protection, concealment, advertisement, or deception?," in *Bird Coloration, Volume II: Function and Evolution*, G. E. Hill and K. J. McGraw, Eds. Cambridge, MS: Harvard University Press, 2006, pp. 3–35.

[58] R. H. C. Bonser, "Melanin and the abrasion resistance of feathers.," *Condor*, vol. 97, pp. 590–591, 1995.

[59] R. W. Schreiber, E. Schreiber, A. M. Peele, and E. H. J. Burtt, "Pattern of damage to albino Great Frigatebird flight feathers supports hypothesis of abrasion by airborne

particles.," *Condor*, vol. 108, pp. 736–741, 2006.

[60] A. Palumbo, "Melanogenesis in the ink gland of Sepia officinalis.," *Pigment Cell Res.*, vol. 16, pp. 517–522, 2003.

[61] K. D. Clark and M. R. Strand, "Hemolymph melanization in the silkmoth bombyx mori involves formation of a high molecular mass complex that metabolizes tyrosine.," *J. Biol. Chem.*, vol. 288, pp. 14476–14487, 2013.

[62] E. Dadachova and A. Casadevall, "Ionizing radiation: how fungi cope, adapt, and exploit with the help of melanin," *Curr. Opin. Microbiol.*, vol. 11, no. 6, pp. 525–531, 2008.

[63] G. Prota, "Melanins, Melanogenesis and Melanocytes: Looking at Their Functional Significance from the Chemist's Viewpoint," *Pigment Cell Res.*, vol. 13, no. 4, pp. 283–293, 2000.

[64] Y. Liu and J. D. Simon, "The effect of preparation procedures on the morphology of melanin from the ink sac of Sepia officinalis.," *Pigment Cell Res.*, vol. 16, pp. 72–80, 2003.

[65] E. Di Mauro, D. Rho, and C. Santato, "Biodegradation of bio-sourced and synthetic organic electronic materials towards green organic electronics," *Nat. Commun.*, vol. 12, no. 1, pp. 1–10, 2021.

[66] M. Magarelli, P. Passamonti, and C. Renieri, "Purification , characterization and analysis of sepia melanin from commercial sepia ink (Sepia Officinalis)," *Rev. CES Med. Vet. y Zootec.*, vol. 5(2), pp. 18–28, 2010.

[67] M. Araujo, J. R. Xavier, C. D. Nunes, P. D. Vaz, and M. Humanes, "Marine sponge melanin: A new source of an old biopolymer," *Struct. Chem.*, vol. 23, no. 1, pp. 115–122, 2012.

[68] A. Pezzella, D. Vogna, and G. Prota, "Atropoisomeric melanin intermediates by oxidation of the melanogenic precursor 5,6-dihydroxyindole-2-carboxylic acid under biomimetic conditions.," *Tetrahedron*, vol. 58, no. 19, pp. 3681–3687, 2002.

[69] S. Ito and K. Wakamatsu, "Chemistry of mixed melanogenesis - Pivotal roles of dopaquinone," *Photochem. Photobiol.*, vol. 84, no. 3, pp. 582–592, 2008.

[70] E. V. Gan, H. F. Haberman, and I. A. Menon, "Electron transfer properties of melanin," *Arch. Biochem. Biophys.*, vol. 173, no. 2, pp. 666–672, 1973.

[71] F. H. J. Figge, "Melanin: A Natural Reversible Oxidation-Reduction System and Indicator," *Exp. Biol. Med.*, vol. 41, p. 127, 1939.

[72] M. Reali *et al.*, "Electronic Transport in the Biopigment Sepia Melanin," *ACS Appl. Bio Mater.*, vol. 3, no. 8, pp. 5244–5252, 2020.

[73] V. Capozzi *et al.*, "Optical and photoelectronic properties of melanin," *Thin Solid Films*, vol. 511–512, pp. 362–366, 2006.

[74] J. Cheng, S. C. Moss, and M. Eisner, "X-Ray Characterization of Melanins—I," *Pigment Cell Res.*, vol. 7, no. 4, pp. 263–273, 1994.

[75] J. Cheng, S. C. Moss, M. Eisner, and P. Zschack, "X-Ray Characterization of Melanins-II," *Pigment Cell Res.*, vol. 7, pp. 255–262, 1994.

[76] A. Napolitano, A. Pezzella, and G. Prota, "A Reassessment of the Structure of 5,6-Dihydroxyindole-2-carboxylic Acid Melanins by Matrix-assisted Laser Desorption/Ionization Mass Spectrometry.," *Rapid Comm. Mass Spectr.*, vol. 10, pp. 204–208, 1996.

[77] A. Napolitano, A. Pezzella, and G. Prota, "Structural Analysis of Synthetic Melanins from 5,6-Dihydroxyindole by Matrix-Assisted Laser Desortion/Ionization Mass Spectroscopy.," *Rapid Comm. Mass Spectr.*, vol. 10, pp. 468–472, 1996.

[78] A. Pezzella, A. Napolitano, M. D'Ischia, G. Prota, R. Seraglia, and P. Traldi, "Identification of Partially Degraded Oligomers of 5,6-Dihydroxyindole-2-carboxylic Acid in Sepia Melanin by Matrix-assisted Laser Desorption/Ionization Mass Spectrometry.," *Rapid Comm. Mass Spectr.*, vol. 11, pp. 368–372, 1997.

[79] M. L. Alfieri *et al.*, "Structural Basis of Polydopamine Film Formation: Probing 5,6-Dihydroxyindole-Based Eumelanin Type Units and the Porphyrin Issue.," *ACS Appl. Mater. Interfaces*, vol. 10, pp. 7670–7680, 2018.

[80] S. Reale, M. Crucianelli, A. Pezzella, M. D'Ischia, and F. De Angelis, "Exploring the frontiers of synthethic eumelanin polymers by high-resolution matrix-assisted

laser/desorption ionization mass spectrometry.," *J. Mass Spectrom.*, vol. 47, pp. 49–53, 2012.

[81] Y. Liu and J. D. Simon, "Isolation of Biophysical Studies of Natural Eumelanins: Application of Imaging Technologies and Ultrafast Spectroscopy.," *Pigment Cell Res.*, vol. 16, no. 6, pp. 608–618, 2003.

[82] Y. Liu and J. D. Simon, "Metal-ion interactions and the structural organization of Sepia eumelanin," *Pigment Cell Res.*, vol. 18, no. 1, pp. 42–48, 2005.

[83] F. De Marchi *et al.*, "Self-assembly of 5,6-dihydroxyindole-2-carboxylic acid: Polymorphism of a eumelanin building block on Au(111)," *Nanoscale*, vol. 11, no. 12, pp. 5422–5428, Mar. 2019.

[84] C. Grieco, F. R. Kohl, A. T. Hanes, and B. Kohler, "Probing the heterogeneous structure of eumelanin using ultrafast vibrational fingerprinting," *Nat. Commun.*, vol. 11, no. 1, pp. 1–9, 2020.

[85] M. Xiao, W. Chen, W. Li, J. Zhao, and Y. Hong, "Elucidation of the hierarchical structure of natural eumelanins," *J. R. Soc. Interface*, vol. 15, pp. 1–10, 2018.

[86] M. Arzillo *et al.*, "Eumelanin buildup on the nanoscale: Aggregate growth/assembly and visible absorption development in biomimetic 5,6-dihydroxyindole polymerization.," *Biomacromolecules*, vol. 13, no. 8, pp. 2379–2390, 2012.

[87] A. Antidormi, C. Melis, E. Canadell, and L. Colombo, "Understanding the Polymerization Process of Eumelanin by Computer Simulations," *J. Phys. Chem. C*, vol. 122, no. 49, pp. 28368–28374, 2018.

[88] S. Meng and E. Kaxiras, "Theoretical models of eumelanin protomolecules and their optical properties," *Biophys. J.*, vol. 94, no. 6, pp. 2095–2105, 2008.

[89] K. B. Stark *et al.*, "Effect of stacking and redox state on optical absorption spectra of melanins-comparison of theoretical and experimental results," *J. Phys. Chem. B*, vol. 109, no. 5, pp. 1970–1977, 2005.

[90] K. B. Stark, J. M. Gallas, G. W. Zajac, M. Eisner, and J. T. Golab, "Spectroscopic study and simulation from recent structural models for eumelanin: I. Monomer, dimers," *J. Phys.*

Chem. B, vol. 107, no. 13, pp. 3061–3067, 2003.

[91] A. Büngeler, B. Hämisch, K. Huber, W. Bremser, and O. I. Strube, "Insight into the Final Step of the Supramolecular Buildup of Eumelanin," *Langmuir*, vol. 33, no. 27, pp. 6895–6901, 2017.

[92] M. D'Ischia, A. Napolitano, A. Pezzella, P. Meredith, and T. Sarna, "Chemical and structural diversity in eumelanins: Unexplored bio-optoelectronic materials," *Angew. Chemie - Int. Ed.*, vol. 48, pp. 3914–3921, 2009.

[93] L. Panzella *et al.*, "Atypical Structural and π-Electron Features of a Melanin Polymer That Lead to Superior Free-Radical-Scavenging Properties," *Angew. Chemie - Int. Ed.*, vol. 52, no. 48, pp. 1–5, 2013.

[94] C. M. R. Clancy and J. D. Simon, "Ultrastructural organization of eumelanin from Sepia officinalis measured by atomic force microscopy," *Biochemistry*, vol. 40, no. 44, pp. 13353–13360, 2001.

[95] E. Molteni, G. Cappellini, G. Onida, and G. Mula, "Extensive stacking of DHI-like monomers as a model of out-of-plane complexity in eumelanin protomolecules: Chemical and structural sensitivity of optical absorption spectra," *Chem. Phys.*, vol. 524, no. February, pp. 92–100, 2019.

[96] M. d'Ischia, A. Napolitano, A. Pezzella, P. Meredith, and M. Buehler, "Melanin Biopolymers: Tailoring Chemical Complexity for Materials Design," *Angew. Chemie - Int. Ed.*, vol. 59, no. 28, pp. 11196–11205, 2020.

[97] L. Ascione, A. Pezzella, V. Ambrogi, C. Carfagna, and M. D'Ischia, "Intermolecular π-electron perturbations generate extrinsic visible contributions to eumelanin black chromophore in model polymers with interrupted interring conjugation," *Photochem. Photobiol.*, vol. 89, no. 2, pp. 314–318, 2013.

[98] P. Meredith, B. J. Powell, J. Riesz, S. P. Nighswander-Rempel, M. R. Pederson, and E. G. Moore, "Towards Structure-Property-Function Relationships for Eumelanin," *Soft Matter*, vol. 2, no. 1, pp. 37–44, 2006.

[99] A. Pezzella, M. D'Ischia, A. Napolitano, A. Palumbo, and G. Prota, "An integrated approach to the structure of sepia melanin. Evidence for a high proportion of degraded 5,6-

Dihydroxyindole-2-carboxylic acid units in the pigment backbone," *Tetrahedron*, vol. 53, no. 24, pp. 8281–8286, 1997.

[100] M. D'Ischia, A. Napolitano, and A. Pezzella, "5,6-dihydroxyindole chemistry: Unexplored opportunities beyond eumelanin," *European J. Org. Chem.*, no. 28, pp. 5501–5516, 2011.

[101] P. K. J. P. D. Wanasundara and F. Shahidi, "Antioxidants: Science, Technology, and Applications," in *Bailey's Industrial Oil and Fat Products*, F. Shadidi, Ed. John Wiley & Sons, 2005, pp. 431–432.

[102] Y. J. Kim, W. Wu, S.-E. Chun, J. F. Whitacre, and C. J. Bettinger, "Biologically derived melanin electrodes in aqueous sodium-ion energy storage devices.," *Proc. Natl. Acad. Sci.*, vol. 110, no. 52, pp. 20912–20917, 2013.

[103] D. McNaught and A. Wilkinson, *IUPAC. Compendium of Chemical Terminology*. Oxford, UK: Blackwell Scientific Publications, 2019.

[104] R. Micillo *et al.*, "Eumelanin broadband absorption develops from aggregation-modulated chromophore interactions under structural and redox control," *Sci. Rep.*, vol. 7, no. 1, p. 41532, 2017.

[105] J. Riesz, "The spectroscopic properties of melanin," PhD thesis, University of Queensland, AU, 2007.

[106] I. A. Vitkin, J. Woolsey, B. . Wilson, and R. R. Anderson, "Optical and thermal characterisation of natural (Sepia-officinalis) melanin.," *Photochem. Photobiol.*, vol. 59, pp. 455–462, 1994.

[107] C. T. Chen, C. Chuang, J. Cao, V. Ball, D. Ruch, and M. J. Buehler, "Excitonic effects from geometric order and disorder explain broadband optical absorption in eumelanin," *Nat. Commun.*, vol. 5, no. May, pp. 1–10, 2014.

[108] M. D'Ischia, A. Napolitano, V. Ball, C. T. Chen, and M. J. Buehler, "Polydopamine and eumelanin: from structure-property relationships to a unified tailoring strategy.," *Acc .Chem. Res.*, vol. 47, no. 12, pp. 3541–3550, 2014.

[109] J. M. Gallas and M. Eisner, "Fluorescence of Melanin???Dependence Upon Excitation Wavelength and Concentration," *Photochem. Photobiol.*, vol. 45, no. 5, pp. 595–600,

1987.

[110] A. S. Ito, G. C. Azzellini, S. C. Silva, O. Serra, and A. G. Szabo, "Optical absorption and fluorescence spectroscopy studies of ground state melanin-cationic porphyrins complexes," *Biophys. Chem.*, vol. 45, no. 1, pp. 79–89, 1992.

[111] L. Mosca, C. De Marco, M. Fontana, and M. A. Rosei, "Fluorescence properties of melanins from opioid peptides," *Arch. Biochem. Biophys.*, vol. 371, no. 1, pp. 63–69, 1999.

[112] J. Brian Nofsinger and J. D. Simon, "Radiative Relaxation of Sepia Eumelanin is Affected by Aggregation," *Photochem. Photobiol.*, vol. 74, no. 1, pp. 31–37, 2007.

[113] S. P. Nighswander-Rempel, J. Riesz, J. Gilmore, J. P. Bothma, and P. Meredith, "Quantitative fluorescence excitation spectra of synthetic eumelanin," *J. Phys. Chem. B*, vol. 109, no. 43, pp. 20629–20635, 2005.

[114] S. P. Nighswander-Rempel, J. Riesz, J. Gilmore, and P. Meredith, "A quantum yield map for synthetic eumelanin," *J. Chem. Phys.*, vol. 123, no. 19, 2005.

[115] J. U. Sutter and D. J. S. Birch, "Metal ion influence on eumelanin fluorescence and structure," *Methods Appl. Fluoresc.*, vol. 2, no. 2, pp. 024005–024012, 2014.

[116] S. Meng and E. Kaxiras, "Mechanisms for ultrafast nonradiative relaxation in electronically excited eumelanin constituents," *Biophys. J.*, vol. 95, no. 9, pp. 4396–4402, 2008.

[117] M. Gauden, A. Pezzella, L. Panzella, A. Napolitano, M. D'Ischia, and V. Sundstro, "Ultrafast excited state dynamics of 5,6-dihydroxyindole, a key eumelanin building block: nonradiative decay mechanism," *J. Phys. Chem. B*, vol. 113, no. 37, pp. 12575–12580, 2009.

[118] S. E. Forest, W. C. Lam, D. P. Millar, J. B. Nofsinger, and J. D. Simon, "A Model for the Activated Energy Transfer within Eumelanin Aggregates," *J. Phys. Chem. B*, vol. 104, no. 4, pp. 811–814, 2000.

[119] I. R. Piletic, T. E. Matthews, and W. S. Warren, "Probing near-infrared photorelaxation pathways in eumelanins and pheomelanins.," *J. Phys. Chem. A*, vol. 114, no. 43, pp.

11483–11491, 2010.

[120] B. Larsson and H. Tjälve, "Studies on the melanin-affinity of metal ions.," *Acta Physiol. Scand.*, vol. 104, p. 479, 1978.

[121] S. Chen *et al.*, "Adsorption of Pb(II) and Cd(II) by squid Ommastrephes bartramii melanin.," *Bioinorg. Chem. Appl.*, p. 1, 2009.

[122] L. K. Povlich, J. Le, J. Kim, and D. Martin, "Poly(5,6-dimethoxyindole- 2-carboxylic acid) (PDMICA): a melanin-like polymer with unique electro-chromic and structural properties.," *Macromolecules*, vol. 43, p. 3770, 2010.

[123] L. G. Albano, E. Di Mauro, P. Kumar, F. Cicoira, C. F. Graeff, and C. Santato, "Novel insights on the physicochemical properties of eumelanins and their DMSO derivatives.," *Polym. Int.*, vol. 26, p. 19007, 2016.

[124] L. Hong and J. D. Simon, "Physical and chemical characterization of iris and choroid melanosomes isolated from newborn and mature cows.," *Photochem. Photobiol.*, vol. 81, p. 517, 2007.

[125] L. Hong and J. D. Simon, "Insight into the binding of divalent cations to Sepia eumelanin from IR absorption spectroscopy.," *Photochem. Photobiol.*, vol. 82, p. 1265, 2006.

[126] L. Hong, Y. Liu, and J. D. Simon, "Binding of metal ions to melanin and their effects on the aerobic reactivity.," *Photochem. Photobiol.*, vol. 80, p. 477, 2004.

[127] Y. Liu, L. Hong, V. R. Kempf, K. Wakamatsu, S. Ito, and J. D. Simon, "Ion-exchange and adsorption of Fe(III) by Sepia melanin.," *Pigment Cell Res.*, vol. 17, p. 262, 2004.

[128] W. D. Bush and J. D. Simon, "Quantification of Ca^{2+} binding to melanin supports the hypothesis that melanosomes serve a functional role in regulating calcium homeostasis.," *Pigment Cell Res.*, vol. 20, p. 134, 2007.

[129] J. Borovanský, "Zinc in pigmented cells and structures, interactions and possible roles.," *Sb. Lékasky J.*, vol. 95, p. 309, 1994.

[130] B. Szpoganicz, S. Gidanian, P. Kong, and P. Farmer, "Metal binding by melanins: studies of colloidal dihydroxyindole-melanin, and its complex- ation by Cu(II) and Zn(II) ions. 89, 45 (2002)," *J. Inorg. Biochem.*, vol. 89, p. 45, 2002.

[131] Y. J. Kim, W. Wu, S. E. Chun, J. F. Whitacre, and C. J. Bettinger, "Catechol-mediated reversible binding of multivalent cations in eumelanin half-cells.," *Adv. Mater.*, vol. 26, p. 6572, 2014.

[132] S. Aime, M. Botta, and I. Camurati, "NMR studies of L-dopa melanin- manganese(II) complex in water solution.," *J. Inorg. Biochem.*, vol. 36, p. 1, 1989.

[133] A. Samokhvalov, Y. Liu, and J. D. Simon, "Characterization of the Fe (III)-binding site in Sepia eumelanin by resonance Raman confocal microspectroscopy.,"*Photochem. Photobiol.*, vol. 80, p. 84, 2007.

[134] T. G. Costa, R. Younger, C. Poe, P. J. Farmer, and B. Szpoganicz, "Studies on synthetic and natural melanin and its affinity for Fe(III) ion.," *Bioinorg. Chem. Appl.*, vol. 2012, p. 1, 2012.

[135] L. Klosterman and C. Bettinger, "Calcium-mediated control of polydopamine film oxidation and iron chelation.," *Int. J. Mol. Sci.*, vol. 18, p. 14, 2016.

[136] T. Sarna, W. Froncisz, and J. S. Hyde, "Cu^{2+} probe of metal-ion binding sites in melanin using electron paramagnetic resonance spectroscopy.," *Nat. Melanin Arch. Biochem. Biophys.*, vol. 202, p. 304, 1980.

[137] J. Stainsack, A. S. Mangrich, C. M. B. F. Maia, V. G. Machado, J. C. P. dos Santos, and S. Nakagaki, "Spectroscopic investigation of hard and soft metal binding sites in synthetic melanin.," *Inorg. Chim. Acta*, vol. 356, p. 243, 2003.

[138] A. B. Mostert *et al.*, "Engineering proton conductivity in melanin using metal doping," *J. Mater. Chem. B*, vol. 8, no. 35, pp. 8050–8060, 2020.

[139] R. Xu, C. T. Prontera, E. Di Mauro, A. Pezzella, F. Soavi, and C. Santato, "An electrochemical study of natural and chemically controlled eumelanin," *APL Mater.*, vol. 5, no. 12, Dec. 2017.

[140] R. Xu, F. Soavi, and C. Santato, "An Electrochemical Study on the Effect of Metal Chelation and Reactive Oxygen Species on a Synthetic Neuromelanin Model," *Front. Bioeng. Biotechnol.*, vol. 7, no. October, pp. 1–11, 2019.

[141] M. Kang *et al.*, "Reverse Engineering to Characterize Redox Properties: Revealing

Melanin's Redox Activity through Mediated Electrochemical Probing," *Chem. Mater.*, vol. 30, no. 17, pp. 5814–5826, 2018.

[142] F. Solano, "Photoprotection versus photodamage: updating an old but still unsolved controversy about melanin.," *Polym. Int.*, vol. 65, no. 11, pp. 1276–1287, 2016.

[143] S. E. Forest and J. D. Simon, "Wavelength-dependent Photoacoustic Calorimetry Study of Melanin," *Photochem. Photobiol.*, vol. 68, no. 3, pp. 296–298, 1998.

[144] I. A. Menon and H. F. Haberman, "Mechanisms of action of melanins.," *Br. J. Dermatol.*, vol. 97, no. 1, pp. 109–112, 1977.

[145] G. Szewczyk, A. Zadlo, M. Sarna, S. Ito, K. Wakamatsu, and T. Sarna, "Aerobic photoreactivity of synthetic eumelanins and pheomelanins: generation of singlet oxygen and superoxide anion," *Pigment Cell Melanoma Res.*, vol. 29, no. 6, pp. 669–678, 2016.

[146] S. Ito, M. Kikuta, S. Koike, M. Szewczyk, Grzegorz, Sarna, A. Zadlo, and K. Sarna, Tadeusz Wakamatsu, "Roles of reactive oxygen species in UVA-induced oxidation of 5,6-dihydroxyindole-2-carboxylic acid-melanin as studied by differential spectrophotometric method.," *Pigment Cell Melanoma Res.*, vol. 29, no. 3, pp. 340–351, 2016.

[147] S. Ito, K. Wakamatsu, and T. Sarna, "Photodegradation of Eumelanin and Pheomelanin and Its Pathophysiological Implications.," *Photochem. Photobiol.*, vol. 94, no. 3, pp. 409–420, 2018.

[148] T. Herrling, K. Jung, and J. Fuchs, "The role of melanin as protector against free radicals in skin and its role as free radical indicator in hair.," *Spectrochim. Acta - Part A Mol. Biomol. Spectrosc.*, vol. 69, no. 5, pp. 1429–1435, 2008.

[149] J. B. Nofsinger, Y. Liu, and J. D. Simon, "Aggregation of eumelanin mitigates photogeneration of ROS.," *Free Rad. Biol. Med.*, vol. 32, no. 8, pp. 720–730, 2002.

[150] T. Cecchi *et al.*, "On the antioxidant activity of eumelanin biopigments: a quantitative comparison between free radical scavenging and redox properties," *Nat. Prod. Res.*, vol. 34, no. 17, pp. 2465–2473, 2020.

[151] F. Agapito and B. J. Costa Cabral, "Energetics of radical formation in eumelanin building blocks: Implications for understanding photoprotection mechanisms in eumelanin," *J.*

Phys. Chem. A, vol. 120, no. 50, pp. 10018–10022, 2016.

[152] L. Marcocci, J. J. Maguire, M. T. Droy-Lefaix, and L. Packer, "The nitric oxide-scavenging properties of Ginkgo biloba extract EGb 761," *Biochemical and Biophysical Research Communications*, vol. 201, no. 2. pp. 748–755, 1994.

[153] P. Goupy, C. Dufour, M. Loonis, and O. Dangles, "Quantitative kinetic analysis of hydrogen transfer reactions from dietary polyphenols to the DPPH radical," *J. Agric. Food Chem.*, vol. 51, no. 3, pp. 615–622, 2003.

[154] R. Re, N. Pellegrini, A. Proteggente, A. Pannala, M. Yang, and C. Rice-Evans, "Antioxidant activity applying an improved ABTS radical cation decolorization assay," *Free Radic. Biol. Med.*, vol. 26, no. 2007, pp. 1231–1237, 1999.

[155] R. C. Sealy, "Free radicals in melanin formation, structure and reactions.," in *In Free radicals in molecular biology, aging and diseases*, A. Armstrong, R. S. Sohal, R. G. Cutler, and T. F. Slater, Eds. New York, NY: Raven Press, 1980, pp. 67–75.

[156] T. Sarna and H. M. Swartz, "Interaction of melanin with oxygen (and related species).," in *Atmospheric Oxidation and Antioxidants*, G. Scott, Ed. Amsterdam: Elsevier, 1993, pp. 129–169.

[157] S. S. Chio, J. S. Hyde, and R. C. Sealy, "Paramagnetism in melanins; pH dependence.," *Arch. Biochem. Biophys.*, vol. 215, pp. 100– 106, 1982.

[158] A. B. Mostert, "On the free radical redox chemistry of 5,6-dihydroxyindole," *Chem. Phys.*, vol. 546, no. November 2020, p. 111158, 2021.

[159] S. S. Chio, J. S. Hyde, and R. C. Sealy, "Temperature-dependent paramagnetism in melanin polymers.," *Arch. Biochem. Biophys.*, vol. 199, pp. 133–139, 1980.

[160] K. J. Reszka, Z. Matuszak, and C. F. Chignell, "Lactoperoxidase-catalyzed oxidation of melanin by reactive nitrogen species derived from nitrite: an EPR study.," *Free Radic. Biol. Med.*, vol. 25, pp. 208–216, 1998.

[161] C. C. Felix, J. S. Hyde, and R. C. Sealy, "Photoreactions of melanin: a new transient species and evidence for triplet state involvement.," *Biochem. Biophys. Res. Commun.*, vol. 88, pp. 456–461, 1979.

[162] C. C. Felix, J. S. Hyde, T. Sarna, and R. C. Sealy, "Interactions of Melanin with Metal Ions. Electron Spin Resonance Evidence for Chelate Complexes of Metal Ions with Free Radicals," *J. Am. Chem. Soc.*, vol. 100, no. 12, pp. 3922–3926, 1978.

[163] R. C. Sealy *et al.*, "Novel free radical in synthetic and natural pheomelanins: distinction between dopa melanins and cysteinyldopa melanins by ESR spectroscopy.," *Proc. Natl. Acad. Sci.*, vol. 79, pp. 2885–2889, 1982.

[164] R. C. Sealy, J. S. Hyde, C. C. Felix, L. A. Menon, and G. Prota, "Eumelanins and pheomelanins: characterization by electron spin resonance spectroscopy.," *Science*, vol. 217, pp. 545–547, 1982.

[165] M. Blois, A. Zahlan, and J. Maling, "Electron spin resonance studies on melanin.," *Biophys. J.*, vol. 4, no. 6, pp. 471–490, 1964.

[166] P. Meredith, K. Tandy, and A. B. Mostert, "A Hybrid Ionic-Electronic Conductor: Melanin, the First Organic Amorphous Semiconductor?," in *Organic Electronics: Emerging Concepts and Technologies*, 2013.

[167] M. Rozanowska, T. Sarna, E. J. Land, and T. G. Truscott, "Free radical scavenging properties of melanin: interaction of eu- and pheo-melanin models with reducing and oxidising radicals.," *Free Radic. Biol. Med.*, vol. 26, pp. 518–525, 1999.

[168] C. L. Serpentini, C. Gauchet, D. de Montauzon, M. Comtat, J. Ginestar, and N. Paillous, "First electrochemical investi- gation of the redox properties of DOPA-melanin by means of carbon paste electrode.," *Electrochem. Acta*, vol. 45, pp. 1663–1668, 2000.

[169] Gidanian, S. and P. J. Farmer, "Redox behavior of melanins: direct electrochemistry of dihydroxyindole-melanin and its Cu and Zn adducts.," *J. Inorg. Biochem.*, vol. 89, pp. 54–60, 2002.

[170] G. M. Robinson, E. I. Iwuoha, and M. R. Smyth, "Characterisation of electrosynthetic L-dopamelanin films by electrochemical and spectroelectrochemical techniques.," *Electrochim. Acta*, vol. 43, no. 23, pp. 3489–3496, 1998.

[171] V. Horak and G. Weeks, "Poly (5, 6-dihydroxyindole) melanin film electrode.," *Bioorg.Chem.*, vol. 21, no. 1, pp. 24–33, 1993.

[172] A. J. Clulow *et al.*, "The structural impact of water sorption on device-quality melanin thin films," *Soft Matter*, vol. 13, no. 21, pp. 3954–3965, 2017.

[173] A. D. G. Albanese, M.G. Bridelli, "Structural Dynamics of Melanins Investigated by Rayleigh Scattering of Mossbauer Radiation," *Biopolymers*, vol. 23, pp. 1481–1498, 1984.

[174] J. A. Martinez-Gonzales, H. Cavaye, J. D. Mcgettrick, P. Meredith, K. A. Motovilov, and A. B. Mostert, "Interfacial water morphology in hydrated melanin.," *Soft Matter*, vol. 17, pp. 7940–7952, 2021.

[175] J. P. Luther and H. Lipke, "Degradation of melanin by Aspergillus fumigatus.," *Appl. Environ. Microbiol.*, vol. 40, no. 1, pp. 145–155, 1980.

[176] M. Mohorčič, J. Friedrich, I. Renimel, P. André, D. Mandin, and J.-P. Chaumont, "Production of melanin bleaching enzyme of fungal origin and its application in cosmetics.," *Biotechnol. Bioprocess Eng.*, vol. 12, no. 3, pp. 200–206, 2007.

[177] A. S. Wilson, H. I. Dodson, R. C. Janaway, A. M. Pollard, and D. J. Tobin, "Selective biodegradation in hair shafts derived from archaeological, forensic and experimental contexts.," *Br. J. Dermatol.*, vol. 157, no. 3, pp. 450–457, 2007.

[178] M. Kuo and M. Alexander, "'Inhibition of the Lysis of Fungi by Melanins.," *J. Bacteriol.*, vol. 94, no. 3, pp. 624–629, 1967.

[179] A. El Nahhas, T. Pascher, L. Leone, L. Panzella, A. Napolitano, and V. Sundström, "Photochemistry of pheomelanin building blocks and model chromophores: Excited-state intra- and intermolecular proton transfer," *J. Phys. Chem. Lett.*, vol. 5, no. 12, pp. 2094–2100, 2014.

[180] J. M. Fearnley and A. J. Lees, "Ageing and Parkinson's Disease: Substantia Nigra Regional Selectivity.," *Brain*, vol. 144, pp. 2283–2301, 1991.

[181] F. A. Zucca *et al.*, "Interactions of iron, dopamine and neuromelanin pathways in brain aging and Parkinson's disease," *Prog. Neurobiol.*, vol. 155, pp. 96–119, 2017.

[182] S. N. Dezidério, C. A. Brunello, M. I. N. Da Silva, M. A. Cotta, and C. F. O. Graeff, "Thin films of synthetic melanin," *J. Non. Cryst. Solids*, vol. 338–340, no. 1 SPEC. ISS., pp. 634–638, 2004.

[183] M. I. N. Da Silva, S. N. Dezidério, J. C. Gonzalez, C. F. O. Graeff, and M. A. Cotta, "Synthetic melanin thin films: Structural and electrical properties," *J. Appl. Phys.*, vol. 96, no. 10, pp. 5803–5807, 2004.

[184] E. S. Bronze-Uhle, A. Batagin-Neto, P. H. P. Xavier, N. I. Fernandes, E. R. De Azevedo, and C. F. O. Graeff, "Synthesis and characterization of melanin in DMSO," *J. Mol. Struct.*, vol. 1047, pp. 102–108, 2013.

[185] C. J. Bettinger, J. P. Bruggeman, A. Misra, J. T. Borenstein, and R. Langer, "Biocompatibility of biodegradable semiconducting melanin films for nerve tissue engineering," *Biomaterials*, vol. 30, no. 17, pp. 3050–3057, 2009.

[186] J. Wünsche, F. Cicoira, C. F. O. Graeff, and C. Santato, "Eumelanin thin films: solution-processing, growth, and charge transport properties," *J. Mater. Chem. B*, vol. 1, no. 31, pp. 3836–3842, 2013.

[187] A. Pezzella *et al.*, "Spontaneous wrinkle emergence in nascent eumelanin thin films," *Soft Matter*, pp. 9261–9270, 2019.

[188] J. P. Bothma, J. De Boor, U. Divakar, P. E. Schwenn, and P. Meredith, "Device-quality electrically conducting melanin thin films," *Adv. Mater.*, vol. 20, no. 18, pp. 3539–3542, 2008.

[189] M. Abbas *et al.*, "Structural, electrical, electronic and optical properties of melanin films," *Eur. Phys. J. E*, 2009.

[190] M. Abbas *et al.*, "Control of structural, electronic, and optical properties of eumelanin films by electrospray deposition," *J. Phys. Chem. B*, vol. 115, no. 38, pp. 11199–11207, 2011.

[191] F. Bloisi, A. Pezzella, M. Barra, F. Chiarella, A. Cassinese, and L. Vicari, "Matrix assisted pulsed laser deposition of melanin thin films," *J. Appl. Phys.*, vol. 110, no. 2, pp. 8–11, 2011.

[192] F. Bloisi *et al.*, "Effect of substrate temperature on MAPLE deposition of synthetic eumelanin films," *Appl. Phys. A Mater. Sci. Process.*, vol. 105, no. 3, pp. 619–627, 2011.

[193] P. Díaz *et al.*, "Electrochemical self-assembly of melanin films on gold," *Langmuir*, vol.

21, no. 13, pp. 5924–5930, 2005.

[194] S. Subianto, G. Will, and P. Meredith, "Electrochemical synthesis of melanin free-standing films," *Polymer (Guildf).*, vol. 46, no. 25, pp. 11505–11509, 2005.

[195] P. Borghetti *et al.*, "Effects of potassium on the supramolecular structure and electronic properties of eumelanin thin films," *Langmuir*, vol. 26, no. 24, pp. 19007–19013, 2010.

[196] N. W. Ashcroft and N. D. Mermin, *Solid State Physics*. Hartcourt College Publishers, 1976.

[197] G. Grosso and G. P. Parravicini, *Solid State Physics*, Second. Oxford, UK: Elsevier, 2014.

[198] C. Kittel, *Introduction to Solid State Physics*, Eight. Wiley J. and Sons Inc., 2005.

[199] R. Noriega *et al.*, "A general relationship between disorder, aggregation and charge transport in conjugated polymers," *Nat. Mater.*, vol. 12, no. 11, pp. 1038–1044, 2013.

[200] A. Salleo, "Electronic Traps in Organic Semiconductors, Ch. 14," in *Organic Electronics: Emerging Concepts and Technology*, C. Cicoira, F., Santato, Ed. Wiley-VCH, 2013, pp. 341–373.

[201] E. A. Davis and N. F. Mott, "Conduction in non-crystalline systems V. Conductivity, optical absorption and photoconductivity in amorphous semiconductors," *Philos. Mag.*, vol. 22, no. 179, pp. 0903–0922, 1970.

[202] M. F. Thorpe and D. Weaire, "Electronic Density of States of Amorphous Si and Ge," *Phys. Rev. Lett.*, vol. 27, pp. 1581–1584, 1971.

[203] M. R. Powell and B. Rosenberg, "The Nature of the Charge Carriers in Solvated Biomacromolecules," *Bioenergetics*, vol. 1, no. 6, pp. 493–509, Nov. 1970.

[204] B. Rosenberg, "Electrical Conductivity of Proteins," *Nature*, vol. 193, no. 4813, pp. 364–365, 1962.

[205] B. Rosenberg, "Electrical conductivity of proteins. II. Semiconduction in crystalline bovine hemoglobin," *J. Chem. Phys.*, vol. 36, no. 3, pp. 816–823, 1962.

[206] D. D. Eley and D. I. Spivey, "Semiconductivity of organic substances. Part 9. - Nucleic Acid in the Dry State," *Trans. Faraday Soc.*, vol. 58, pp. 411–415, 1961.

[207] B. Giese, J. Amaudrut, A. K. Köhler, M. Spormann, and S. Wessely, "Direct observation of hole transfer through DNA by hopping between adenine bases and by tunnelling," *Nature*, vol. 412, no. 6844, pp. 318–320, 2001.

[208] N. P. Armitage, M. Briman, and G. Grüner, "Charge transfer and charge transport on the double helix," *Phys. Status Solidi*, vol. 241, no. 1, pp. 69–75, 2004.

[209] C. H. Wohlgamuth, M. A. McWilliams, and J. D. Slinker, "DNA as a molecular wire: Distance and sequence dependence," *Anal. Chem.*, vol. 85, no. 18, pp. 8634–8640, 2013.

[210] A. J. Bard and L. R. Faulkner, "Electrochemical methods: fundamentals and applications," D. Harris, E. Swain, and E. Aiello, Eds., J. Wiley and Sons Inc., 2001, pp. 1–814.

[211] J. F. Nagle and H. J. Morowitz, "Molecular mechanisms for proton transport in membranes," *Proc. Natl. Acad. Sci.*, vol. 75, no. 1, pp. 298–302, 1978.

[212] H. J. Morowitz, "Proton semiconductors and energy transduction in biological systems," *Am. J. Physiol. - Regul. Integr. Comp. Physiol.*, vol. 4, no. 2, pp. R99–R114, 1978.

[213] J. K. Lanyi, "Bacteriorhodopsin," *Annu. Rev. Physiol.*, vol. 66, pp. 665–686, 2004.

[214] D. Walz and S. R. Caplan, "Bacterial flagellar motor and H^+/ATP synthase: Two proton-driven rotary molecular devices with different functions," *Bioelectrochemistry*, vol. 55, no. 1–2, pp. 89–92, 2002.

[215] M. Capasso, T. E. DeCoursey, and M. J. S. Dyer, "pH regulation and beyond: Unanticipated functions for the voltage-gated proton channel, HVCN1," *Trends Cell Biol.*, vol. 21, no. 1, pp. 20–28, 2011.

[216] T. Arbring Sjöström *et al.*, "A Decade of Iontronic Delivery Devices," *Adv. Mater. Technol.*, vol. 3, no. 5, pp. 1700360–1700370, 2018.

[217] X. Strakosas, J. Selberg, Z. Hemmatian, and M. Rolandi, "Taking Electrons out of Bioelectronics: From Bioprotonic Transistors to Ion Channels," *Adv. Sci.*, vol. 4, no. 7, pp. 1–7, 2017.

[218] T. Miyake and M. Rolandi, "Grotthuss mechanisms: From proton transport in proton wires to bioprotonic devices," *Journal of Physics Condensed Matter*, vol. 28, no. 023001. Institute of Physics Publishing, pp. 1–11, 2016.

[219] Z. Hemmatian *et al.*, "Taking electrons out of bioelectronics: Bioprotonic memories, transistors, and enzyme logic," *J. Mater. Chem. C*, vol. 3, no. 25, pp. 6407–6412, 2015.

[220] E. E. Josberger, Y. Deng, W. Sun, R. Kautz, and M. Rolandi, "Two-terminal protonic devices with synaptic-like short-term depression and device memory," *Adv. Mater.*, vol. 26, no. 29, pp. 4986–4990, 2014.

[221] P. Atkins and J. De Paula, *Physical Chemistry*, Ninth edit. New York, NY: Freeman W.H. and Company, 2010.

[222] E. D. Głowacki, M. Irimia-Vladu, S. Bauer, and N. S. Sariciftci, "Hydrogen-bonds in molecular solids from biological systems to organic electronics," *J. Mater. Chem. B*, vol. 1, no. 31, pp. 3742–3753, 2013.

[223] P. Padma Kumar and S. Yashonath, "Ionic Conduction in the Solid State," *J. Chem. Sci.*, vol. 118, no. 1, pp. 135–154, 2006.

[224] S. Cukierman, "Et tu, Grotthuss! and other unfinished stories," *Biochim. Biophys. Acta - Bioenerg.*, vol. 1757, no. 8, pp. 876–885, 2006.

[225] L. Glasser, "Proton Conduction and Injection in Solids," *Chem. Rev.*, vol. 75, no. 1, pp. 21–65, 1975.

[226] D. Porath, A. Bezryadin, S. De Vries, and C. Dekker, "Direct measurement of electrical transport through DNA molecules," *Nature*, vol. 403, pp. 635–638, 2000.

[227] G. H. Bardelmeyer, "Electrical conduction in hydrated collagen. I. Conductivity mechanisms," *Biopolymers*, vol. 12, no. 10, pp. 2289–2302, 1973.

[228] L. Eigen, M., De Maeyer, "Self-dissociation and protonic charge transport in water and ice," *Proc. R. Soc.*, vol. 247, no. 1251, pp. 505–533, 1958.

[229] S. N. Pnevmatikos and G. P. Tsironis, "Protonic Conductivity : a New Application of Soliton Theory," *Le J. Phys. Colloq.*, vol. 50, no. C3, pp. C3-3-C3-10, 1989.

[230] N. Pavlenko, "Proton wires in an electric field: The impact of the Grotthuss mechanism on charge translocation," *J. Phys. Condens. Matter*, vol. 15, no. 2, pp. 291–307, 2003.

[231] S. Pnevmatikos, "Soliton proton conductivity," *Phys. Rev. Lett.*, vol. 60, no. 15, pp. 1534–1537, 1988.

[232] J. F. Nagle, M. Mille, and H. J. Morowitz, "Theory of hydrogen bonded chains in bioenergetics," *J. Chem. Phys.*, vol. 72, no. 7, pp. 3959–3971, 1980.

[233] D. Hadži, "Proton transfers in biological mechanisms," *J. Mol. Struct.*, vol. 177, no. C, pp. 1–21, 1988.

[234] X. Y. Zhang, J. Shao, S. X. Jiang, B. Wang, and Y. Zheng, "Structure-dependent electrical conductivity of protein: Its differences between alpha-domain and beta-domain structures," *Nanotechnology*, vol. 26, no. 12, p. 125702, 2015.

[235] H. C. Longuet-Higgins, "On the Origin of the Free Radical Property of Melanins," *Arch. Biochem. Biophys.*, vol. 86, pp. 231–232, 1960.

[236] A. Pullman and B. Pullman, "The band structure of melanins," *BBA - Biochim. Biophys. Acta*, vol. 54, no. 2, pp. 384–385, 1961.

[237] M. J. Galvão, D. S., Caldas, "Polymerization of 5,6-indolequinone: A view into the band structure of melanins," *J. Chem. Phys.*, vol. 88, pp. 4088–4091, 1988.

[238] M. M. Jastrzebska, H. Isotalo, J. Paloheimo, and H. Stubb, "Electrical conductivity of synthetic DOPA-melanin polymer for different hydration states and temperatures," *J. Biomater. Sci. Polym. Ed.*, vol. 7, no. 7, pp. 577–586, 1995.

[239] M. M. Jastrzebska, S. Jussila, and H. Isotalo, "Dielectric response and a.c. conductivity of synthetic dopa-melanin polymer," *J. Mater. Sci.*, vol. 33, no. 16, pp. 4023–4028, 1998.

[240] P. R. Crippa, V. Cristofoletti, and N. Romeo, "A band model for melanin deduced from optical absorption and photoconductivity experiments," *Biochim. Biophys. Acta*, vol. 538, no. 1, pp. 164–170, 1978.

[241] M. M. Jastrzebska, A. Kocot, and L. Tajber, "Photoconductivity of synthetic dopa-melanin polymer," *J. Photochem. Photobiol. B Biol.*, vol. 66, pp. 201–206, 2002.

[242] I. McKenzie, "The positive muon and μSR spectroscopy: powerful tools for investigating the structure and dynamics of free radicals and spin probes in complex systems," *Annu. Sect. Phys. Chem.*, vol. 109, pp. 65–112, 2013.

[243] J. Wünsche *et al.*, "In situ formation of dendrites in eumelanin thin films between gold electrodes," *Adv. Funct. Mater.*, vol. 23, no. 45, pp. 5591–5598, 2013.

[244] J. Wünsche *et al.*, "Protonic and Electronic Transport in Hydrated Thin Films of the Pigment Eumelanin," *Chem. Mater.*, vol. 27, no. 2, pp. 436–442, 2015.

[245] J. W. Lee *et al.*, "Dye-sensitized solar cells using purified squid ink nanoparticles coated on TiO_2 nanotubes/nanoparticles," *J. Ceram. Soc. Japan*, vol. 121, no. 1409, pp. 123–127, 2013.

[246] L. Migliaccio *et al.*, "Eumelanin–PEDOT:PSS Complementing En Route to Mammalian-Pigment-Based Electrodes: Design and Fabrication of an ITO-Free Organic Light-Emitting Device," *Adv. Electron. Mater.*, vol. 3, no. 5, pp. 1–6, 2017.

[247] L. Migliaccio *et al.*, "Impact of Eumelanin–PEDOT Blending: Increased PEDOT Crystalline Order and Packing–Conductivity Relationship in Ternary PEDOT:PSS:Eumelanin Thin Films," *Adv. Electron. Mater.*, vol. 5, no. 3, pp. 1–8, 2019.

[248] T. F. Wu and J. D. Hong, "Synthesis of water-soluble dopamine-melanin for ultrasensitive and ultrafast humidity sensor," *Sensors Actuators, B Chem.*, vol. 224, pp. 178–184, 2016.

[249] T. F. Wu, B. H. Wee, and J. D. Hong, "An Ultrasensitive and Fast Moisture Sensor Based on Self-Assembled Dopamine-Melanin Thin Films," *Adv. Mater. Interfaces*, vol. 2, no. 15, 2015.

[250] M. Piacenti Da Silva, J. C. Fernandes, N. B. De Figueiredo, M. Congiu, M. Mulato, and C. F. De Oliveira Graeff, "Melanin as an active layer in biosensors," *AIP Adv.*, vol. 4, no. 3, 2014.

[251] Q. Fan et al., "Transferring biomarker into molecular probe: Melanin nanoparticle as a naturally active platform for multimodality imaging.," *J. Am. Chem. Soc.*, vol. 136, no. 43, pp. 15185–1519, 2014.

[252] M. Araújo et al, "Bioactivity, mechanical properties and drug delivery ability of bioactive glass-ceramic scaffolds coated with a natural-derived polymer.," *Mater. Sci. Eng. C*, vol. 77, pp. 342–351, 2017.

[253] K. Jimbow et al., "Characterization of Melanogenesis and Morphogenesis of Melanosomes by Physicochemical Properties of Melanin and Melanosomes in Malignant Melanoma.," *Cancer Res.*, vol. 44, pp. 1128–1134, 1984.

[254] F. Solano, "Melanin and melanin-related polymers as materials with biomedical and biotechnological applications: Cuttlefish ink and mussel foot proteins as inspired biomolecules," *Int. J. Mol. Sci.*, vol. 18, no. 7, p. 1561, 2017.

[255] H. A. Galeb *et al.*, "Melanins as Sustainable Resources for Advanced Biotechnological Applications," *Glob. Challenges*, vol. 5, no. 2, p. 2000102, 2021.

[256] B. Voigtländer, "Artifacts in AFM," in *Atomic force microscopy designs*, B. Voigtländer, Ed. Berlin, GE: Springer-Verlag, 2019, pp. 137–147.

[257] Y. Gan, "Atomic and subnanometer resolution in ambient conditions by atomic force microscopy," *Surf. Sci. Rep.*, vol. 64, no. 3, pp. 99–121, 2009.

[258] J. I. Goldstein, D. E. Newbury, J. R. Michael, N. W. M. Ritchie, J. H. J. Scott, and D. C. Joy, *Scanning Electron Microscopy and X-Ray Microanalysis*. New York, NY: Springer, 2018.

[259] G. Binning, F. Quate, and C. Gerber, "Atomic Force Microscope," *Phys. Rev. Lett.*, vol. 56, no. 9, pp. 930–933, 1986.

[260] R. Reinfenberger, *Fundamentals of Atomic Force Microscopy. Part I: Foundations*, vol. 4. Hackensack, NJ: World Scientific, 2016.

[261] M. Raposo, Q. Ferreira, and P. A. Ribeiro, "A Guide for Atomic Force Microscopy Analysis of Soft-Condensed Matter."

[262] G. Haugstad, *Atomic Force Microscopy. Understanding Basic Modes and Advanced Applications*. Hoboken, NJ: Wiley J. and Sons Inc., 2012.

[263] J. I. Goldstein, D. E. Newbury, J. R. Michael, N. W. M. Ritchie, J. H. J. Scott, and D. C. Joy, "Electron Beam-Specimen Interactions: Interaction Volume," in *Scanning Electron Microscopy and X-Ray Microanalysis*, D. E. Newbury, N. W. M. Ritchie, J. H. J. Scott, and D. C. Joy, Eds. New York, NY: Springer, 2018, pp. 1–14.

[264] J. I. Goldstein, D. E. Newbury, J. R. Michael, N. W. M. Ritchie, J. H. J. Scott, and D. C. Joy, "Backscattered Electrons," in *Scanning Electron Microscopy and X-Ray Microanalysis*, D. E. Newbury, N. W. M. Ritchie, J. H. J. Scott, and D. C. Joy, Eds. New York, NY: Springer, 2018, pp. 15–28.

[265] "Scanning Electron Microscopes A to Z. Basic Knowledge For Using The SEM," 2012.

[266] J. I. Goldstein, D. E. Newbury, J. R. Michael, N. W. M. Ritchie, J. H. J. Scott, and D. C. Joy, "Secondary Electrons," in *Scanning Electron Microscopy and X-Ray Microanalysis*, D. E. Newbury, N. W. M. Ritchie, J. H. J. Scott, and D. C. Joy, Eds. New York, NY: Springer, 2018, pp. 29–37.

[267] P. Atkins and J. De Paula, "Molecular Structure," in *Physical Chemistry*, New York, NY: Freeman W.H. and Company, 2010, pp. 371–410.

[268] E. Pretsch, P. Bühlmann, and M. Badertscher, "Principles," in *UV-Vis Spectroscopy and Its Applications*, Berlin: Springer-Verlag, 1992, pp. 3–9.

[269] E. Pretsch, P. Bühlmann, and M. Badertscher, "Photometers and Spectrophotometers," in *UV-Vis Spectroscopy and Its Applications*, Berlin: Springer-Verlag, 1992, pp. 10–24.

[270] P. J. Larkin, "Introduction: Infrared and Raman Spectroscopy," in *Infrared and Raman Spectroscopy: Principles and Spectra Interpretation*, Waltham, MA: Elsevier Inc., 2011, pp. 1–7.

[271] B. C. Smith, *Fundamentals of fourier transform infrared spectroscopy*. Boca Raton, FL: Taylor & Francis Group, LLC, 2011.

[272] J. R. Ferraro, K. Nakamoto, and C. W. Brown, *Introductory Raman Spectroscopy*. San Diego, CA: Academic Press, 2003.

[273] P. J. Larkin, "Basic Principles," in *Infrared and Raman Spectroscopy: Principles and Spectra Interpretation*, Waltham, MA, 2011, pp. 7–27.

[274] P. van der Heide, *X-Ray Photoelectron Spectroscopy. An Introduction to Principles and Practices*. Hoboken, NJ: Wiley J. and Sons Inc., 2012.

[275] J. F. Moulder, W. F. Stickle, P. E. Sobol, and K. D. Bomben, *Handbook of X-ray photoelectron spectroscopy (XPS)*. Eden Prairie, MN: Perkin-Elmer Corporation, 1992.

[276] M. E. Orazem and B. Tribollet, *Electrochemical impedance spectroscopy*, vol. 48. John Wiley & Sons, 2008.

[277] S. Wang, J. Zhang, O. Gharbi, V. Vivier, M. Gao, and M. E. Orazem, "Electrochemical Impedance Spectroscopy," *Nat. Rev.*, vol. 41, no. 1, pp. 1–21, 2021.

[278] V. Di Noto, "Electrical spectroscopy studies of lithium and magnesium polymer electrolytes based on PEG400," *J. Phys. Chem. B*, vol. 106, no. 43, pp. 11139–11154, 2002.

[279] R. A. Huggins, "Simple Method to Determine Electronic and Ionic Components of the Conductivity in Mixed Conductors. A Review," *Ionics (Kiel).*, vol. 8, pp. 300–313, 2002.

[280] D. M. Alloway *et al.*, "Tuning the effective work function of gold and silver using ω-functionalized alkanethiols: Varying surface composition through dilution and choice of terminal groups," *J. Phys. Chem. C*, vol. 113, no. 47, pp. 20328–20334, 2009.

[281] I. Valitova *et al.*, "Carbon nanotube electrodes in organic transistors," *Nanoscale*, vol. 5, no. 11, pp. 4638–4646, 2013.

[282] M. Amit, S. Appel, R. Cohen, G. Cheng, I. W. Hamley, and N. Ashkenasy, "Hybrid proton and electron transport in peptide fibrils," *Adv. Funct. Mater.*, vol. 24, no. 37, pp. 5873–5880, 2014.

[283] D. D. Ordinario *et al.*, "Bulk protonic conductivity in a cephalopod structural protein," *Nat. Chem.*, vol. 6, no. 7, pp. 596–602, 2014.

[284] M. Amit, S. Roy, Y. Deng, E. Josberger, M. Rolandi, and N. Ashkenasy, "Measuring Proton Currents of Bioinspired Materials with Metallic Contacts," *ACS Appl. Mater. Interfaces*, vol. 10, no. 2, pp. 1933–1938, Jan. 2018.

[285] C. Zhong, Y. Deng, A. F. Roudsari, A. Kapetanovic, M. P. Anantram, and M. Rolandi, "A polysaccharide bioprotonic field-effect transistor," *Nat. Commun.*, vol. 2, no. 1, pp. 2–6, 2011.

[286] E. Di Mauro *et al.*, "Resistive switching controlled by the hydration level in thin films of the biopigment eumelanin," *J. Mater. Chem. C*, vol. 4, no. 40, pp. 9544–9553, 2016.

[287] A. Napolitano, A. Pezzella, M. R. Vincensi, and G. Prota, "Oxidative degradation of melanins to pyrrole acids: A model study," *Tetrahedron*, vol. 51, no. 20, pp. 5913–5920, 1995.

[288] Y. Diao *et al.*, "Understanding polymorphism in organic semiconductor thin films through nanoconfinement," *J. Am. Chem. Soc.*, vol. 136, no. 49, pp. 17046–17057, 2014.

[289] S. Riera-Galindo, A. Tamayo, and M. Mas-Torrent, "Role of Polymorphism and Thin-Film Morphology in Organic Semiconductors Processed by Solution Shearing," *ACS Omega*, vol. 3, no. 2, pp. 2329–2339, 2018.

[290] M. Ambrico *et al.*, "Hysteresis-type current-voltage characteristics in Au/eumelanin/ITO/glass structure: Towards melanin based memory devices," *Org. Electron.*, vol. 11, pp. 1809–1814, 2010.

[291] A. A. R. Watt, J. P. Bothma, and P. Meredith, "The supramolecular structure of melanin," *Soft Matter*, vol. 5, no. 19, pp. 3754–3760, 2009.

[292] A. Büngeler, B. Hämisch, and O. I. Strube, "The supramolecular buildup of eumelanin: Structures, mechanisms, controllability," *International Journal of Molecular Sciences*, vol. 18, no. 9. MDPI AG, 2017.

[293] R. Edge *et al.*, "Dopaquinone redox exchange with dihydroxyindole and dihydroxyindole carboxylic acid," *Pigment Cell Res.*, vol. 19, no. 5, pp. 443–450, 2006.

[294] T. C. Halsey, "Diffusion-limited aggregation: A model for pattern formation," *Phys. Today*, vol. 53, no. 11, pp. 36–41, 2000.

[295] R. D. Deegan, O. Bakajin, T. F. Dupont, G. Huber, S. R. Nagel, and T. A. Witten, "Capillary flow as the cause of ring stains from dried liquid drops.," *Nature*, vol. 389, no. 23, pp. 827–829, 1997.

[296] J. S. Huang, J. Sung, M. Eisner, S. C. Moss, and J. Gallas, "The fractal structure and the dynamics of aggregation of synthetic melanin in low pH aqueous solutions," *J. Chem. Phys.*, vol. 90, no. 1, pp. 25–29, 1989.

[297] M. G. Bridelli, "Self-assembly of melanin studied by laser light scattering," *Biophys. Chem.*, vol. 73, no. 3, pp. 227–239, 1998.

[298] R. Mukherjee and A. Sharma, "Instability, self-organization and pattern formation in thin soft films," *Soft Matter*, vol. 11, no. 45, pp. 8717–8740, 2015.

[299] A. Baldan, "Progress in Ostwald ripening theories and their applications to nickel-base superalloys. Part I: Ostwald ripening theories," *J. Mater. Sci.*, vol. 37, no. 11, pp. 2171–2202, 2002.

[300] M. Raposo, Q. Ferreira, and P. a Ribeiro, "A Guide for Atomic Force Microscopy Analysis of Soft- Condensed Matter," *Mod. Res. Educ. Top. Microsc.*, pp. 758–769, 2007.

[301] M. L. Roldán, S. A. Centeno, and A. Rizzo, "An improved methodology for the characterization and identification of sepia in works of art by normal Raman and SERS, complemented by FTIR, Py-GC/MS, and XRF," *J. Raman Spectrosc.*, vol. 45, no. 11–12, pp. 1160–1171, 2014.

[302] S. A. Centeno and J. Shamir, "Surface enhanced Raman scattering (SERS) and FTIR characterization of the sepia melanin pigment used in works of art," *J. Mol. Struct.*, vol. 873, no. 1–3, pp. 149–159, 2008.

[303] G. S. Kiran, S. A. Jackson, S. Priyadharsini, A. D. W. Dobson, and J. Selvin, "Synthesis of Nm-PHB (nanomelanin-polyhydroxy butyrate) nanocomposite film and its protective effect against biofilm-forming multi drug resistant Staphylococcus aureus," *Sci. Rep.*, vol. 7, no. 1, pp. 1–13, 2017.

[304] H. Okuda, K. Wakamatsu, S. Ito, and T. Sota, "Possible oxidative polymerization mechanism of 5,6-dihydroxyindole from ab initio calculations," *J. Phys. Chem. A*, vol. 112, no. 44, pp. 11213–11222, 2008.

[305] G. G. B. Alves, F. C. Lavarda, C. F. O. Graeff, and A. Batagin-Neto, "Reactivity of eumelanin building blocks: A DFT study of monomers and dimers," *J. Mol. Graph. Model.*, vol. 98, p. 107609, 2020.

[306] M. D'Ischia *et al.*, "Structural effects on the electronic absorption properties of 5,6-dihydroxyindole oligomers: The potential of an integrated experimental and DFT approach to model eumelanin optical properties," *Photochem. Photobiol.*, vol. 84, no. 3, pp. 600–607, 2008.

[307] D. Campbell, R. A. Pethrick, and J. R. White, "Ultraviolet – visible spectroscopy," *Polym. Charact.*, pp. 58–66, 2018.

[308] K.-Y. Ju, M. C. Fischer, and W. S. Warren, "Understanding The Role Of Aggregation In The Broad Absorption Bands Of Eumelanin," *ACS Nano*, vol. 12, pp. 12050–12061, 2018.

[309] H. S. Majumdar, A. Bandyopadhyay, A. Bolognesi, and A. J. Pal, "Memory device applications of a conjugated polymer: Role of space charges," *J. Appl. Phys.*, vol. 91, no.

3, pp. 2433–2437, 2002.

[310] Y. J. Lin, "Hysteresis-type current-voltage characteristics of indium tin oxide/poly (3,4-ethylenedioxythiophene) doped with poly (4-styrenesulfonate)/indium tin oxide devices," *J. Appl. Phys.*, vol. 103, no. 6, pp. 1–5, 2008.

[311] M. Matta, A. Pezzella, and A. Troisi, "Relation between Local Structure, Electric Dipole, and Charge Carrier Dynamics in DHICA Melanin: A Model for Biocompatible Semiconductors," *J. Phys. Chem. Lett.*, vol. 11, no. 3, pp. 1045–1051, 2020.

[312] J. B. Patrick A. Riley, Ed., *Melanins and Melanosomes, Biosynthesis, Biogenesis, Physiological and Pathological Functions*. Weinheim, Germany: Wiley-Blackwell, Wiley-VCH Verlag & Co. KGaA, 2011.

[313] L. Liu, Y., Ai, K., Lu, "Polydopamine and Its Derivative Materials: Synthesis and Promising Applications in Energy, Environmental, and Biomedical Fields," *Chem. Rev.*, vol. 114, p. 5057, 2014.

[314] L. Haeshin, S. M. Dellatore, W. M. Miller, and P. B. Messersmith, "Mussel-Inspired Surface Chemistry for Multifunctional Coatings," *Science*, vol. 318, pp. 426–430, 2007.

[315] J. Lindgren *et al.*, "Molecular preservation of the pigment melanin in fossil melanosomes," *Nat. Commun.*, vol. 3, no. May, pp. 1–7, 2012.

[316] M. Ambrico *et al.*, "Melanin Layer on Silicon: an Attractive Structure for a Possible Exploitation in Bio-Polymer Based Metal-Insulator-Silicon Devices," *Adv. Mater.*, vol. 23, no. 29, pp. 3332–3336, 2011.

[317] H. F. Haneef, A. M. Zeidell, and O. D. Jurchescu, "Charge carrier traps in organic semiconductors: A review on the underlying physics and impact on electronic devices," *J. Mater. Chem. C*, vol. 8, no. 3, pp. 759–787, 2020.

[318] T. Jiang *et al.*, "Single-chain heteropolymers transport protons selectively and rapidly," *Nature*, vol. 577, pp. 216–220, 2020.

[319] A. C. Ferrari, "Raman spectroscopy of graphene and graphite: Disorder, electron-phonon coupling, doping and nonadiabatic effects," *Solid State Commun.*, vol. 43, pp. 47–57, 2007.

[320] K. L. Saenger, J. C. Tsang, A. A. Bol, J. O. Chu, A. Grill, and C. Lavoie, "In situ x-ray diffraction study of graphitic carbon formed during heating and cooling of amorphous-C/Ni bilayers," *Appl. Phys. Lett.*, vol. 96, pp. 2010–2013, 2010.

APPENDIX A   SUPPORTING INFORMATION ARTICLE 1

Eumelanin: From molecular to Film State

Manuel Reali[1], Anthony Camus[1], Guillaume Beaulieu[1], Jordan De Angelis[2], Christian Pellerin[3], Alessandro Pezzella[4], Clara Santato[*1]

[1]Department of Engineering Physics, Polytechnique Montreal, C.P. 6079, Succ. Centre-ville, Montréal, QC, H3C 3A7, Canada

[2]Department of Electronic, Electrical and Information Engineering (DEI), University of Bologna, Viale del Risorgimento 2, 40136, Italy

[3]Département de chimie, Université de Montréal, C.P. 6128, Succ. Centre-ville, Montréal, QC, H3C 3J7, Canada

[4]Department of Physics "Ettore Pancini", University of Naples "Federico II", Complesso Universitario Monte S. Angelo, Via Cintia 1, 80126, Naples, Italy.

*Clara Santato (Email: clara.santato@polymtl.ca)

Keywords Eumelanin, (5,6)-dihydroxyindole (DHI), (5,6)-dihydroxyindole-2-carboxylic acid (DHICA), self-assembly, polymerization, films

Table A.1 Height of crystal-like aggregates of AC-L-DHI films and their vertical formation rate.

AC-L-DHI: Crystal-like Aggregates		
Time of observation (h)	Height z(t) (nm)	Vertical formation rate (nm h^{-1})
24	132 ± 2	27 ± 1
25	159 ± 3	30 ± 1
26	192 ± 2	26 ± 1
27	211 ± 2	19 ± 1

Table A.2 Height, width, surface density, root mean square roughness and vertical formation rate (v_z (t)) of rod-shaped structures of AC-L-DHICA films.

AC-L-DHICA: Rod-Shaped Structures					
Time from deposition (h)	Height z(t) (nm)	Width (nm)	Surface density (μm^{-2})	Root mean square roughness (nm)	$v_z(t)$ (nm h^{-1})
1.0	68 ± 1	94 ± 1	3.3 ± 0.3	15 ± 1	6.8 ± 0.1
1.2	70 ± 2	113 ± 2	4.9 ± 0.3	22 ± 1	3.7 ± 0.1
11.0	71 ± 1	133 ± 1	7.7 ± 0.3	32 ± 2	0.5 ± 0.1
38.0	83 ± 2	147 ± 2	8.7 ± 0.3	29 ± 1	0.2 ± 0.1
168.0	95 ± 1	179 ± 1	11.8 ± 0.2	36 ± 1	0.2 ± 0.1
504.2	175 ± 3	264 ± 1	4.0 ± 0.4	56 ± 2	0.1 ± 0.1
672.0	181 ± 3	270 ± 1	3.7 ± 0.1	65 ± 2	0 ± 0.1

Table A.3 Absorption wavelength and optical energy gap evaluated over time by the Tauc Model for AC-L-DHI, AC-L-DHICA, AISSP-L-DHI and AISSP-L-DHICA films.

Name	Time	Absorption wavelength (nm)	Optical energy gap (eV)
AC-L-DHI	As prepared (1 h)	307 ± 1	1.19 ± 0.25
	One day	305 ± 1	1.06 ± 0.19
	4 days	306 ± 1	0.98 ± 0.16
	7 days	306 ± 1	0.94 ± 0.19
AC-L-DHICA	As prepared (1 h)	364 ± 1	2.41 ± 0.23
	One day	363 ± 1	2.39 ± 0.05
	4 days	363 ± 1	2.24 ± 0.04
	7 days	359 ± 1	2.20 ± 0.04
AISSP-L-DHI	As prepared (1 h)	$\times$	$\times$
	3 days	$\times$	$\times$
AISSP-L-DHICA	As prepared (1 h)	351 ± 1	$\times$
	3 days	351 ± 1	$\times$

Table A.4 Positive and negative current densities at zero voltage (J_+ (V=0), J- (V=0)), positive and negative voltage at zero current density (V_+ (J=0), V- (J=0)), charge stored (q) at the Au/DHICA and Au/DHI interfaces room temperature electrical conductivity (σ) at 1.5 V as a function of the voltage scan rate.

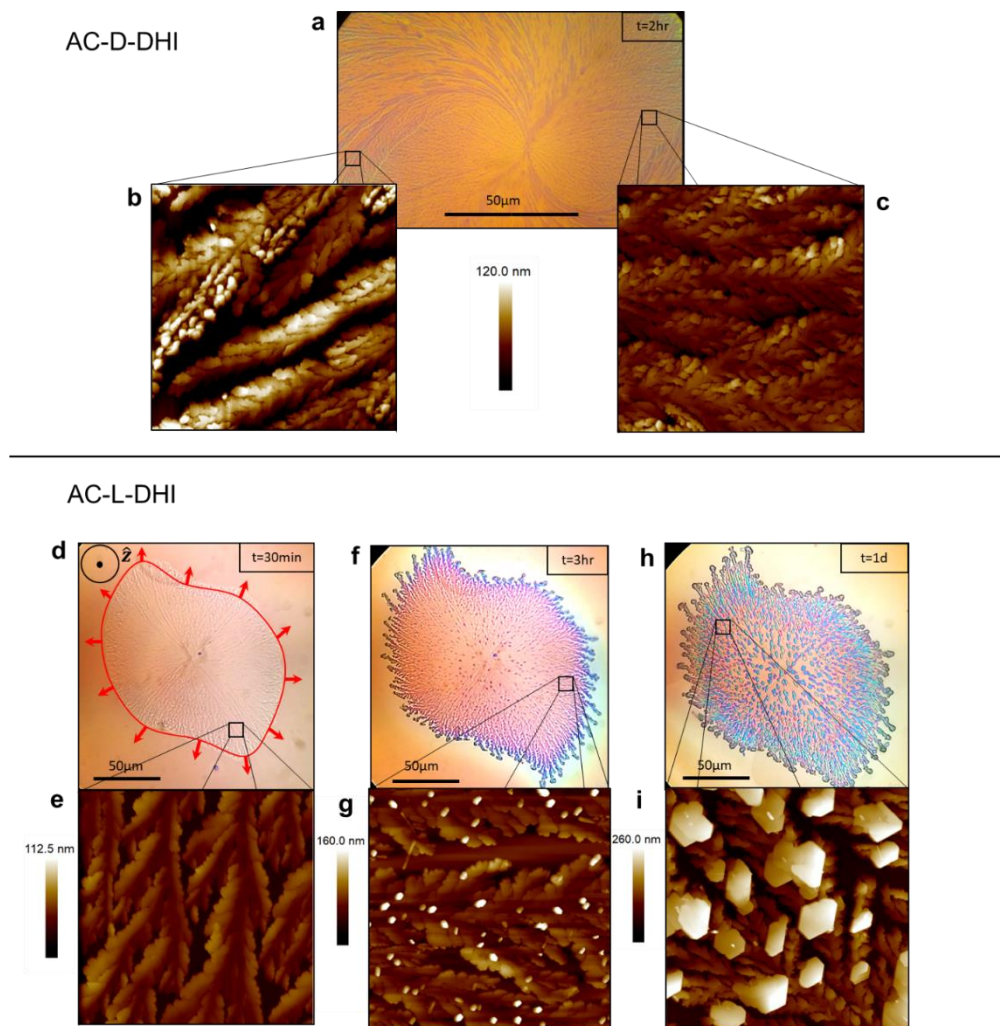| Electrical hysteresis of AC-L-DHICA and AC-L-DHI Films								
Building block	Voltage scan rate (mVs⁻¹)	J_+ ($V = 0$) (μA cm⁻²)	J_- ($V = 0$) (μA cm⁻²)	V_+ ($J = 0$) (V)	V_- ($J = 0$) (V)	q (μC)	Hysteresis area (nA V)	σ at 1.5 V (S cm⁻¹)
DHICA	25	0.20	−0.20	1.1	−1.1	2.4	60	4.6×10^{-11}
	50	0.50	−0.20	0.4	−0.8	1.5	75	6.8×10^{-11}
DHI	25	0.05	−0.06	1.2	−1.2	0.2	3.8	1.1×10^{-11}
	50	0.08	−0.09	1.1	−1.1	0.1	5.6	1.4×10^{-11}

Figure A.1 Morphological evolution of AC-DHI films over a period of 1 day. In (a) optical image of AC-D-DHI spiral-like shapes 2 h after deposition and in (b) and (c) AFM images in different regions of the spiral-like shape revealing the different density of fern as a function of the distance from the center of the spiral. In (d) an optical image of AC-L-DHI spiral-like shapes (red arrows denoting the front propagation direction and the flow of solvent according to the coffee-ring effect, dark dot circle is the $\hat{z}$ direction) and (e) its nanoscale structure revealed by AFM image 30 minutes after the deposition. Optical images of AC-DHI spiral-like shapes after (f) 3 h and (h) 1 day after the deposition at AC-L, with their respective AFM height images (g) and (i). Pillar-like and crystal-like aggregates forming on top of fern-like structures are shown respectively in (g) and (i). The size of the AFM images is 10 µm×10 µm. AC-DHI films feature an average number of spiral-like shapes of about 10.
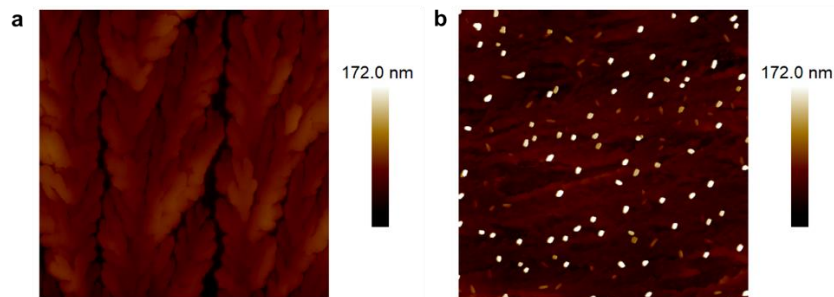
Figure A.2 10 µm×10 µm AFM height image showing the morphologies of AC-DHI films (a) stored one day in the dark and (b) exposed one day to laboratory daylight (see Experimental).
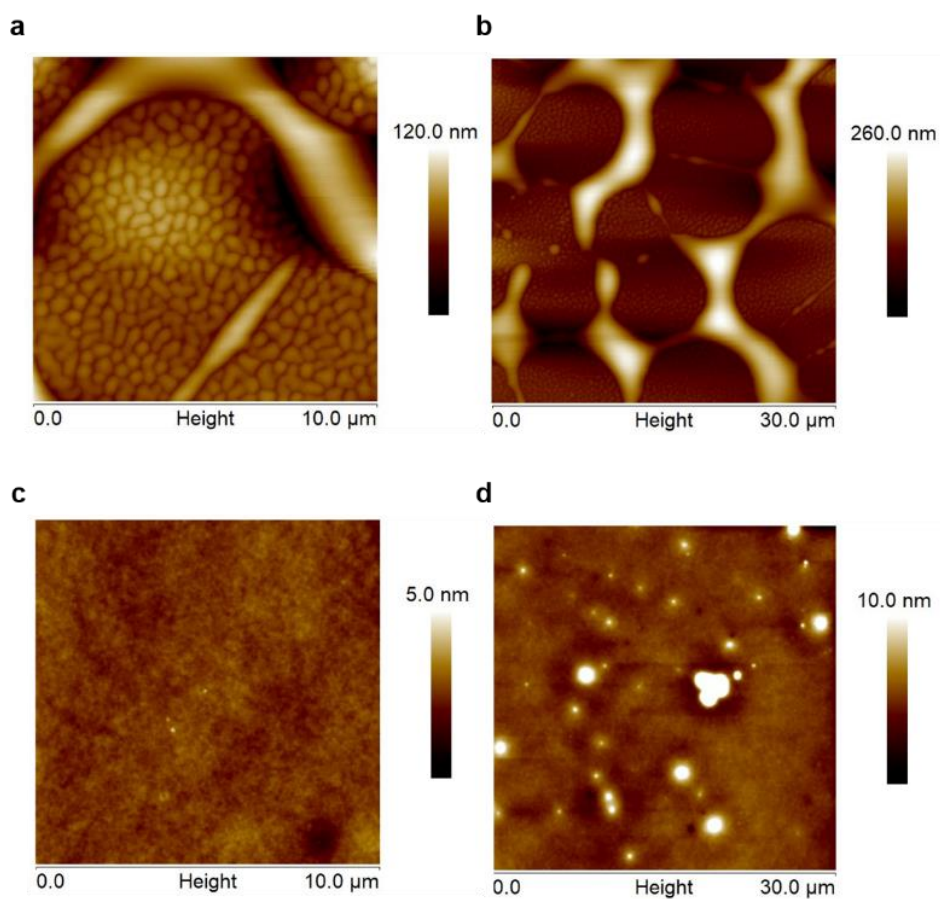

Figure A.3 AFM height images of spin-coated AISSP-D-DHI films from powders received after: (a) and (b) 10 day-shipping; and (c) and (d) 30 day-shipping.

We cannot exclude that an aging of the DHI powder takes place during its shipping (e.g., because of changes in the oxidation state of DHI), possibly affecting the morphology of DHI-based films (see Experimental). De-wetting processes are observed for AISSP-D-DHI films fabricated from powders received after a shipping time of ten days (Figure A.3 (a), (b)). On the other hand, AISSP-D-DHI films fabricated from powders received after a shipping time of thirty days are smooth and featureless, in agreement with literature[36] (Figure A.3 (c), (d)).
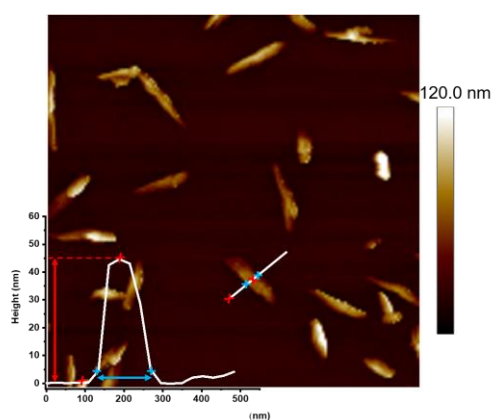

Figure A.4 3 µm×3 µm AFM height image of AC-L-DHICA showing the profile of rod-shaped like structures forming at ambient conditions after 1 h from fabrication.
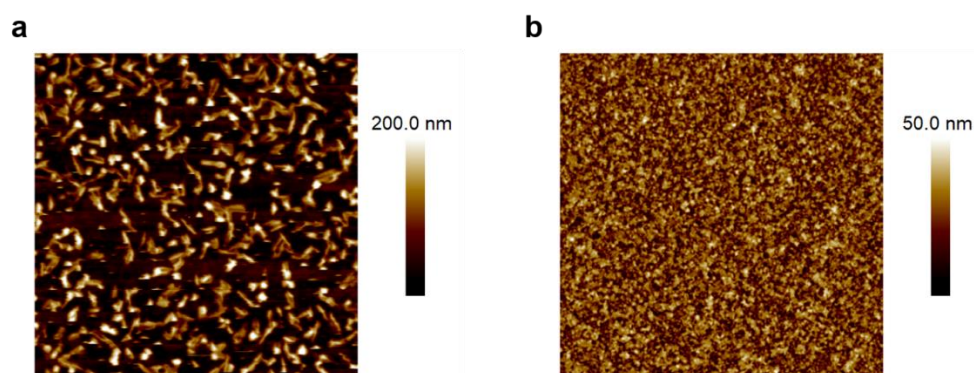
Figure A.5 10 µm×10 µm AFM height image showing the morphologies of (a) AC-D-DHICA and (b) AISSP-D-DHICA films stored one day in the dark.
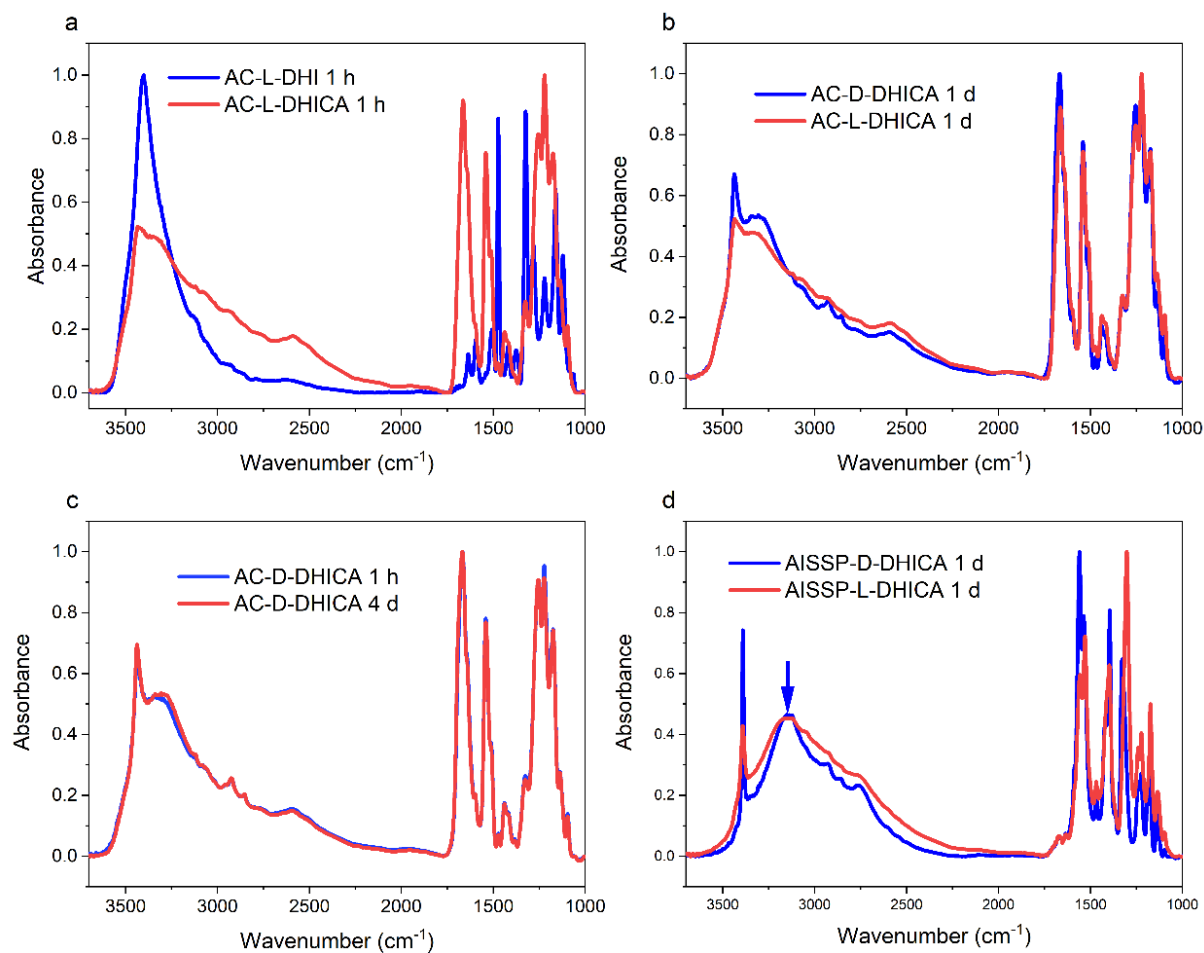
Figure A.6 IR spectra of (a) AC-L-DHI and AC-L-DHICA films recorded after 1 h, (b) AC-L and D-DHICA films recorder after one day, (c) AC-D-DHICA films at different stages of formation and (d) AISSP-D-DHICA films acquired after one day. DHI spectra were normalized to the maximum peak (ca. 1300 cm^{-1}). For further details on abbreviations see Table 5.1 and experimental section.
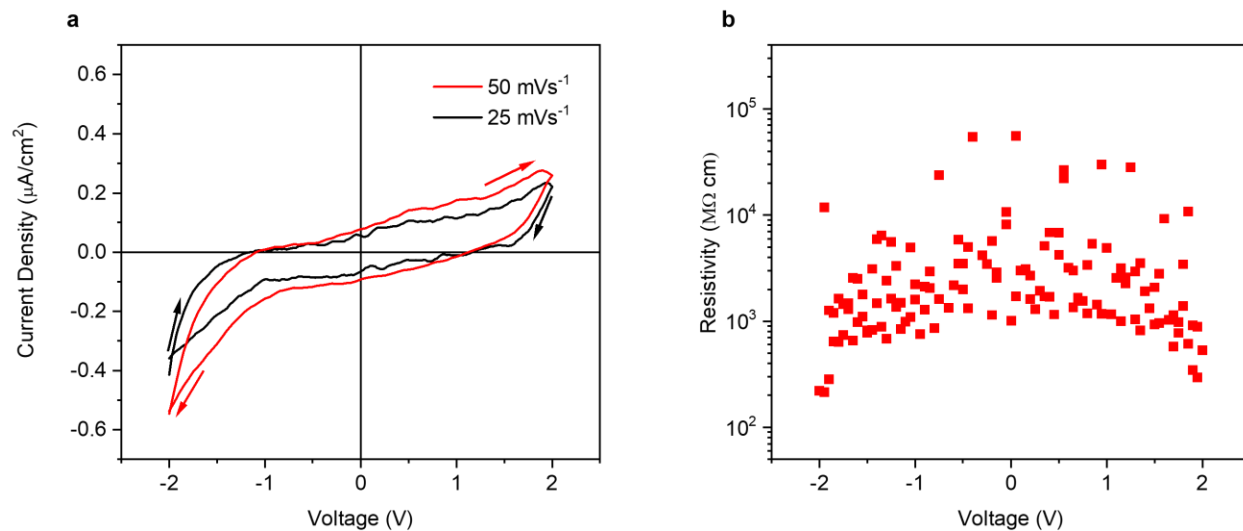
Figure A.7 AC-L-DHI films (a) J-V hysteresis at different voltage can rates on circular interdigitated Ti/Au electrodes (W=24.5 mm L=10 µm). In (b) Resistivity vs voltage at 50 mVs^{-1}.

APPENDIX B   SUPPORTING INFORMATION ARTICLE 2

Electronic Transport in the Biopigment Sepia Melanin

Manuel Reali[1], Abdelaziz Gouda[1], Jonathan Bellemare[1], David Ménard[1], Jean-Michel Nunzi[2,3], Francesca Soavi[4], Clara Santato[1*]

[1]Department of Engineering Physics, Polytechnique Montreal, Montreal, H3C 3A7, Canada

[2]Department of Physics, Engineering Physics & Astronomy, Queen's University, Kingston, K7L 3N6, Canada

[3]Department of Chemistry, Queen's University, Kingston, K7L 3N6, Canada

[4]Department of Chemistry "Giacomo Ciamician", Alma Mater Studiorum Università di Bologna, Bologna, 40126, Italy

*email address: clara.santato@polymtl.ca

Raman Spectroscopy of dry and wet Sepia melanin powders

The Raman Spectroscopy surveys of dry and wet Sepia melanin powders from pellets before and after the electrical resistive switching do not show any peak and or shoulder attributable to graphitic carbon (Figures B.6 A, B, C and Table B.6). Typical Raman modes of graphitic carbon are indeed located at ca. 2750 cm^{-1} (2D$_2$ band) and at 2700 cm^{-1} (2D$_1$ shoulder) [319].

High-resolution X-ray photoemission spectra (XPS) of dry Sepia melanin powders

The high-resolution C$_{1s}$ XPS spectra of dry Sepia melanin powders obtained from pellets before and after the electrical resistive switching do not indicate the presence of graphitic carbon (Figure B.6 D and E, Tables B.7 and B.8).

Typical signatures of graphitic carbon are a C$_{1s}$ peak at BE=291.4 eV and an unusually thin C$_{1s}$ component at BE=284.6 eV. The high-resolution C$_{1s}$ XPS spectra of dry Sepia melanin powder show a satellite peak at BE=291.4 eV; this is expected in eumelanin because of the cyclic carbon structure. The C$_{1s}$ component at BE=284.7 eV is broad and not as sharp as expected in graphitic carbon (Figure B.6 E).

The concentration of C-O, C-OH, or C-O-C groups (BE=286.7 eV) is high compared to the other chemical groups observed (Tables B.7 and B.8). The concentration of C-O groups, compared to C-N and C=C groups, is also higher than expected. Nevertheless, the C$_{1s}$ spectra before and after switching of Sepia melanin powders are similar, except for a slight increase in C-O and decrease in C-N after switching.

X-ray diffraction (XRD) survey of dry Sepia melanin powders

In agreement with Raman spectroscopy and XPS surveys, XRD patterns of dry Sepia melanin powders, obtained from pellets before and after the electrical resistive switching, show a broad XRD spectrum with a small shoulder around $2\theta \sim 27°$, not due to graphitic carbon (Figure B.7). The typical (002) and (004) graphitic planes correspond indeed to sharp peaks located respectively at $2\theta \sim 27°$ and $2\theta \sim 54°$[320].

Table B.1 Percentage of weight gained (% wt) after hydration (24 hr) at different percentages of relative humidity (% RH) for Sepia melanin pellets (see experimental section, main file).

	%RH	%wt gained
	90 ± 0.3	19.0 ± 1.0
Sepia Melanin	dry	0

Table B.2 Threshold voltage (V_T) and R_{ON}/R_{OFF} for dry and wet pellets at different voltage scan rates (see main file for the meaning of R_{ON} and R_{OFF}).

Sample	Scan Rate (mVs^{-1})	V_T (V)	$\dfrac{R_{ON}}{R_{OFF}}$
Dry	1	41.7	0.191
	100	51.6	0.18
19.0% wt, wet	1	68.5	0.003
	100	55.1	0.05
	1000	143.2	0.025
	2000	97.0	0.070

Table B.3 Values of a in $I \propto V^a$ at a different voltage scan rate, for dry and wet pellets.

Sample	Scan Rate (mVs⁻¹)	a
Dry	100 (Cycle 2)	0.959 ± 0.005
	100 (Cycle 3)	1.059 ± 0.003
	1000	1.137 ± 0.018
	2000	1.168 ± 0.081
	3000	1.344 ± 0.026
	4500	1.250 ± 0.010
19.0% wt, wet	3000	1.325 ± 0.116
	4500	1.001 ± 0.067

Table B.4 Fitting parameters for the transient characteristics of wet pellets, at V_T, after electrical resistive switching. The transient characteristics fit a biexponential function of the form $I(t) = I_0 + \sum_{j=1}^{2} A_j \exp\left(-\frac{t}{\tau_j}\right)$, where I_0 is the *quasi-plateau* current, τ_1 and τ_2 the characteristic decay times, A_1 and A_2 the amplitudes of the decay profile.

I_0 (mA)	τ_1 (s)	τ_2 (s)	A_1 (mA)	A_2 (mA)
10.49 ± 0.07	162.9 ± 5.3	1.17 ± 0.05	12.25 ± 0.20	62.52 ± 0.88

Table B.5 Fitting parameters of the equivalent circuit of both dry and wet Sepia melanin pellet in the frequency range 3 kHz -3 Hz and 3 kHz -145 Hz for dry and wet pellet respectively. R_{tot} includes the electronic resistance R_e, the ionic resistance R_i, the interface resistance R_{if}, i.e., $R_{tot} = R_e + R_i + R_{if}$, Q (CPE the constant phase element) is the series combination of melanin's geometrical capacitance and the capacitance at melanin/metal interface that describes any deviation from an ideal capacitive response and n is a dispersion parameter that determines the physical meaning of Q. The CPE impedance is $Z_{CPE} = \dfrac{1}{Q\,(j2\pi f)^n}$, where f is the frequency. If n = 1, the CPE reduces to an ideal capacitor. If n = 0, the CPE reduces to a real resistor, and if n = 0.5, the CPE reduces to a Warburg element (describes any process controlled by ionic or electronic diffusion).
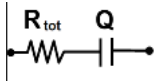
Fitting parameters	Dry Pellet		Wet pellet	
R_{tot} ⎓ Q (circuit)	Before switching	After switching	Before switching	After switching
R_{total}	4.5 GΩ	172 Ω	9 KΩ	719 Ω
$Q\ (F.s^{n-1})$	6.70×10^{-12}	6.77×10^{-9}	2.60×10^{-8}	3.80×10^{-10}
n	0.81	0.94	0.58	0.88

Table B.6 Fitting parameters of the deconvolution of the Raman modes of melanin pellets before and after electrical tests. The deconvolution function is a Gaussian distribution of the form $y = y_o + \frac{A}{w\sqrt{\pi/2}} \exp\left\{-2\left[\frac{x-x_c}{w}\right]^2\right\}$, where x_c is the Raman shift of the mode, w the standard deviation and A the amplitude of the distribution (Figures B.6 A, B and C).

Wet pellet after switching					
Raman Mode #	$y_o \pm \Delta y_0$	$A \pm \Delta A$ (cm⁻¹)	$w \pm \Delta w$ (cm⁻¹)	$x_c \pm \Delta x_c$ (cm⁻¹)	FWHM (cm⁻¹)
1	0.036 ± 0.001	203.2 ± 1.9	251.1 ± 2.6	1363.9 ± 1.3	295.6
2	0.036 ± 0.001	91.8 ± 1.5	101.3 ± 1.1	1583.3 ± 0.5	215.1
Wet pellet before switching					
1	0.024 ± 0.001	183.9 ± 1.7	287.6 ± 2.5	1389.9 ± 1.4	338.6
2	0.024 ± 0.001	82.3 ± 1.2	92.3 ± 0.8	1587.4 ± 0.3	108.6
Dry pellet after switching					
1	0.026 ± 0.001	158.5 ± 1.5	177.9 ± 2.0	1346.3 ± 0.9	209.5
2	0.026 ± 0.001	95.4 ± 1.1	93.6 ± 1.2	1581.6 ± 0.6	110.2

Table B.7 Atomic percentage of the elements and binding energies obtained from the XPS survey scan of the dry pellets, before and after resistive switching.

Name	BE (eV)	At. %	
		Before switching	After switching
S_{2p}	166.6	0.2	0.4
C_{1s}	284.9	61.8	61.6
N_{1s}	399.1	4.5	5.6
O_{1s}	531.8	32.9	31.5
Na_{1s}	1070.7	0.5	0.9

Table B.8 Attribution of chemical bond from high resolution XPS scans (C$_{1s}$ only) of dry pellets before and after resistive switching (Figures B.6 D and E).

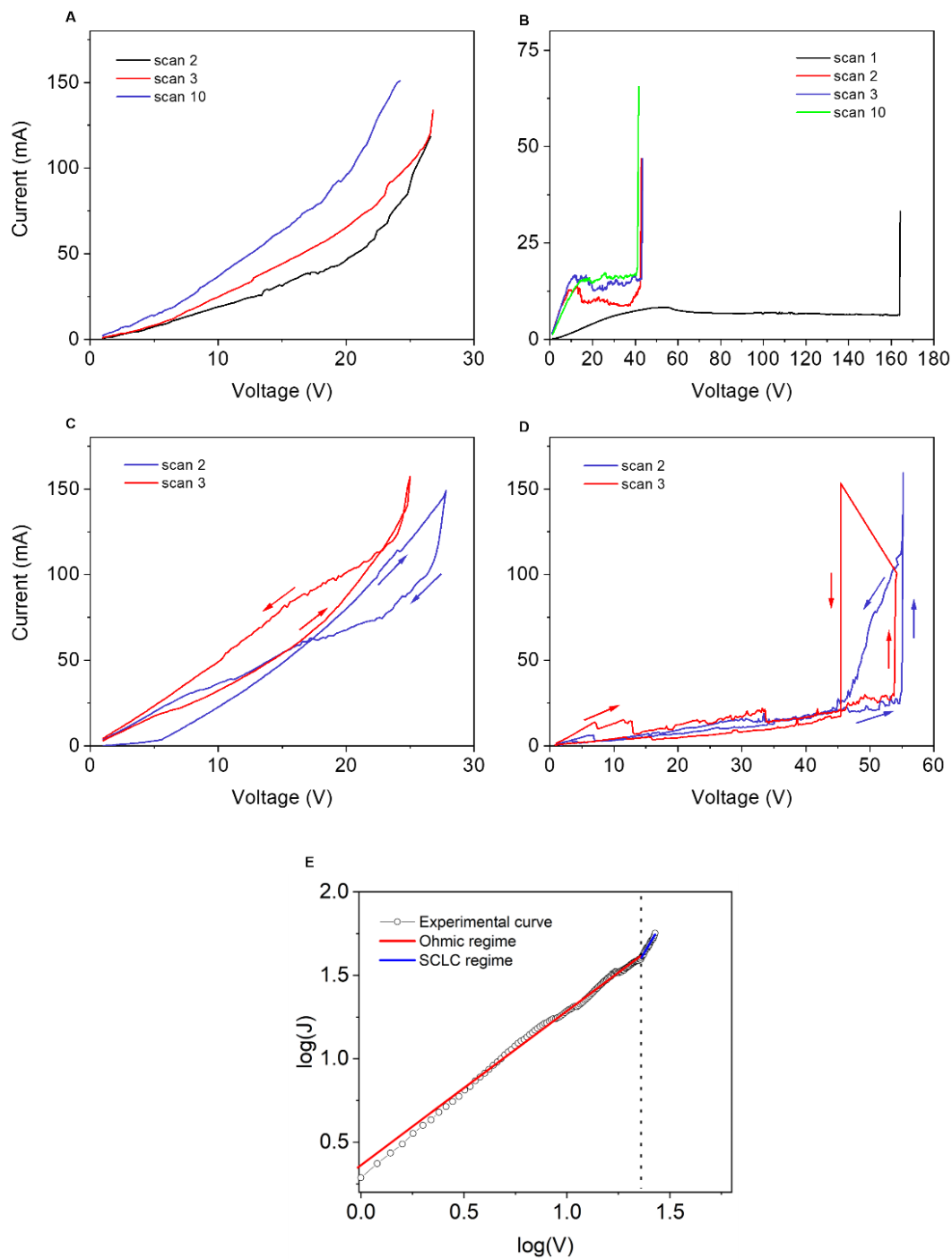| Name	BE (eV)	Identification	At. %	
			Before switching	After switching
C_{1s}	284.7	$C - C$ and $C = C$	30.7	34.0
	285.3	$C - N$	16.1	9.3
	286.7	$C - O, C - O - C,$ $C - OH$	29.4	35.5
	287.6	$C = O$	11.9	8.5
	289.1	$O - C = O, COOH$	11.1	11.5
	291.4	$\pi \rightarrow \pi^*$ of $C = C$	0.8	1.2

Figure B.1 Dry: (A) forward scan only and (C) forward and backward scans (cycles); 19.0% wt wet: (B) forward scan only and (D) forward and backward scans (cycles). In (E) log (J)-log (V) plot for dry pellets showing the change of slope between the Ohmic and the Space Charge Limited Current (SCLC) regime (red and blue solid line with slope of 0.93±0.06 and 2.09±0.02 respectively).
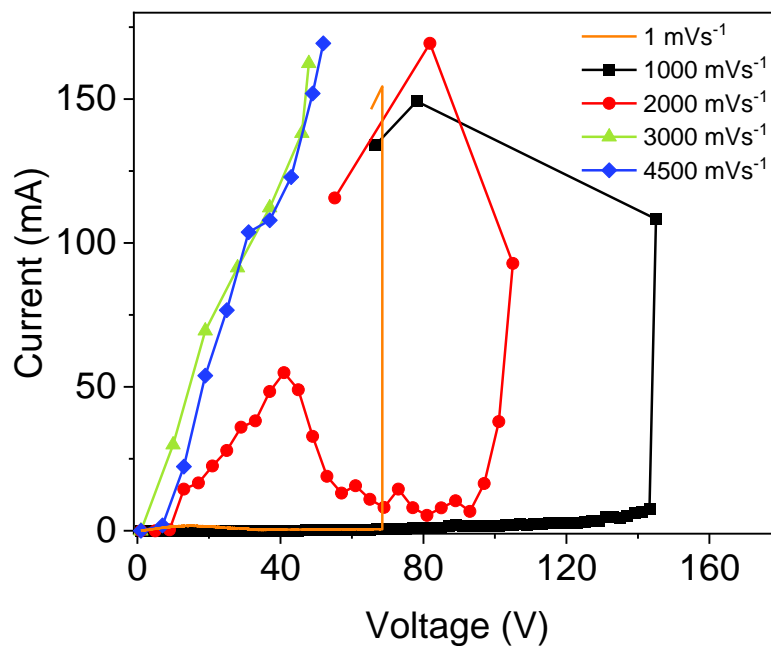
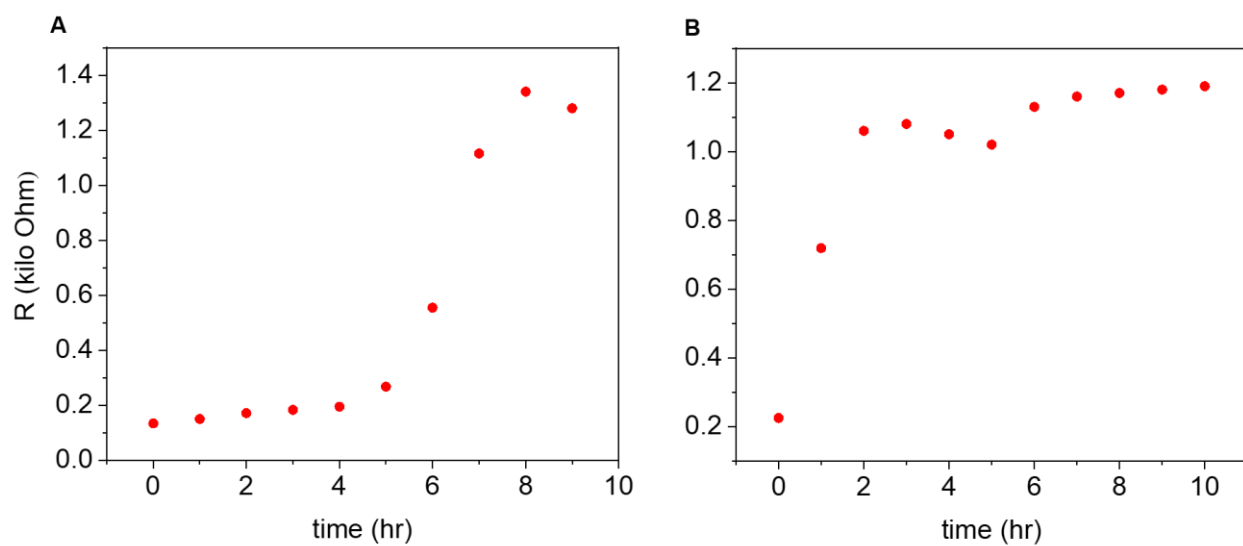Figure B.2 Sequential current-voltage acquisitions from low to high scan rates for wet pellets.

Figure B.3 Resistance vs time in unbiased conditions (i.e., without electrical bias) after the electrical resistive switching for Sepia melanin pellets. (A) dry and (B) 19.0% wt wet.
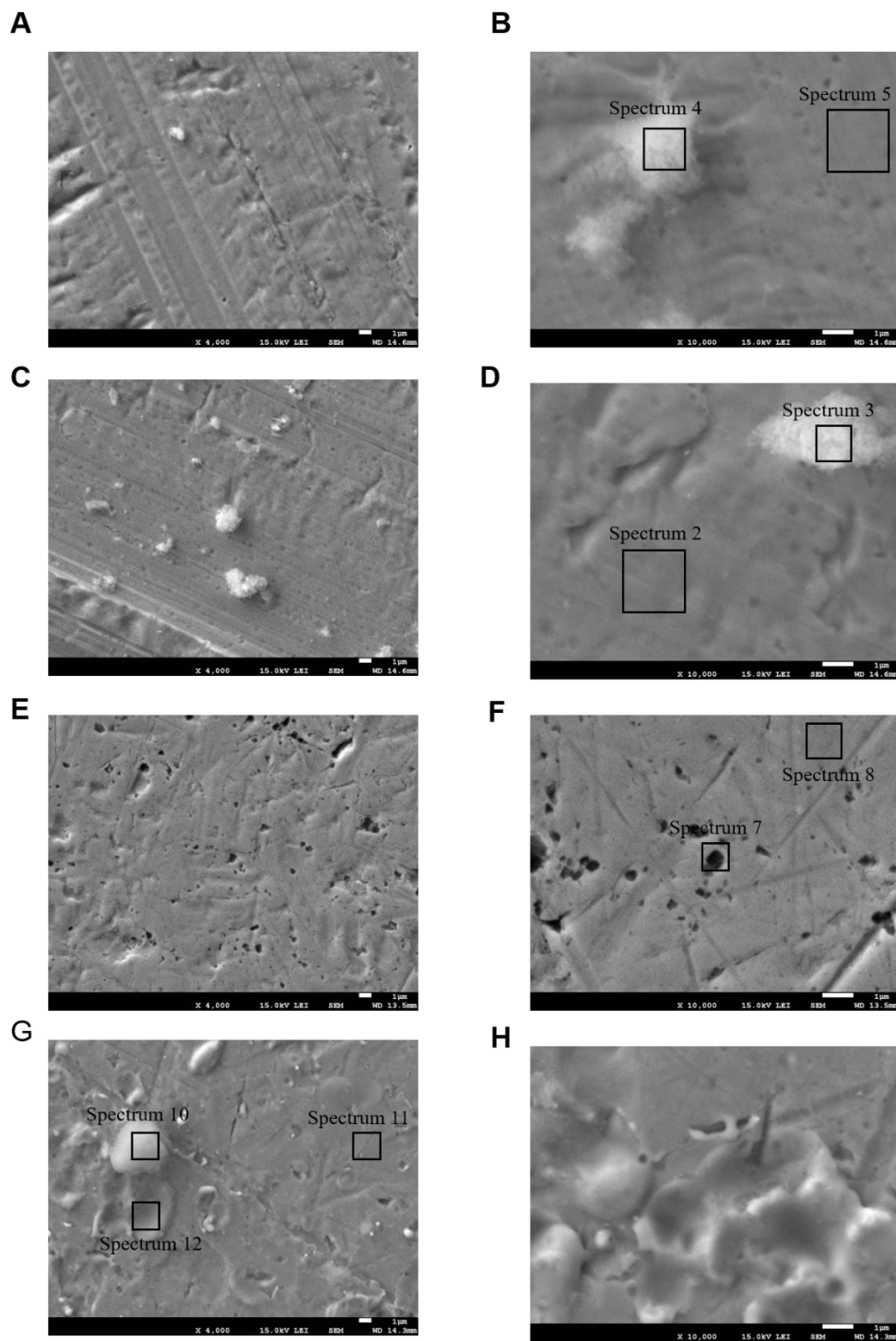
Figure B.4 Scanning electron microscopy (SEM) of copper and stainless-steel electrodes. SEM images of copper and stainless-steel electrodes (A), (B), (E) and (F) before electrical resistive switching; (C) and (D), (G) and (H) after electrical resistive switching.
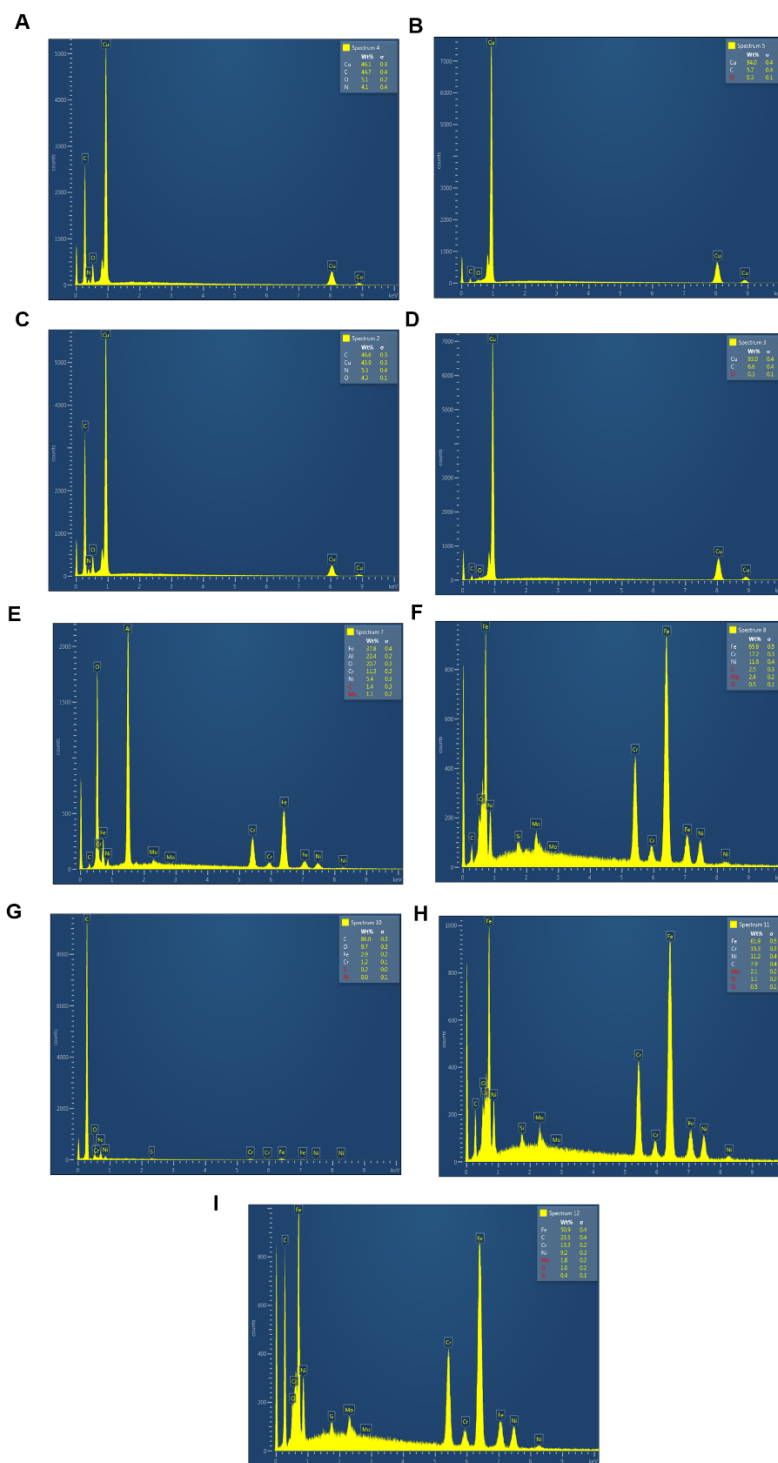
Figure B.5 EDX spectra of copper and stainless-steel electrodes. EDX spectra of copper and stainless-steel electrodes (A), (B), (F) and (G) before electrical resistive switching; (C), (D), (E), (H) and (I) after electrical resistive switching (Figure B.4).

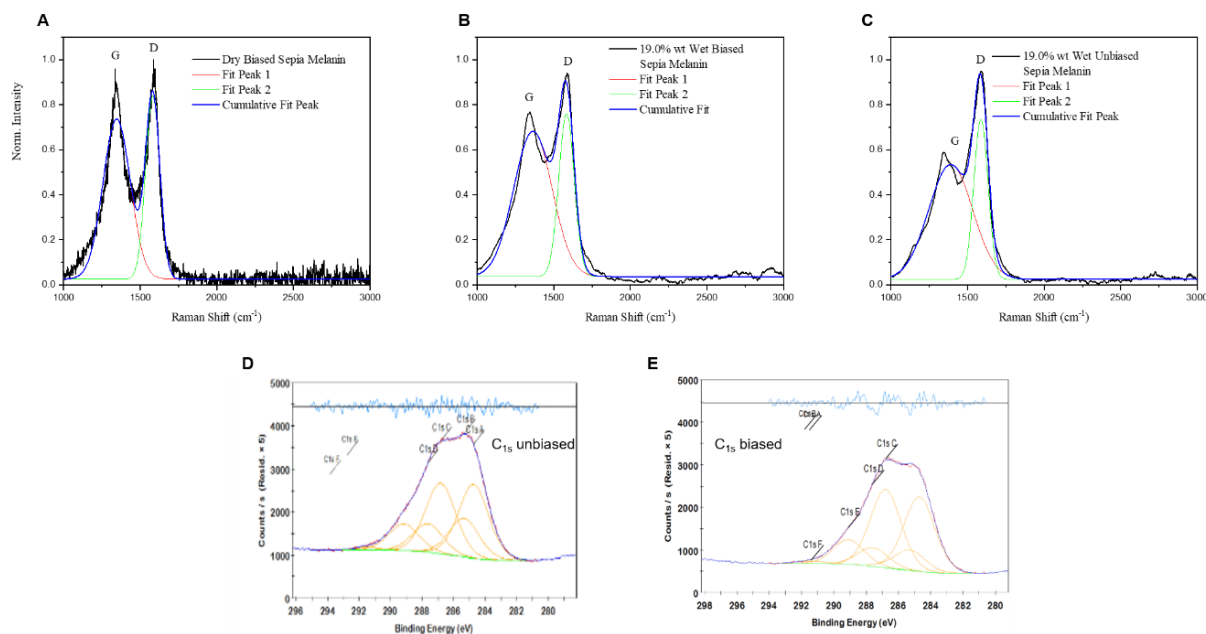Figure B.6 Raman and XPS characteristics of dry and wet Sepia Melanin pellets. Raman spectra after resistive switching for pellets dry (A) and wet (B) pellets. Raman spectrum before resistive switching for wet pellets (C). High resolution C_{1s} XPS spectra of dry pellets before switching (D) and after switching (E).
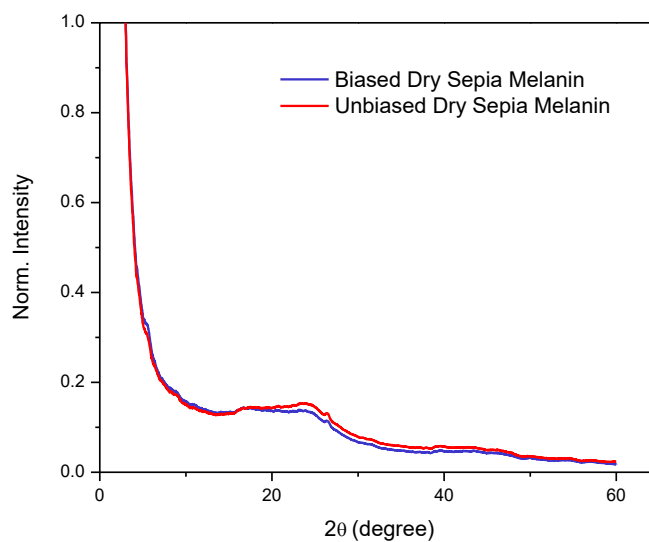

Figure B.7 Structural characterization of dry Sepia Melanin. XRD patterns before and after resistive switching.

APPENDIX C   LIST OF PUBLICATIONS AT POLYTECHNIQUE MONTREAL

1. **Reali, M.**, & Santato, C. (2019). Eumelanin: semiconductor, protonic conductor or mixed electronic-ionic conductor? *Handbook of Nanoengineering, Quantum Science and Nanotechnology*, Chapter 5, pp. 101-103, Edited by S. E. Lyshevski (Publisher: CRC Press).

2. Gouda, A., Bobbara, S. R., **Reali, M.**, & Santato, C. (2019). Light-assisted melanin-based electrochemical energy storage: physicochemical aspects. *Journal of Physics D: Applied Physics*, 53(4), 043003.

3. **Reali, M.**, Gouda, A., Bellemare, J., Ménard D., Nunzi, J. M., Soavi, F., & Santato, C. (2020). Electronic Transport in the Biopigment Sepia Melanin. *ACS Applied Bio Materials*, 3(8), 5244-5252.

4. **Reali, M.**, Camus, A., Beaulieu, G., De Angelis, J., Pellerin, C., Pezzella, A., & Santato, C. (2021). Eumelanin: From Molecular State to Film. *The Journal of Physical Chemistry C*, 125(6), 3567-3576.

5. **Reali, M.**, Saini, P., & Santato, C. (2020). Electronic and protonic transport in bio-sourced materials: a new perspective on semiconductivity. *Materials Advances*, 2(1), 15-31.

6. **Reali, M.**, Camus, A., Rozel, M., & Santato, C. (2021). Ultra-high conductivity of Sepia melanin ink films for environmentally benign printed electronics (manuscript submitted).

7. **Reali, M.**[*], Camus, A[*]., Pezzella, A., MacLeod, J., & Santato, C. (2021). Toward a Structure-property Relationship Phase Diagram for Eumelanin Films (manuscript in preparation).

8. Camus, A., **Reali, M.** & Santato, C. (2021). Recent Advances in High-Resolution Printed Transistors: the Case of Organic and Bio-sourced Materials (invited review article submitted to *Current Opinions in Green Sustainable Chemistry* on October 31st, 2021)

9. Gouda, A.[*], **Reali, M.[*],** M. Masson, A., Byway N., Zvezdin, A., Rho, D., & Santato, C. (2021). Biodegradability and compostability aspects of organic electronics materials and devices: Recycling and Reprocessing for a Sustainable Future, Edited by Holuszko M. E. and Kumar A. (Publisher: Wiley-VHC).

10. Niyonkuru, D., Ambrose, R., Carrière, A., Gouda, A., **Reali, M.,** Camus, A., Pezzella, A., Hill, I., & Santato, C. (2021). Locating the bandgap edges of eumelanin thin films for their possible Applications in organic electronics, *Journal of Chemical Technology and Biotechnology*, 1-7.

([*]Authors equally contributed to this work)

APPENDIX D   PARTICIPATION TO CONFERENCES

1. **Reali, M.**, Camus, A., Mausavi Masouleh, S., Botton, G., and Santato, C. Printed Electronics: the Case of Sepia Melanin Ink. 2021 Material Research Society (MRS) Meeting and Exhibit, Boston, Massachusetts, USA, November 29th-December 2nd, 2021. (ORAL)

2. **Reali, M.,** Camus, A., Pezzella, A., MacLeod, J., and Santato, C. Toward a Structure-Property Relationship Phase Diagram for Eumelanin Films. 2021 Material Research Society (MRS) Meeting and Exhibit, Boston, Massachusetts, USA, November 29th-December 2nd, 2021. (ORAL)

3. Camus, A., **Reali, M.**, Beaulieu, G., De Angelis, J., Pellerin, C., Pezzella, A. and Santato, C. Eumelanin: from Molecular State to Film. 2021 Material Research Society (MRS) Meeting and Exhibit, Boston, Massachusetts, USA, November 29th-December 2nd, 2021. (POSTER)

4. **Reali, M.**, and Santato, C. The Issue of Electronic Waste: from a Linear to a New Circular Vision for Electronics. Opsidian switch meeting, Natural Sciences and Engineering Research Council (NSERC) workshop, virtual meeting, Montreal, Quebec, Canada, September 10th, 2021. (ORAL)

5. Santato, C., **Reali, M.**, and Camus, A. En Route Towards Sustainable Electronics and Its Powering Elements. Printed Electronics Symposium, Natural Sciences and Engineering Research Council-Green Electronics Network (NSERC-GreEN) virtual meeting, Calgary, Alberta, Canada, September 2nd, 2021. (ORAL)

6. **Reali, M.**, Camus, A., Pezzella, A., MacLeod, J., and Santato, C. Toward a Structure-Property Relationship Phase Diagram for Eumelanin Films. IEEE International Conference in Nanotechnology (IEEE-NANO 2021), Montreal, Quebec, Canada, July 28th-30th, 2021. (ORAL)

7. **Reali, M.**, Camus, A., and Santato C. Sepia Melanin Ink Printed Electrodes for Energy Storage Applications. Natural Sciences and Engineering Research Council-Green

Electronics Network (NSERC-GreEN) flash presentation virtual meeting, May 5th-6th, 2021. (ORAL)

8. **Reali, M.**, Gouda, A., Bellemare, J., Ménard, D., Nunzi, J. M., Soavi, F., and Santato, C. Electronic Transport in the Biopigment Sepia Melanin: Towards Sustainable Electronics. Regroupement Québécois de Matériaux de Pointe (RQMP), Fall School, Montreal, Quebec, Canada, October 22nd-23rd, 2020. (ORAL)

9. Camus, A., **Reali, M.**, and Santato C. On the Transition from the Molecular to the Thin Film Form: the Case of Eumelanin Biopigment. Regroupement Québécois de Matériaux de Pointe (RQMP), Fall School, Montreal, Quebec, Canada, October 22nd-23rd, 2020. (ORAL)

10. **Reali, M.,** Camus, A., and Santato, C. On the Transition from the Molecular to the Thin Film Form: the Case of Eumelanin Biopigment. Natural Sciences and Engineering Research Council-Green Electronics Network (NSERC-GreEN) flash presentation virtual meeting, June 9th-11th, 2020. (ORAL)

11. **Reali, M.**, Camus, A., Beaulieu, G., De Angelis, J., Pellerin, C., Pezzella, A. and Santato, C. Supramolecular Self-assembly of Chemically Controlled Thin Films of (5,6)-dihydroxyindole and (5,6)-dihydroxyindole-2-carboxyl acid Eumelanin Building Blocks. McGill Molecular Science Mini-Meeting (M&MS 2020), Montreal, Quebec, Canada, June 1st-3rd, 2020. (ORAL)

12. Gouda, A., **Reali, M.**, and Santato, C. Bio-sourced Eumelanin Pigments: Charge Transport Properties and Beyond. 237th Electrochemical Society Meeting (ECS), Montreal, Quebec, Canada, May 10th-14th 2020. (ORAL)

13. **Reali, M.,** Gouda, A., and Santato, C. Bio-sourced Eumelanin Pigments: Charge Transport Properties and Beyond. American Physical Society (APS March Meeting), Denver, Colorado, USA, March 2nd-6th, 2020. (ORAL)

14. Gouda, A., **Reali, M.**, and Santato, C. Charge Transport Properties of Eumelanin Electrodes in Buffered Aqueous Media at Different pH. American Physical Society (APS March Meeting), Denver, Colorado, USA, March 2nd-6th, 2020. (ORAL)

15. **Reali, M.**, Gouda, A., Bellemare, J., Ménard, D., Nunzi, J. M., Soavi, F., and Santato, C. Charge Transport Properties of the Biopigment Sepia Melanin: Towards Sustainable Electronics. 2019 Material Research Society (MRS) Fall Meeting and Exhibit, Boston, Massachusetts, USA, December 1st-6th, 2019. (ORAL)

16. **Reali, M.**, Gouda, A., Bellemare, J., Ménard, D., Nunzi, J. M., Soavi, F., and Santato, C. Evidence of Electronic Transport in the Biopigment Sepia Melanin. 2019 Material Research Society (MRS) Fall Meeting and Exhibit, Boston, Massachusetts, USA, December 1st-6th, 2019. (POSTER)

17. Camus, A., **Reali, M.**, Beaulieu, G., De Angelis, J., Pellerin, C., Pezzella, A., and Santato, C. Self-Assembly and Polymerization in Chemically Controlled Thin Films of Eumelanin Building Blocks. 2019 Material Research Society (MRS) Fall Meeting and Exhibit, Boston, Massachusetts, USA, December 1st-6th, 2019. (POSTER)

18. **Reali, M.,** and Santato, C. Toward a Circular Vision of Electronics. XXVIII International Materials Research Congress (IMRC), Cancun, Quintana Roo, Mexico, August 18th-23rd, 2019. (ORAL)

19. **Reali, M.,** Gouda, A., and Santato, C. Toward a Circular Vision for Electronics. 2019 IEEE Sustainability Through ICT Summit, Montreal, Quebec, Canada, June 18th-19th 2019. (ORAL)

20. **Reali, M.**, Gouda A., and Santato C. Electrical Resistive Switching Behavior of the Biopigment Eumelanin. 2018 Material Research Society (MRS) Meeting and Exhibit, Boston, Massachusetts, USA, November 25th-30th, 2018. (ORAL)

21. **Reali, M.,** Camus, A., Beaulieu, G., Pezzella, A., and Santato, C. Early Stages of the Growth of Melanin Biopigment Films. 2018 Material Research Society (MRS) Meeting and Exhibit, Boston, Massachusetts, USA, November 25th-30th, 2018. (POSTER)

22. **Reali, M.**, Gouda, A., and Santato, C. Detailed Study On the Origin of the Electrical Resistive Switching Behavior of Melanin: Toward Memory Application Devices. International conference on energy, materials, and photonics (EMP18), Montreal, Quebec, Canada, July 8th-10th, 2018. (POSTER)

APPENDIX E LIST OF GRANTS AND AWARDS RECEIVED AT POLYTECHNIQUE MONTREAL

1. July 30th, 2021, 1st place Best Paper Award at the IEEE International Conference in Nanotechnology (IEEE-NANO 2021), Montreal, Quebec, Canada.

2. The manuscript "Electronic and Protonic Transport in Bio-sourced Materials: a New Perspective on Semiconductivity" by **Reali, M.,** Saini, P. and Santato, C. featured in 2020 Materials Advances HOT Articles, November 2020.

3. FRQNT (Fonds de recherche du Quebec-Nature and Technologies), PhD, 2019.

4. CMC Microsystem microfabrication grant, 2017.